ISOBARIC HEAT CAPACITY OF SUPERCRITICAL FLUIDS: EXPERIMENTAL MEASUREMENTS AND MODELING

A Dissertation

Presented to the Faculty of the Graduate School

of Cornell University

in Partial Fulfillment of the Requirements for the Degree of

Doctor of Philosophy

by

Mitchell Price Ishmael

May 2017

ISOBARIC HEAT CAPACITY OF SUPERCRITICAL FLUIDS: EXPERIMENTAL MEASUREMENTS AND MODELING

Mitchell Price Ishmael, Ph. D.

Cornell University 2017

Fluids at high temperature and pressure are commonplace across engineering applications. These fluids are sometimes the product of a harsh environment, as in subsurface operations such as oil and gas development or geothermal energy production, or at other times, exploited for their desirable transport and thermodynamic properties in, for example, chemical extractions and material synthesis. At these elevated conditions, many single and multi-component fluids exist in a supercritical state, where small changes in temperature and pressure cause significant property variations without induction of a phase change. A fluid's isobaric heat capacity (C_p), a property important to most thermal processes, fluctuates strongly in the supercritical region, ranging from a few times the ideal gas state C_p to infinity exactly at the critical point for pure fluids. Accurately capturing the thermophysical behavior of supercritical pure fluids and mixtures is necessary for optimal design and efficient operation of numerous engineering processes that utilize these substances.

The main goal of this research was to increase understanding of isobaric heat capacity property changes in supercritical fluids. The first step in a threefold approach was to design and construct a calorimeter for precise and accurate measurements of C_p in the supercritical region. Second was to carry out experimental C_p measurements for pure fluids and representative fluid mixtures in pressure-temperature-composition regions with only limited available data. Systems studied included: CO_2-methanol, common in supercritical fluid

extraction and chemical processing; CO_2-decane, relevant to tertiary recovery in oil and gas applications; and R1234yf, a low-global-warming-potential drop-in replacement refrigerant for R134a which is currently used in heat pumps and power cycles. And finally, the third step was to use equations of state and molecular simulations to extend C_p data and predict behavior in the supercritical region.

A flow calorimeter was built to operate over a wide range of temperatures (20-150 °C), pressures (1-300 bar), and densities (1-1000 kg/m^3). By precisely placing both the measurement devices and the heating element in direct contact with the fluid, and by limiting experimental heat losses through vacuum insulation and immersion of the entire apparatus in a fluidized thermal bath, the calorimeter achieved ±1% accurate measurements of C_p. To further our ability to model mixtures at supercritical conditions, measurements of CO_2-methanol were compared to Monte Carlo molecular simulation predictions of C_p. The average absolute deviation, when compared to experiment, of the simulation results is comparable with the current state-of-the-art equation of state (4% versus 3%, respectively). However, the molecular simulations were significantly less correct predicting C_p in the near critical region where C_p was most sensitive to small changes in temperature and pressure. This region of greatest sensitivity, called the "heat capacity ridge," was mapped onto temperature-pressure-composition coordinates for CO_2-methanol and CO_2-decane using experimental measurements. For single component fluids and binary mixtures, the subtle difference in the relationship between a fluid's heat capacity ridge and its critical point was demonstrated.

BIOGRAPHICAL SKETCH

Mitchell Ishmael graduated from Rose-Hulman Institute of Technology in Terre Haute, IN, in 2011 with a bachelor's degree in Chemical Engineering and a minor in Economics. As an undergraduate, Mitchell took interest in the field of thermodynamics, especially with respect to energy utilization, storage, and conversion. His interest in these topics brought him to Cornell University in Ithaca, NY, for graduate studies in Materials Science and Engineering. Working under the supervision of Prof. Jefferson Tester, Mitchell has pursued his dream to study the intricacies of classical thermodynamics, described in this thesis, as well as gained exposure to a wide array of sustainable energy topics, both through course work and participation in the Earth-Energy IGERT program. Entrepreneurship also holds Mitchell's interest; he acted as vice president for Technology Entrepreneurship at Cornell for two and half years. In the final year of his studies, he joined the College of Engineering's inaugural class of PhD Commercialization Fellows and learned-by-doing, following lean startup principles to evaluate the commercial potential of an energy storage technology he developed.

ACKNOWLEDGMENTS

Thank you to my primary adviser, Dr. Jefferson Tester. He cares professionally and personally for each of his students, and I still find myself in disbelief sometimes, amazed our paths crossed and happy to work under his tutelage. His interest and enthusiasm crosses the spectrum of sustainable technology and invaluably broadens each of his student's perspectives.

Thank you to my thesis committee members, Dr. Michael Thompson and Dr. Emmanuel Giannelis. Dr. Thompson, my first semester at Cornell, supremely reinforced my background in thermodynamics and has remained a valuable mentor ever since. Dr. Giannelis not only provided access to his lab and student's experimental expertise, but also helped mentor me through the PhD Commercialization Fellowship.

Thank you to Tom Schryver, Ken Rother, Brad Treat, Steve Gal, and Brian Bauer for their mentorship and coaching during the PhD Commercialization Fellowship. And thank you to Doug Buerkle, Jason Salfi, and Devin Sandon for helping me continue my commercialization work through the NEXUS-NY program.

Thank you to Polly Marion. I haven't found a problem, whether it is Cornell's bureaucracy or an issue with a supplier, that Polly can't solve. Her attention to our needs as researchers is second to none, and I am so glad to have worked with her.

Thank you to Will (Billy) Gregg and He (Richard) Wan, both undergraduate researchers who worked for me. Billy contributed to many pieces of many projects; I appreciate his patience with me as I developed my managerial skills. Richard aided in my research on encapsulated phase change materials; I appreciate his continued effort on a very frustrating project.

Thank you to the Tester Research Group. A special thank you to Maciek Lukawski, who worked with me on a number of these projects; he is a thoughtful and hard-working partner. I am very

lucky to have worked with him and hope we will collaborate in the future. And Lauren Stutzman for all of her work on molecular simulations and coauthoring "Heat capacities of supercritical fluid mixtures: Comparing experimental measurements with Monte Carlo molecular simulations for carbon dioxide-methanol mixtures," (*The Journal of Supercritical Fluids* 123 (2017): 40-49.) with me.

Thank you to Glenn Swan for all the early calorimeter part fabrication, then encouraging me to learn to machine on my own. With each part I've made, I appreciate more his skill and the friendly way in which he does his work (whenever I want a creative, simple solution, I go to Glenn). He is an invaluable asset to the College of Engineering.

Thank you to Nate Ellis. Not only for teaching me to machine high quality parts, a skill I'll keep with me throughout my life, but also for all the conversations and council. The accumulated frustration he has seen throughout the years, it's made him at least as good a mentor to students as a machinist. Hope to see you him in TN one day.

A sincere thank you for the financial support that made this work possible, provided by the College of Engineering, Cornell Energy Institute, Atkinson Center for a Sustainable Future, ARPA-E, and The US Department of Energy.

To Mom, Dad, Marsh and Syd, let brevity reflect sincerity: thank you for your love and support.

And finally, to my wife, Betsy Ellis, anybody would want it to be so flat.

TABLE OF CONTENTS

LIST OF FIGURES

LIST OF TABLES

LIST OF ABBREVIATIONS

AWG – American Wire Gauge

Avg. – Average

Avg. Abs. – Average Absolute

CO_2 – Carbon Dioxide

CP – Critical Point

CPU – Central Processing Unit

Crit. – Critical

CEI – Cornell Energy Institute

DOE – Department of Energy

DMFC – Direct Measurement Flow Calorimetry

Decane – n-Decane (or Normal Decane)

DSC – Differential Scanning Calorimetry

EDX – Energy Dispersive X-ray Spectroscopy

EGS – Enhanced Geothermal Systems

EOS – Equation of State

GERG – The European Gas Research Group

GWP – Global Warming Potential

HPLC – High Pressure Liquid Chromatography

ID – Inner Diameter

IGERT – Integrative Graduate Education Research Traineeship

LOESS – Locally Weighted Scatterplot Smoothing

MC – Monte Carlo

MCMS – Monte Carlo Molecular Simulation

MS – Molecular Simulation

Ni-Cr – Nichrome

NPT – Number of moles-Pressure-Temperature

OD – Outer Diameter

ORC – Organic Rankine Cycle

PCM – Phase Change Material

PEG – Polyethylene Glycol

PPG – Polypropylene Glycol

PRT – Platinum Resistance Thermometer

PVT – Pressure-Volume-Temperature

REFPROP – NIST Reference Fluid Thermodynamic and Transport Properties Database

R1234yf – 2,3,3,3-Tetrafluoropropene

R134a – 1,1,1,2-Tetrafluoroethane

SEM – Scanning Electron Microscope

TEOS – Tetraethyl orthosilicate

TraPPE – Transferable Potentials for Phase Equilibria Force Field

UA – United Atom (in association with TraPPE)

vdW EOS – van der Waals Equation of State

VLE – Vapor-Liquid Equilibria

LIST OF SYMBOLS

A – Helmholtz energy	[J/g]
a – van der Waals EOS attractive forces parameter	[L^2bar/mol^2]
B – Maximum work	[J/g]
b – van der Waals EOS excluded volume	[L/mol]
$\underline{C}$ – Generic extensive heat capacity	[J/K]

C – Generic heat capacity [J/gK]

C_p – Isobaric heat capaciy [J/gK]

C_v – Isochoric heat capaciy [J/gK]

E – Electric potential [V]

G – Gibbs free energy [J/g]

H – Enthalpy [J/g]

$\widehat{H}$ – Configurational Enthalpy [J/g]

k – Thermal conductivity [W/m-K]

k_B – Boltzmann's constant [J/K]

l – length [m]

M – Molar mass or molecular weight [g/mol]

$\dot{m}$ – Mass flow rate [kg/s]

N – Number of moles [mol]

$\mathcal{N}$ – Avogadro's number [atoms/mol]

P – Pressure [bar]

$\dot{Q}$ – Heat flow rate [W]

Q – Heat flow [J]

S – Entropy [J/gK]

R – Gas constant [J/molK]

T – Temperature [K or ºC]

U – Internal energy [J/g]

V – Specific volume [m^3/kg]

$\dot{W}$ – Power [W]

W – Work [J]

X – Mole fraction [-]

x – Generic path or property [-]

$\bar{x}$ – Average value [-]

LIST OF GREEK SYMBOLS

α – Thermal diffusivity [m^2/s]

$\propto$ – Proportional to (depending on the context) [not a unit]

α_p – Thermal expansion coefficient [1/K]

β – Thermodynamic beta (or inverse temperature) [1/K]

Δ – Difference [-]

δ – Overall uncertainty in the measured heat capacity [%]

δ_{ij} – Binary interaction parameter [-]

σ – Standard deviation [various]

ε – Thermocouple response or Seebeck coefficient [V/K]

κ_T – Coefficient of isothermal compressibility [1/bar]

λ – Fraction of energy moving through a thermocouple compared to surroundings [-]

μ – Chemical potential [J/g]

μ_{JT} – Joule-Thomson coefficient [°C/bar]

ρ – Density [kg/m^3]

ϕ_{JT} – Isothermal Joule-Thomson coefficient [J/g-bar]

Ω – Density of states [-]

LIST OF SUBSCRIPTS

c – Critical point of working fluid

exp – Experimental value

i, j – Indexing variables

JT – Joule-Thomson

lit – Literature value

mix – Mixture

o – Ideal state

p – Pressure

r – Reduced, i.e., divided by the respective value at the critical point

rand – Random uncertainty

rev – Reversible

sys – Systematic uncertainty

vap – Vaporization (e.g. Vaporization pressure)

* – Condition under study

LIST OF SUPERSCRIPTS

exp – Experimental

MS – Molecular Simulation

o – Ideal state

res – Residual function

ext – Intermolecular forces

‘’ – Representing a flux

* – Condition under study

1. INTRODUCTION AND MOTIVATION

1.1. Introduction to supercritical fluid phenomena

A pure fluid is said to be "supercritical" when both its temperature and pressure are above the fluid's critical temperature and critical pressure (Berche, Henkel, & Kenna, 2009; Cagniard de la Tour, 1822, 1823; Sengers, 1998). In this single phase region of a pure fluid's phase space, when the temperature or pressure of the fluid is increased, there is no point at which multiple macroscopically distinct stable phases occur. Plotted below in Figure 1-1 is a density-pressure diagram for pure CO_2 (carbon dioxide), which shows both sub- and supercritical regions of phase space for CO_2 (Eric W Lemmon, Huber, & Mclinden, 2013; Span & Wagner, 1996).

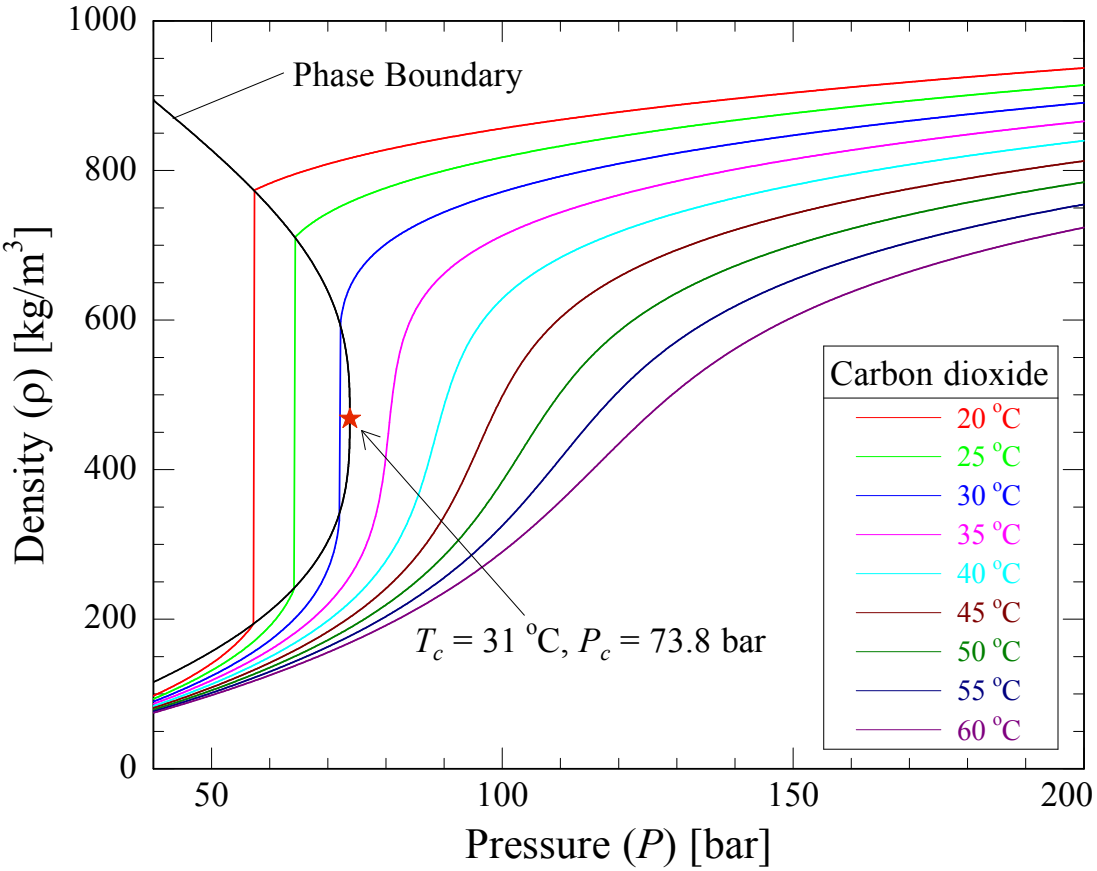

Figure 1-1: Density versus pressure for a number of different isotherms for carbon dioxide (Eric W Lemmon et al., 2013; Span & Wagner, 1996). *The black dome represents the phase boundary separating liquid and vapor states, and it is terminated by a star, the critical point of CO_2.*

Neighboring the critical point in Figure 1-1, large changes in density are possible with only small changes in pressure, at a constant temperature. Significant fluctuations from small perturbations are the hallmark of supercritical fluids, giving them their rich behavior and advantageous properties. Properties such as isothermal compressibility, isobaric heat capacity, and the isobaric expansion coefficient strongly diverge at the critical point, and properties such as the isochoric heat capacity and thermal conductivity weakly diverge at the critical point (Chimowitz, 2005; Sengers, 1998). Solvation and diffusive capabilities in the near critical region are also known to be enhanced (Gallo, Corradini, & Rovere, 2014; Sengers, 1998). Many of these features exist as a consequence of the intermolecular duality of supercritical fluids, liquid-like clusters of molecules dispersed throughout space with the rarity of a vapor (Sengers, 1998)

Assigning the term "supercritical" to multicomponent fluid mixtures is less straightforward. As one example, at the critical point of some binary mixtures, increasing the temperature isobarically can lead to a single phase fluid becoming multiphase (this critical temperature is known as an "upper critical solution temperature"). Instead of using a strict definition, it is more appropriate to label fluids "supercritical" somewhat qualitatively, where, in the proximity to the critical point, fluids see significant changes in their properties with relatively small changes in temperature and pressure. The enhancement of some properties (particularly solubility) and the tunability of others gives supercritical fluids their unique features useful to many of today's industrial applications.

1.2. Industrial applications of supercritical fluids

Supercritical fluids have seen increased adoption over past decades in such areas as chemical extractions, materials processing, and power production (Chen, Goswami, & Stefanakos, 2010; Eckert, Knutson, & Debenedetti, 1996; Herrero, Mendiola, Cifuentes, &

Ibáñez, 2010; Zougagh, Valcarcel, & Rios, 2004). Driving adoption of supercritical fluids (especially carbon dioxide) in both the chemical extraction and materials processing industries is the chemically benign nature (non-toxic, non-flammable) and low cost of the solvent. Perhaps the most well-known application, carbon dioxide is used in the food industry to decaffeinate coffee and tea. Supercritical fluid extractions commonly use co-solvents, such as light hydrocarbons or alcohols, to increase solubility and extraction efficiency (Beckman, 2004; Brennecke & Eckert, 1989). For example, the addition of methanol to supercritical CO_2 has been used to extract soy isoflavones (Herrero et al., 2010), high value pharmaceutical compounds from microalgae (Mendes, Nobre, Cardoso, Pereira, & Palavra, 2003), and divalent metal ions from fly ash (Kersch, van Roosmalen, Woerlee, & Witkamp, 2000). Reprocessing spent nuclear fuel with supercritical fluids is of great interest to the nuclear industry (Wai, 2002).

Many materials synthesis platforms have greatly benefitted from using supercritical fluid technology. Almost every step of polymer processing may use a supercritical solvent (Sengers, 1998). Two such examples are polymerization reactions of fluoropolymers in CO_2 and reactions where the supercritical media is the solvent as well as the reactant (Beckman, 2004; Kiran, 2000). Inorganic materials have also been synthesized using a supercritical fluid platform. Using emulsions of water in carbon dioxide, sometimes referred to as "microreactors," supercritical fluids have been used to synthesize many different types of nanoparticles (Ji, Chen, Wai, & Fulton, 1999; Kometani, Toyoda, Asami, & Yonezawa, 2000; Wai, 2002).

Many aspects of energy production are touched by fluids at supercritical conditions. Deep subsurface conditions, like those encountered in oil and gas and geothermal reservoirs, involve complex multi-component fluids at high temperatures and pressures. Supercritical carbon dioxide has been used commercially to enhance light oil recovery from subsurface reservoirs

(Thomas, 2008). Other subsurface engineering applications such as carbon sequestration and geothermal power production, which includes deep hydrothermal and Enhanced Geothermal Systems (EGS), necessarily require handling near-critical or supercritical fluids. Thermal energy storage, which could help enable intermittent renewable power production, could make use of the large energy density of supercritical fluids (Ganapathi & Wirz, 2012; Lakeh, Lavine, Kavehpour, Ganapathi, & Wirz, 2013; Tse, Ganapathi, Wirz, & Lavine, 2012). As one final example, power generation cycles, especially those that utilize hydrocarbons and refrigerants as working fluids, commonly operate as transcritical cycles (Chen et al., 2010). Operating above the working fluid's critical pressure, transcritical cycles reduce exergetic (second law of thermodynamics) losses by better matching the working fluid temperature to the thermal source temperature, increasing total conversion of thermal energy to electric work. The preponderance of technologies making use of the unique features of supercritical fluids motivates the need for accurate property data and modeling tools.

1.3. Availability of supercritical fluid thermophysical property data

In order to design, construct, and operate equipment for supercritical fluid processing and to determine and optimize process operating conditions, accurate thermophysical property values are required. The natural gas industry, for instance, has recently adopted a new equation of state that is accurate to greater than ±0.1% in density and ±1% in caloric properties for typical gas compositions under pipeline conditions (Kunz & Wagner, 2012). Pure fluids and mixtures used in these large scale operations typically need this level of accuracy. Experimental measurements support almost all other property estimation methods, either through direct measurement with one or more experimental techniques, or experimentally validated calculations using

thermodynamic relationships. By repeating measurements in different laboratories, each with its own method and rigorous uncertainty assessment, a foundation is laid for credible property estimation.

Experimentally measuring supercritical fluid properties is fundamentally more challenging than making measurements at near-atmospheric conditions. Obtaining data far from room temperature on fluids that are both pressurized and compressible requires significant quantities of material for containment and insulation, making the measurement apparatus bulky, costly, time-intensive, and, if poorly constructed, hazardous. For these reasons, as well as the pressure-temperature sensitivity, property data is relatively scarce in the supercritical region (Poling, Prausnitz, & O'Connell, 2001). Derived properties, such as isobaric heat capacity, especially in the near critical region where very slight changes in temperature and pressure (even the effect of gravity) can cause significant measurement and prediction error, can be extremely hard to characterize in the near critical region (Poling et al., 2001). For fluid mixtures, where the bulk of chemical engineering work lies, only a few fluids (natural gas and air) have been well characterized in this region, making optimization of many of the aforementioned processes more difficult (Kunz & Wagner, 2012; E. W. Lemmon, Jacobsen, Penoncello, & Friend, 2000; Span, 2013). New data and improved modeling in this functionally rich region of phase space enables supercritical fluid technologies to reach their potential.

1.4. Estimating the thermophysical properties of supercritical fluids

Equations of state (EOS), frequently used to calculate the thermodynamic properties of fluids, are typically fit by regressing a particular model to experimental data. The accuracy and range of a given EOS, whether it is specific to a single fluid or a particular set of similar fluids,

depends on the measured experimental properties on which it was built. In order to reliably predict properties, accurate experimental data are needed over a broad range of temperatures and pressures for pure fluids and fluid mixtures. Predictive accuracy of fluid properties is compromised when property data are sparse (e.g. for many fluid mixtures) or the thermophysical behavior of the fluid is difficult to measure (e.g. near a fluid's critical point). To satisfy the process simulation and modeling requirements of practicing chemical engineers, highly accurate, multiparameter EOSs are needed for about 1000 pure substances and their mixtures (Span, Wagner, Lemmon, & Jacobsen, 2001). Molecular simulations, though not as widely adopted as EOSs, have found a foothold in property estimation (Allen & Tildesley, 1989) by providing a compelling atomistic depiction of the system's state. Fluid property measurements from across the phase diagram will help continue to advance the intra- and intermolecular interaction models used by these simulations, improving their overall accuracy and utility.

To validate and improve EOSs, other empirically based correlations, and molecular simulations, accurate experimental measurements of thermodynamic properties are required over a range of temperatures, pressures and compositions. Measurements offer a check to current models, from which these models maybe eventually be improved and refined.

1.5. References

Allen, M. P., & Tildesley, D. J. (1989). *Computer simulation of liquids*. Oxford University Press.

Beckman, E. J. (2004). Supercritical and near-critical CO2 in green chemical synthesis and processing. *Journal of Supercritical Fluids*, *28*, 121–191. http://doi.org/10.1016/S0896-8446(03)00029-9

Berche, B., Henkel, M., & Kenna, R. (2009). Critical phenomena: 150 years since Cagniard de la Tour. *J. Phys. Studies*, *13*(3201).

Brennecke, J. F., & Eckert, C. A. (1989). Phase equilibria for supercritical fluid process design. *AIChE Journal*, *35*(9), 1409–1427. http://doi.org/10.1002/aic.690350902

Cagniard de la Tour, C. (1822). Exposé de quelques résultats obtenu par l'action combinée de la chaleur et de la compression sur certains liquides, tels que l'eau, l'alcool, l'éther sulfurique et l'essence de pétrole rectifiée. *Ann. Chim. Phys.*, *21*, 127–132.

Cagniard de la Tour, C. (1823). Nouvelle note sur les effets qu'on obtient par l'application simultanée de la chaleur et de la compression a certains liquides. *Ann. Chim. Phys.*, *22*, 410–415.

Chen, H., Goswami, D. Y., & Stefanakos, E. K. (2010). A review of thermodynamic cycles and working fluids for the conversion of low-grade heat. *Renewable and Sustainable Energy Reviews*, *14*(9), 3059–3067. http://doi.org/10.1016/j.rser.2010.07.006

Chimowitz, E. H. (2005). *Introduction to Critical Phenomena in Fluids*. Oxford University Press.

Eckert, C. A., Knutson, B. L., & Debenedetti, P. G. (1996). Supercritical fluids as solvents for chemical and materials processing. *Nature*, *383*, 313–318.

Gallo, P., Corradini, D., & Rovere, M. (2014). Widom line and dynamical crossovers as routes to understand supercritical water. *Nature Communications*, *5*, 1–6. http://doi.org/10.1038/ncomms6806

Ganapathi, G. B., & Wirz, R. (2012). High Density Thermal Energy Storage With Supercritical Fluids. In *ASME 2012 6th International Conference on Energy Sustainability* (pp. 1–9).

Herrero, M., Mendiola, J. A., Cifuentes, A., & Ibáñez, E. (2010). Supercritical fluid extraction: Recent advances and applications. *Journal of Chromatography A*, *1217*(16), 2495–511. http://doi.org/10.1016/j.chroma.2009.12.019

Ji, M., Chen, X., Wai, C. M., & Fulton, J. L. (1999). Synthesizing and Dispersing Silver Nanoparticles in a Water-in-Supercritical Carbon Dioxide Microemulsion. *Journal of the American Chemical Society*, *121*(11), 2631–2632. http://doi.org/10.1021/ja9840403

Kersch, C., van Roosmalen, M. J. E., Woerlee, G. F., & Witkamp, G. J. (2000). Extraction of

heavy metals from fly ash and sand with ligands and supercritical carbon dioxide. *Industrial and Engineering Chemistry Research*, *39*(12), 4670–4672. http://doi.org/10.1021/ie0002226

Kiran, E. (2000). Polymerizations and Polymer Modification Reactions in Near and Supercritical Fluids. In E. Kiran, P. G. Debenedetti, & C. J. Peters (Eds.), *Supercritical Fluids Fundamentals and Applications*.

Kometani, N., Toyoda, Y., Asami, K., & Yonezawa, Y. (2000). An Application of the Water/ Supercritical CO2 Microemulsion to a Novel "Microreactor ." *Chemistry Letters*, (2), 3–4.

Kunz, O., & Wagner, W. (2012). The GERG-2008 wide-range equation of state for natural gases and other mixtures: An expansion of GERG-2004. *Journal of Chemical and Engineering Data*, *57*(11), 3032–3091. http://doi.org/10.1021/je300655b

Lakeh, R. B., Lavine, A. S., Kavehpour, H. P., Ganapathi, G. B., & Wirz, R. E. (2013). Effect of Laminar and Turbulent Buoyancy-Driven Flows on Thermal Energy Storage using Supercritical Fluids. *Numerical Heat Transfer, Part A: Applications*, *64*(12), 955–973. http://doi.org/10.1080/10407782.2013.811349

Lemmon, E. W., Huber, M. L., & Mclinden, M. O. (2013). *NIST Standard Reference Database 23: Reference Fluid Thermodynamic and Transport Properties-REFPROP, Version 9.1*. Gaithersburg.

Lemmon, E. W., Jacobsen, R. T., Penoncello, S. G., & Friend, D. G. (2000). Thermodynamic properties of air and mixtures of nitrogen, argon, and oxygen from 60 to 2000 K at pressures to 2000 MPa. *Journal of Physical and Chemical Reference Data*, *29*(3), 331–385.

Mendes, R. L., Nobre, B. P., Cardoso, M. T., Pereira, A. P., & Palavra, A. F. (2003). Supercritical carbon dioxide extraction of compounds with pharmaceutical importance from microalgae. *Inorganica Chimica Acta*, *356*, 328–334. http://doi.org/10.1016/S0020-1693(03)00363-3

Poling, B. E., Prausnitz, J. M., & O'Connell, J. P. (2001). *Properties of Gases and Liquids* (5th ed.). McGraw-Hill Education.

Sengers, J. M. H. L. (1998). Supercritical Fluids: Their properties and applications. In E. Kiran, P. G. Debenedetti, & C. J. Peters (Eds.), *Supercritical Fluids Fundamentals and Applications1* (pp. 1–31). Kluwer Academic Publishers.

Span, R. (2013). *Multiparameter Equations of State*. *Journal of Chemical Information and Modeling* (Vol. 53). Springer. http://doi.org/10.1017/CBO9781107415324.004

Span, R., & Wagner, W. (1996). A new EOS for carbon dioxide covering the fluid region from the triple-point temperature to 1100K at pressures up to 800 MPa. *Journal of Physical and Chemical Reference Data*. http://doi.org/10.1063/1.555991

Span, R., Wagner, W., Lemmon, E. W., & Jacobsen, R. T. (2001). Multiparameter equations of state — recent trends and future challenges. *Fluid Phase Equilibria*, *183–184*, 1–20.

http://doi.org/10.1016/S0378-3812(01)00416-2

Thomas, S. (2008). Enhanced Oil Recovery – An Overview. *Oil & Gas Science and Technology*, *63*(1), 9–19. http://doi.org/10.2516/ogst

Tse, L., Ganapathi, G., Wirz, R., & Lavine, A. (2012). SYSTEM MODELING FOR A SUPERCRITICAL THERMAL ENERGY STORAGE SYSTEM. In *ASME 2012 6th International Conference on Energy Sustainability*.

Wai, C. M. (2002). Metal Processing in Supercritical Carbon Dioxide. In Y.-P. Sun (Ed.), *Supercritical Fluid Technology in Materials Science and Engineering*.

Zougagh, M., Valcarcel, M., & Rios, A. (2004). Supercritical fluid extraction: a critical review of its analytical usefulness. *Trends in Analytical Chemistry*, *23*(5), 399–405. http://doi.org/10.1016/S0165-9936(04)00524-2

2. RESEARCH OBJECTIVES AND APPROACH

2.1. Objectives and approach

In order to effectively use and model supercritical fluids, both experimental property data as well as analysis of the accuracy of today's predictive techniques (equations of state, molecular simulation, etc.) are necessary, helping exploit the powerful solvation, heat transfer, and energy storage characteristics of these substances. Particularly, isobaric heat capacity is a fundamental derivative thermodynamic property which exhibits large fluctuations in the vicinity of the critical point which, chiefly for mixtures, must be characterized beyond today's lacking description. The overall objective of this research is to characterize and better understand isobaric heat capacity behavior in the near and supercritical region for representative pure fluid and binary mixtures.

The objective of this thesis is to increase understanding of both pure and mixture supercritical fluid behavior, using accurate experimental measurements of isobaric specific heat capacity to evaluate and enhance our ability to describe their complex behavior. To achieve this end, the following approach was set:

1. Review basic thermodynamic relationships used to estimate fluid heat capacities in the near critical and supercritical region for pure fluids and binary mixtures
2. Review previously demonstrated experimental methods and heat capacity data generated from earlier measurements
3. Design, build and validate an accurate high temperature, high pressure supercritical fluid flow calorimeter (classified as a direct measurement flow calorimeter)

4. Increase the amount of high quality isobaric heat capacity data for supercritical carbon dioxide and supercritical mixtures of carbon dioxide-methanol and -decane as well as for a new, low global-warming-potential refrigerant (R1234yf)
5. Provide an assessment of the current state-of-the-art models used to estimate isobaric heat capacity of complex supercritical fluid mixtures, investigating both equations of state and molecular simulations
6. Clarify the relationship between the path of a fluid's critical isochore on a pressure-temperature plane and the path which a fluid's locus of maximum isobaric heat capacity follows (with respect to isotherms or isobars in the supercritical region)

2.2. Dissertation content

Chapter 1 provided motivation for this work, and Chapters 2-4 set forth the necessary background material, meeting the first two goals and offering context and reference for the thermodynamic methods used in this thesis to measure and describe supercritical fluids.

The first goal of this thesis, from the list above, is primarily addressed in Chaper 6, where the design and validation of the supercritical fluid flow calorimeter are fully documented. Wholly detailing the design of the calorimeter, as well as providing numerous references to previous builds in Chapter 5, helps achieve the main objective of this thesis. By specifying the dimensions, materials, operation, etc. with which the calorimeter was built and run, future researchers may more quickly construct a flow calorimeter, avoiding the plentiful pitfalls and allowing them to pay attention to the most important details. Helping enable future generations of researchers make measurements of their own increases the potential for future understanding of supercritical fluid behavior.

Chapters 6-9 contain high quality experimental measurements obtained with the flow calorimeter described herein. For pure carbon dioxide, the accumulated literature measurement range has been broadened (to 150 °C at pressures from 250-300 bar) (see Chapter 4 for references), and new C_p measurements have been made in the supercritical region for pure R1234yf, a low GWP refrigerant (along 120 and 140 °C isotherms). For both carbon dioxide-methanol and carbon dioxide-decane, isobaric heat capacity measurements at completely new compositions over a wide range of temperatures and pressures have been obtained. Combined, these experimental C_p measurements achieve the fourth listed goal. These data were used to evaluate our ability to model and theoretically describe supercritical fluid mixtures, part of the main thesis objective.

The output from Monte Carlo molecular simulations and the GERG-2008 EOS (Kunz & Wagner, 2012), two advanced methods for calculating property data, were compared to experimental C_p measurements for CO_2-methanol, in the supercritical region, over a wide range of compositions (5-30 mol% methanol). As pure fluids, carbon dioxide and methanol interact in very different ways; the former's intermolecular forces are dominated by primarily weak quadrupolar forces, whereas methanol is bound by hydrogen bonding (Lepilleur, Beckman, Schonemann, & Krukonis, 1997; Potoff & Siepmann, 2001; Roskkar, Dombro, Prentice, Westgate, & McHugh, 1992). The different molecular nature of these fluids provides a difficult modeling challenge for both the molecular simulation and the EOS. In order to evaluate the performance of these two models and meet the fifth goal, systematic uncertainties in the molecular simulations were estimated, and both the average accuracy as well as the pressure-temperature descriptive capability of each model was quantified. This assessment of both predictive techniques increases understanding of how well mixtures of this type are modeled

today, and when coupled with the new experimental data (Lemmon, 2015), this work enhances the capabilities of future models, helping accomplish the main objective of this thesis.

Chapter 8 focuses on a fluid's ridge in isobaric heat capacity, the pressure-temperature path the ridge will follow, and distinguishes the difference in the ridge's behavior for pure fluids and binary mixtures, previously left misleadingly ambiguous in the available literature (see Chapter 8 for references). As the final goal of this thesis, experimentally determined C_p ridges for each mixture were compared with their critical point measurements (Gil et al., 2012; Gurdial, Foster, Yun, & Tilly, 1993), demonstrating the distinctly different behavior of pure supercritical fluids and mixtures. The van der Waals EOS, paired with van Konynenburg and Scott's methods (van Konynenburg & Scott, 1980), was used to fundamentally explain the (potentially) different paths of the critical isochore and the isobaric heat capacity ridge for binary fluid mixtures. By clarifying and refining the theoretical understanding of the C_p ridge, a region of phase space noted for its sensitive properties, one of the main calls of this thesis is answered.

Chapters 6-9 present the main body of work undertaken to achieve the specified objectives and goals. Uniting all the tools an engineer has to work with, experimental measurements, empiricism, and theory, this thesis elucidates and furthers our ability to measure and predict thermodynamic properties of supercritical fluids.

2.3. Author's note

Material from this thesis has been previously published in the following two articles:

Ishmael, Mitchell PE, Maciej Z. Lukawski, and Jefferson W. Tester. "Isobaric heat capacity (C_P) measurements of supercritical fluids using flow calorimetry: equipment design and experimental validation with carbon dioxide, methanol, and carbon dioxide-methanol mixtures." *The Journal of Supercritical Fluids* 117 (2016): 72-79.

Ishmael, Mitchell PE, Lauren B. Stutzman, Maciej Z. Lukawski, Fernando A. Escobedo, and Jefferson W. Tester. "Heat capacities of supercritical fluid mixtures: Comparing experimental measurements with Monte Carlo molecular simulations for carbon dioxide-methanol mixtures." *The Journal of Supercritical Fluids* 123 (2017): 40-49.

2.4. References

Gil, L., Blanco, S. T., Rivas, C., Laga, E., Fernández, J., Artal, M., & Velasco, I. (2012). Experimental determination of the critical loci for {n-C6H14 or CO2 + alkan-1-ol} mixtures. Evaluation of their critical and subcritical behavior using PC-SAFT EoS. *The Journal of Supercritical Fluids*, *71*(0), 26–44. http://doi.org/http://dx.doi.org/10.1016/j.supflu.2012.07.008

Gurdial, G. S., Foster, N. R., Yun, S. L. J., & Tilly, K. D. (1993). Phase Behavior of Supercritical Fluid — Entrainer Systems. In E. Kiran (Ed.), *Supercritical Fluid Engineering Science* (pp. 34–45). Washington, DC: American Chemical Society. http://doi.org/10.1021/bk-1992-0514.ch003

Kunz, O., & Wagner, W. (2012). The GERG-2008 wide-range equation of state for natural gases and other mixtures: An expansion of GERG-2004. *Journal of Chemical and Engineering Data*, *57*(11), 3032–3091. http://doi.org/10.1021/je300655b

Lemmon, E. W. (2015). Personal communication, November 19, 2015. Thermophysical Properties Division, Nation Institute of Standards and technology (NIST).

Lepilleur, C., Beckman, E. J., Schonemann, H., & Krukonis, V. J. (1997). Effect of molecular architecture on the phase behavior of fluoroether-functional graft copolymers in supercritical CO2. *Fluid Phase Equilibria*, *134*, 285–305.

Potoff, J. J., & Siepmann, J. I. (2001). Vapor–liquid equilibria of mixtures containing alkanes, carbon dioxide, and nitrogen. *AIChE J.*, *47*(7), 1676–1682. http://doi.org/10.1002/aic.690470719

Roskkar, V., Dombro, R. A., Prentice, G. A., Westgate, C. R., & McHugh, M. A. (1992). Comparison of the dielectric behavior of mixtures of methanol with carbon dioxide and ethane in the mixture-critical and liquid regions. *Fluid Phase Equilibria*, *77*, 241–259. http://doi.org/10.1016/0378-3812(92)85106-I

van Konynenburg, P., & Scott, R. (1980). Critical lines and phase equilibria. *Philosophical Transactions of the Royal Society of London A: Mathematical, Physical and Engineering Sciences*, *298*(1442), 495–540.

3. BACKGROUND THERMODYNAMICS

3.1. Formal relations between thermodynamic variables and isobaric heat capacity

One goal of classical thermodynamics is to meaningfully relate physically measurable and derived quantities in the context of a set of postulatory constraints that describe the behavior of equilibrium states and systems. For example, using the first and second laws of thermodynamics, we can calculate the theoretically obtainable efficiency of a process from a given set of constraints. Derived properties, such as entropy, play an important role in determining both a system's state and its response to a stimulus, but without defining a formal relationship between these immeasurable properties and physically accessible properties, such as temperature, pressure, or volume, the concepts of thermodynamics are weakened to near irrelevance. Fortunately, through mathematical derivative relations and the path independence of many different thermodynamic state functions, parameters of interest at any set of conditions may be readily related to experimentally measureable quantities.

To the experimentalist, the burden lies in selecting simultaneously both readily measurable properties as well as properties with utility. Related to sensible heat changes, a substance's heat capacity meets both of these criteria. A material's heat capacity, defined in Equation 3-1 as $\underline{C}$, is equal to the flow of heat resultant a differential change in the temperature along path *x*.

$$\underline{C}_x = \lim_{\Delta T \to 0} \left(\frac{\Delta Q}{\Delta T} \right) \Big|_x \qquad (3\text{-}1)$$

The specific heat capacity (C) is defined by normalizing the extensive form of heat capacity ($\underline{C}$) by the mass of the material present. Through selection of the differential's path, the appropriate thermodynamic potential function is designated. For example, consider the first law of

thermodynamics for a simple, closed, pure system, where pressure-volume work is the only relevant work term, shown in Equation 3-2.

$$dU = \delta Q + \delta W = \delta Q - PdV \tag{3-2}$$

In Equation 3-2, U is the internal energy of the system; Q and W are related to flows of thermal energy and work, respectively; P is the system pressure; and V is the system specific volume. Along a path of constant volume, the isochoric heat capacity is then defined as:

$$C_V \equiv \left(\frac{\partial U}{\partial T}\right)_V \tag{3-3}$$

If enthalpy, defined in Equation 3-4, is used as the state function, then under constant pressure conditions, the isobaric heat capacity is defined by Equation 3-5:

$$H \equiv U + PV \tag{3-4}$$

$$C_p \equiv \left(\frac{\partial H}{\partial T}\right)_P \tag{3-5}$$

The definition of isobaric heat capacity can be reformulated using the differential change in entropy (represented as S in Equation 3-6, where Q_{rev} signifies a reversible heat flow) to give Equation 3-7:

$$dS = \frac{\delta Q_{rev}}{T} \tag{3-6}$$

$$\frac{C_p}{T} = \left(\frac{\partial S}{\partial T}\right)_P \tag{3-7}$$

Other forms of heat capacity may be defined. Another common form is a material's heat capacity along a phase boundary, particularly for a liquid in equilibrium with its vapor (Rowlinson & Swinton, 1982).

The particular importance of C_p as a material property is due the prevalence of experimental measurements run under constant pressure conditions. Heat exchange processes in

chemical engineering unit operations are commonly assumed to have negligible pressure losses. Calculations of maximum work using exergy (or availability) for constant pressure flows, defined as B in Equation 3-8, where T_o is the dead state (or the environmental conditions), when rewritten in terms of experimentally measurable temperature changes, make use of the isobaric heat capacity, shown in Equation 3-9.

$$dB = dH - T_o dS \tag{3-8}$$

$$dB = C_p dT \; - T_o \frac{C_p}{T} dT \tag{3-9}$$

In addition to the characteristic description of these processes, C_p, as with all derivative properties, can be interrelated to other thermodynamic variables of interest through transformations such as the triple product rule:

$$-1 = \left(\frac{\partial H}{\partial T}\right)_P \left(\frac{\partial P}{\partial H}\right)_T \left(\frac{\partial T}{\partial P}\right)_H = \frac{C_p \mu_{JT}}{\phi_{JT}} \tag{3-10}$$

Here μ_{JT} is the Joule-Thomson coefficient $\left(\frac{\partial T}{\partial P}\right)_H$, and ϕ_{JT} is the isothermal Joule-Thomson coefficient $\left(\frac{\partial P}{\partial H}\right)_T$, both experimentally important properties. Usefully, only two of these three properties are independent. Isobaric heat capacity also plays an important role in transport phenomena, and it is present in the calculation of thermal diffusivity, α:

$$\alpha = \frac{k}{\rho C_p} \tag{3-11}$$

where k is the thermal conductivity and ρ is the density.

The dependence of a fluid's heat capacity on intensive properties, such as temperature and pressure, is of primary importance. For gases under ideal conditions, C_p is usually obtained using spectroscopic measurements; polynomial expressions are fit against temperature to these data for practical engineering and scientific use (Tester & Modell, 1997). In the ideal gas limit,

C_p is only a function of temperature. Pressure dependence becomes significant only when considering substances whose intermolecular forces play an important role, such as liquids and supercritical fluids. Residual functions are used to calculate thermodynamic property changes due to changes in pressure, typically computed as the difference between the condition of interest and an ideal gas at the same temperature and pressure. The residual function for isobaric heat capacity comes from the interchangeability of second partial derivatives of entropy:

$$\left(\frac{\partial^2 S}{\partial T \partial P}\right)_{T,P} = \left(\frac{\partial \left(\frac{\partial S}{\partial T}\right)_P}{\partial P}\right)_T = \left(\frac{\partial \left(\frac{C_p}{T}\right)}{\partial P}\right)_T = \left(\frac{\partial \left(\frac{\partial S}{\partial P}\right)_T}{\partial T}\right)_P = \left(\frac{-\partial \left(\frac{\partial V}{\partial T}\right)_P}{\partial T}\right)_P \qquad (3\text{-}12)$$

$$= -\left(\frac{\partial^2 V}{\partial T^2}\right)_P$$

At constant temperature, the third and final terms in Equation 3-12 can be integrated to give Equation 3-13, where the '*o*' super- and subscript represents ideal gas behavior:

$$C_p - C_p^o = -T \int_{P_o}^{P} \left(\frac{\partial^2 V}{\partial T^2}\right)_P dP \qquad (3\text{-}13)$$

Unfortunately Equation 3-13 is not of much practical importance because most engineering equations of state (EOS) are pressure explicit and Equation 3-13 is written in terms of a volume differential. To sidestep the volume differential, isobaric heat capacity is related to isochoric heat capacity and its residual function. From the properties of differentials and various thermodynamic relationships:

$$C_p = C_V - \frac{TV{\alpha_p}^2}{\kappa_T} = C_V - \frac{T\left(\frac{\partial P}{\partial T}\right)_V^2}{\left(\frac{\partial P}{\partial V}\right)_T} \qquad (3\text{-}14)$$

Where α_p is the isobaric coefficient of thermal expansion $\frac{1}{V}\left(\frac{\partial V}{\partial T}\right)_P$, and κ_T is the isothermal compressibility $-\frac{1}{V}\left(\frac{\partial V}{\partial P}\right)_T$. Following the same procedure used to derive Equation 3-13, the residual function for the isochoric heat capacity may be obtained:

$$C_V - C_V^o = T\int_\infty^V \left(\frac{\partial^2 P}{\partial T^2}\right)_P dV \qquad (3\text{-}15)$$

Combining Equation 3-14 and Equation 3-15 and using the ideal gas relation ($C_p^{\,o} = C_v^{\,o} + R$), a pressure explicit residual function for isobaric heat capacity may be written:

$$C_p - C_p^o = T\int_\infty^V \left(\frac{\partial^2 P}{\partial T^2}\right)_V dV - T\frac{\left(\frac{\partial P}{\partial T}\right)_V^2}{\left(\frac{\partial P}{\partial V}\right)_T} - R \qquad (3\text{-}16)$$

Using path independence, the isobaric heat capacity for a dense pure fluid or mixture may be obtained using a combination of the ideal gas heat capacity relation and the departure function (either with an appropriate EOS or fluid property data).

3.2. Classical formulation of the critical point

In one formulation of classical thermodynamics, the extremum principle postulates that a system will adopt the macroscopic configuration that maximizes its entropy (equivalently minimize the thermodynamic potential associated with the system's environment), subject to the imposed constraints (Callen, 1985). The extremum principle immediately demands that the shape of the fundamental surface for a material (internal energy as a function volume and entropy for a fixed number of moles of material) be concave up. Therefore, the limit of stability is set of points at which the surface changes concavity; in other words, where the second derivative of the fundamental surface, along any possible path, is zero. However, a system satisfying the criteria

of stability does not guarantee that this system state may be stable with respect to all other potential system configurations. Taken one step further, in order for a system state to be globally stable as opposed to locally stable (i.e. at least meets the stability requirements), a plane tangent to the fundamental surface at the specified point must not touch the surface in any other location; otherwise, a combination of other points on the surface could provide a lower total system free energy. The physical implication of the extremum principle is the presence of multiphase media all with a single temperature, pressure, and chemical potential.

For a pure fluid, there is one point on a phase diagram that is simultaneously globally stable *and* at the limit of stability. It is termed the critical point. Figure 3-1 depicts the termination of a two-phase region by a critical point using the Helmholtz potential (working with the Helmholtz potential (A) instead of the internal energy (U) is a choice of convenience; Helmholtz energy is an explicit function of temperature and volume, which makes the illustration more readily apparent). As the temperature of the fluid is increased from sub- to supercritical, the concavity of the Helmholtz surface becomes strictly concave up.

Stability and critical criterion are closely related. Using the formalism of Gibbs to represent partial derivatives, thermal stability is given by:

$$\left(\frac{\partial^2 U}{\partial S^2}\right)_V = U_{SS} \geq 0 \qquad (3\text{-}17)$$

In order to ensure the surface is concave up irrespective of the path, the Hessian of internal energy must be evaluated:

$$\begin{vmatrix} U_{SS} & U_{SV} \\ U_{VS} & U_{VV} \end{vmatrix} \geq 0 \qquad (3\text{-}18)$$

Equation 3-17 is commonly reformed into the condition of mechanical stability:

$$\frac{\begin{vmatrix} U_{SS} & U_{SV} \\ U_{VS} & U_{VV} \end{vmatrix}}{U_{SS}} = A_{VV} = -\left(\frac{\partial P}{\partial V}\right)_T \geq 0 \qquad (3\text{-}19)$$

A system that is mechanically stable is necessarily thermally stable, but a thermally stable system may not necessarily be mechanically stable. Mechanical stability will thus be of primary importance for pure fluids (Rowlinson & Swinton, 1982).

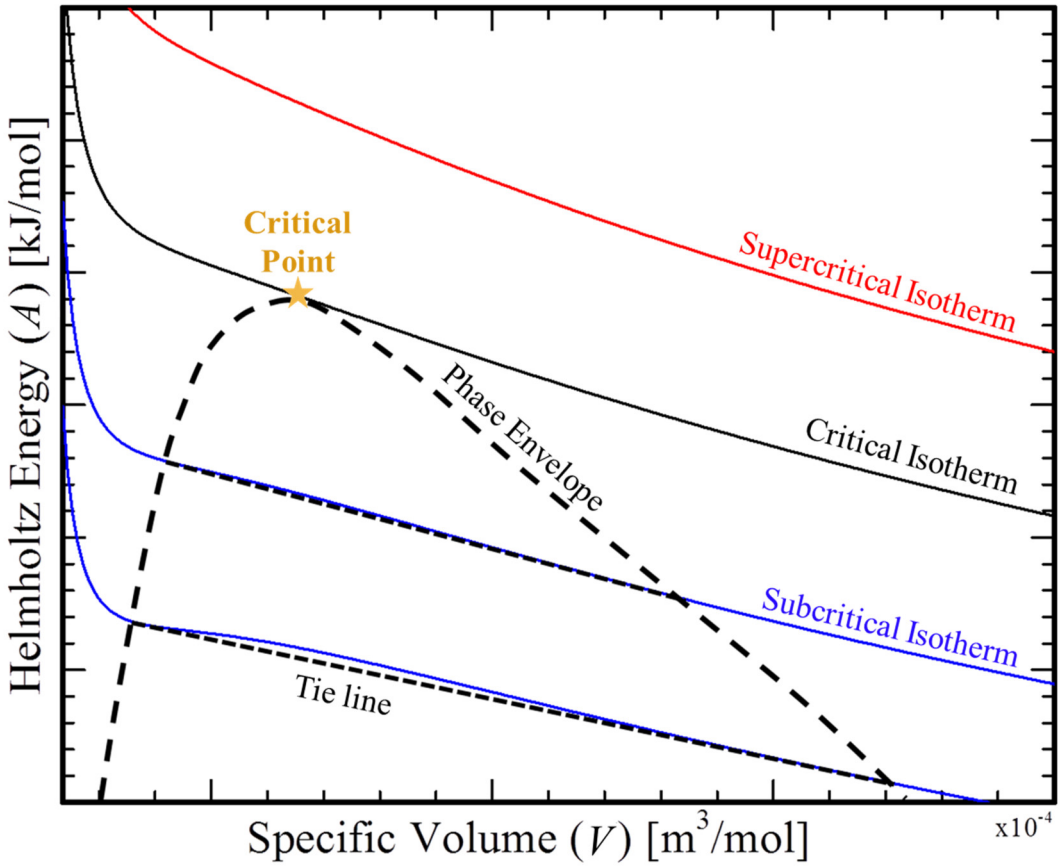

Figure 3-1: Helmholtz energy versus specific volume at four different temperatures for a generic pure fluid. The phase envelope, represented by a large dashed line, is built from the intersections of the tie lines with the subcritical isotherms, and terminates in the critical point, at its apex, represented by a star.

Thermodynamic stability says only that a system state *may* exist, not that it *must* exist. This is the distinction between a locally stable point and a globally stable point. Within the phase envelope exist metastable (locally stable) points that meet the conditions of mechanical stability, but a tangent plane drawn at these locally stable points intersects the fundamental surface at

another position. Given enough time, these metastable states will decompose into multiple globally stable states, whose tangent planes lie completely below the fundamental surface. States at the limit of mechanical stability are generally only locally stable.

With one notable exception, a critical point is a globally stable point at the limit of stability. This stronger statement requires an additional specification beyond Equation 3-19. For a pure fluid the critical point is given by:

$$A_{VV} = -\left(\frac{\partial P}{\partial V}\right)_T = 0 \; ; \; A_{VVV} = -\left(\frac{\partial^2 P}{\partial V^2}\right)_T = 0 \qquad (3\text{-}20)$$

Above a fluid's critical temperature and pressure, a pure fluid does not exhibit a phase change with increasing temperature or pressure, but large property variations in the near critical region are observed for relatively small changes in temperature or pressure. Consider the values of the following properties at a pure fluid critical point:

$$\lim_{State \to CP} C_p = \infty \qquad (3\text{-}21)$$

$$\lim_{State \to CP} \kappa_T = \infty \qquad (3\text{-}22)$$

In both the residual function for C_p (Equation 3-16) and the definition of κ_T, the differential of pressure with respect to volume at constant temperature (negative A_{VV} in Equation 3-20) appears in the denominator; when this derivative approaches zero at the critical point, C_p and κ_T become arbitrarily large.

Density variations of 100% at the critical pressure are common for a few degrees temperature change. Figure 3-2, using carbon dioxide as an example, illustrates the extent of the fluctuations in isobaric heat capacity in the near critical region (Lemmon, Huber, & Mclinden, 2013; Span & Wagner, 1996). There are a number of properties that macroscopic classical thermodynamics incorrectly predict to be finite at the critical point which have proven, through

experiment and statistical mechanical calculations, to diverge weakly at the critical point (Chimowitz, 2005; Poling, Prausnitz, & O'Connell, 2001). Isochoric heat capacity is a good example; it was unexpectedly found to diverge at the critical point (Abdulagatov, Polikhronidi, & Batyrova, 1994; Haupt & Straub, 1999; Polikhronidi, Abdulagatov, Magee, & Stepanov, 2002).

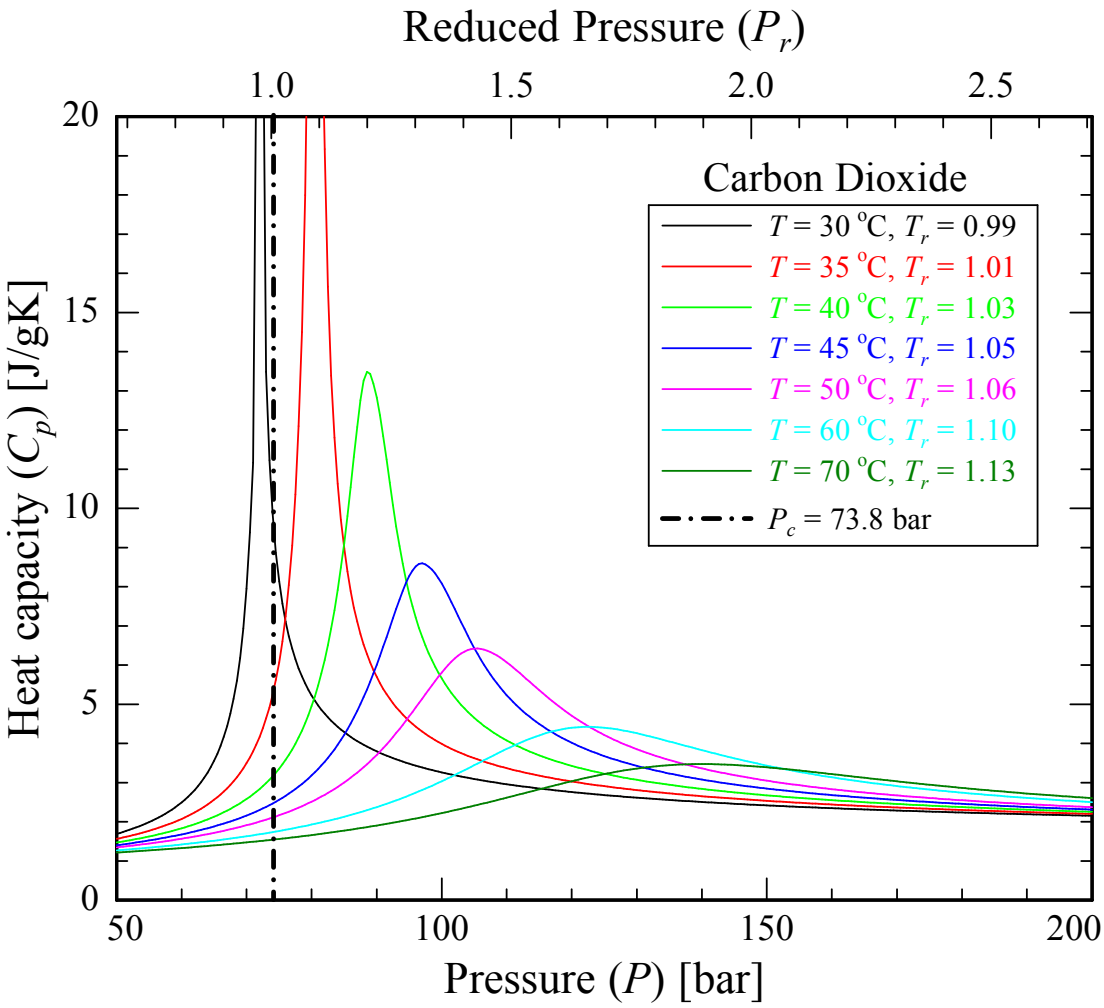

Figure 3-2: Isobaric heat capacity versus pressure for a number of isotherms for carbon dioxide (Span & Wagner, 1996).

Mixture critical behavior deviates from pure fluid critical behavior due to the increase in dimensionality of the system. The mixture composition increases the number of available

parameters for fluctuation. As such, a new stability criteria is defined, the limit of material stability for a binary mixture:

$$\frac{\begin{vmatrix} A_{VV} & A_{XV} \\ A_{VX} & A_{XX} \end{vmatrix}}{A_{VV}} = G_{XX} = \left(\frac{\partial \mu}{\partial X}\right)_{T,P} \geq 0 \qquad (3\text{-}23)$$

The thermodynamic potentials (A and G) reference the substance compositionally referred to by X, written in terms of a mole fraction. The criterion of a critical point for a binary mixture builds off the limit of material stability, including the specification for global stability:

$$G_{XX} = \left(\frac{\partial \mu}{\partial X}\right)_{T,P} = 0 \; ; \; G_{XXX} = \left(\frac{\partial^2 \mu}{\partial X^2}\right)_{T,P} = 0 \qquad (3\text{-}24)$$

For a binary mixture, if the system is materially stable, then it is necessarily mechanically stable, but the inverse statement is not necessarily true (similar to the relationship between thermal and mechanical stability for a pure fluid) (Rowlinson & Swinton, 1982). An azeotrope is an example fluid mixture whose critical point is simultaneously at the limit of material and mechanical stability, and, in this case, the azeotropic mixture's critical behavior is qualitatively the same as that of a pure fluid. A generic mixture's critical point at a given composition will typically be only at the limit of material stability.

Using Equation 3-23, the critical behavior for binary fluid mixtures has been qualitatively mapped by van Konynenburg and Scott using the van der Waal's EOS, which, through years of experimental measurements, has proven the rich qualitative description this EOS can provide (van Konynenburg & Scott, 1980). The features of nearly every binary mixture have been described using this rather simplistic model (Gauter & Peters, 2000; Rowlinson & Swinton, 1982) and many of them have been categorized according to van Konynenburg and Scott's classification system (Hicks & Young, 1975). Extending beyond binary mixtures, stability

criteria can be derived following the same procedure used to produce Equation 3-19 and Equation 3-23 (Beegle, Modell, & Reid, 1974; Tester & Modell, 1997).

The different nature of a generic fluid mixture's critical point has implications for the various derivative properties of interest; for example, a mixture held at a constant composition will exhibit a weakly divergent isobaric heat capacity and isochoric heat capacity will remain finite at the critical point (Chimowitz, 2005). Weakly diverging isobaric heat capacity for a binary mixture is in stark contrast to the strong divergence shown by pure fluids. Increasing the number of components, from binary to ternary mixtures and so forth, continues to change the nature of the stability criteria and the critical point, and it is possible to make predictions about the behavior of derivative properties for each mixture at its critical point (Griffiths & Wheeler, 1970).

3.3. Summary of key thermodynamic relationships

A material's isobaric heat capacity at a given temperature, held at a constant pressure, defines the quantity of thermal energy liberated (or absorbed) by infinitesimally lowering (or raising) the temperature of that substance. The need to account for flows of thermal energy in chemical processes, the experimental accessibility, and the usefulness when calculating other thermodynamic properties, all account for the great degree to which C_p has been studied and will continue to be studied. Supercritical fluids, which exhibit large, phase-change-like thermal effects, yet remain macroscopically single phase, offer complex and rich behavior of C_p for study. In order to calculate a supercritical fluid's heat capacity, a departure function is used, referencing an ideal gas state (Equation 3-16), and corrects for the non-idealities incurred by intermolecular interactions. The appearance of one condition of pure fluid criticality (Equation 3-

20, where A_{VV} equals zero) in the denominator of the C_p departure function illustrates why the fluctuations in heat capacity are extremely pronounced, and hard to measure, in the near- and supercritical region of phase space. Importantly, when a second component is added, the nature of the fluid's critical point changes and so does the behavior of the fluid's heat capacity in the critical region. Accurately capturing, through experiment and calculation, the behavior of isobaric heat capacity in supercritical fluids, explicitly parsing the difference in nature between pure fluids and binary mixtures, are two of the central themes of this work.

3.4. References

Abdulagatov, I. M., Polikhronidi, N. G., & Batyrova, R. G. (1994). Measurements of the isochoric heat capacities Cv of carbon dioxide in the critical region. *J. Chem. Thermodynamics*, *26*, 1031–1045.

Beegle, B. L., Modell, M., & Reid, R. C. (1974). Thermodynamic stability criterion for pure substances and mixtures. *AIChE Journal*, *20*(6), 1200–1206. http://doi.org/10.1002/aic.690200621

Callen, H. B. (1985). *Thermodynamics and an Introduction to Thermostatistics* (2nd ed.).

Chimowitz, E. H. (2005). *Introduction to Critical Phenomena in Fluids*. Oxford University Press.

Gauter, K., & Peters, C. J. (2000). Phase equilibria in near-critical solutions: Binary and ternary mixtures of carbon dioxide and certain solutes and the occurrence of two-phase holes. In *Supercritical Fluids Fundamentals and Applications* (pp. 69–89).

Griffiths, R. B., & Wheeler, J. C. (1970). Critical Points in Multicomponent Systems. *Physical Review A*, *2*(3), 1047–1064.

Haupt, A., & Straub, J. (1999). Evaluation of the isochoric heat capacity measurements at the critical isochore of SF6 performed during the German Spacelab Mission D-2. *Physical Review E*, *59*(2), 1795–1802.

Hicks, C. P., & Young, C. L. (1975). The Gas-Liquid Critical Properties of Binary Mixtures. *Chemical Reviews*, *75*(2), 119–175.

Lemmon, E. W., Huber, M. L., & Mclinden, M. O. (2013). *NIST Standard Reference Database 23: Reference Fluid Thermodynamic and Transport Properties-REFPROP, Version 9.1*. Gaithersburg.

Polikhronidi, N. G., Abdulagatov, I. M., Magee, J. W., & Stepanov, G. V. (2002). Isochoric Heat Capacity Measurements for Heavy Water Near the Critical Point. *International Journal of Thermophysics*, *23*(3), 1–3.

Poling, B. E., Prausnitz, J. M., & O'Connell, J. P. (2001). *Properties of Gases and Liquids* (5th ed.). McGraw-Hill Education.

Rowlinson, J. S., & Swinton, F. L. (1982). *Liquids and Liquid Mixtures* (2nd Editio). Butterworths.

Span, R., & Wagner, W. (1996). A new EOS for carbon dioxide covering the fluid region from the triple-point temperature to 1100K at pressures up to 800 MPa. *Journal of Physical and Chemical Reference Data*. http://doi.org/10.1063/1.555991

Tester, J. W., & Modell, M. (1997). *Thermodynamics and Its Applications* (3rd ed.). Prentice-

Hall.

van Konynenburg, P., & Scott, R. (1980). Critical lines and phase equilibria. *Philosophical Transactions of the Royal Society of London A: Mathematical, Physical and Engineering Sciences*, *298*(1442), 495–540.

4. MACROSCOPIC EQUATIONS OF STATE AND MOLECULAR MODELING APPROACHES TO CALCULATING THERMODYNAMIC PROPERTIES

4.1. Macroscopic equations of state representation of fluid behavior

Chemical engineers routinely estimate fluid behavior and properties using macroscopic equations of state (EOS). These equations can be generally categorized into one of three types: the first being highly empirical, multiparameter equations fit to large collections of experimental data; the second, commonly referred to as the "van der Waals type," follow a corresponding states framework and require fewer input parameters (a generalized cubic EOS can be expressed in five or less parameters (Poling, Prausnitz, & O'Connell, 2001) fit to experimental data (e.g. critical temperature, critical pressure, acentric factor)); the third type, the "cubic crossover" EOS, is distinguished by its attempt to bridge the gap between classical fluid behavior and the universal scaling behavior observed as the critical point is approached (Gregorowicz, O'Connell, & Peters, 1996). Cubic crossover EOSs describe the near critical region by making use of experimentally determined critical exponents.

When experimental data is readily available, more typically the case for common pure fluids and mixtures, multiparameter equations can provide excellent accuracy when estimating pressure-volume-temperature (*PVT*) properties as well as derivative properties (such as C_p, α_p, or κ_T), for example vapor-liquid equilibrium (VLE) density calculations are frequently within 0.1% of experimental measurements (Span, 2013). Fluids with extremely accurate multiparameter equations of state include argon, nitrogen, carbon dioxide, water, methane, and ethylene (Span, 2013). Mixtures with high quality multiparameter EOSs are rarer and generally of lower

accuracy than state-of-the-art pure fluid EOSs, but they offer a distinct advantage in accuracy over van der Waals type EOS, for example with natural gas-like mixtures (Kunz & Wagner, 2012) and air (Lemmon, Jacobsen, Penoncello, & Friend, 2000).

The major advantage of multiparameter EOSs is their high accuracy wherever experimental data is available. Disadvantages with this approach include the empirical nature, which may lead to non-physical results outside of the region where the data has been fit (though checking for non-physical behavior outside of the EOS fitted region is typically checked when constructing the EOS) (Span, 2013). Implementation, though greatly facilitated through advances in computational methods (debugging, etc.) and available software packages, remains a challenge. For mixtures, when weighing the relative merits of multiparameter EOSs, sometimes a marginal increase in accuracy is nullified by the numerous fitted constants these equations require (Frey et al., 2007).

The property estimation workhorse of chemical engineers still follows the corresponding states framework set forth in 1877 by van der Waals. Models of this type offer many advantages in terms of simplicity, few numbers of parameters, and decades of familiarity and published descriptions of their behavior. In Equation 4-1, the van der Waal's EOS (vdW EOS) includes two parameters, *a* and *b*, in its relation of *PVT* properties.

$$P = \frac{RT}{V-b} - \frac{a}{V^2} \qquad (4\text{-}1)$$

$$a = \frac{27R^2T_c^2}{64P_c}\ ; b = \frac{RT_c}{8P_c}\ ; b = \frac{V_c}{3} \qquad (4\text{-}2)$$

A pure fluid's critical point is generally associated with three quantities: the critical temperature, critical pressure, and critical molar volume (or density). The vdW EOS scales its description of a given fluid's behavior in relation to its critical point, the hallmark of the corresponding states

approach. But assigning values to two parameters (a, b) in Equation 4-2 from three potential constants (T_c, P_c, V_c) leaves the process somewhat ambiguous. Using experimentally determined critical temperatures and pressures remains the favored approach as these two quantities are more easily directly measurable and more accurately determinable. Equations of state built around modifications of the vdW EOS are termed 'cubic EOS' because the equations are third order in volume. Most other cubic EOSs have adopted a and b parameters calculated from critical temperatures and pressures, including two of the most beloved, the Redlich-Kwong-Soave EOS and the Peng-Robinson EOS (Peng & Robinson, 1976).

Using the critical temperature and pressure to calculate the a and b parameters is not without consequences; cubic equations of state incorrectly predict the critical molar volume (or density) for most fluids, consequentially lowering the accuracy of density predictions for liquid, compressed gas, and supercritical regions of phase space. Additional parameters, such as Pitzer's accentric factor which is easily measureable and abundantly reported, increase the quality of the most popular cubic EOS employed today (Poling et al., 2001), however, these attempts merely improve but do not solve inaccurate density predictions. Volume-translation represents a distinct attempt to correct misrepresented liquid densities by cubic EOS (Frey et al., 2007). By adjusting the molar volume of the fluid, for example by a constant or through a temperature dependent correction, the original form of the cubic EOS is maintained, simplifying this method's implementation. When using simple volume-translation functions, there is a tradeoff; the local accuracy of the EOS is enhanced at the expense of its universal accuracy (Frey, 2010).

Cubic EOSs' description of fluid behavior readily extends to mixtures. The prevalence of fluid mixtures in chemical engineering operations makes this feature of cubic EOS especially attractive. The most pervasive mixing rules are defined so that mixture EOS maintains the same

functional form as the pure fluid EOS. For example, the mixing rules typically used with the vdW EOS:

$$a_{mix} = \sum_i \sum_j x_i x_j \sqrt{a_i a_j} \qquad (4\text{-}3)$$

$$b_{mix} = \sum_i x_i b_i \qquad (4\text{-}4)$$

Using Equations 4-3 and 4-4, new *a* and *b* terms may be calculated for a given composition and plugged directly into the vdW EOS, essentially averaging the constituent behavior and describing the result as a pure fluid. However, what is gained in ease of implementation is lost in the EOS's predictive capabilities, especially for behavior in the near critical region. By averaging pure fluid parameters in Equations 4-3 and 4-4, the new pseudocritical constants (T_c, P_c, V_c from a_{mix} and b_{mix} via Equation 4-2) allow for calculation of *PVT* properties, but the true mixture critical points differ significantly from those obtained with mixing rules (Poling et al., 2001). It is possible to use mixture critical criteria (e.g. Equation 3-24 for binary mixtures) to fit EOSs to experimental data for mixture critical point, but a combination of tedious math and scarce experimental data make this an impractical solution (Frey, 2010; van Konynenburg & Scott, 1980). As a final note on calculations of constants for cubic EOSs describing mixtures, a mixture dependent binary interaction parameter, δ_{ij}, is often include in the calculation of the a_{mix} parameter:

$$a_{mix} = \sum_i \sum_j x_i x_j (1 - \delta_{ij}) \sqrt{a_i a_j} \qquad (4\text{-}5)$$

Mixing rules encountered throughout industry and academia can be very ad hoc, with little to no theoretical basis, and the buyer must beware. Cubic EOS can provide reasonable descriptions of

pure fluids, but when extended to mixtures such as carbon dioxide-water, these equations provide completely inadequate and misleading information.

The ability of cubic EOSs to represent fluid behavior in the near critical region is suspect (irrespective of the non-classical behavior of fluids *very* near their critical points, such as the divergence of isochoric heat capacity at the critical point of pure fluids). Volume translation is one method for correcting inaccuracies in densities, but the effect on the accuracy of phase equilibria predictions is not appreciable (Frey, 2010). Cubic EOS have been shown to poorly represent the extrema in isobaric heat capacity in the supercritical region, and Gregorowicz et al. have suggested that heat capacity data needs to be included during fitting in order to achieve reasonable thermal property estimates (making the *b* parameter temperature dependent is one way to adjust the model to fit experimental, supercritical thermophysical properties) (Gregorowicz et al., 1996).

Cubic crossover EOSs attempt to marry cubic EOSs' robust behavior and reasonable global accuracy to the universal scaling behavior of near critical fluids, providing a smooth transition between two distinctly different functional forms (Anisimov, Kiselev, Sengers, & Tang, 1992). With this approach, good accuracy in heat capacity calculations has been demonstrated in the near critical region. For carbon dioxide, steam, and ethane, the weak divergence in isochoric heat capacity has been reproduced, and the description of the maxima in isobaric heat capacity has been improved (Chen, Abbaci, Tang, & Sengers, 1990; Chen, Albright, & Sengers, 1990). The powerful ability to smoothly transition between classical and non-classical theory comes at the expense of increased number of parameters required to implement the model (Chen, Albright, et al., 1990).

Table 4-1: Equations of state used in this work

Equation of State	Type	Reference
van der Waals	Cubic EOS	(Tester & Modell, 1997)
Span & Wagner (CO_2)	Multiparameter	(Span & Wagner, 1996)
de Reuck & Craven (Methanol)	Multiparameter	(De Reuck & Craven, 1993)
GERG-2008 (Natural gas mixtures)	Multiparameter	(Kunz & Wagner, 2012)
Tillner-Roth & Baehr (R134a)	Multiparameter	(Tillner-Roth & Baehr, 1994)
Richer et al. (R1234yf)	Multiparameter	(Richter, McLinden, & Lemmon, 2011)

4.2. Monte Carlo molecular simulation of fluid behavior

As opposed to cubic EOSs, which utilize a mean field approximation to calculate individual molecular interactions, molecular simulation methods leverage the enormous leaps in computing power made in the past few decades and can treat each molecule's environment individually. To calculate thermodynamic properties of fluids, two general forms of simulation are used today, molecular dynamics and Monte Carlo methods. Molecular dynamics simulations calculate properties of ergodic systems by time averaging the system states, while Monte Carlo simulations calculate properties from an ensemble average, limiting the Monte Carlo style of modeling strictly to non-dynamic, equilibrium properties (Frenkel & Smit, 2002). When the system under consideration lies within a region with large density fluctuations, for example near a critical point, Monte Carlo simulations are preferred over molecular dynamics simulations because they provide shorter equilibration times (Stutzman, 2016). For this reason Monte Carlo methods were used in collaborative work on molecular simulations in our group to estimate C_p and will be the primary focus of this overview.

In most practical treatments using statistical mechanical to calculate thermodynamic quantities, classical approximations are used with rigorous configurational integrals. For example Equation 4-6 and 4-7 shows a calculation of a generic property, x, in the NPT and grand canonical ensemble, respectively:

$$\langle x \rangle = \frac{\sum_U \sum_V x\, \Omega(N,V,U)\, e^{-\beta(U+PV)}}{\sum_U \sum_V e^{-\beta(U+PV)}} \qquad (4\text{-}6)$$

$$\langle x \rangle = \frac{\sum_U \sum_V x\, \Omega(N,V,U)\, e^{-\beta(U-\mu N)}}{\sum_U \sum_V e^{-\beta(U-\mu N)}} \qquad (4\text{-}7)$$

Here, Ω represents the density of states function. These summations become essentially unmanageable as the system size is increased. The "Metropolis importance sampling algorithm" focuses computational effort on the most statistically important system states, greatly decreasing the size of the summation (Frenkel & Smit, 2002; Metropolis, Rosenbluth, Rosenbluth, Teller, & Teller, 1953). Briefly, the algorithm runs as follows: a molecular move is made (translation, rotation, etc.); the energy of the new system state is calculated; if the new state's energy is lower than the previous state, then the move is accepted, but if the move increases the system's energy, the move is accepted with a probability determined by Boltzmann statistics (Frenkel & Smit, 2002). In this way the Metropolis method directs the model towards the most probable states, restricting the summation to only the most important regions of configurational space.

To account for inter- and intramolecular interactions, simulations use force fields (for example, with terms for coulomb, Lennard Jones, and harmonic potentials). The fitted parameters that describe the assumed potential functions typically come from vapor-liquid equilibria data (Stutzman, 2016). For mixtures, if data are sparse, combining rules such as Lorentz-Berthelot may be used for estimating parameters for dissimilar molecules. Additionally, atoms within a molecule may be treated as single pseudo-atoms to reduce the computational time further (Stutzman, 2016).

As shown in Chapter 3, thermophysical properties can be broken into ideal and residual components, where ideal behavior corresponds to the intramolecular contributions with negligible intermolecular interactions and residual functions account for interactions between

molecular species that affect their potential energy. Monte Carlo molecular simulations of fluids are only useful for calculating the residual behavior (Stutzman, 2016). Similar to EOSs, when considering isobaric heat capacity, Monte Carlo molecular simulations also rely on accurate experimental ideal gas measurements, which are commonly available (Tester & Modell, 1997). The fluctuation method is used to calculate the residual portion of heat capacity (Lagache, Ungerer, Boutin, & Fuchs, 2001), where:

$$C_p^{res} = \mathcal{N}\left[\frac{1}{Nk_BT^2}\left(\langle U^{ext}\widehat{H}\rangle - \langle U^{ext}\rangle\langle\widehat{H}\rangle\right) + \frac{P}{Nk_BT^2}\left(\langle V\widehat{H}\rangle - \langle V\rangle\langle\widehat{H}\rangle\right) - k_B\right] \quad (4\text{-}8)$$

The calculation is done over a number of molecules (N), requiring the quantity to by multiplied by Avogadro's number ($\mathcal{N}$). The intermolecular potential energy is represented by U^{ext}, and the configurational enthalpy is ($\widehat{H}$), which represent a sum of the intermolecular and intramolecular energies and a pressure-volume term (Lagache et al., 2001).

4.3. Summary of equations of state and molecular simulation models used to calculate C_p

The experimental isobaric heat capacities reported in this work are primarily compared to multiparameter equations of state calculations and Monte Carlo molecular simulation results. By comparing accurate measurements to current state-of-the-art models, improvements may be made to said models, particularly to the supercritical fluid region of phase space where property fluctuations are difficult for models to represent (without high quality, fine resolution measurements available for fitting). The van der Waals EOS is used for its ability to qualitatively represent the critical behavior (critical loci, critical end points, etc.) of binary mixtures.

4.4. References

Anisimov, M. A., Kiselev, S. B., Sengers, J. V, & Tang, S. (1992). Crossover approach to global critical phenomena in fluids. *Physica A*, *188*, 487–525.

Chen, Z. Y., Abbaci, A., Tang, S., & Sengers, J. V. (1990). Global thermodynamic behavior of fluids in the critical region. *Physical Review A*, *42*(8), 4470–4484.

Chen, Z. Y., Albright, P. C., & Sengers, J. V. (1990). Crossover from singular critical to regular classical thermodynamic behavior of fluids. *Physical Review A*, *41*(6), 3161–3177.

De Reuck, K. M., & Craven, R. J. B. (1993). *Methanol, international thermodynamic tables of the fluid state, vol. 12*. Blackwell Scientific Publications.

Frenkel, D., & Smit, B. (2002). *Understanding Molecular Simulation: From Algorithms to Applications*. Academic Press.

Frey, K. (2010). *Improving Thermodynamic Property Estimation through Volume Translation*. MIT.

Frey, K., Augustine, C., Ciccolini, R. P., Paap, S., Modell, M., & Tester, J. (2007). Volume translation in equations of state as a means of accurate property estimation. *Fluid Phase Equilibria*, *260*(2), 316–325. http://doi.org/10.1016/j.fluid.2007.07.061

Gregorowicz, J., O'Connell, J., & Peters, C. (1996). Some characteristics of pure fluid properties that challenge equation-of-state models. *Fluid Phase Equilibria*, *116*, 94–101.

Kunz, O., & Wagner, W. (2012). The GERG-2008 wide-range equation of state for natural gases and other mixtures: An expansion of GERG-2004. *Journal of Chemical and Engineering Data*, *57*(11), 3032–3091. http://doi.org/10.1021/je300655b

Lagache, M., Ungerer, P., Boutin, A., & Fuchs, A. H. (2001). Prediction of thermodynamic derivative properties of fluids by Monte Carlo simulation. *Physical Chemistry Chemical Physics*, *3*(19), 4333–4339. http://doi.org/10.1039/b104150a

Lemmon, E. W., Jacobsen, R. T., Penoncello, S. G., & Friend, D. G. (2000). Thermodynamic properties of air and mixtures of nitrogen, argon, and oxygen from 60 to 2000 K at pressures to 2000 MPa. *Journal of Physical and Chemical Reference Data*, *29*(3), 331–385.

Metropolis, N., Rosenbluth, A. W., Rosenbluth, M. N., Teller, A. H., & Teller, E. (1953). Equation of state calculations by fast computing machines. *Journal Chemical Physics*, *21*(6), 1087–1092. http://doi.org/http://dx.doi.org/10.1063/1.1699114

Peng, D.-Y., & Robinson, D. B. (1976). A New Two-Constant Equation of State. *Industrial & Engineering Chemistry Fundamentals*, *15*(1), 59–64. http://doi.org/10.1021/i160057a011

Poling, B. E., Prausnitz, J. M., & O'Connell, J. P. (2001). *Properties of Gases and Liquids* (5th ed.). McGraw-Hill Education.

Richter, M., McLinden, M. O., & Lemmon, E. W. (2011). Thermodynamic Properties of 2, 3, 3, 3-Tetrafluoroprop-1-ene (R1234yf): Vapor Pressure and p–ρ–T Measurements and an Equation of State. *Journal of Chemical & Engineering Data*, *56*(7), 3254–3264.

Span, R. (2013). *Multiparameter Equations of State*. *Journal of Chemical Information and Modeling* (Vol. 53). Springer. http://doi.org/10.1017/CBO9781107415324.004

Span, R., & Wagner, W. (1996). A new EOS for carbon dioxide covering the fluid region from the triple-point temperature to 1100K at pressures up to 800 MPa. *Journal of Physical and Chemical Reference Data*. http://doi.org/10.1063/1.555991

Stutzman, L. B. (2016). *Monte Carlo Molecular Simulations To Determine The Isobaric Heat Capacity Of Co2, Methanol, And Their Mixtures Using Thermodynamic Fluctuations In The Isothermal-Isobaric Ensemble And The Grand Canonical Ensemble*. Cornell University.

Tester, J. W., & Modell, M. (1997). *Thermodynamics and Its Applications* (3rd ed.). Prentice-Hall.

Tillner-Roth, R., & Baehr, H. D. (1994). An international standard formulation for the thermodynamic properties of 1, 1, 1, 2-Tetrafluoroethane (HFC-134a) for temperatures from 170 K to 455 K and pressures up to 70 MPa. *Journal of Physical and Chemical Reference Data*, *23*(5), 657–729.

van Konynenburg, P., & Scott, R. (1980). Critical lines and phase equilibria. *Philosophical Transactions of the Royal Society of London A: Mathematical, Physical and Engineering Sciences*, *298*(1442), 495–540.

5. REVIEW OF ISOBARIC HEAT CAPACITY MEASUREMENT METHODS FOR FLUIDS AT ELEVATED TEMPERATURES AND PRESSURES

5.1. Motivation

When assessing the accuracy of available heat capacity data (or building a new piece of equipment to generate data), understanding the theoretical underpinnings of the measurement is important to ensure that experiments have been (or will be) executed correctly. Many published measurements of isobaric heat capacity exist for pure fluids and mixtures, over a range of conditions, from the ideal gas state to superfluidic conditions to supercriticality, each system utilizing specialized measurement equipment tailored to the application of interest (Ernst & Busser, 1970; Lipa, Swanson, Nissen, Chui, & Isrealsson, 1996; Yarountsev & Medvedev, 1977). Specifically considering the measurements at high temperatures and pressures, three methods are most commonly employed; this review aims to succinctly describe the advantages and disadvantages of each method and to adequately document each method in order to illustrate the numerous experimental approaches undertaken by various reputed researchers.

5.2. Commonly used measurement methods

The three predominate calorimetric methods for measuring a dense, pressurized fluid's isobaric heat capacity are Tian-Calvet calorimetry, Workman calorimetry (also known as the heat-exchange method), and direct-measurement flow calorimetry. Both Tian-Calvet and Workman type calorimeters measure heat capacity through comparative methods, while direct-

measurement flow calorimetry is an absolute measurement. Each has its own advantages and disadvantages, suiting particular methods for particular measurements.

5.2.1. The Tian-Calvet calorimetric method

Tian-Calvet calorimeters measure flows of thermal energy under no-flow conditions in reference to a calibrated standard. Originally developed to measure isothermal heat flows, Tian built the first iteration (Tian, 1924), and Calvet later improved upon the original by carefully constructing symmetrical thermopiles in the measurement cells and including a second test cell to act as a reference (Calvet & Prat, 1963).

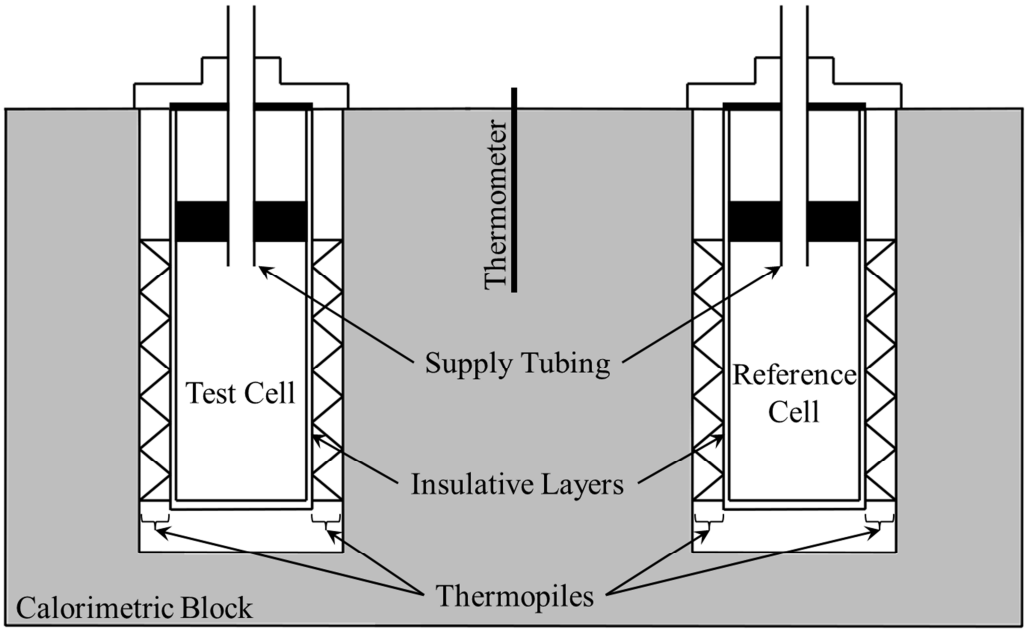

Figure 5-1: Tian-Calvet calorimeter cross section.

As shown in Figure 5-1, each cell is composed of a container to house the material of interest, a thin insulative material, and an array of thermopiles making direct contact between the insulative layer and the surrounding highly conductive calorimetric block. Bilateral symmetry of the calorimetric block is vital to eliminating thermal inhomogeneities and ensuring equal wall temperatures of the calorimetric block in contact with the test and reference cells (Calvet & Prat,

1963). A thermometer measures the temperature of the block. External to the calorimetric block a heater regulates the temperature of the total assembly.

Heat flux is measured at the cell level by the surrounding thermopiles. For a single thermocouple, the thermal energy transfer through its associated cross-sectional area is given by:

$$Q_i'' = \frac{k}{\varepsilon\lambda l} E_i \qquad (5\text{-}1)$$

Where Q'' represents the heat flux, k is the thermal conductivity, ε denotes the Seebeck coefficient, λ signifies the fraction of thermal energy moving through the thermocouple (as opposed to the surrounding area), and E is the electric potential signal. When regularly placed, the prefactor may be treated as a constant allowing the total heat flux may be summed over all i. For a carefully constructed Tian-Calvet cell the heat flux is proportional to the measured potential across the thermopile:

$$Q'' \propto E \qquad (5\text{-}2)$$

Calibration is completed in two steps. First, a "zero" is set by filling each cell with the same reference material. Second, other measurement imperfections are accounted for by filling the test cell with a different, well-characterized material and measuring its properties in comparison to the reference (Attree, Cushing, Ladd, & Pieroni, 1958). Heat capacity measurements are typically made in one of two ways: either a step change in the temperature of the calorimeter block or a gradual temperature ramping is induced (Bessieres, Guirons, Daridon, & Coxam, 2000).

Tian-Calvet calorimeters provide good accuracy when measuring the heat capacities of liquids and liquid mixtures, and one of the main advantages of this technology is the commercial availability of calorimeters of this type. Setaram models C-80 (Coxam, Quint, & Grolier, 1991) and BT 2.15 (Manya, Antal, Kinoshita, & Masutani, 2011) are two such examples. Both of the

major fundamental limitations of this method stem from its static fluid-in-cell arrangement. Because the measurement is made on a constant volume of fluid, the density of the substance of interest must be known, requiring two separate measurements. Some authors have built combination densitometer/calorimeters to mitigate errors in sample density estimation (Bessieres et al., 2000). Using this type of calorimeter to make measurements of compressible fluids, especially those in the near critical region where density fluctuations are large, presents the other major issue with a constant-volume type measurement of a constant pressure property. In order to maintain the system under constant pressure conditions, the inlet tubing connects the test cell to a large reservoir of material. A heat capacity measurement produces mass loss from the test cell to the large reservoir, or vice versa. Quantifying this mass transfer between these two volumes introduces another source of error, again, especially significant in near critical region where large changes in density occur over a small temperature range. Resultant pressure fluctuations during a measurement are also quite significant, up to ±1 bar for example, reducing the system's accuracy and precision (Coxam et al., 1991).

5.2.2. Flow calorimetric methods

In order to avoid the aforementioned inherent challenges of measuring C_p with a static, constant-volume method, flow calorimeters continually move material through the measurement section of the device. The field of flow calorimetry, including both absolute and comparative methods, encompasses numerous techniques to measure flows of thermal energy: Picker flow calorimeters (Fortier, Benson, & Picker, 1976; Picker, Leduc, Philip, & Desnoyers, 1971) for C_p measurements of dilute electrolyte mixtures (Rogers & Pitzer, 1981; Smith-Magowan & Wood, 1981) and enthalpy-of-mixing calorimeters for determination of excess mixing enthalpies

(McGlashan & Stoeckli, 1969; Wormald & Colling, 1983) are two examples of available flow calorimetric techniques (in addition to Workman calorimetry and direct-measurement flow calorimetry). Flow calorimeters designed to measure a substance's isobaric heat capacity approximate the thermodynamic definition as:

$$C_p(T,\ P,\ X)\ \equiv\ \left(\frac{\partial H}{\partial T}\right)_{P,\,X}\ \approx\ \left.\frac{\dot{Q}}{\dot{m}\Delta T}\right|_{low\ \Delta P} \qquad (5\text{-}3)$$

Flow calorimetry involves pumping fluid at a constant rate ($\dot{m}$) through a length of tubing at a specified temperature and pressure, delivering a known amount of thermal energy ($\dot{Q}$) to that fluid, and measuring the resulting temperature rise (ΔT), maintaining a small pressure drop across the measurement tubing (*low* ΔP).

The Workman calorimeter, sometimes referred to as the heat-exchange calorimeter, measures the ratio of C_p^* at the condition of interest to C_p^o at a known, typically ideal, condition. Initially proposed by Burnett (Burnett, 1905) and developed by Workman (Workman, 1930), the technique offers an advantage by eliminating both the necessity of a mass (or volumetric) flow rate measurement as well as a measurement of the heat flow (P. Bishnoi, 1971).

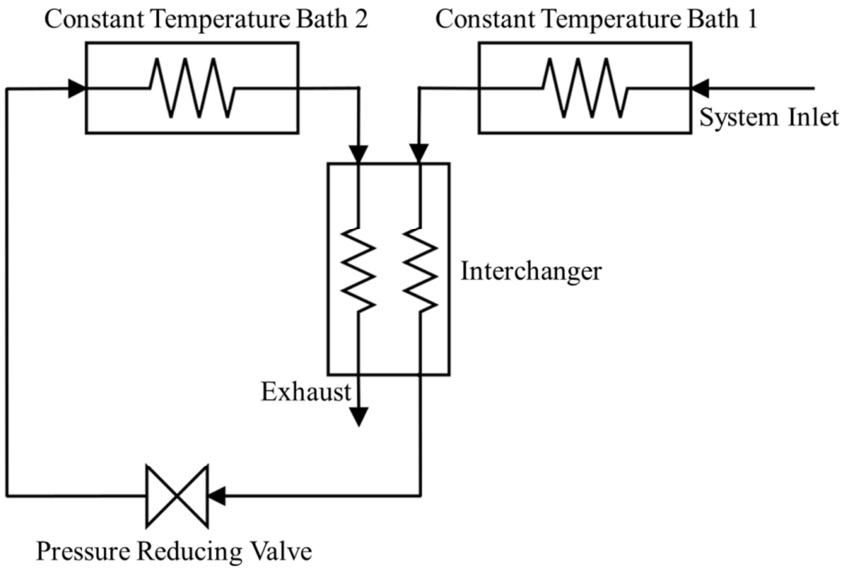

Figure 5-2: Schematic of a Workman-type calorimeter.

Represented in Figure 5-2, the fluid, compressed to the desired pressure, enters Constant Temperature Bath 1 and proceeds to the interchanger, where thermal energy is exchanged between the fluid at the condition of interest and the fluid at an ideal gas condition. The interchanger, a renamed heat exchanger specific to Workman calorimetry, incorporates the flow tubing into a mass of highly conductive material, ensuring the outlets are nearly thermally equilibrated. Following the interchanger, the fluid's pressure is reduced through a valve to ideal gas conditions. The fluid, now under conditions where its properties are known with accuracy, passes through Constant Temperature Bath 2 at a different (generally greater) temperature than Constant Temperature Bath 1. Once through the interchanger, the fluid is exhausted from the system.

The fluid's mass flow rate is constant throughout the system, and if heat loss from the interchanger is eliminated, all of the thermal energy leaving the fluid under pressure (Q_*) must be accepted by the fluid at ideal gas conditions (Q_o):

$$Q_* = -Q_o \tag{5-4}$$

Therefore:

$$\left.\frac{\dot{Q}}{\dot{m}}\right|_* = -\left.\frac{\dot{Q}}{\dot{m}}\right|_o \tag{5-5}$$

Following the flow calorimetric approximation of the definition of isobaric heat capacity shown in Equation 5-3, the heat capacity of the pressurized fluid may be recast in terms of the ideal gas state heat capacity and the measured temperature changes:

$$C_p^* = -C_p^o \frac{\Delta T_o}{\Delta T_*} \tag{4-6}$$

The reduction in the required number of measurements is a significant advantage of the Workman technique, and the abundance of fluids with known ideal properties and easily

experimentally attainable ideal conditions suites this technique to a wide range of pure fluids and fluid mixtures. However, in Workman calorimetry's greatest advantage lies its most profound weakness. First, the properties at the reference condition must be accurate. New refrigerant compounds, for example, may not have experimental data at ideal conditions, requiring two calorimetric systems instead of one. Second, the reference condition must be attainable. Mixture measurements, for example, could exhibit complex phase behavior at ambient pressures, and pulling vacuum at the exhaust would increase the system complexity and not necessarily guarantee ideal gas conditions.

5.2.3. Direct measurement flow calorimetric methods

Direct-measurement flow calorimeters make absolute measurements of each of the quantities in Equation 5-3. Empirical calibration of a system, determining correction factors from experimental measurements of well-characterized fluids, is not uncommon (Fortier et al., 1976; Rogers & Pitzer, 1981; Smith-Magowan & Wood, 1981; White & Downes, 1988). When a correction factor is included, direct-measurement flow calorimetry is no longer a strict absolute measurement and must be considered comparative, with reference to the data with which the equipment was calibrated.

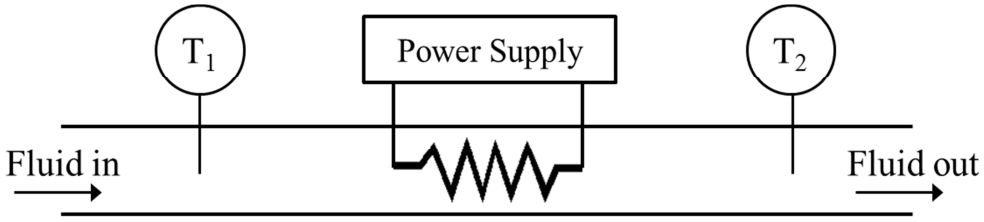

Figure 5-3: Representation of a direct-measurement flow calorimeter.

A flow calorimeter under steady state operating conditions approximates the thermodynamic definition of C_p by replacing differential quantities with finite differences, as shown in Equation

5-3. While maintaining a small pressure drop across the calorimeter, heat $(\dot{Q})$ is continuously added to a fluid at steady mass flow ($\dot{m}$) passing through the calorimeter, and the resulting temperature rise (ΔT) is measured. Equation 5-3 conveys some of the challenges of flow calorimetry: for an accurate measurement, the heat loss must be nearly eliminated or accurately quantified; the fluid must be well-mixed and its mass flow rate needs to be measured accurately; the pressure drop across the calorimeter must be small in order to approximate the isobaric condition; and the loss in accuracy due to approximating differentials with finite quantities needs to be addressed, especially in the near critical region.

As a final note, one convention commonly used in high temperature, high pressure fluid calorimetry must be clarified. In nearly all of the references cited in this Chapter, "direct-measurement flow calorimetry" is referred to simply as "flow calorimetry." This terminology can be misleading as there are many different types of flow calorimeters (Workman, Picker, etc.). Naming the method "direct-measurement flow calorimetry" (for non-comparative methods of measuring isobaric heat capacity, using Equation 5-3) provides some needed refinement to an otherwise extremely broad term. However, in the remainder of this thesis, outside of this Chapter, the common convention is retained; any mention of flow calorimetry refers to the direct-measurement flow calorimetric method.

5.3. Previous isobaric heat capacity measurements of pressurized fluids at elevated temperatures

Table 5-1 provides a list of C_p measurements of pure fluids at elevated temperatures and pressures reported by a number of researchers. The specific measurement techniques that each group used are also given. It should be noted that there are a plethora of indirect methods

available to estimate a substance's heat capacity, such as the triple product relation shown in Equation 3-10 or through density measurements coupled with a residual function (Equation 3-16). Speed of sound measurements are also frequently used for estimating other thermodynamic properties (Estrada-Alexanders, Trusler, & Zarari, 1995). Though related but generally involving significantly different techniques, total enthalpy change measurements were not included because the measurement is not an approximation of the enthalpy differential (Costa & Smith, 1963; Eubank & Smith, 1962; Mccracken, Storvick, & Smith, 1960). Table 4-2 includes similar measurements made on primarily binary fluid mixtures, though a few additional multi-component mixtures such as natural gas have been included. To sum up, Tables 5-1 and 5-2 are not meant to provide a complete listing of experimental C_p measurements. They are a representative group of measurements often utilizing only incremental variations of proven methods.

Table 5-1: Previously published isobaric heat capacity measurements for a range of pure fluids at elevated temperatures and pressures. Direct-measurement flow calorimetery is denoted "DMFC." The symbol "" represents a distinctly different constant volume type method, with no flow. For a more exhaustive list of* C_p *measurements at both ambient and elevated temperatures and pressures please refer to* (Zábranský, Kolská, Růžička, & Domalski, 2010).

Pure Fluid	**Measurement Method**	**Temperature Range [°C]**	**Pressure Range [bar]**	**Accuracy [% of measurement]**	**Reference**
1-Butanol	DMFC	20-190	15	1	(San Jose, Mellinger, & Reid, 1976)
1-Hexanol	Tian-Calvet	15-45	1-600	0.2	(Valencia, Gonza, Troncoso, Carballo, & Romani, 2009)
3-Ethyl-3-pentanol	Tian-Calvet	10-150	600	0.2	(Cerdeirin et al., 2007)
3-Methyl-3-pentanol	Tian-Calvet	10-150	600	0.2	(Cerdeirin et al., 2007)
3-Pentanol	Tian-Calvet	10-150	600	0.2	(Cerdeirin et al., 2007)
Ammonia	DMFC	25-150	1-100	-	(Osborne, Stimson, & Sligh, 1925; Osborne, Stimson, Sligh, & Cragoe, 1925)
Argon	Tian-Calvet	50-150	50-270	1	(Laurent Dordain et al., 1995)
Benzene	DMFC	160-220	20-35	1	(San Jose et al., 1976)
C_2F_5Cl (R115)	DMFC	20-80	0.5-14	0.1	(Ernst & Busser, 1970)
C_6F_{14} (Pefluorohexane)	DMFC	30-150	0.2-1.5	0.15	(Ernst, Gurtner, & Wirbser, 1997a)
Carbon dioxide	DMFC	35-530	1-70	0.5	(Schrock, 1952)
Carbon dioxide	DMFC	60-120	5-900	0.2-0.9	(Ernst, Maurer, &

Pure Fluid	Measurement Method	Temperature Range [°C]	Pressure Range [bar]	Accuracy [% of measurement]	Reference
					Wiederuh, 1989)
Carbon dioxide	DMFC	30	3-520	0.2-1	(Ernst & Hochberg, 1989)
Carbon dioxide	DMFC	10-120	90-250	1-2	(Rivkin & Gukov, 1968)
Carbon dioxide	DMFC	20-50	70-85	1.5	(Koppel & Smith, 1960)
Carbon dioxide	Tian-Calvet	50-150	50-250	1.5	(L. Dordain, Coxam, & Grolier, 1994; Laurent Dordain et al., 1995)
CCl_2F_2 (HFC-142b)	DMFC	0-80	10-30	0.4	(Shinsuke Nakagawa, Hori, Sato, & Watanabe, 1993)
$C_2H_4F_2$ (HFC-152a)	DMFC	0-90	10-30	0.4	(Shinsuke Nakagawa et al., 1993)
$CClF_3$ (R13)	Workman	30-55	15-70	0.8-3	(Hobaica & Stein, 1991)
$CF_2ClCFCl_2$ (R113)	DMFC	20-80	0.2-1.5	0.1	(Ernst & Busser, 1970)
$CF_2ClCFCl_2$ (R113)	DMFC	15-230	6-300	0.2-1	(Wirbser, Brauning, & Ernst, 1992b)
CF_3CHFCF_3 (R227)	DMFC	-20-120	3-150	0.15-3.5	(Wirbser, Brauning, & Ernst, 1992a)
CF_3Cl (R13)	DMFC	0-90	0.5-7	0.15	(Ernst et al., 1997a)
$CFCl_3$ (R11)	DMFC	15-230	6-300	0.2-1	(Wirbser et al., 1992b)
CH_2ClCF_3	DMFC	20-80	0.5-5	0.1	(Ernst & Busser,

Pure Fluid	Measurement Method	Temperature Range [°C]	Pressure Range [bar]	Accuracy [% of measurement]	Reference
					1970)
CH_2FCF_3 (R134a)	DMFC	0-50	10-30	0.3	(Saitoh, Shinsuke, Sato, & Watanabe, 1990)
CH_2FCF_3 (R134a)	Tian-Calvet	-50-10	7.5-180	0.5	(Hykrda, Coxam, & Majer, 2004)
CH_2FCF_3 (R134a)	DMFC	60-150	5-200	0.15	(Ernst, Gurtner, & Wirbser, 1997b)
$C_2Cl_2F_4$ (R114)	DMFC	0-140	5-30	0.4	(Saitoh, Sato, & Watanabe, 1989)
$C_3H_2F_4$ (R1234yf)	Tian-Calvet	30-80	15-50	1.7	(N. Gao, Jiang, Wu, He, & Chen, 2014)
$C_3H_2F_4$ (R1234yf)	DMFC	30-100	15-120	1	(Liu, Zhao, Lv, & He, 2017)
$C_3H_2F_4$ (R1234yf)	Relaxation Method*	40-90	30-50	0.4	(Tanaka, Higashi, Akasaka, & Section, 2010)
C_3HF_7 (R227)	Tian-Calvet	-50-10	11-200	0.5	(Hykrda et al., 2004)
$CH_3CH_2OC(CH_3)_3$	DMFC (cooling)	0-60	1-200	0.5	(Segovia, Vega-Maza, Chamorro, & Martín, 2008)
CHF_2Cl (R22)	DMFC	20-80	0.5-34	0.1	(Ernst & Busser, 1970)
CHF_2Cl (R22)	DMFC	60-80	1-140	0.1	(Bier, Ernst, & Maurer, 1974)
CHF_3 (R23)	DMFC	20-100	0.5-8	0.15	(Ernst et al., 1997a)
Cyclohexane	DMFC	125-250	5-40	1	(San Jose et al., 1976)
Decane	Tian-Calvet	15-45	1-600	0.2	(Valencia et al., 2009)

Pure Fluid	Measurement Method	Temperature Range [°C]	Pressure Range [bar]	Accuracy [% of measurement]	Reference
Dodecane	Tian-Calvet	15-45	1-600	0.2	(Valencia et al., 2009)
Ethane	DMFC	30-120	3-500	0.2-1.2	(Ernst & Hochberg, 1989)
Ethane	DMFC	25-50	45-130	0.4	(Miyazaki, Hejmadi, & Powers, 1980)
Ethanol	DMFC	30-75	5	0.5-0.9	(Miyazawa, Kondo, Suzuki, & Sato, 2012)
$C_2HCl_2F_3$ (HCFC-123)	DMFC	0-170	5-32	0.4	(S Nakagawa, Sato, & Watanabe, 1991)
Heavy water	DMFC	20-450	50-300	0.8	(Rivkin & Egorov, 1959, 1963)
Hexane	Tian-Calvet	15-45	1-600	0.2	(Valencia et al., 2009)
HFE-7000	DMFC	-20-25	1-200	2	(Zheng, Wei, & Song, 2016)
HFE-7100 ($C_4F_9OCH_3$)	DMFC	-20-50	1-200	2	(Zheng et al., 2016)
HFE-7200	DMFC	-25-80	1-150	2	(Zheng, Gao, Chen, Meng, & Wu, 2014)
HFE-7500	DMFC	-25-80	1-150	2	(Zheng et al., 2014)
Isobutane	DMFC	20-80	0.5-8	0.1	(Ernst & Busser, 1970)
Isopropanol	Tian-Calvet	-20-50	1-400	2	(Casás, Plantier, Piñeiro, Legido, & Bessières, 2010)
Kerosene	DMFC*	25-450	24-40	6	(X. K. Gao et al., 2016)
Methane	DMFC	-20-80	1-300	0.2	(Ernst, Keil,

Pure Fluid	Measurement Method	Temperature Range [°C]	Pressure Range [bar]	Accuracy [% of measurement]	Reference
					Wirbser, & Jaeschke, 2001)
Methanol	DMFC	-25-200	5-125	0.3	(Dettmann, Ernst, & Wirbser, 2006)
m-Xylene	DMFC	140-270	10-25	1	(San Jose et al., 1976)
n-Heptane	DMFC	140-240	10-20	1	(San Jose et al., 1976)
n-Hexane	Tian-Calvet	40-400	1-1000	0.6	(Bessieres et al., 2000)
Nitrogen	DMFC	30-150	1-800	0.5	(Mackey & Krase, 1930)
Nitrogen	DMFC	20-150	1-700	0.5	(Mackey & Krase, 1930)
Nonane	Tian-Calvet	15-45	1-600	0.2	(Valencia et al., 2009)
n-Pentane	DMFC	50-250	2-100	0.3	(Sandarusi, Mulia, & Yesavage, 1992)
Oxygen	Workman	25	15-100	-	(Workman, 1930)
Propane	DMFC	20-80	0.5-14	0.1	(Ernst & Busser, 1970)
Propylene	DMFC	70	5	0.2	(Bier et al., 1974)
Tetradecane	Tian-Calvet	15-45	1-600	0.2	(Valencia et al., 2009)
Toluene	DMFC	120-230	10-25	1	(San Jose et al., 1976)
Toluene	DMFC (cooling)	0-60	1-200	0.5	(Segovia et al., 2008)
Tridecane	Tian-Calvet	15-45	1-600	0.2	(Valencia et al., 2009)
Undecane	Tian-Calvet	15-45	1-600	0.2	(Valencia et al.,

Pure Fluid	Measurement Method	Temperature Range [°C]	Pressure Range [bar]	Accuracy [% of measurement]	Reference
					2009)
Water	DMFC	25-400	200-500	0.2-50 (near critical)	(Ernst & Philippi, 1990)
Water	DMFC	120-390	30-260	1	(He, Su, Liu, Qi, & Lv, 2015)
Water	DMFC	50-300	0.8-110	0.3	(Sandarusi et al., 1992)
Water	DMFC	-	-	-	(Sirota, 1958; Sirota & Maltsev, 1962)
Water	-	20-450	30-120	-	(Knoblauch & Koch, 1929)
Water	Tian-Calvet	25-190	40	0.8	(Manya et al., 2011)

Table 5-2: Previously published isobaric heat capacity measurements for a range of fluid mixtures at elevated temperatures and pressures. Symbol "" represents a method by Segovia and co-workers, who simultaneously heat and cool during the measurement.*

Mixture Component 1:2	**Measurement Method**	**Composition [mol% of x_1]**	**Temperature Range [°C]**	**Pressure Range [bar]**	**Accuracy [% of measurement]**	**Reference**
1-Butanol:1-Hexene	DMFC*	0-100	20-40	1-250	0.3	(Torin-Ollarves, Segovia, Mart, & Villaman, 2013)
1-Butanol:Cyclohexane	DMFC*	0-100	20-60	1-250	0.5	(Torín-ollarves, Martín, Chamorro, & Segovia, 2014)
1-Hexene:Ethanol	DMFC*	0-100	40	1-200	0.3	(Vega-maza, Martín, Trusler, & Segovia, 2013)
Carbon dioxide:Decane	Tian-Calvet	50	35-95	200-400	0.6	(Bessieres et al., 2000)
Carbon dioxide:Ethane	DMFC	50	30-120	3-500	0.1-0.2	(Ernst & Hochberg, 1989)
Carbon dioxide:Methane	Workman	50	30-50	7-60	0.6	(Boulton & Stein, 1988)
Carbon dioxide:Methane	Workman	60-85	40-150	7-60	0.6	(P. Bishnoi, 1971)
Carbon dioxide:Methanol	Workman	98-99	50-60	10-80	1	(Boulton & Stein, 1993)
Carbon dioxide:Nitrogen	Workman	70-95	40-90	35-145	0.5-1	(P. R. Bishnoi, Hamaliuk, & Robinson, 1972)
CF_4:CHF_3	Workman	46-52	-10-60	10-120	0.5-2	(Marruffo & Stein, 1991)
Cyclohexane:1-Hexene	DMFC*	0-100	40	1-200	0.3	(Vega-maza et

Mixture Component 1:2	Measurement Method	Composition [mol% of x_1]	Temperature Range [°C]	Pressure Range [bar]	Accuracy [% of measurement]	Reference
						al., 2013)
Cyclohexane:Ethanol	DMFC*	0-100	40	1-200	0.3	(Vega-maza et al., 2013)
Diphenyl ether:Biphenyl	DMFC*	55-100	40-80	1-250	2	(Cabaleiro, Segovia, Martín, & Lugo, 2016)
Hexane:Paraffin	Tian-Calvet	20-100	30-100	1-400	0.4	(Bessieres, Saint-Guirons, Daridon, Xans, & Coxam, 1998)
i-Butane:R115	DMFC	45	20-80	0.5-8	0.1	(Bier, Busser, & Ernst, 1973)
i-Butane:R22	DMFC	45	20-80	0.5-8	0.1	(Bier et al., 1973)
Methane:Ethane	DMFC	85	-20-80	5-300	0.2-1.5	(Ernst, et al., 2001)
Methanol:Acetone	DMFC	25-75	150-250	10-80	0.4	(Mulia & Yesavage, 1999)
Methanol:Water	DMFC	10-90	50-240	20-100	0.3	(Dettmann et al., 2006)
N_2:CF_4:CHF_3	Workman	(33,33,33)	-10-60	10-120	0.5-2	(Marruffo & Stein, 1991)
Natural gas	Tian-Calvet	Many components	150-200	150-400	2	(Barreau, Janneteau, & Gaillard, 1996)
Natural gas	Tian-Calvet	Many components	20-140	1-300	0.5	(Jarrahian, Karami, & Heidaryan, 2014)

Mixture Component 1:2	**Measurement Method**	**Composition [mol% of x_1]**	**Temperature Range [°C]**	**Pressure Range [bar]**	**Accuracy [% of measurement]**	**Reference**
n-Pentane:Acetone	DMFC	25-75	150-250	8-95	0.4	(Mulia & Yesavage, 1999)
Propane:R115	DMFC	50	20-80	0.5-12	0.1	(Bier et al., 1973)
Propane:R22	DMFC	50	20-80	0.5-14	0.1	(Bier et al., 1973)
R11:R113	DMFC	50-50	15-230	6-300	0.2	(Ernst & Wirbser, 2002)
R115:R22	DMFC	20-70	20-80	0.5-7	0.1	(Bier et al., 1973)

5.4. References

Attree, R. W., Cushing, R. L., Ladd, J. A., & Pieroni, J. J. (1958). Differential Calorimeter of the Tian-Calvet Type. *The Review of Scientific Instruments*, *29*(6), 491–496. http://doi.org/10.1063/1.1716233

Barreau, A., Janneteau, P., & Gaillard, K. (1996). Isobaric heat capacity of natural gases. Measurements and modelling. *Fluid Phase Equilibria*, *119*(1–2), 197–212. http://doi.org/10.1016/0378-3812(95)02986-9

Bessieres, D., Saint-Guirons, H., Daridon, J. L., Xans, P., & Coxam, J.-Y. (1998). HEAT CAPACITY OF A SYNTHETIC DISTILLATION CUT + n-HEXANE SYSTEM UNDER PRESSURE. *Journal of Thermal Analysis*, *51*, 923–931.

Bessieres, Guirons, Daridon, & Coxam. (2000). Apparatus for simultaneous determination of the densities and heat capacities of liquids and of liquids with dissolved gas under an extended range of pressure (0.1-100MPa). *Measurement Science Technology*, *11*, N-69-N72.

Bier, K., Busser, J., & Ernst, G. (1973). Experimental heat capacities Cp of non-ideal binary gaseous mixtures from C3H8, i-C4H10, CHF2Cl, and C2F5Cl. *J. Chem. Thermodynamics*, *5*, 83–96.

Bier, K., Ernst, G., & Maurer, G. (1974). Flow apparatus for measuring the heat capacity and the Joule-Thomson coefficient of gases. *The Journal of Chemical Thermodynamics*, *6*(11), 1027–1037. http://doi.org/10.1016/0021-9614(74)90065-2

Bishnoi, P. (1971). *Experimental heat capacities of carbon dioxide-methane mixtures at elevated pressures and the coorrelation of volumetric and thermal properties*. University of Alberta.

Bishnoi, P. R., Hamaliuk, G. P., & Robinson, D. B. (1972). Experimental Heat Capacities of Nitrogen Carbon Dioxide Mixtures at Elevated Pressures. *The Canadian Journal of Chemical Engineering*, *50*, 677–679.

Boulton, J. R., & Stein, F. P. (1988). Effect of pressure on the constant-pressure heat capacity of a methane-carbon dioxide mixture. *J. Chem. Eng. Data*, *198*(8), 196–198.

Boulton, J. R., & Stein, F. P. (1993). The constant pressure heat capacity of supercritical carbon dioxide-methanol and carbon dioxide-ethanol co-solvent mixtures. *Fluid Phase Equilibria*, *91*, 159–176. http://doi.org/10.1016/0378-3812(93)85086-2

Burnett, E. (1905). *The specific heats of fluids as functions of temperature and pressure*. University of Wisconsin.

Cabaleiro, D., Segovia, J. J., Martín, M. C., & Lugo, L. (2016). Isobaric heat capacity at high pressure, density, and viscosity of (diphenyl ether + biphenyl) mixtures. *THE JOURNAL OF CHEMICAL THERMODYNAMICS*, *93*, 86–94. http://doi.org/10.1016/j.jct.2015.09.028

Calvet, E., & Prat, H. (1963). *Recent progress in microcalorimetry*. (H. Skinner, Ed.). John Wiley & Sons.

Casás, L. M., Plantier, F., Piñeiro, M. M., Legido, J. L., & Bessières, D. (2010). Calibration of a low temperature calorimeter and application in the determination of isobaric heat capacity of 2-propanol. *Thermochimica Acta*, *507–508*, 123–126. http://doi.org/10.1016/j.tca.2010.05.012

Cerdeirin, C. A., Troncoso, J., Gonza, D., Garcı, G., Bessie, D., Medeiros, M., … Costas, M. (2007). Heat Capacity of Associated Systems. Experimental Data and Application of a Two-State Model to Pure Liquids and Mixtures. *J. Phys. Chem. B.*, *111*, 1119–1128.

Costa, E. C., & Smith, J. M. (1963). Enthalpy Data for the Benzene-1-Propanol System. *J. Chem. Eng. Data*, *8*(3), 2–4.

Coxam, J.-Y., Quint, J. R., & Grolier, J.-P. (1991). Modification of a C-80 Setaram calorimeter for measuring heat capacities of liquids at temperatures up to 548 K and pressures up to 20 MPa. *J. Chem. Thermodynamics*, *23*, 1075–1083.

Dettmann, C., Ernst, G., & Wirbser, H. (2006). Excess enthalpy HE and massic heat capacity cp of (water + methanol) at temperatures between 323 K and 513 K and pressures up to 10 MPa. *J. Chem. Thermodynamics*, *38*, 56–67. http://doi.org/10.1016/j.jct.2005.03.012

Dordain, L., Coxam, J.-Y., & Grolier, J.-P. E. (1994). Measurements of isobaric heat capacities of gases from 323.15 to 573.15 K up to 30 MPa. *Review of Scientific Instruments*, *65*(10), 3263. http://doi.org/10.1063/1.1144560

Dordain, L., Coxam, J.-Y., Quint, J. R., Grolier, J.-P., Lemmon, E. W., & Penoncello, S. G. (1995). Isobaric Heat Capacities of Carbon Dioxide and Argon Between 323 and 423 K and at Pressures up to 25 MPa. *The Journal of Supercritical Fluids*, *8*, 228–235.

Ernst, G., Keil, B., Wirbser, H., & Jaeschke, M. (2001). Flow-calorimetric results for the massic heat capacity Cp and the Joule–Thomson coefficient of CH4, of (0.85 CH4 + 0.15 C2H6), and of a mixture similar to natural gas. *The Journal of Chemical Thermodynamics*, *33*(6), 601–613. http://doi.org/10.1006/jcht.2000.0740

Ernst, G., & Busser, J. (1970). Ideal and real gas state heat capacities Cp of C3H8, i-C4H10, C2F5Cl, CH2ClCF3, CF2ClCFCl2, and CHF2Cl. *J. Chem. Thermodynamics*, *2*, 787–791.

Ernst, G., Gurtner, J., & Wirbser, H. (1997a). Flow-calorimetric massic heat capacities at low pressures of CF3Cl and CHF3 (refrigerants R13 and R23) and of C6F14 (perfluoro-2-methyl-pentane); vapour pressure curve and critical data of C6F14. *J. Chem. Thermodynamics*, *3*, 1125–1128.

Ernst, G., Gurtner, J., & Wirbser, H. (1997b). Massic heat capacities and Joule–Thomson coefficients of CH2FCF3 (R134a) at pressures up to 30 MPa and temperatures between about 253 K and 523 K. *J. Chem. Thermodynamics*, *3*, 1113–1124.

Ernst, G., & Hochberg, U. E. (1989). Flow-calorimetric results for the specific heat capacity Cp of CO2, of C2H6, and of (0.5CO2 + 0.5C2H6) at high pressures. *J. Chem. Thermodynamics*, *21*, 407–414.

Ernst, G., Maurer, G., & Wiederuh, E. (1989). Flow calorimeter for the accurate determination of the isobaric heat capacity at high pressures; results for carbon dioxide. *The Journal of Chemical Thermodynamics*, *21*(1), 53–65. http://doi.org/10.1016/0021-9614(89)90007-4

Ernst, G., & Philippi, R. (1990). Flow-calorimetric results for the specific heat capacity Cp of water at high pressures between 20 and 50 MPa and temperatures between 298.15 and 673.15 K. *J. Chem. Thermodynamics*, *22*, 211–218.

Ernst, G., & Wirbser, H. (2002). Flow-calorimetric massic heat capacity cp of (0.5CFCl3+0.5CF2ClCFCl2) at pressures up to 30 MPa and temperatures between 288 K and 503 K. *J. Chem. Thermodynamics*, *34*, 573–578. http://doi.org/10.1006/jcht.2002.0758

Estrada-Alexanders, A. F., Trusler, J. P. M., & Zarari, M. P. (1995). Determination of Thermodynamic Properties from the Speed of Sound. *International Journal of Thermophysics*, *16*(3), 663–673.

Eubank, P. T., & Smith, J. M. (1962). Enthalpy Data for Polar Compounds. *Journal of Chemical & Engineering Data*, *7*(1), 75–78. http://doi.org/10.1021/je60012a023

Fortier, J. L., Benson, G. C., & Picker, P. (1976). Heat capacities of some organic liquids determined with the Picker flow calorimeter. *The Journal of Chemical Thermodynamics*, *8*(3), 289–299. http://doi.org/10.1016/0021-9614(76)90108-7

Gao, N., Jiang, Y., Wu, J., He, Y., & Chen, G. (2014). Measurements of the isobaric heat capacity of R1234yf in liquid phase at temperatures from 305 K to 355 K and pressures up to 5 MPa. *Fluid Phase Equilibria*, *376*, 64–68. http://doi.org/10.1016/j.fluid.2014.05.029

Gao, X. K., Wen, X., Zhou, H., Zhu, Q., Wang, J. L., & Li, X. Y. (2016). Novel measurement of isobaric specific heat capacity for kerosene RP-3 at high temperature and high pressure. *Thermochimica Acta*, *638*, 113–119. http://doi.org/10.1016/j.tca.2016.06.015

He, M., Su, C., Liu, X., Qi, X., & Lv, N. (2015). Measurement of isobaric heat capacity of pure water up to supercritical conditions. *The Journal of Supercritical Fluids*, *100*, 1–6. http://doi.org/10.1016/j.supflu.2015.02.007

Hobaica, S. C., & Stein, F. P. (1991). The effect of pressure on the constant-pressure heat capacity of trifluorochloromethane (CClF3). *Fluid Phase Equilibria*, *69*, 235–250.

Hykrda, R., Coxam, J. Y., & Majer, V. (2004). Experimental Determination of Isobaric Heat Capacities of R227 (CF3CHFCF3) from 223 to 283 K at Pressures up to 20 MPa. *International Journal of Thermophysics*, *25*(6), 1677–1694.

Jarrahian, A., Karami, H. R., & Heidaryan, E. (2014). On the isobaric specific heat capacity of natural gas. *Fluid Phase Equilibria*, *384*, 16–24. http://doi.org/10.1016/j.fluid.2014.10.021

Knoblauch, O., & Koch, W. (1929). The Specific Heat of Superheated Steam at Pressures from 30 to 120 Atmospheres and from Saturation Temperatures to 450 C. *Mechanical Engineering*, *51*, 147–150.

Koppel, L. B., & Smith, J. M. (1960). Thermal Properties of carbon dioxide in the critical region. *J. Chem. Eng. Data*, *5*(4), 437–440.

Lipa, J. A., Swanson, D. R., Nissen, J. A., Chui, T. C. P., & Isrealsson, U. E. (1996). Heat Capacity and Thermal Relaxation of Bulk Helium very near the Lambda Point. *Physical Review Letters*, *76*(6), 944–947.

Liu, Y., Zhao, X., Lv, S., & He, H. (2017). Isobaric Heat Capacity Measurements for R1234yf from 303 to 373 K and Pressures up to 12 MPa. *J. Chem. Eng. Data*, (2). http://doi.org/10.1021/acs.jced.6b00959

Mackey, B. H., & Krase, N. W. (1930). Specific Heats of Gases at High Pressures, III-Results for Nitrogen to 150 C and 700 atmospheres. *Industrial & Engineering Chemistry*, *22*(10), 1060–1062. http://doi.org/10.1021/ie50250a015

Manya, J. J., Antal, M. J., Kinoshita, C. K., & Masutani, S. M. (2011). Specific Heat Capacity of Pure Water at 4.0 MPa between 298.15. *Industrial & Engineering Chemistry Research*, *50*, 6470–6484.

Marruffo, F., & Stein, F. P. (1991). The effect of pressure on the constant-pressure heat capacity of CF4-CHF3 and N2-CF4-CHF3 mixtures. *Fluid Phase Equilibria*, *69*, 235–250.

Mccracken, P. G., Storvick, S. S., & Smith, J. M. (1960). Phase behavior from enthalpy measurements, Benzene-Ethyl Alcohol and n-Pentane-Ethyl Alcohol Systems. *J. Chem. Eng. Data*, *5*(2), 3–5.

McGlashan, M., & Stoeckli, H. (1969). A flow calorimeter for enthalpies of mixing, The enthalpy of mixing of n-hexane + cyclohexane at 298.15 K. *Journal of Chemical Thermodynamics*, (6), 589–594.

Miyazaki, T., Hejmadi, A. V., & Powers, J. E. (1980). A new high-pressure recycle-flow calorimeter and results of determinations with ethane. *The Journal of Chemical Thermodynamics*, *12*(2), 105–124. http://doi.org/10.1016/0021-9614(80)90122-6

Miyazawa, T., Kondo, S., Suzuki, T., & Sato, H. (2012). Specific heat capacity at constant pressure of ethanol by flow calorimetry. *Journal of Chemical & Engineering Data*, *57*, 1700–1707.

Mulia, K., & Yesavage, V. F. (1999). Isobaric heat capacity measurements for the n -pentane – acetone and the methanol – acetone mixtures at elevated temperatures and pressures. *Fluid Phase Equilibria*, *158–160*, 1001–1010.

Nakagawa, S., Hori, T., Sato, H., & Watanabe, K. (1993). Isobaric Heat Capacity for Liquid 1-Chloro-1, 1-difluoroethane and 1,1-Difluoroethane. *J. Chem. Eng. Data*, *38*, 70–74.

Nakagawa, S., Sato, H., & Watanabe, K. (1991). Isobaric Heat Capacity Data for Liquid HCFC-123 (CHC12CF3, 2,2-Dichloro-1,1,1-trifluoroethane). *J. Chem. Eng. Data*, *123*(6), 156–159.

Osborne, N. S., Stimson, H. F., & Sligh, T. S. (1925). A FLOW CALORIMETER FOR SPECIFIC HEATS OF GASES. *Scientific Papers of the Bureau of Standards*, *20*(503).

Osborne, N. S., Stimson, H. F., Sligh, T. S., & Cragoe, C. S. (1925). Specific heat of superheated ammonia vapor. *Govt. Print Off.*, *20*(501).

Picker, P., Leduc, P., Philip, P. R., & Desnoyers, J. E. (1971). Heat capacity of solutions by flow microcalorimetry. *J. Chem. Thermodynamics*, *3*, 631–642.

Rivkin, S. L., & Egorov, B. N. (1959). Experimental investigation of the heat capacity of heavy water. *Atomnaya Energiya*, *7*(5), 462–465.

Rivkin, S. L., & Egorov, B. N. (1963). SPECIFIC HEAT OF HEAVY WATER AT HIGH TEMPERATURES AND PRESSURES. *Atomnaya Energiya*, *14*(4), 4-16–418.

Rivkin, & Gukov. (1968). Experimental study of the isobaric specific heat of carbon dioxide at supercritical pressures. *Teploenergetika*, *15*(10), 72–75.

Rogers, P. S. Z., & Pitzer, K. S. (1981). High-Temperature thermodynamic properties of aqueous sodium sulfate solutions. *Journal of Physical Chemistry*, *85*(4), 2886–2895. http://doi.org/10.1021/j150620a008

Saitoh, A., Sato, H., & Watanabe, K. (1989). A new apparatus for the measurement of the isobaric heat capacity of liquid refrigerants. *International Journal of Thermophysics*, *10*(3), 649–659.

Saitoh, A., Shinsuke, N., Sato, H., & Watanabe, K. (1990). Isobaric Heat Capacity Data for Liquid HFC-134a. *J. Chem. Eng. Data*, *35*, 107–110.

San Jose, J. L., Mellinger, G., & Reid, R. C. (1976). Measurement of the isobaric heat capacity of liquids and certain mixtures above the normal boiling point. *Journal of Chemical and Engineering Data*, *21*(4), 414–417.

Sandarusi, J. a., Mulia, K., & Yesavage, V. F. (1992). An automated flow calorimeter for the determination of liquid and vapor isobaric heat capacities: Test results for water and n-pentane. *Review of Scientific Instruments*, *63*(2), 1810. http://doi.org/10.1063/1.1143342

Schrock, V. E. (1952). *Calorimetric determination of constant-pressure specific heats of carbon dioxide at elevated pressures and temperatures*.

Segovia, J. J., Vega-Maza, D., Chamorro, C. R., & Martín, M. C. (2008). High-pressure isobaric heat capacities using a new flow calorimeter. *The Journal of Supercritical Fluids*, *46*(3), 258–264. http://doi.org/10.1016/j.supflu.2008.01.011

Sirota, A. M. (1958). Specific heat and enthalpy of steam at supercritical pressures. *Teploenergetika*, *5*(7), 10–13.

Sirota, A. M., & Maltsev, B. K. (1962). Experimental determination of the heat capacity of Water in the Critical Region. *Teploenergetika*, *9*(1), 52–61.

Smith-Magowan, D., & Wood, R. H. (1981). Heat capacity of aqueous sodium chloride from 320 to 600 K measured with a new flow calorimeter. *The Journal of Chemical Thermodynamics*, *13*(11), 1047–1073. http://doi.org/10.1016/0021-9614(81)90004-5

Tanaka, K., Higashi, Y., Akasaka, R., & Section, E. (2010). Measurements of the Isobaric Specific Heat Capacity and Density for HFO-1234yf in the Liquid State. *J. Chem. Eng. Data*, *55*, 901–903.

Tian, A. (1924). Mesures des intensités des petites sources de chaleur: emploi d'un microcalorimètre à compensation. *CR Acad. Sci*, *178*, 705–707.

Torín-ollarves, G. A., Martín, M. C., Chamorro, C. R., & Segovia, J. J. (2014). Densities, viscosities , and isobaric heat capacities of the system (1-butanol + cyclohexane) at high pressures. *J. Chem. Thermodynamics*, *74*, 153–160. http://doi.org/10.1016/j.jct.2014.01.020

Torin-Ollarves, G. A., Segovia, J. J., Mart, M. C., & Villaman, M. A. (2013). Density, Viscosity, and Isobaric Heat Capacity of the Mixture (1-Butanol + 1-Hexene). *J. Chem. Eng. Data*, *58*, 2717–2723.

Valencia, L., Gonza, D., Troncoso, J., Carballo, E., & Romani, L. (2009). Thermophysical Characterization of Liquids Using Precise Density and Isobaric Heat Capacity Measurements As a Function of Pressure. *J. Chem. Eng. Data*, *54*, 904–915.

Vega-maza, D., Martín, M. C., Trusler, J. P. M., & Segovia, J. J. (2013). Heat capacities and densities of the binary mixtures containing ethanol, cyclohexane or 1-hexene at high pressures. *The Journal of Chemical Thermodynamics*, *57*, 550–557. http://doi.org/10.1016/j.jct.2012.07.018

White, D. R., & Downes, C. J. (1988). Heat loss corrections for heat capacity flow calorimeters. *Journal of Solution Chemistry*, *17*(8), 733–750. http://doi.org/10.1007/BF00647419

Wirbser, H., Brauning, G., & Ernst, G. (1992a). Flow-calorimetric specific heat capacities and Joule Thomson coefficients of CF3CHFCF3 (R227) - a new working fluid in energy technics - at pressures up to 15 MPa and temperatures between 253 K and 423 K. *J. Chem. Thermodynamics*, *3*, 761–772.

Wirbser, H., Brauning, G., & Ernst, G. (1992b). Flow-calorimetric specific heat capacities of the refrigerants CFCl3 (R11) and CF2ClCFCl2 (R113) at pressures between 0.6 MPa and 30 MPa and temperatures between 288.15 K and 503.15 K. *J. Chem. Thermodynamics*, *2721*, 783–784.

Workman, E. J. (1930). A new method of measuring the variation of the specific heats (Cp) of gases with pressure. *Physical Review*, *36*(6), 1083–1090.

Wormald, C. J., & Colling, C. N. (1983). Excess enthalpies (water + nitrogen) (g) up to 698.2 K and 12.6 MPa. *Journal of Chemical Thermodynamics*, *15*, 725–737. http://doi.org/10.1016/0021-9614(85)90141-7

Yarountsev, & Medvedev. (1977). Measurement of isobarbic specific heat of He4 and He-He2 mixtures. *Cryogenics*, (September), 509–517.

Zábranský, M., Kolská, Z., Růžička, V., & Domalski, E. S. (2010). Heat capacity of liquids: Critical review and recommended values. Supplement ii. *Journal of Physical and Chemical Reference Data*, *39*(1), 3–404. http://doi.org/10.1063/1.3182831

Zheng, Y., Gao, H., Chen, Q., Meng, X., & Wu, J. (2014). Isobaric heat capacity measurements of liquid HFE-7200 and HFE-7500 from 245 to 353 K at pressures up to 15 MPa. *Fluid Phase Equilibria*, *372*, 56–62. http://doi.org/10.1016/j.fluid.2014.03.017

Zheng, Y., Wei, Z., & Song, X. (2016). Fluid Phase Equilibria Measurements of isobaric heat capacities for HFE-7000 and HFE-7100 at different temperatures and pressures. *Fluid Phase Equilibria*, *425*, 335–341. http://doi.org/10.1016/j.fluid.2016.06.024

6. FLOW CALORIMETER DESIGN, CONSTRUCTION, AND CALIBRATION

6.1. Previously published material describing flow calorimeter design, construction, and calibration

The work described in this chapter has been documented in the following article: Ishmael, Mitchell P. E., Maciej Z. Lukawski, and Jefferson W. Tester. "Isobaric heat capacity (C_P) measurements of supercritical fluids using flow calorimetry: equipment design and experimental validation with carbon dioxide, methanol, and carbon dioxide-methanol mixtures." *The Journal of Supercritical Fluids* 117 (2016): 72-79.

6.2. Selection of the flow calorimetric system

Of the most commonly used high pressure calorimetric systems listed in Chapter 5, the direct-measurement flow calorimeter (for the remainder of this work referred to simply as "flow calorimeter") offers the most flexibility in terms of fluid composition and accuracy in the supercritical region. Flow calorimeters of this type have been well documented by Ernst and coworkers (Bier, Busser, & Ernst, 1973; Bier, Ernst, & Maurer, 1974; Ernst, Keil, Wirbser, & Jaeschke, 2001; Ernst, Maurer, & Wiederuh, 1989; Ernst & Philippi, 1990; Wirbser, Brauning, & Ernst, 1992), and each modification to their apparatus offered insight into successful design of these delicate systems. For its robust measurement capabilities and available documentation, the flow calorimeter was chosen as the experimental tool best fit to achieve the objective and goals of this work.

6.3. Description of flow system

As shown in Figure 6-1, a dual syringe pump (1A) draws a compressible fluid from a gas cylinder (1B) and dispenses it through a check valve (1C) at a constant volumetric flow rate into one port of a mixing tee (1F). A second component enters through the other port of the mixing tee pumped by a reciprocating positive displacement pump (1E), also operating at constant volumetric flow rate. The mass flow rate of the incompressible fluid is measured using a scale (1D) and a stop watch. The fluid mixture, exiting the mixing tee, enters a Coriolis mass flow meter (1G) where the mixture flow rate is measured. Next, the fluid passes through three sections of tubing placed inside of a temperature controlled fluidized alumina bath (1J): a preheat section, the calorimeter assembly, and an exhaust section. Preheat and exhaust tubing (1K and 1L) ensure temperature stability of the fluid at the inlet and outlet of the calorimeter assembly, and the thermal bath maintains a temperature stability of ±0.1 °C.

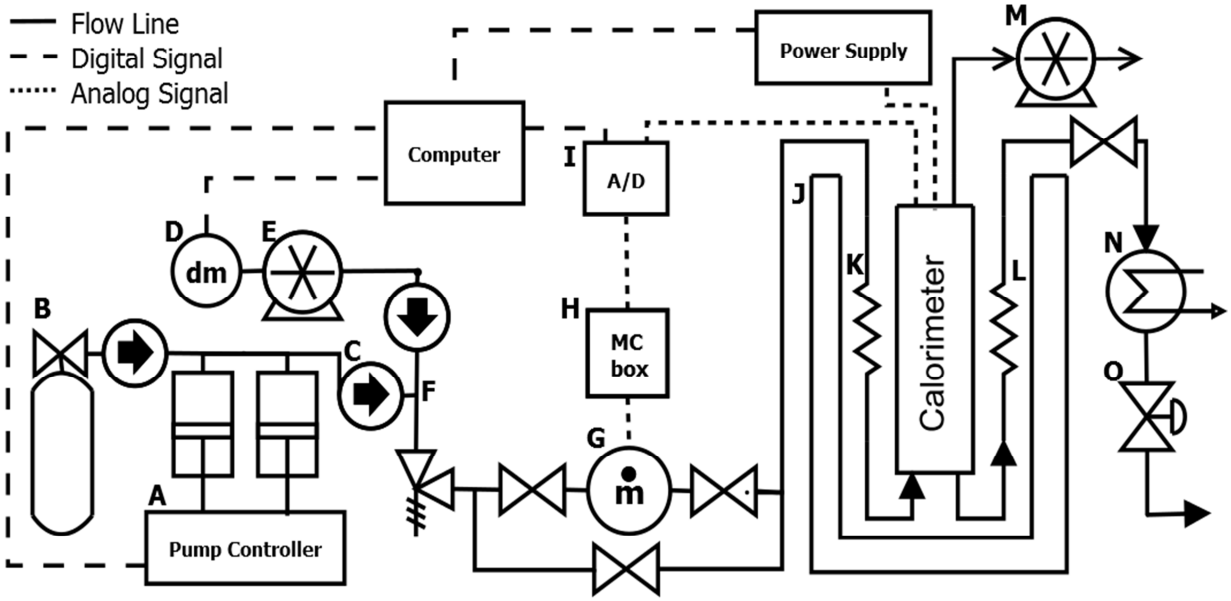

Figure 6-1: Process flow diagram of the calorimeter system. Dual syringe pump and controller (A), gas cylinder (B), check valve (C), mass balance (D), high pressure liquid chromatography (HPLC) pump (E), mixing tee (F), coriolis mass flow meter (G), measurement conversion box (H), analog to digital conversion box (I), fluidized alumina sand bath (J), vacuum pump (M), thermal equilibration tubing (K & L), exhaust heat exchanger (N), back pressure regulator (O).

The calorimeter assembly, schematically detailed in Figure 6-2, consists of a U-tube (2B) placed inside a vacuum chamber (2C) held at 0.05 mbar by a vacuum pump (1M). Two thermocouples (2A and 2I), placed at the inlet and outlet of the calorimeter, and a heating element (2F), near the bend of the U-tube, are kept in direct contact with the fluid being measured. A power supply provides electric current through insulated copper wires (2H) to the heating element made of Ni-Cr wire (2F). Pressure taps placed at the inlet and outlet of the calorimeter assembly are used to measure absolute pressure. A back pressure regulator (1O) controls and maintains the pressure in the flow system, and a series of pressure regulators (not shown) are used to let down the pressure before exhaust. Suppliers and model numbers for selected sub-components used in the flow calorimeter, as well as a picture of the physical system, are given in Appendix A.

A number of design measures have been incorporated into the system to increase the calorimeter's accuracy and decrease the measurement time. Heat losses were reduced by simultaneously lowering the driving forces for heat transfer and increasing the thermal resistance (Ernst et al., 1989; Rivkin & Gukov, 1968). Use of thin-walled (1.2 mm thickness) 6.35 mm outer diameter Inconel tubing in the calorimeter reduced both heat conduction along the fluid flow path and the measurement section's thermal inertia. The heating element, its connecting wires, and the thermocouples were placed in direct thermal contact with the fluid, decreasing heat loss and reducing the time needed to reach steady state during experiment typically to 1.5 minutes (a complete measurement takes 10 minutes). Convective heat losses from the calorimeter's U-tube were curtailed by encasing it in a vacuum chamber. To reduce heat losses by radiation, the flow tubing has been thoroughly polished. In addition, any residual heat losses from the calorimeter were compensated by placing it in a thermal bath held at the inlet

temperature of the calorimeter, substantially lowering the thermal driving force for conduction, convection, and radiation to produce nearly adiabatic conditions inside the calorimeter.

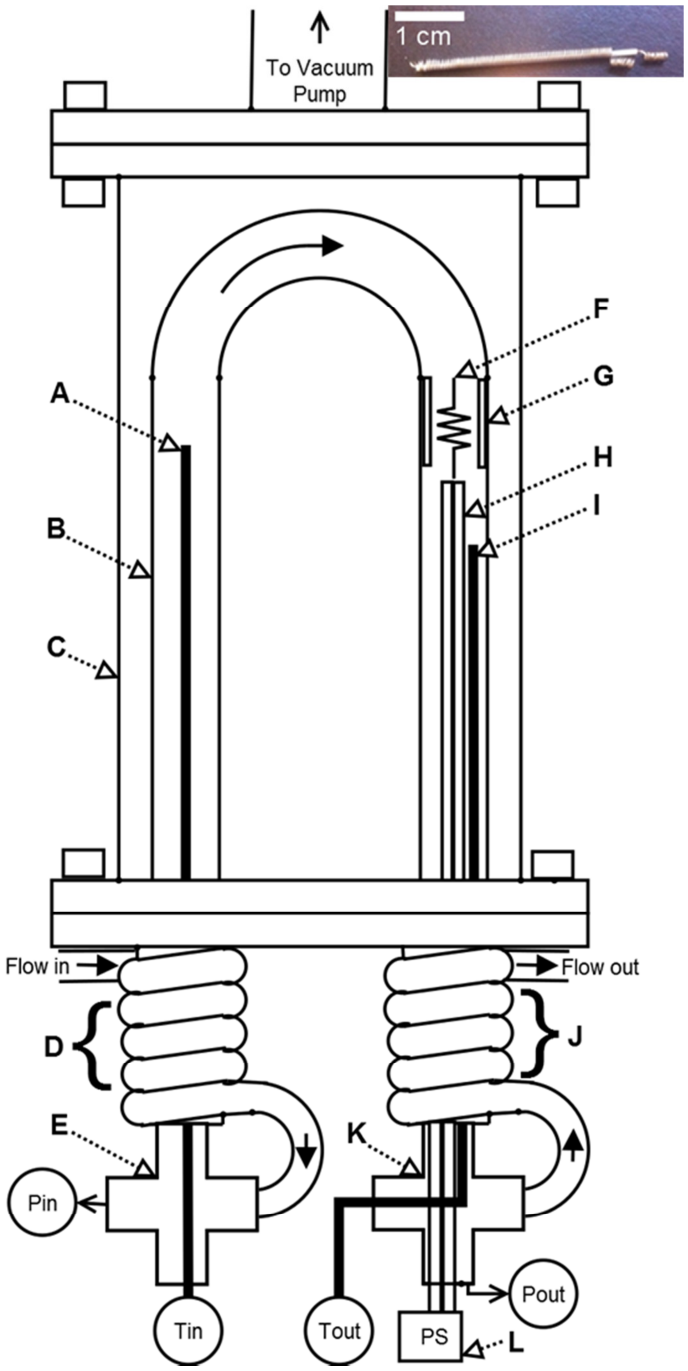

Figure 6-2: Schematic of the calorimeter assembly. Vacuum chamber with 6.35 cm OD and 21 cm in length (C), Inconel flow tubing with 0.635 cm OD and 0.39 cm ID (B), thermocouples (A and I), heating element/Ni-Cr resistor (F), ceramic insulation (G), 18 AWG copper wires attached to the heating element (H), inlet and outlet thermal equilibration tubing, 0.32 cm OD (D and J respectively), crosses at the fluid inlet (E) and outlet (K), power supply (L, placed outside the heated bath). Inset: The custom-made Ni-Cr heating element (F).

The fluid must be well mixed while maintaining a small pressure drop for Equation 4-3 to be valid. To assure efficient heat transfer between the heating element and the passing fluid, the bare Ni/Cr heater wire, shown inset in Figure 6-2, was wound in a coil to act as a turbulence promoter. The measurement section of tubing is short (0.4 m), and the consequential pressure drop, approximately 0.05 bar, is negligible. Further information, detailing certain operating procedures and troubleshooting, is included in Appendix B and C, respectively.

6.4. Assessment of measurement uncertainty

The uncertainties of the constitutive measurements for calculating isobaric heat capacity are listed in Table 6-1 along with the uncertainty contributions from assigning a measured C_p value to a particular temperature, pressure, and composition.

Table 6-1: The measurements required for a flow calorimetric determination of C_p. *Contribution of each measured property to the overall measurement uncertainty is provided.*

Measured Property	**Property Range**	**Uncertainty contributions**	**Range uncertainty**	**Contribution to C_p uncertainty**
Temperature	25–150 °C	Platinum resistance thermometer (PRT) standard	± 0.05 °C	± 0.4-0.01%
		Thermocouple stability and repeatability	± 0.05 °C	± 0.4-0.01%
Differential temperature	2.0–3.5 °C	Observed inconsistency in the average temperature difference	± 0.006 °C	± 0.3%
Total mass flow rate	10–19 g/min	Coriolis mass flow meter accuracy	± 0.05 g/min	± 0.4%
		Signal drift for a constant flow rate	± 0.05 g/min	± 0.4%
Methanol mass flow rate	0.1– 0.15 g/min	Mass change measurement of the fluid reservoir	± 0.04 g	± 0.2%
		Stopwatch accuracy	± 0.05 s	~ 0%
Pressure	1–300 bar	Accuracy and repeatability of pressure transducer	± 0.4 bar	± 0.5-0.05%
Heater power	1.1–2.2 W	Accuracy and stability	± 0.002 W	± 0.1%

To reduce the temperature measurement uncertainty, the thermocouple located at the inlet of the calorimeter was calibrated with a platinum resistance thermometer (PRT) standard. The total uncertainty in this absolute temperature measurement is listed in Table 6-1 and includes uncertainties in the following: the PRT's ice point calibration, conversion of the PRT's resistance signal to temperature, analog to digital signal conversion of the PRT signal, and the repeatability of the thermocouple measurement when compared to the PRT standard.

The difference in the fluid's temperature as it passes through the calorimeter, denoted as ΔT in Equation 5-3, is defined as the temperature of the fluid exiting the calorimeter minus the temperature of the fluid at the entrance to the calorimeter. This quantity is continuously monitored over the course of a heat capacity measurement. Sources of error, such as the Joule-Thomson effect (due to pressure loss or changes within the system) or any measurement offsets between the thermocouples, are greatly reduced by comparing the temperature difference over two distinct periods of operation, when heat ($\dot{Q}$) is being added and when it is not. Measurement of the temperature difference when heat is not being added to the fluid, termed a "blank experiment" by some researchers (Ernst et al., 1989), significantly reduces many potential systematic errors. The observed temperature inconsistency, listed in Table 6-1, refers to a repeated experimental observation; the temperature difference before heat ($\dot{Q}$) was applied was regularly slightly unequal to the temperature difference after the heater was again off. The most likely cause of this temperature difference inconsistency was temperature fluctuations within the fluidized alumina bath.

Based on repeated C_p measurements, an optimal induced temperature difference in the calorimeter was established to be 2.0-3.5 °C. This range represents a compromise between measurement uncertainty and resolution. The method of approximating the differential

temperature increase with a finite temperature increase, as shown in Equation 5-3, and repeated here:

$$C_p(T,\ P,\ X)\ \equiv\ \left(\frac{\partial H}{\partial T}\right)_{P,\,X} \approx\ \left.\frac{\dot{Q}}{\dot{m}\Delta T}\right|_{low\ \Delta P} \qquad (5\text{-}3)$$

results in an inherent error at conditions where C_p shows strong dependence on pressure, temperature, and composition. This systematic error is particularly large in the vicinity of a critical point, where physical properties show strong dependence on these variables. Depending on the sensitivity of the heat capacity function, one may incur significant errors by inducing too large a temperature change, as illustrated in Figure 6-3 for pure carbon dioxide.

A Coriolis mass flow meter was used to measure mass flow rate, eliminating the need for fluid density data. Accuracy specifications from the manufacturer were used and further in-house calibration was done to establish typical measurement drift. Mass flow rate of the fluid mixture's less volatile component (methanol in this study of CO_2-methanol mixtures) is taken by measuring the mass difference of the fluid reservoir with time.

The pressure transducer was installed as supplied from the manufacturer, with no further calibration done. The listed accuracy of the transducer includes additional uncertainty from analog to digital signal conversion.

The power supply to the heating element was calibrated with a highly accurate multimeter. Uncertainty in the heater power, listed in Table 6-1, includes a correction for the additional resistance of the copper wire linking the power supply to the heating element.

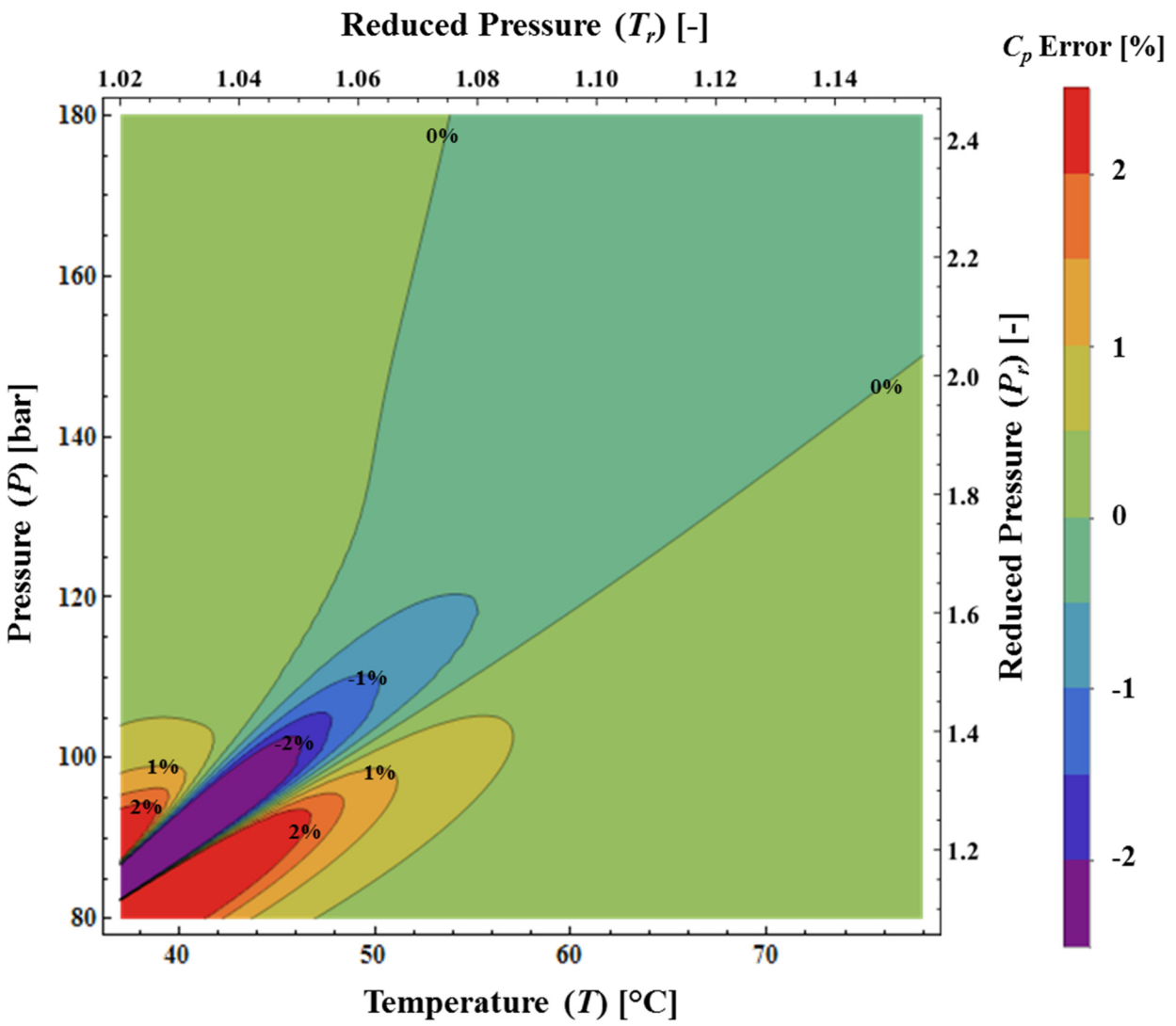

Figure 6-3: Calculated systematic errors in heat capacity, shown as a percent error in the color coded scale, due to the replacement of a differential temperature rise with a finite temperature rise (the distinction lies between the definition of C_p *and the experimental approximation in Equation 5-3), here* $\Delta T = 4$ *°C. The Span and Wagner EOS* (Lemmon, Huber, & Mclinden, 2013; Span & Wagner, 1996) *for carbon dioxide is treated as the true heat capacity function. Integral averages of heat capacity were calculated over the induced temperature rise and compared to the true heat capacity value at the average temperature. A finite temperature rise of 4 °C was chosen based on existing calorimeters described in literature* (Ernst et al., 1989; Rivkin & Egorov, 1959; Wu, Yu, Zhong, & Lin, 1995).

As a next step, the overall uncertainty in measured heat capacity due to assigning a particular temperature, pressure, and composition was assessed. If a fluid's heat capacity is very sensitive to incremental changes in its temperature, pressure, and composition, the total C_p

uncertainty will be heavily influenced by the uncertainty in these three variables. To quantify this effect, experimental data as well as three different EOS models were used to evaluate the following partial derivatives for carbon dioxide, methanol, and carbon dioxide-methanol mixtures (De Reuck & Craven, 1993; Kunz & Wagner, 2012; Span & Wagner, 1996):

$$\left(\frac{\partial C_p}{\partial T}\right)_{P,\,X}, \left(\frac{\partial C_p}{\partial P}\right)_{T,\,X}, \text{and } \left(\frac{\partial C_p}{\partial X}\right)_{T,\,P} \qquad (6\text{-}1)$$

Using these partial derivatives, all uncertainties in temperature, pressure, and composition have been converted into uncertainty in the measured heat capacity value. The partial derivatives in Equation 6-1 were also used to shift the experimentally measured values to round values of temperature, pressure, and composition listed in Tables 6-2 through 6-4. The resulting adjustments to the measured heat capacity values were insignificant when compared to measurement uncertainties. Finally, in an effort to reduce the uncertainty from random noise, repeatability, and hysteresis, each experimental measurement was repeated at least twice and in the majority of cases, including all of the carbon dioxide measurements, three times.

To demonstrate that the calorimeter operated with negligible heat loss, heat capacity measurements of carbon dioxide were taken at a high temperature (150 ºC and 200 bar) where the fluid's heat capacity is relatively low (~1.64 J/gK) and the partial derivatives of C_p with respect to temperature and pressure are small. Keeping flow rate constant, different amounts of thermal energy were added to the fluid in order to vary the induced temperature rise. An increase in the observed heat capacity would indicate heat loss from the calorimeter due to the increased temperature difference between the calorimeter and its surroundings. Figure 6-4 verifies the near adabaticity of the calorimeter because the heat capacity measurement shows no perceivable dependence on the induced temperature difference up to 4.4 °C.

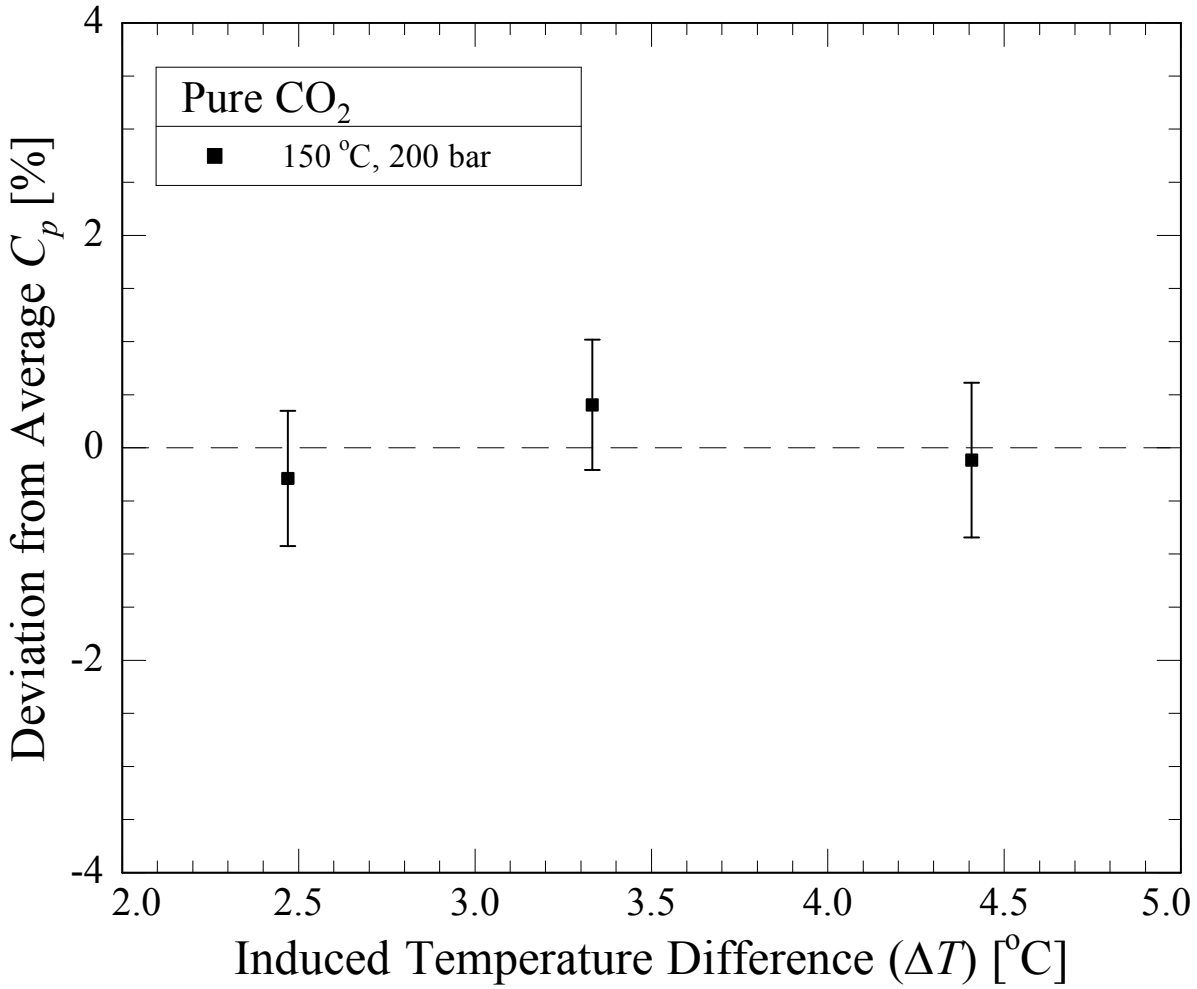

Figure 6-4: Measured isobaric heat capacity variations of pure carbon dioxide taken at 150 °C and 200 bar as a function of the induced temperature difference. The y-axis is the percent deviation of a singular experimental measurement from the average value of all the measurements at this condition. The plotted measurements were at the same mass flow rate (10 g/min). With the induced temperature difference nearly doubled (4.4 ºC compared to 2.5 ºC), no appreciable change in the measured heat capacity was observed.

6.5. Results and discussion

The calorimeter's accuracy was verified with experimental measurements of both pure fluids and fluid mixtures. Carbon dioxide experiments were used to establish satisfactory measurement of the base quantities ($\dot{Q}$, $\dot{m}$, ΔT, P, and T) because it is an extremely well characterized fluid (Span, 2013). Measurements of pure methanol, under fluid conditions very different from supercritical carbon dioxide, helped to demonstrate the calorimeter's versatility

over a range of fluid densities. With regard to mixtures, the accuracy of the fluid's composition (X) and its effect on measured heat capacity were determined by comparing our results to the literature C_p values of mixtures of methanol in carbon dioxide at low mole fractions of methanol (Boulton & Stein, 1993).

6.5.1. Physical calibration of the calorimeter

Following the practice established by other researchers (Fortier, Benson, & Picker, 1976; Rogers & Pitzer, 1981; Smith-Magowan & Wood, 1981; White & Downes, 1988), after determining the optimal ranges of mass flow rate, induced temperature rise, and heater power, a physical calibration of calorimeter was performed. Physical calibration accounts for non-idealities and systematic experimental errors present within the calorimeter which have not been mitigated by careful equipment design and operating procedures. Calibration was done by comparing 34 heat capacity measurements of pure CO_2 at 150 ºC and pressures between 100 and 300 bar to reference values calculated with the Span and Wagner EOS (Span & Wagner, 1996). Span and Wagner report an accuracy of ±0.6% for C_p in this temperature and pressure region. Minimization of the absolute differences between experimental measurements and the EOS yielded a 1.3% correction factor. All the heat capacity values presented in this paper are 1.3% lower than the raw experimental measurements. Subsequent sections will demonstrate that this 1.3% physical calibration factor is largely independent of the temperature, pressure, and density for carbon dioxide, methanol, and carbon dioxide-methanol mixtures. This work's calibration correction compares favorably with corrections of 2–15% reported by others (Fortier et al., 1976; Rogers & Pitzer, 1981; Smith-Magowan & Wood, 1981; White & Downes, 1988).

6.5.2. Measurements of pure carbon dioxide and pure methanol

The isobaric heat capacity of pure carbon dioxide was measured along 60, 90, 120, and 150 ºC isotherms over pressures ranging from 100 to 300 bar. The results are listed in Table 6-2 and plotted in Figure 6-5 using carbon dioxide's critical point (31 ºC and 73.8 bar) to calculate reduced temperatures and pressures. The measurements of this study agree well with both the high accuracy predictions of the Span & Wagner EOS (Span & Wagner, 1996) and the experimental data collected by Ernst et al. (Ernst et al., 1989), as indicated by mean percent differences of 0.2% and -0.1%, respectively. The Span and Wagner estimates are often taken as the standard reference values by numerous investigators (Span, 2013). Appendix D lists all EOS implementation information in this thesis. In nearly all cases, this study's measurements, the measurements by Ernst et al., and calculations from the Span & Wagner EOS, are within the estimated uncertainty bounds of this study listed in Table 6-2. Measured heat capacity along the 60 °C isotherm tended to be somewhat larger than the associated literature values, while the measurements at 120 °C fell below the literature results. The small positive and negative deviations between our results and the literature standards at these isotherms can likely be ascribed to random errors (such as thermocouple drift or pressure transducer hysteresis) or slight inaccuracies in component calibration. The 60 °C isotherm corresponds to a reduced temperature of 1.1 for CO_2, proving this apparatus's ability to make accurate measurements proximate to the critical point, where C_p maxima are large.

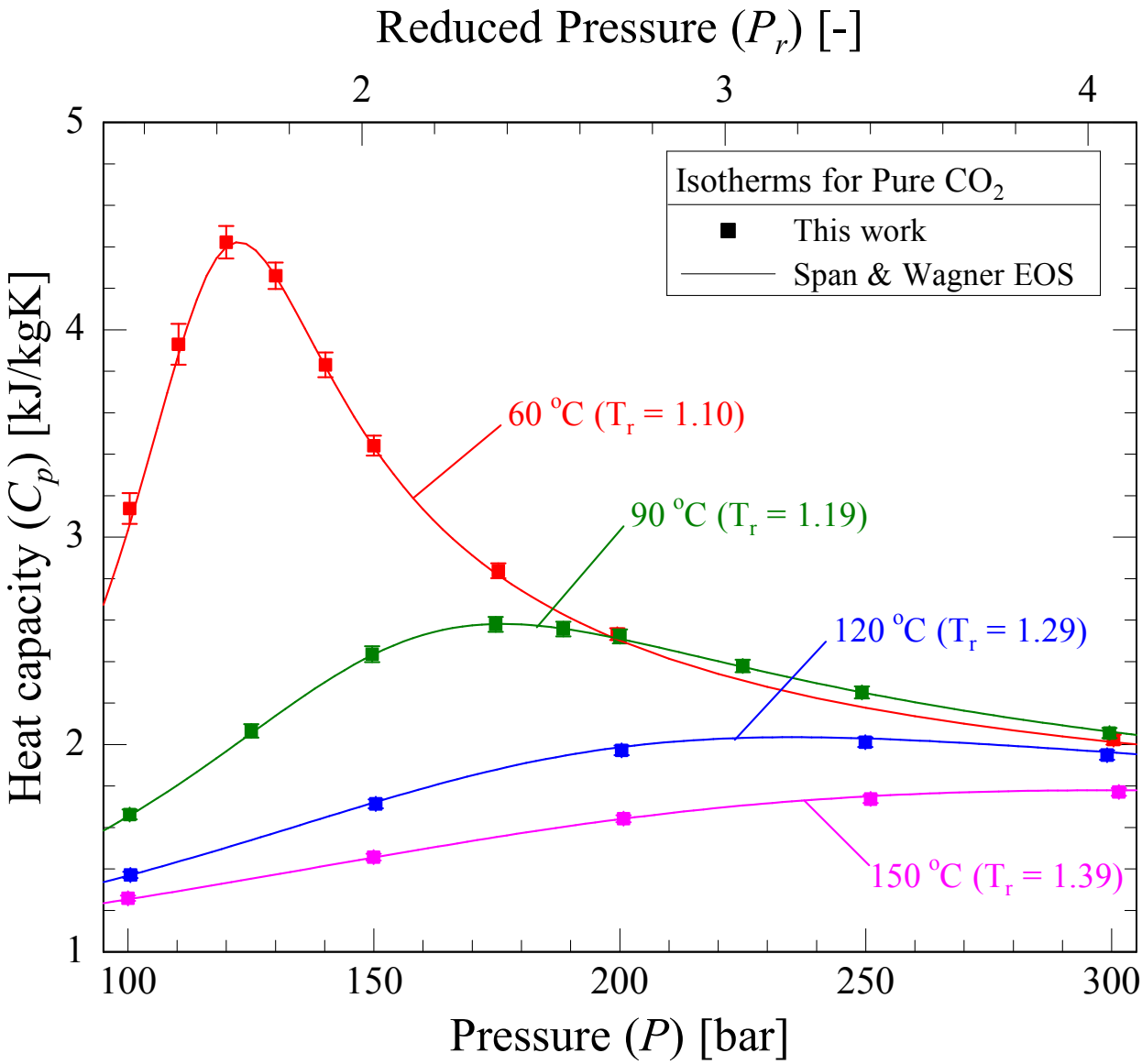

Figure 6-5: Comparison of the C_p *measurements of* CO_2 *made in this work to reference values reported by Span and Wagner EOS* (Span & Wagner, 1996). *The data agree with the Span and Wagner EOS values within the specified measurement uncertainty. Experimental measurements made by Ernst et al. agree with the Span and Wagner EOS calculations in this supercritical region* (Ernst et al., 1989).

Table 6-2: Measured isobaric heat capacity values (C_p) of pure carbon dioxide from 60-150 ºC and 100-300 bar. The overall uncertainty (δ) is presented as a percentage of the measured heat capacity. Our measurements are compared to the experimental measurements made by Ernst et al. and the Span and Wagner EOS ($C_{p,lit}$) (Ernst et al., 1989; Span & Wagner, 1996).

Pure CO_2				
***P* [bar]**	**C_p [J/gK] This Study**	**Estimated Uncertainty δ [%]**	**Comparison 100 ($C_{p,lit}$ - C_p)/C_p**	
			Ernst et al.	**Span and Wagner EOS**
		T = 60 °C (333.15 K)		
100	3.09	2.4	-0.3	-1.7
110	3.89	2.5	0.8	-0.8
120	4.39	1.8	0.9	0.2
130	4.26	1.5	-0.4	0.0
140	3.84	1.6	-0.5	-0.2
150	3.44	1.4	-0.1	-0.2
175	2.85	1.3	-0.6	-0.8
200	2.53	1.1	-1.5	-1.0
300	2.02	1.2	-1.3	-0.6
		T = 90 °C (363.15 K)		
100	1.65	1.4	0.3	-0.1
125	2.06	1.6	0.3	-0.3
150	2.44	1.6	0.4	-0.2
175	2.58	1.4	0.4	0.0
189	2.55	1.4	-	0.1
200	2.52	1.3	-0.4	-0.5
225	2.38	1.3	0.7	-0.2
249	2.25	1.3	0.8	0.0
300	2.05	1.2	0.6	0.3
		T = 120 °C (393.15 K)		
100	1.37	1.1	0.0	0.1
150	1.71	1.3	1.2	0.6
200	1.97	1.2	1.4	0.9
250	2.01	1.1	0.9	0.9
300	1.95	1.1	0.8	0.7
		T = 150 °C (423.15 K)		
100	1.26	1.0	-	-0.4
150	1.46	1.1	-	-0.2
200	1.64	1.0	-	-0.1
250	1.74	1.1	-	0.7
300	1.77	1.0	-	0.4
		Average Absolute Error:	0.6	0.4

Heat capacity measurements of pure methanol (T_c = 239.5 °C, P_c = 81 bar) in both liquid and vapor states at 150 ºC are listed in Table 6-3 and plotted in Figure 6-6. In the liquid state, this work's measurements agree to within 2% of the EOS predictions (De Reuck & Craven, 1993; Lemmon et al., 2013). Previous heat capacity measurements of liquid methanol at high temperature (Boyette & Criss, 1988) show large discrepancies with the EOS predictions, where the EOS is 8% lower on average than the measured values. Given the uncertainty allocation for the methanol EOS in this region, this work's measurements of C_p fit the EOS predictions well and represent an improvement to previous high temperature, high pressure C_p measurements of pure methanol. Methanol's heat capacity in the vapor state is more accurately quantified by the EOS, to within 1%. The C_p values in this study are about 1% larger than the calculated methanol vapor C_p, which is within the 1.2% experimental uncertainty. The measurements for methanol conducted in this study confirm the accuracy of calorimeter across a broad range of fluid densities from 2 to 660 kg/m^3.

Table 6-3: Measured isobaric heat capacity (C_p) of pure liquid and vapor methanol at 150 °C. The overall uncertainty (δ) is listed as a percentage of the measured heat capacity. The measurements made in this work are compared to the De Reuck and Craven EOS for methanol ($C_{p,lit}$) (De Reuck & Craven, 1993).

Pure Methanol			
***P* [bar]**	**This Work C_p [J/gK]**	**Estimated Uncertainty δ [%]**	**Comparison 100 ($C_{p,lit}$ - C_p)/C_p De Reuck & Craven EOS**
		T = 150 °C (423.15 K)	
2	1.80	1.3	-1.0
40	3.71	1.3	1.9
70	3.69	1.3	1.1
	Average Absolute Error:		1.3

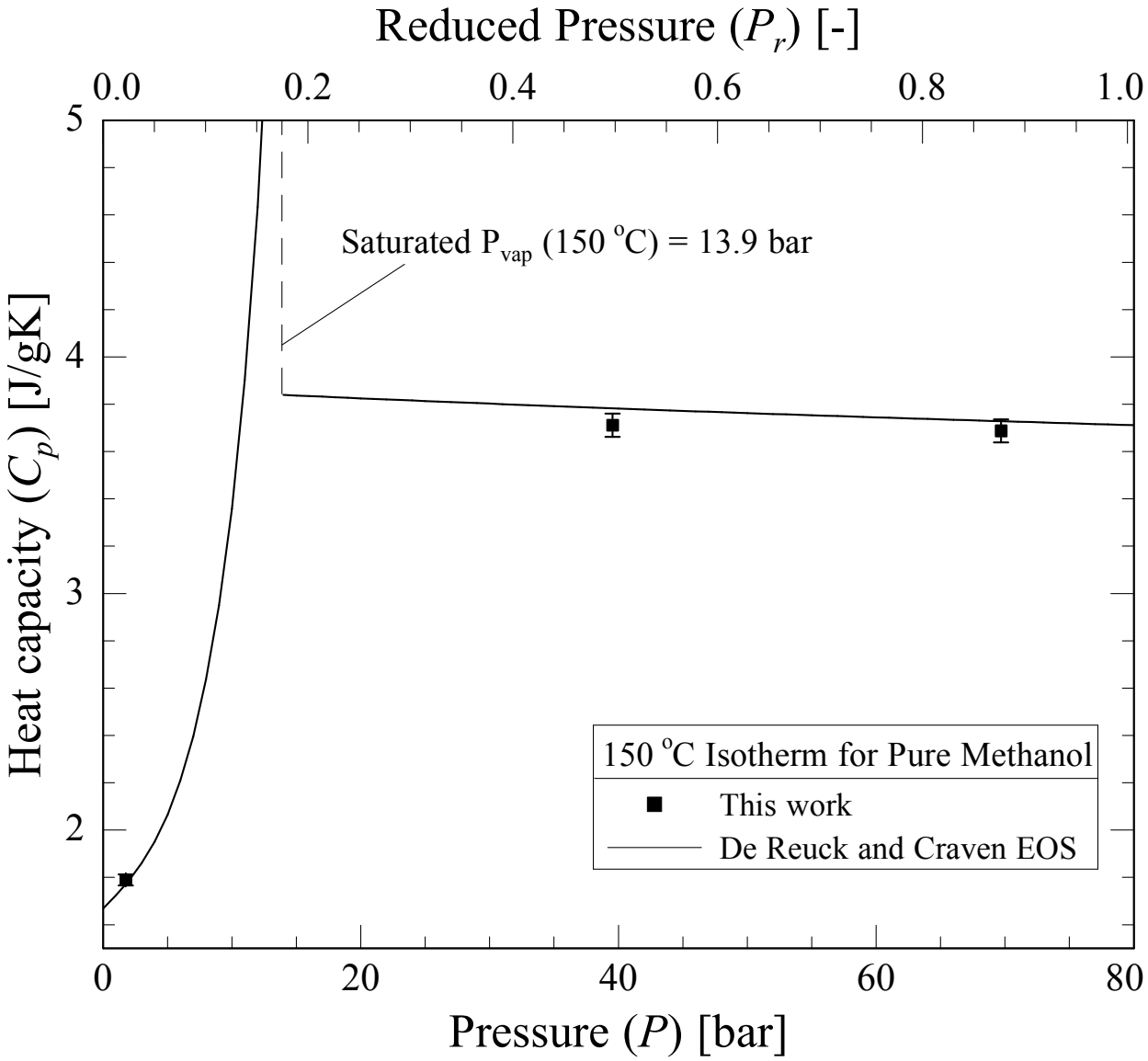

Figure 6-6: Heat capacity measurements of pure methanol at 150 °C as a liquid, at approximately 40 bar and 70 bar, and as a vapor, at approximately 2 bar. The data agrees with the De Reuck and Craven EOS within the specified measurement uncertainty and the accuracy of the EOS (De Reuck & Craven, 1993).

6.5.3. Comparative measurements of low mole fraction methanol mixtures in carbon dioxide

As shown in Table 6-4 and Figure 6-7 measured C_p values from this work compare favorably to the measurements reported in 1993 by Boulton and Stein for low mole fraction methanol-carbon dioxide mixtures. Boulton and Stein employed a Workman calorimeter for these measurements, limiting their measurements to mole fractions of methanol less than 1.5% (Boulton & Stein, 1993). Reduced temperatures and pressures were not calculated for these mixtures used to validate the calorimeter's operation due to the inconsistency of mixture critical points reported in the literature (plotted in Appendix E) (Gurdial, Foster, Yun, & Tilly, 1993; Liu, Qin, Wang, Hou, & Wang, 2003; Yeo, Park, Kim, & Kim, 2000). The uncertainty in methanol mole fraction was estimated to be ±4%, somewhat larger than for more concentrated mixtures as a result of the low methanol flowrate. The GERG-2008 EOS model results are presented as a comparison because of the applicability of this EOS for CO_2 and existing mixing rules. Fitting of the GERG-2008 model to methanol-carbon dioxide data has occurred (Kunz & Wagner, 2012; Lemmon, 2015; Lemmon et al., 2013). The measurement at 1.42 mol% methanol, 50 °C, and 73 bar shows the largest deviation but still falls within the experimental uncertainty. Boulton and Stein's reported uncertainties are also plotted in Figure 6-7. It is likely that in the near critical region, where the isobaric heat capacity changes rapidly with small changes in temperature, pressure/density, and composition, that their uncertainties should be larger than their reported ±1% general estimate. In any case, the results of this study as well as those by Boulton and Stein agree to within their respective uncertainties.

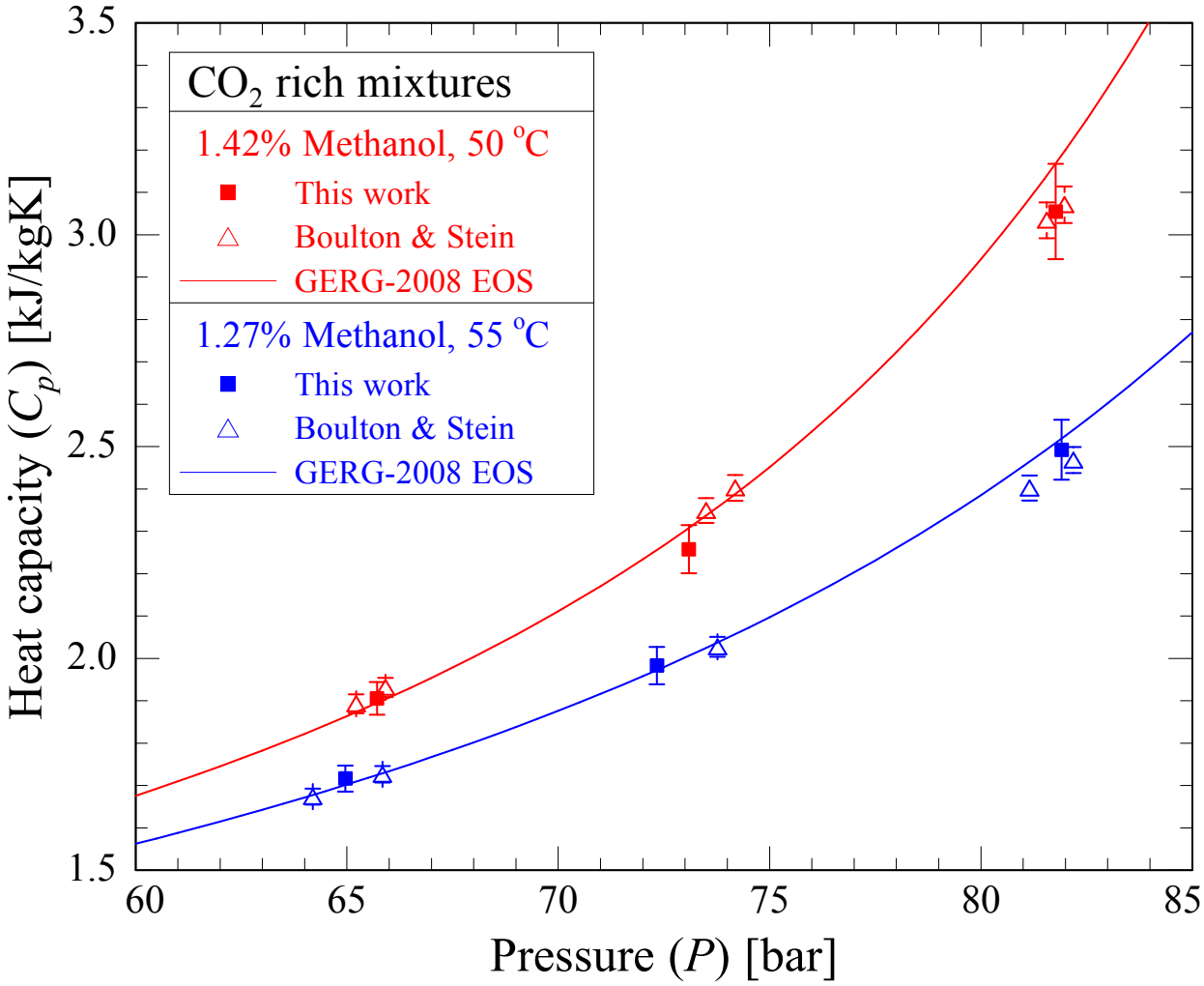

Figure 6-7: Comparison of this study's measurements to Boulton and Stein's heat capacity measurements (Boulton & Stein, 1993) *of low mole fraction methanol in carbon dioxide. The GERG-2008 EOS is compared to both sets of measurements* (Kunz & Wagner, 2012).

Table 6-4: Measured isobaric heat capacity (C_p) of low mole fraction methanol-carbon dioxide mixtures at two isotherms. The overall uncertainty (δ) is listed as a percentage of the heat capacity. The measurements made in this work are compared to the measurements of Boulton and Stein and the GERG-2008 EOS ($C_{p,lit}$) (Boulton & Stein, 1993; Kunz & Wagner, 2012).

Low Mole Fraction Methanol-CO_2 Mixtures				
***P* [bar]**	**This Work C_p [J/gK]**	**Estimated Uncertainty δ [%]**	**Comparison 100 ($C_{p,lit}$ - C_p)/C_p**	
			Boulton & Stein	**GERG-2008**
T = 50 °C (323.15 K), *X* = 1.42% Methanol in CO_2				
66	1.92	2.0	1.0	-1.0
73	2.24	2.5	3.3	2.1
82	3.11	3.6	-1.3	2.4
T = 55 °C (328.15 K), *X* = 1.27% Methanol in CO_2				
65	1.71	1.8	-0.9	-1.0
72	1.96	2.2	-0.7	0.3
82	2.51	2.8	-2.2	1.0

6.6. Conclusions

Successful operation of flow calorimeters over a wide range of densities, compressibilities, and viscosities is often a challenge due to variations in flow regimes, potential heat loss issues, and pressure drop difficulties. After careful design, construction, and calibration, the flow calorimeter detailed here achieved ±1% accuracy at temperatures from 25 to 150 °C and pressures from 1 to 300 bar in the vapor, dense liquid, and supercritical fluid regions for carbon dioxide, methanol, and carbon dioxide-methanol mixtures. The experimental measurements presented here agree with the measurements made by Ernst et al. and Boulton and Stein for pure carbon dioxide and carbon dioxide-methanol mixtures, respectively (Boulton & Stein, 1993; Ernst et al., 1989). The extensive range of operating conditions and high accuracy of the calorimeter, along with its flexibility for studying both pure fluids and mixtures, make it a valuable tool for thermophysical property characterization of fluids under supercritical conditions.

6.7. References

Bier, K., Busser, J., & Ernst, G. (1973). Experimental heat capacities Cp of non-ideal binary gaseous mixtures from C3H8, i-C4H10, CHF2Cl, and C2F5Cl. *J. Chem. Thermodynamics*, *5*, 83–96.

Bier, K., Ernst, G., & Maurer, G. (1974). Flow apparatus for measuring the heat capacity and the Joule-Thomson coefficient of gases. *The Journal of Chemical Thermodynamics*, *6*(11), 1027–1037. http://doi.org/10.1016/0021-9614(74)90065-2

Boulton, J. R., & Stein, F. P. (1993). The constant pressure heat capacity of supercritical carbon dioxide-methanol and carbon dioxide-ethanol co-solvent mixtures. *Fluid Phase Equilibria*, *91*, 159–176. http://doi.org/10.1016/0378-3812(93)85086-2

Boyette, S., & Criss, C. M. (1988). Thermodynamic properties of methanol from 288 to 503 K and at 8.3 MPa. *Journal of Chemical & Engineering Data*, *33*, 426–429. http://doi.org/10.1021/je00054a011

De Reuck, K. M., & Craven, R. J. B. (1993). *Methanol, international thermodynamic tables of the fluid state, vol. 12*. Blackwell Scientific Publications.

Ernst, G., Keil, B., Wirbser, H., & Jaeschke, M. (2001). Flow-calorimetric results for the massic heat capacity Cp and the Joule–Thomson coefficient of CH4, of (0.85 CH4 + 0.15 C2H6), and of a mixture similar to natural gas. *The Journal of Chemical Thermodynamics*, *33*(6), 601–613. http://doi.org/10.1006/jcht.2000.0740

Ernst, G., Maurer, G., & Wiederuh, E. (1989). Flow calorimeter for the accurate determination of the isobaric heat capacity at high pressures; results for carbon dioxide. *The Journal of Chemical Thermodynamics*, *21*(1), 53–65. http://doi.org/10.1016/0021-9614(89)90007-4

Ernst, G., & Philippi, R. (1990). Flow-calorimetric results for the specific heat capacity Cp of water at high pressures between 20 and 50 MPa and temperatures between 298.15 and 673.15 K. *J. Chem. Thermodynamics*, *22*, 211–218.

Fortier, J. L., Benson, G. C., & Picker, P. (1976). Heat capacities of some organic liquids determined with the Picker flow calorimeter. *The Journal of Chemical Thermodynamics*, *8*(3), 289–299. http://doi.org/10.1016/0021-9614(76)90108-7

Gurdial, G. S., Foster, N. R., Yun, S. L. J., & Tilly, K. D. (1993). Phase Behavior of Supercritical Fluid — Entrainer Systems. In E. Kiran (Ed.), *Supercritical Fluid Engineering Science* (pp. 34–45). Washington, DC: American Chemical Society. http://doi.org/10.1021/bk-1992-0514.ch003

Kunz, O., & Wagner, W. (2012). The GERG-2008 wide-range equation of state for natural gases and other mixtures: An expansion of GERG-2004. *Journal of Chemical and Engineering Data*, *57*(11), 3032–3091. http://doi.org/10.1021/je300655b

Lemmon, E. W. (2015). Personal communication, November 19, 2015. Thermophysical

Properties Division, Nation Institute of Standards and technology (NIST).

Lemmon, E. W., Huber, M. L., & Mclinden, M. O. (2013). *NIST Standard Reference Database 23: Reference Fluid Thermodynamic and Transport Properties-REFPROP, Version 9.1*. Gaithersburg.

Liu, J., Qin, Z., Wang, G., Hou, X., & Wang, J. (2003). Critical Properties of Binary and Ternary Mixtures of Hexane + Methanol, Hexane + Carbon Dioxide, Methanol + Carbon Dioxide, and Hexane + Carbon Dioxide + Methanol. *Journal of Chemical & Engineering Data*, *48*(6), 1610–1613. http://doi.org/10.1021/je034127q

Rivkin, S. L., & Egorov, B. N. (1959). Experimental investigation of the heat capacity of heavy water. *Atomnaya Energiya*, *7*(5), 462–465.

Rivkin, & Gukov. (1968). Experimental study of the isobaric specific heat of carbon dioxide at supercritical pressures. *Teploenergetika*, *15*(10), 72–75.

Rogers, P. S. Z., & Pitzer, K. S. (1981). High-Temperature thermodynamic properties of aqueous sodium sulfate solutions. *Journal of Physical Chemistry*, *85*(4), 2886–2895. http://doi.org/10.1021/j150620a008

Smith-Magowan, D., & Wood, R. H. (1981). Heat capacity of aqueous sodium chloride from 320 to 600 K measured with a new flow calorimeter. *The Journal of Chemical Thermodynamics*, *13*(11), 1047–1073. http://doi.org/10.1016/0021-9614(81)90004-5

Span, R. (2013). *Multiparameter Equations of State*. *Journal of Chemical Information and Modeling* (Vol. 53). Springer. http://doi.org/10.1017/CBO9781107415324.004

Span, R., & Wagner, W. (1996). A new EOS for carbon dioxide covering the fluid region from the triple-point temperature to 1100K at pressures up to 800 MPa. *Journal of Physical and Chemical Reference Data*. http://doi.org/10.1063/1.555991

White, D. R., & Downes, C. J. (1988). Heat loss corrections for heat capacity flow calorimeters. *Journal of Solution Chemistry*, *17*(8), 733–750. http://doi.org/10.1007/BF00647419

Wirbser, H., Brauning, G., & Ernst, G. (1992). Flow-calorimetric specific heat capacities and Joule Thomson coefficients of CF3CHFCF3 (R227) - a new working fluid in energy technics - at pressures up to 15 MPa and temperatures between 253 K and 423 K. *J. Chem. Thermodynamics*, *3*, 761–772.

Wu, Y., Yu, Q., Zhong, H., & Lin, R. (1995). A new flow calorimeter for the determination of the isobaric heat capacity of vapors. *Thermochimica Acta*, *254*, 93–101. http://doi.org/10.1016/0040-6031(94)02064-U

Yeo, S.-D., Park, S.-J., Kim, J.-W., & Kim, J.-C. (2000). Critical Properties of Carbon Dioxide + Methanol, + Ethanol, + 1-Propanol, and + 1-Butanol. *Journal of Chemical & Engineering Data*, *45*(5), 932–935. http://doi.org/10.1021/je000104p

7. COMPARISON OF MONTE CARLO MOLECULAR SIMULATIONS AND EQUATION OF STATE CALCULATIONS TO EXPERIMENTAL MEASUREMENTS FOR CARBON DIOXIDE-METHANOL MIXTURES

7.1. Previously published material describing carbon dioxide-methanol simulations and experimental measurements

The work described in this chapter has been documented in the following article:

Ishmael, Mitchell P. E., Lauren B. Stutzman, Maciej Z. Lukawski, Fernando A. Escobedo, and Jefferson W. Tester. "Heat capacities of supercritical fluid mixtures: Comparing experimental measurements with Monte Carlo molecular simulations for carbon dioxide-methanol mixtures." *The Journal of Supercritical Fluids* 123 (2017): 40-49.

Lauren Stutzman deserves credit for all of the molecular simulation calculations contained herein.

7.2. Selection of carbon dioxide-methanol for study by molecular simulation, equation of state and experimental measurement

The selection of carbon dioxide-methanol as the mixture for investigation was made for a number of reasons. First, this mixture is of particular interest for supercritical fluid extraction processes; extraction of metals, pharmaceutical compounds, toxins, oils, and other materials have all used this mixture at proportions similar to the compositions studied in this chapter (Boulton & Stein, 1988; Herrero, Mendiola, Cifuentes, & Ibáñez, 2010; Mendes, Nobre, Cardoso, Pereira, & Palavra, 2003). Second, while both molecules are small, making them relatively easier to model individually, the intermolecular forces exhibited by methanol and carbon dioxide are quite

different. Exploring the mixing rules' ability to represent the thermophysical behavior of this binary mixture in the supercritical region is of interest. Finally, a number of potential/force field models exist for the individual components, and simulations of this mixture have been run under different temperature, pressure, and composition conditions (Chen, Potoff, & Siepmann, 2002; Potoff & Siepmann, 2001; Stubbs & Siepmann, 2004; Stutzman, 2016). Building from the set of models reported by previous researchers, analysis of this mixture was extended to new conditions. Generated results could be used to increase accuracy of empirically fitted EOSs, such as the GERG-2008 (Groupe Européen de Recherches Gazières) (Kunz, Klimeck, Wagner, & Jaeschke, 2007; Kunz & Wagner, 2012). We expect that the results from this representative mixture could be extended to other alcohol mixtures in supercritical carbon dioxide that are also used in supercritical fluid extraction.

7.3. Monte Carlo molecular simulation implementation

The Monte Carlo (MC) molecular simulations were performed using version 7.1.0 of MCCCS Towhee (Martin, 2013). Pseudo-random numbers were generated using DX-1597-2-7 (Deng, 2005). The TraPPE force field was used to model the molecular interactions of CO_2 (Potoff & Siepmann, 2001), and the TraPPE-UA (united atom) force field was used to model the molecular interactions of methanol (Chen et al., 2002). Both force fields use a Lennard-Jones 12-6 potential to model the non-bonded, van der Waals intermolecular interactions. The cut off radius for the Lennard-Jones 12-6 potential was set to 14 Å, and analytical corrections (Allen & Tildesley, 1989) were used to estimate the effects of long range molecular interactions. Lorentz-Berthelot combining rules were used to compute the Lennard-Jones potential for unlike atoms (Maitland, Rigby, Smith, & Wakeham, 1981). Electrostatic interactions between molecules using

a Coulomb potential were determined with Ewald summation tin foil boundary conditions, an Ewald screening parameter of 5, and a K_{max} of 5 (Allen & Tildesley, 1989). A harmonic potential was used to model the bond bending of the methanol molecules. The coupled-decoupled configurational-bias MC method, which has a decoupled bond length selection, two decoupled angle selections, and a decoupled dihedral selection that is coupled to the non-bonded selection, was implemented to save CPU time (Martin & Siepmann, 1999; Martin & Thompson, 2004).

In a previous study, these aforementioned parameters were used in conjunction with the TraPPE and TraPPE-UA force fields to predict the phase equilibria properties of CO_2-methanol binary mixtures at temperatures ranging from 60 to 80 °C and pressures ranging from 40 to 150 bar with mixture compositions ranging from 5 to 90% methanol (Stubbs & Siepmann, 2004). Molecular simulation estimates of C_p matched the results of experimental measurements to within one standard deviation (Stubbs & Siepmann, 2004).

Monte Carlo simulations were run in the isothermal isobaric (*NPT*) ensemble, where the number of molecules (*N*), system pressure (*P*), and system temperature (*T*) were held constant for 10^6 cycles, after equilibration periods of 3.0×10^5 to 10^6 cycles (McDonald, 1972). One cycle consisted of *N* Monte Carlo move attempts. The simulation box volume, configurational energy, and intramolecular energy contributions were saved to an output file every 100 cycles. Ninety percent of the MC moves attempted were rotations or translations of CO_2 and methanol molecules, 8% were conformation changes of the methanol molecules, and the remaining 2% were volume moves. This distribution of moves was based on that of Lagache et al., where 98% of all moves completed by simulations in *NPT* ensemble were translations, rotations or molecular conformation changes (Lagache, Ungerer, Boutin, & Fuchs, 2001). A total of 300 total molecules were used for each simulation.

The statistical uncertainty in the simulation results was calculated using the block average method (Allen & Tildesley, 1989). Following this method, the molecular simulation output for a specified temperature and pressure was divided into 5 sub-sections, the C_p for each sub-section was calculated, and ultimately the standard deviation of the sub-section heat capacities was determined.

7.4. Results and discussion

Tables 7-1 through 7-5 list the results and uncertainties of experimental measurements, molecular simulations, and include a comparison of the experimental measurements to both the molecular simulations and the GERG-2008 EOS predictions (GERG-2008 parameter values used to model all CO_2-methanol conditions studied here are listed in Appendix D) (Kunz & Wagner, 2012; Lemmon, 2015; Lemmon, Huber, & Mclinden, 2013). Figure 7-1 plots the data from Table 7-2 for a 10 mol% methanol mixture to show the general characteristics of heat capacity in the critical region for CO_2-methanol mixtures. Plotted in Figures 7-2 through 7-6 are the observed percentage differences of C_p values determined by the molecular simulation calculations as compared to the experimental measurements. Unsmoothed and unaveraged C_p values for these mixtures are listed in Appendix F.

Table 7-1: Comparison between this work's measurements and molecular simulation calculations of heat capacity values for 5 mol% methanol in carbon dioxide. Deviation from the GERG-2008 EOS predictions have been included as well (Kunz & Wagner, 2012; Lemmon, 2015; Lemmon et al., 2013).

Methanol-CO_2 Mixtures						
	This Work Experimental		**This Work Molecular Simulation**		**Comparison with Experiment**	
***P* [bar]**	**C_p**	**Estimated Uncertainty**	**C_p**	**Estimated Uncertainty**	**100 (C_p - $C_{p,exp}$)/$C_{p,exp}$**	
	[J/gK]	**δ [%]**	**[J/gK]**	**δ [%]**	**Molecular Simulation**	**GERG-2008**
***X* = 5% Methanol**						
			T = 60 °C			
120	5.14	2.3	5.75	7.9	11.9	-7.4
150	3.33	1.8	3.58	9.4	7.4	-2.7
180	2.79	1.5	2.91	5.5	4.3	-2.9
210	2.50	1.4	2.64	1.4	5.4	-2.3
240	2.34	1.3	2.36	2.8	0.8	-2.2
300	2.13	1.3	2.21	3.4	3.6	-1.5
			T = 90 °C			
120	2.48	2.1	2.44	1.0	-1.3	1.7
150	2.92	1.8	3.07	3.9	4.9	1.8
180	2.87	1.6	2.93	3.1	2.2	-0.1
210	2.62	1.3	2.84	2.5	8.3	0.2
240	2.41	1.2	2.57	2.6	6.5	0.6
300	2.17	1.3	2.28	3.9	5.1	0.3
Average Absolute Difference:					**5.1**	**2.0**

Table 7-2: Comparison between this work's measurements and molecular simulation calculations of heat capacity values for 10 mol% methanol in carbon dioxide. Deviation from the GERG-2008 EOS predictions have been included as well (Kunz & Wagner, 2012; Lemmon, 2015; Lemmon et al., 2013)*. Continued on next page.*

Methanol-CO_2 Mixtures						
	This Work Experimental		**This Work Molecular Simulation**		**Comparison with Experiment**	
***P* [bar]**	**C_p**	**Estimated Uncertainty**	**C_p**	**Estimated Uncertainty**	**100 (C_p - $C_{p,exp}$)/$C_{p,exp}$**	
	[J/gK]	**δ [%]**	**[J/gK]**	**δ [%]**	**Molecular Sim.**	**GERG-2008**
X = 10% Methanol						
			T = 60 °C			
110	5.62	3.1	-	-	-	-12.3
120	4.57	2.5	5.00	7.3	9.4	-10.7
130	3.84	2.1	-	-	-	-6.2
150	3.17	1.7	3.28	2.4	3.6	-3.1
165	2.93	1.6	-	-	-	-2.8
180	2.75	1.5	2.77	4.8	0.7	-2.2
210	2.56	1.4	2.67	2.7	4.2	-3.2
240	2.41	1.4	2.46	2.9	1.8	-2.9
300	2.24	1.4	2.28	1.8	1.5	-2.8
			T = 90 °C			
120	3.17	2.4	3.01	1.7	-5.2	4.8
135	3.36	2.0	-	-	-	4.4
150	3.37	1.8	3.61	4.3	7.0	1.8
163	3.25	1.6	-	-	-	1.2
180	3.06	1.5	3.22	4.6	5.1	0.4
210	2.78	1.4	3.00	4.6	7.8	-0.9
240	2.57	1.4	2.64	2.3	2.9	-0.9
300	2.30	1.3	2.29	1.5	-0.6	-0.9

Methanol-CO_2 Mixtures						
	This Work Experimental		This Work Molecular Simulation		Comparison with Experiment	
P [bar]	C_p	Estimated Uncertainty	C_p	Estimated Uncertainty	100 (C_p - $C_{p,exp}$)/$C_{p,exp}$	
	[J/gK]	δ [%]	[J/gK]	δ [%]	Molecular Sim.	GERG-2008
X = 10% Methanol						
			T = 120 °C			
90	1.74	1.6	-	-	-	-4.7
120	2.09	1.7	2.01	0.8	-3.8	-2.4
150	2.38	1.7	2.37	2.2	-0.5	0.3
180	2.53	1.5	2.57	1.0	1.6	-0.1
210	2.53	1.5	2.60	3.6	2.8	-0.6
240	2.44	1.4	2.60	1.0	6.5	-0.4
300	2.25	1.3	2.43	1.6	7.8	0.6
Average Absolute Difference:					**4.0**	**2.9**

(*Table 7-2 is continued on this page*)

Table 7-3: Comparison between this work's measurements and molecular simulation calculations of heat capacity values for 15 mol% methanol in carbon dioxide. Deviation from the GERG-2008 EOS predictions have been included as well (Kunz & Wagner, 2012; Lemmon, 2015; Lemmon et al., 2013).

Methanol-CO_2 Mixtures						
	This Work Experimental		**This Work Molecular Simulation**		**Comparison with Experiment**	
***P* [bar]**	**C_p**	**Estimated Uncertainty**	**C_p**	**Estimated Uncertainty**	**100 (C_p - $C_{p,exp}$)/$C_{p,exp}$**	
	[J/gK]	**δ [%]**	**[J/gK]**	**δ [%]**	**Molecular Sim.**	**GERG-2008**
***X* = 15% Methanol**						
			T = 90 °C			
150	3.55	1.5	4.00	5.3	12.7	4.8
164	3.35	1.8	-	-	-	2.9
180	3.13	1.5	3.19	5.3	1.8	1.7
210	2.81	1.4	2.91	3.3	3.7	1.4
240	2.61	1.4	2.68	2.4	2.7	1.0
300	2.40	1.4	2.45	2.9	2.2	-0.6
			T = 120 °C			
120	2.65	1.9	2.58	2.6	-2.7	-6.6
150	2.83	1.8	2.87	3.7	1.3	-0.3
180	2.88	1.6	3.03	2.2	5.2	-1.3
210	2.78	1.6	2.91	5.3	4.9	-1.0
240	2.62	1.4	2.71	3.4	3.5	0.3
300	2.39	1.5	2.54	3.7	6.4	1.2
Average Absolute Difference:					**4.3**	**1.9**

Table 7-4: Comparison between this work's measurements and molecular simulation calculations of heat capacity values for 20 mol% methanol in carbon dioxide (Kunz & Wagner, 2012; Lemmon, 2015; Lemmon et al., 2013).

Methanol-CO_2 Mixtures						
	This Work Experimental		**This Work Molecular Simulation**		**Comparison with Experiment**	
***P* [bar]**	C_p	**Estimated Uncertainty**	C_p	**Estimated Uncertainty**	**100 (C_p - $C_{p,exp}$)/$C_{p,exp}$**	
	[J/gK]	**δ [%]**	**[J/gK]**	**δ [%]**	**Molecular Sim.**	**GERG-2008**
			***X* = 20% Methanol**			
			T = 90 °C			
150	3.62	1.6	3.78	5.8	4.2	5.1
180	3.12	1.5	3.41	4.4	9.3	3.6
210	2.84	1.5	2.96	2.0	4.0	2.3
240	2.67	1.5	2.68	2.8	0.3	1.2
300	2.46	1.3	2.57	3.3	4.4	0.3
			T = 120 °C			
150	3.25	1.6	3.15	4.0	-3.0	0.4
180	3.13	1.6	3.25	5.1	3.6	0.7
210	2.93	1.4	3.06	5.3	4.3	1.8
230	2.82	1.8	-	-	-	1.7
240	2.79	1.5	3.04	3.3	8.8	0.9
300	2.52	1.4	2.59	2.5	2.9	1.7
			T = 150 °C			
120	2.34	1.6	2.30	3.3	-1.5	-8.2
150	2.57	1.7	2.54	3.0	-1.2	-4.9
180	2.69	1.6	2.63	2.5	-2.3	-3.9
210	2.69	1.5	2.79	3.0	3.8	-3.6
240	2.63	1.5	2.68	3.1	1.9	-2.8
300	2.48	1.3	2.55	1.2	2.4	-1.1
			Average Absolute Difference:		**3.6**	**2.7**

Table 7-5: Comparison between this work's measurements and molecular simulation calculations of heat capacity values for 30 mol% methanol in carbon dioxide. Deviation from the GERG-2008 EOS predictions have been included as well (Kunz & Wagner, 2012; Lemmon, 2015; Lemmon et al., 2013).

Methanol-CO_2 Mixtures						
	This Work Experimental		**This Work Molecular Simulation**		**Comparison with Experiment**	
***P* [bar]**	**C_p**	**Estimated Uncertainty**	**C_p**	**Estimated Uncertainty**	**100 (C_p - $C_{p,exp}$)/$C_{p,exp}$**	
	[J/gK]	**δ [%]**	**[J/gK]**	**δ [%]**	**Molecular Sim.**	**GERG-2008**
X = 30% Methanol						
			T = 120 °C			
150	3.49	1.8	4.01	6.4	14.7	16.6
165	3.53	1.8	-	-	-	10.9
180	3.38	1.7	3.42	5.1	1.3	8.8
210	3.12	1.5	3.23	4.0	3.7	7.4
240	2.92	1.5	3.14	5.9	7.5	6.1
300	2.70	1.4	2.78	1.3	2.9	3.6
			T = 150 °C			
150	3.48	1.8	-	-	-	-6.1
165	3.46	2.1	-	-	-	-6.0
180	3.37	1.7	3.39	2.4	0.8	-4.6
210	3.19	1.6	3.25	4.4	2.1	-1.3
240	3.02	1.4	3.08	3.8	1.9	0.7
300	2.75	1.4	2.86	1.8	4.1	3.3
Average Absolute Difference:					**4.3**	**6.3**

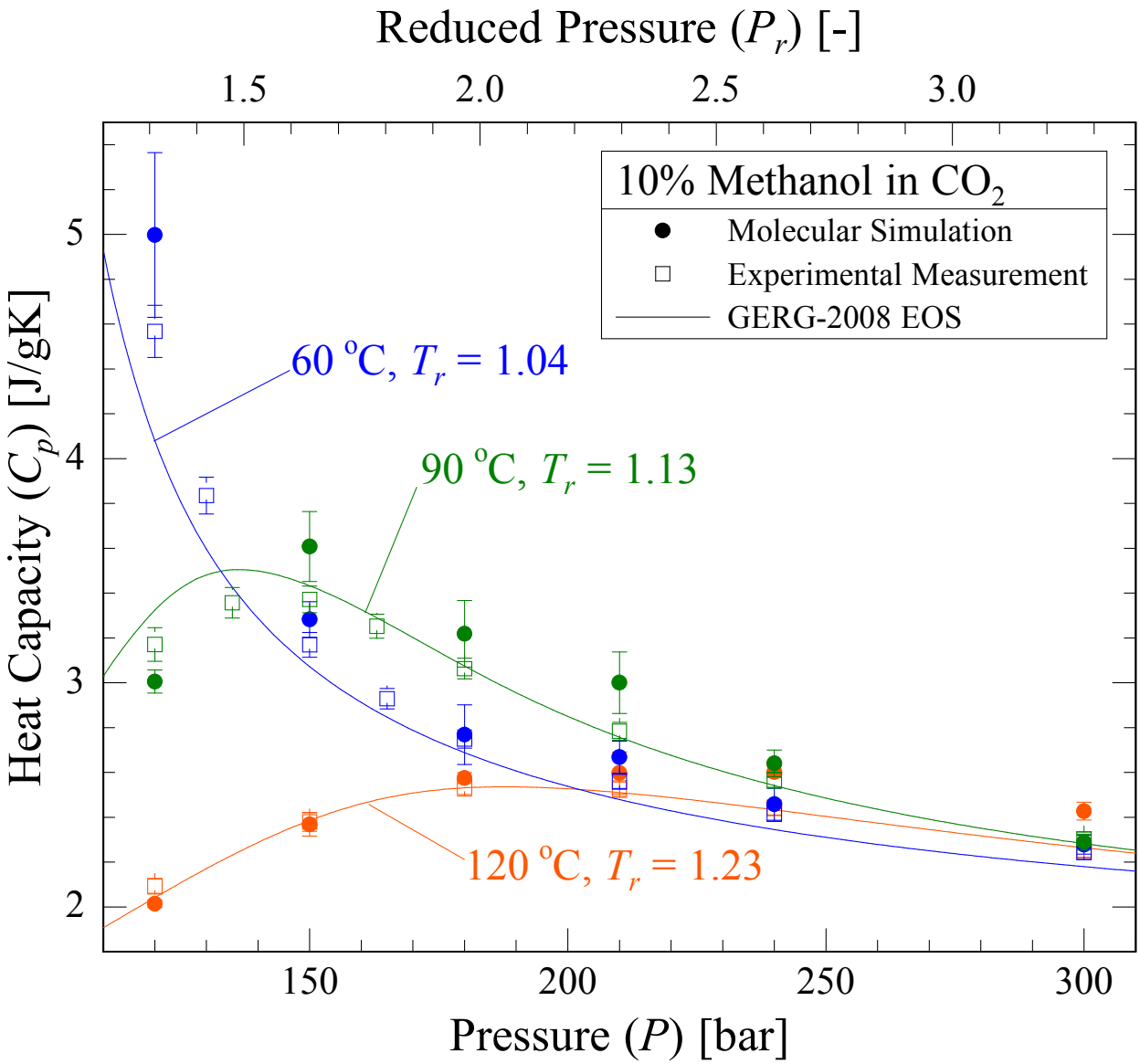

Figure 7-1: Three supercritical isotherms of 10 mol% methanol in carbon dioxide. This representative figure is meant to be illustrative of the fluctuations in heat capacity covered within this Chapter. Reduced temperature and pressure coordinates for the mixture were obtained interpolating between experimental measurements (Gil et al., 2012).

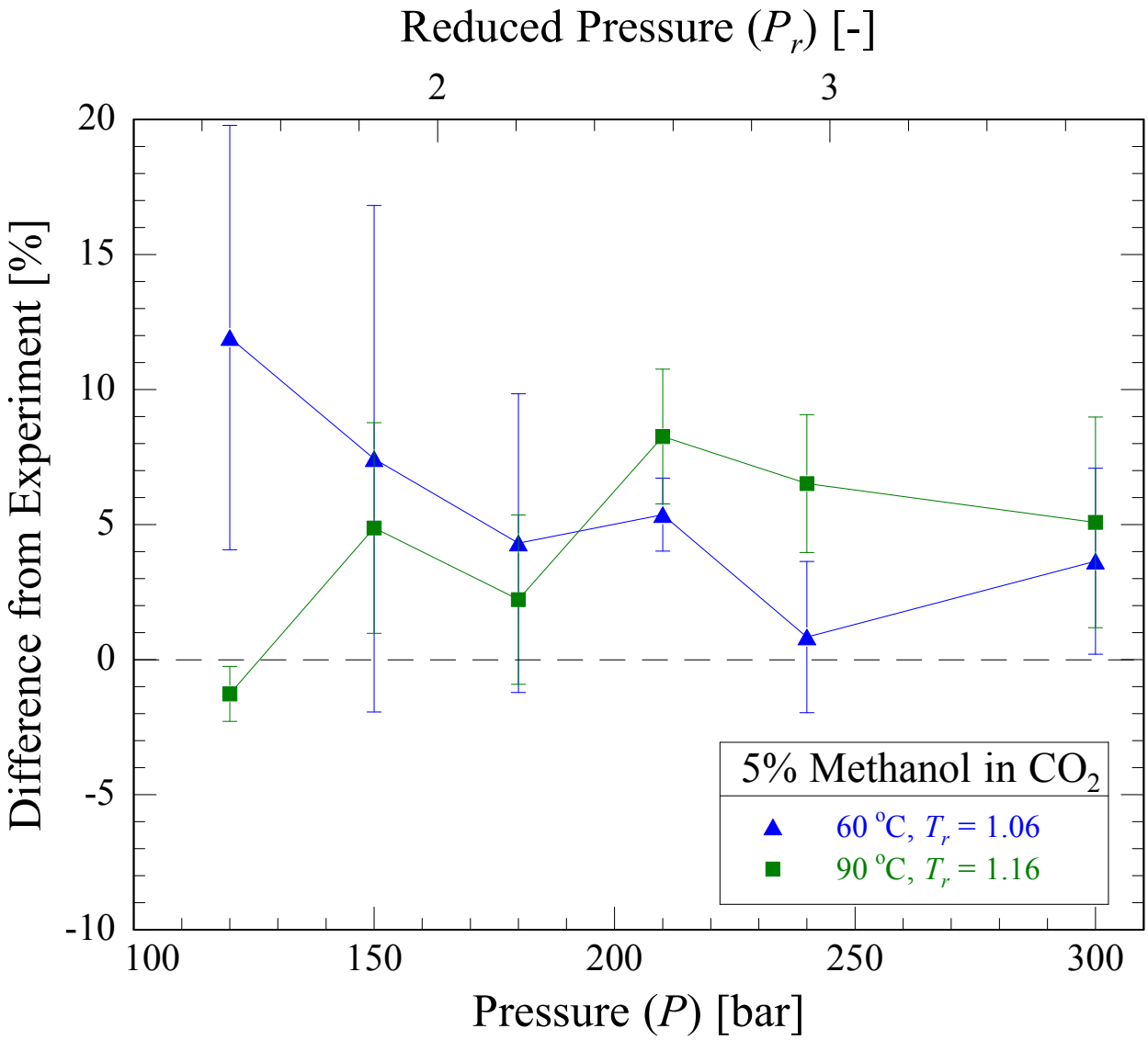

Figure 7-2: Percent difference in heat capacity between molecular simulation and experimentally measured values of 5 mol% methanol in carbon dioxide. Reduced temperatures and pressures were calculated using interpolated critical temperatures and pressures from (Gil et al., 2012).

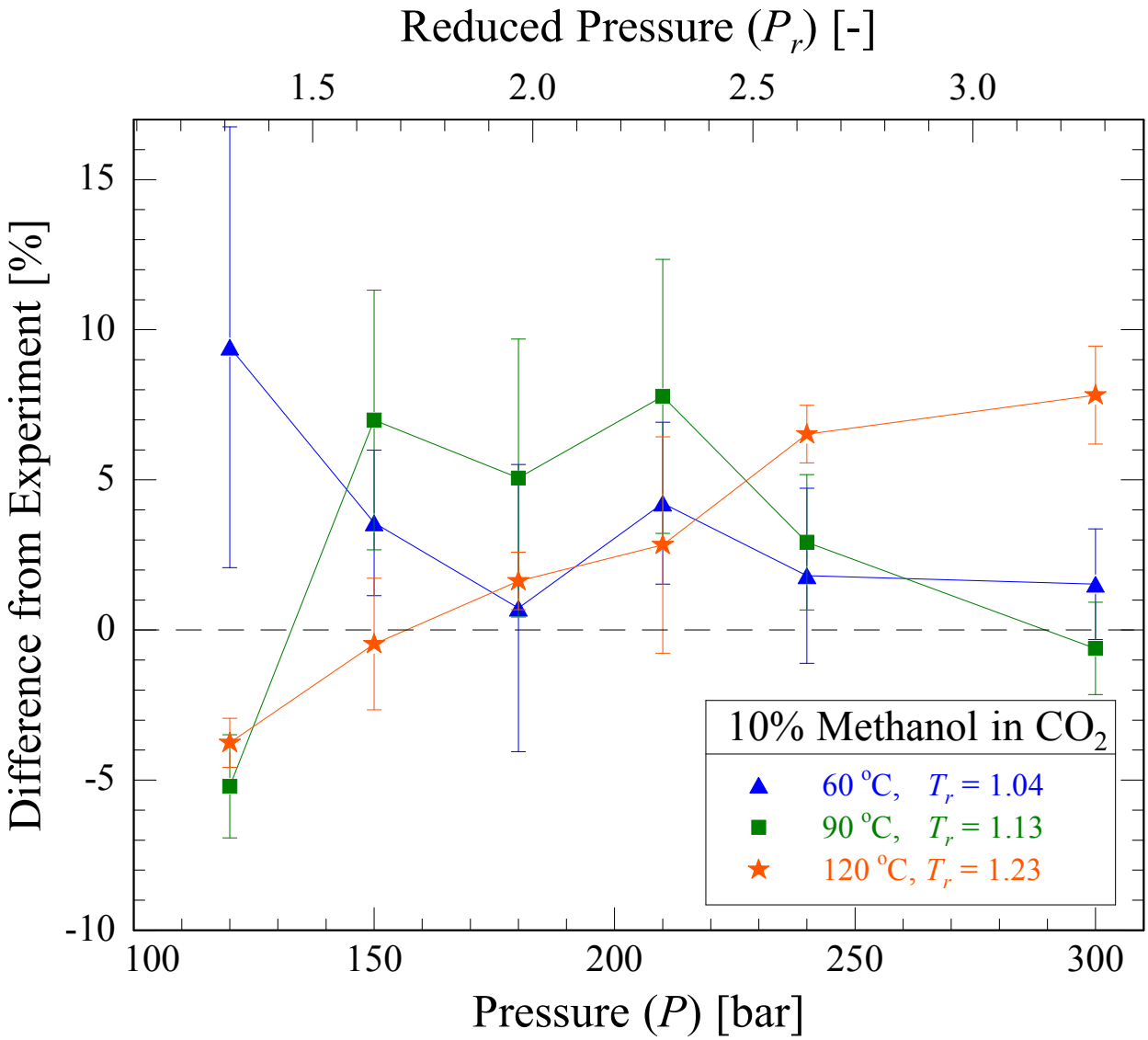

Figure 7-3: Percent difference in heat capacity between molecular simulation and experimentally measured values of 10 mol% methanol in carbon dioxide. Reduced temperatures and pressures were calculated using interpolated critical temperatures and pressures from (Gil et al., 2012).

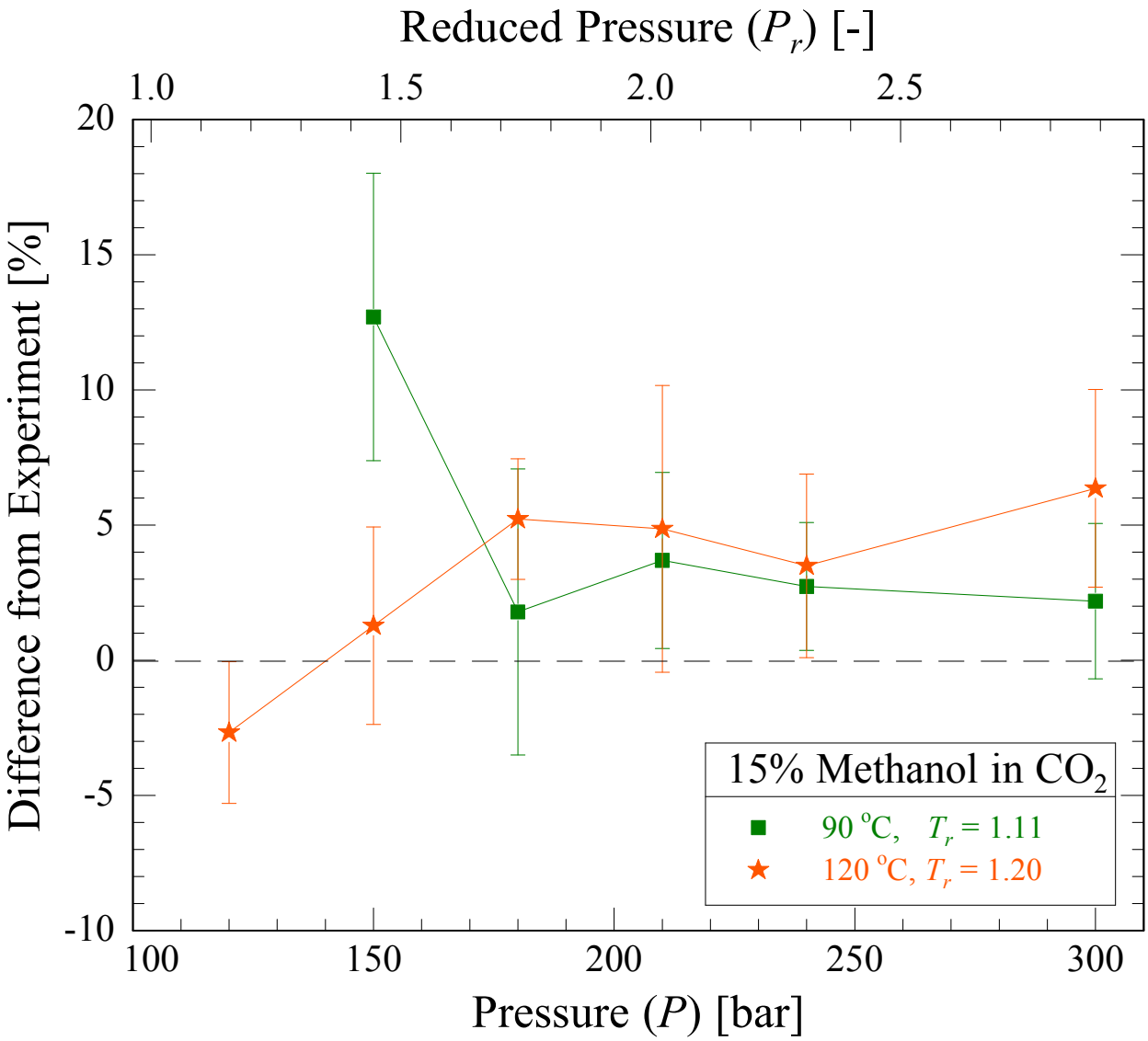

Figure 7-4: Percent difference in heat capacity between molecular simulation and experimentally measured values of 15 mol% methanol in carbon dioxide. Reduced temperatures and pressures were calculated using interpolated critical temperatures and pressures from (Gil et al., 2012).

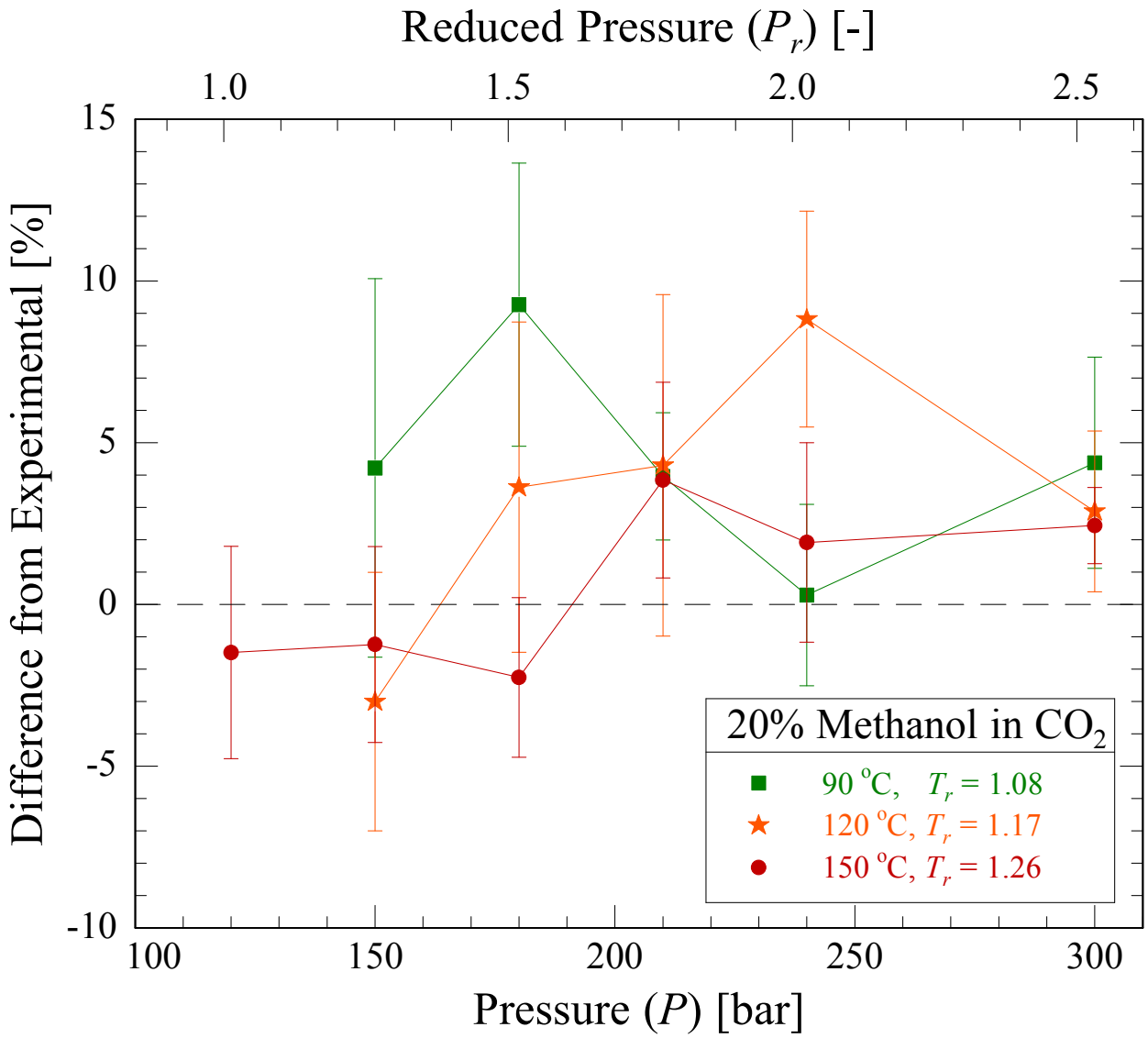

Figure 7-5: Percent difference in heat capacity between molecular simulation and experimentally measured values of 20 mol% methanol in carbon dioxide. Reduced temperatures and pressures were calculated using interpolated critical temperatures and pressures from (Gil et al., 2012).

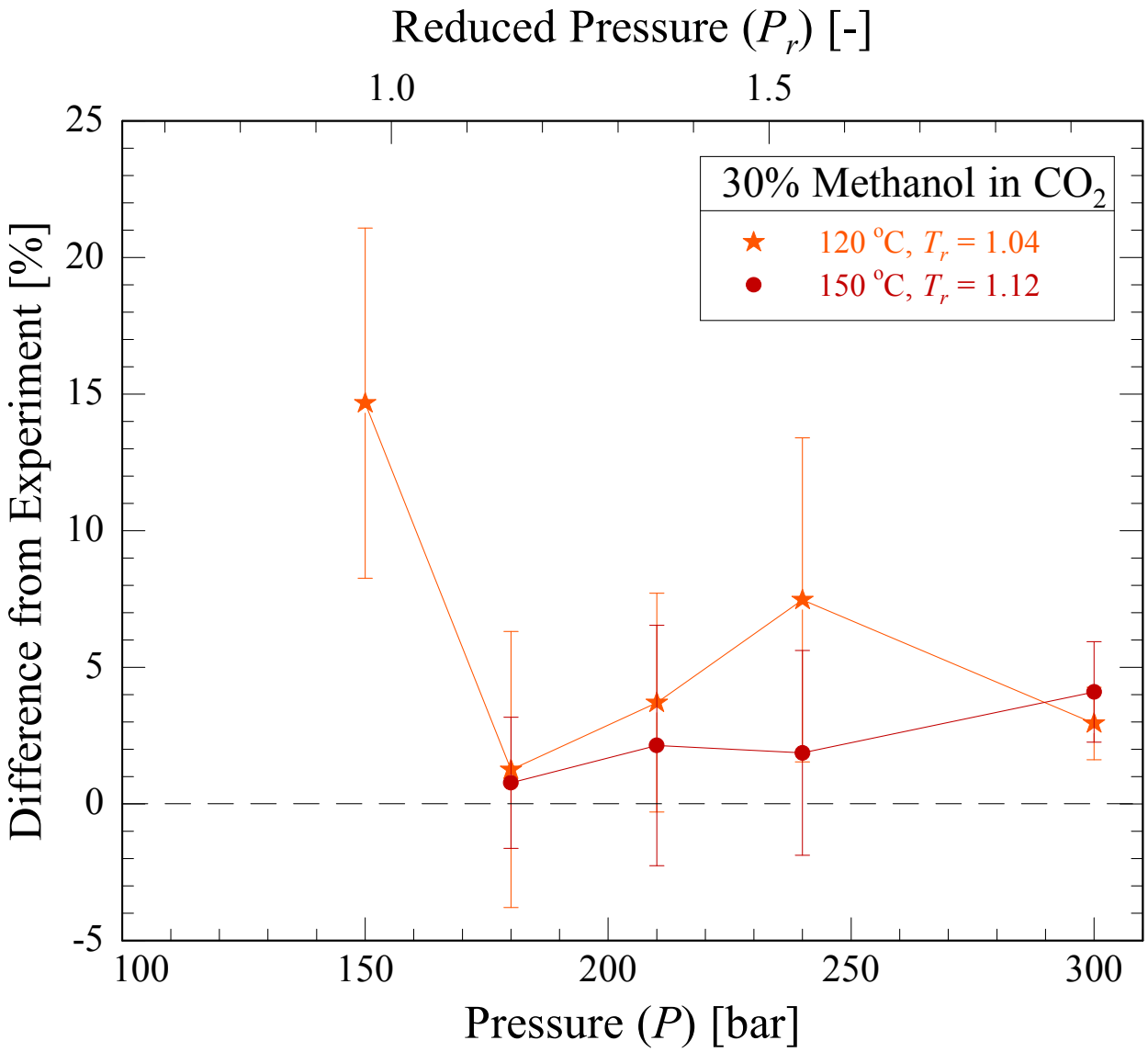

Figure 7-6: Percent difference in heat capacity between molecular simulation and experimentally measured values of 30 mol% methanol in carbon dioxide. Reduced temperatures and pressures were calculated using interpolated critical temperatures and pressures from (Gil et al., 2012).

To express the proximity of each CO_2-methanol mixture to its respective critical point, the temperatures and pressures associated with each measured C_p value were reduced $\left(T_r = \frac{T_{meas}}{T_{c,mix}}, P_r = \frac{P_{meas}}{P_{c,mix}}\right)$ using experimental data from Gil et al. (Gil et al., 2012). Experimental measurements of the CO_2-methanol critical locus are abundant, but there is significant disagreement between the datasets at moderate methanol mole fractions, shown in Appendix E and summarized here. From 0% to 20% methanol, excluding the dataset of Liu (Liu, Qin, Wang, Hou, & Wang, 2003), there is relatively good agreement between the datasets (the measured critical points fall within ~10 °C and ~10 bar for a given composition). Between 20% and 30% methanol, the number of available datasets decreases and the differences become more pronounced (up to 25 °C and 20 bar), indicating a high degree of uncertainty in the critical property estimates. The measurements made by Gil et al. were used in this study because they provide consistent results, represent a good compromise between all of the datasets, and include the largest number of measurements, increasing the resolution of an interpolation between points (Gil et al., 2012). These corresponding state type analogies are not perfect; mixtures of different compositions under identical reduced conditions will behave differently. For example, a mixture with a more equal compositional split will generally show a reduced peak in heat capacity along the same reduced isotherm. Despite these drawbacks, reducing the temperatures and pressures of fluids using a mixture's critical properties provides a straightforward scaling method for qualitatively comparing datasets without necessarily leading to a significant misinterpretation of the results.

As shown in Figures 7-2 through 7-4 and 7-6, for mixtures of 5 and 10 mol% methanol along 60 ^{0}C isotherms, 15% methanol along the 90 ^{0}C isotherm, and 30% methanol along the 120 ^{0}C isotherm, the largest deviation between experimental and simulation results occurs in the

vicinity of the critical point of the mixture. Under these conditions, deviation between the experimental and molecular simulation results often exceed 10%, whereas for temperatures and pressures further away from the critical point, deviations between molecular simulation and experimental results remain under 10%.

In order to evaluate the block average uncertainty estimates of the molecular simulations, a histogram of the differences between the molecular simulation and experimental C_p values was generated, normalizing each difference by the uncertainty of the molecular simulation. Plotted in Figure 7-7, the mean normalized simulation error of +0.96 indicates an average overestimate in heat capacity by the molecular simulations, but it does not adequately address the magnitude of the overestimate; this issue will be revisited in the discussion of Figure 7-8. The normalized difference in Figure 7-7 should contain almost all of its data within three standard deviations (3σ) assuming a normal distribution. The three outliers, pointed out specifically with their compositions, temperatures, and pressures, indicate a likely underestimation of the molecular simulation uncertainty at these points. These underestimates in uncertainties from generally acceptable uncertainty estimates could stem for the complex behavior of methanol in $scCO_2$. Previous analyses of low mole percent methanol in CO_2 have displayed non-random mixing at supercritical conditions (Stubbs & Siepmann, 2004), where methanol molecules form aggregates rather than dispersing into monomers. For mixtures containing 6.4 mol% methanol at temperatures and pressures ranging from 30 ^{0}C to 51.8 ^{0}C and 100 to 400 bar, previous molecular simulation studies have suggested that only 65% of methanol molecules in the mixture occur as monomers. The other 35% of methanol molecules form into aggregates of 2 to 9 molecules (Stubbs & Siepmann, 2004).

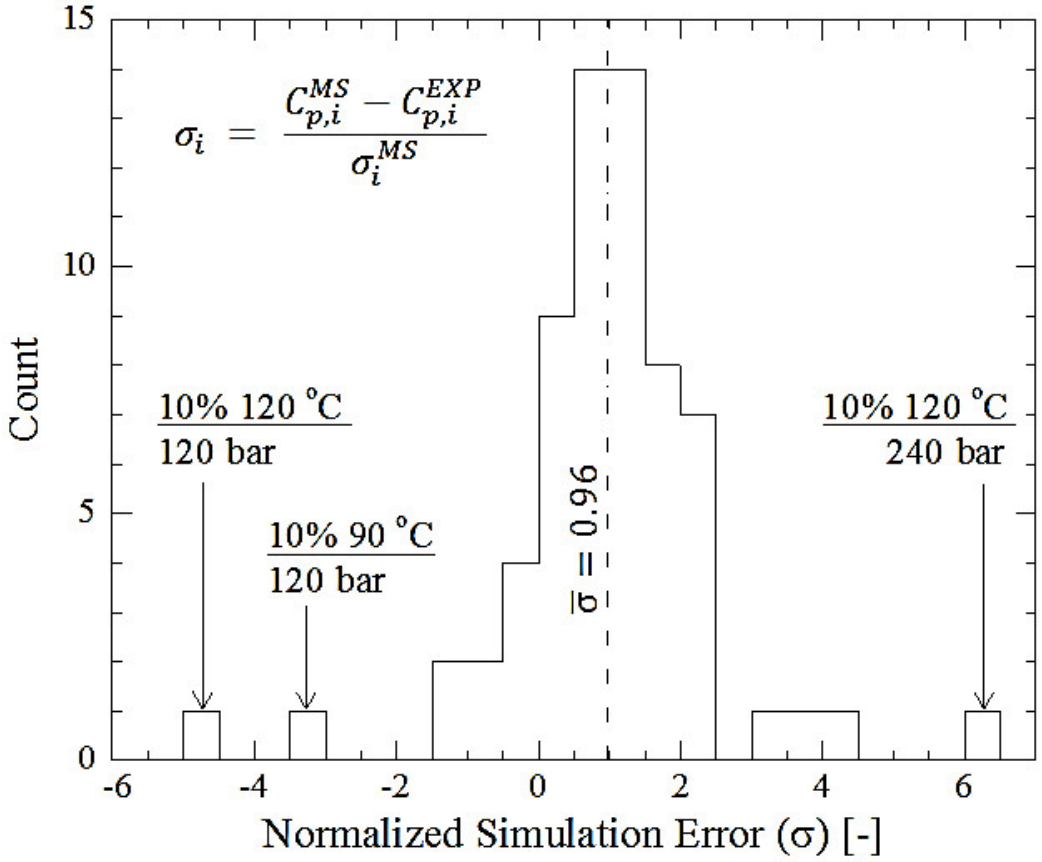

Figure 7-7: Histogram of the molecular simulation error when compared to experimental measurements for all conditions investigated in this work. The difference between simulated and experimentally measured heat capacity values were normalized by the estimated uncertainty of the molecular simulation(σ_i^{MS}). The equation is shown inset. The outliers are described with their compositions, temperatures, and pressures.

To investigate aggregation as a potential source of error, methanol hydroxyl hydrogen-oxygen radial distribution functions (RDFs) were computed for 5, 10, 15, and 20 mol% methanol mixtures at 120 °C and 120 and 240 bar. The 10 mol% methanol mixtures yielded RDFs that corresponded reasonably well with those determined for the 15 and 20 mol% methanol mixtures, suggesting similar aggregation behavior. These three mixtures had RDFs with initial peaks at ~1.9 Å and secondary peaks, which indicate the presence of aggregates larger than dimers, at ~3.3 Å. The heights of the initial peaks were approximately 2.5 to 3 times the heights of the secondary peaks. The 5 mol% methanol mixture yielded RDFs with peaks at ~1.9, ~2.5, and ~3.5 Å, where the initial peaks at ~1.9 Å were approximately triple the height of those at ~2.5 and

~3.5 Å. This increased number of peaks suggests the formation of larger aggregates in the 5 mol% methanol mixture. Furthermore, the peaks for the 5 mol% methanol mixture were roughly 1.5 to 2 times higher than those calculated for the 10, 15, and 20 mol% methanol mixtures, suggesting the presence of a greater number of aggregates in this mixture as well. However, larger deviations between the experimental and simulation results were not observed for the 5 mol% methanol mixture. As molecular simulation error does not correlate with mixture aggregation behavior, we hypothesize that aggregation behavior is not the primary cause of the simulation's disagreement with the experimental measurements.

In addition to the validity of the model's assumptions, molecular simulation accuracy hinges on having access to high-quality experimental data (commonly vapor-liquid equilibrium data, as used in this work) to validate results. The molecular simulation uncertainties listed in Tables 7-1 through 7-5 primarily represent random uncertainties, i.e. the distribution of results one might expect if the simulations were repeated with identical parameters and assumptions. Estimating the systematic uncertainty, or accuracy, of the molecular simulation implementation can prove to be extremely challenging if there are no reliable experimental data or a verified EOS.

The average accuracy of the molecular simulations in this study was estimated using statistical bootstrapping. At a state point, each observed difference between the simulation calculation and experimental measurement was treated as the mean of a hypothetical "true" distribution of differences. Each true distribution was assumed normal, and the standard deviation was set equal to the summed random simulation and experimental uncertainties (square root of the sum of squares). After removing the data points with significantly low uncertainties pointed out in Figure 7-7 (the data well beyond three standard deviations from the mean), 10,000

realizations of the dataset, parameterized by the aforementioned distributions, were taken, and the dataset's average percent difference was stored for each realization. The result, a distribution of the average difference between molecular simulation and experimental measurement, is plotted as a histogram in Figure 7-8. The average of the distribution shown in Figure 7-8 is the same as the original dataset (+3.6% difference). The standard deviation of the distribution of averages is 0.55%. Represented as a red, dashed line, the systematic uncertainty of the calorimetric measurement is approximately 1% of the reported heat capacity value (though the uncertainty increases near the critical point). Using all the parameters, assumptions, and the statistical analysis adopted in this study, the molecular simulations yield on average an over estimate of the true heat capacity by at least +1.5% (95% confidence interval).

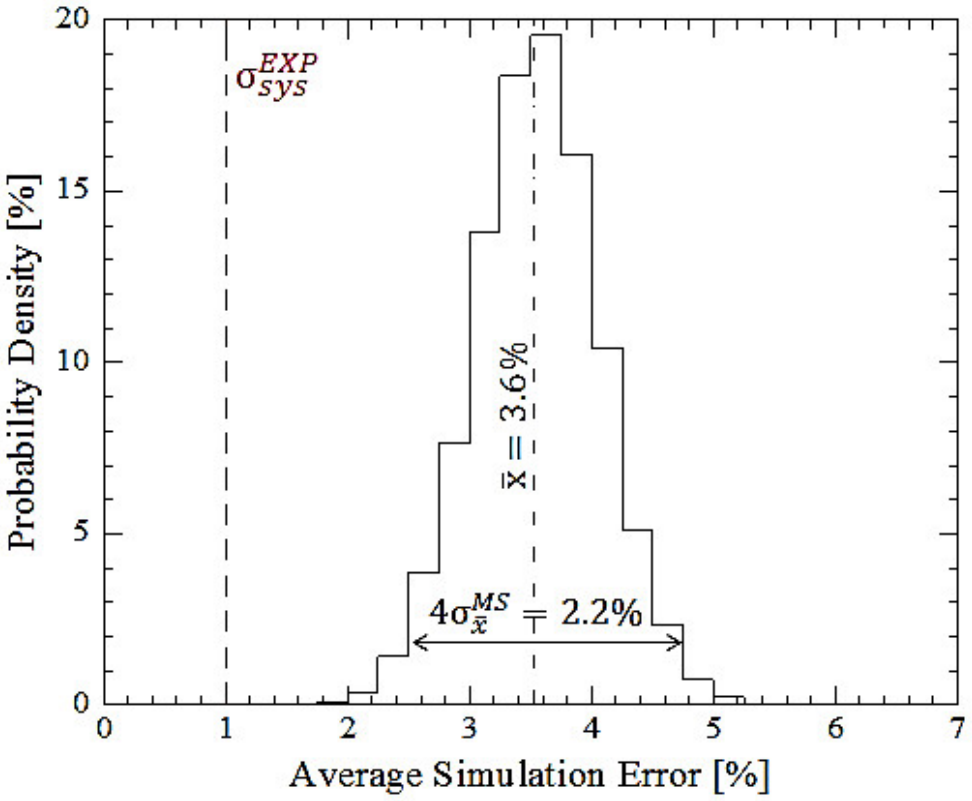

Figure 7-8: Bootstrapped distribution of the average percent error of the molecular simulation when compared to the complementary experimental measurement. The 95% confidence interval of the average simulation error $(2\sigma_{\bar{x}}^{MS})$ *begins to intersect the systematic uncertainty of the experimental measurement*(σ_{sys}^{EXP}) *when the distribution is shifted by 1.5%.*

Moving a step beyond average comparisons, trends in the accuracy of both molecular simulations and the GERG EOS were investigated by reducing the estimated results for each mixture composition by the fluid's critical properties (Gil et al., 2012). A contour map was made of the difference from the experimental result using a LOESS (locally weighted scatterplot smoothing) fit, with a smoothing parameter of 0.25 and weighting each data point by the uncertainty reported in Tables 7-1 through 7-5. Figure 7-9 shows this contour map of deviations as well as the locations of each of the points used for the fit. Reiterating, a corresponding states representation of the data, shown in Figures 7-9 and 7-10, are meant to clearly show qualitative trends that are present within each of the compositional datasets, but not to quantitatively define molecular simulation accuracy. In Figure 7-9, molecular simulations tend to overestimate C_p more severely in the near critical region compared to the average overestimate and underestimate C_p in the gas-like supercritical region. Figure 7-10 shows a similar plot for the GERG EOS. It appears that the discrepancy between the EOS predicted and the experimental C_p values largely comes from misidentification of the location of the peak in C_p on a given isotherm (or isobar) in temperature-pressure space for a given composition. The magnitude and shapes of the EOS curves are generally consistent with experiment.

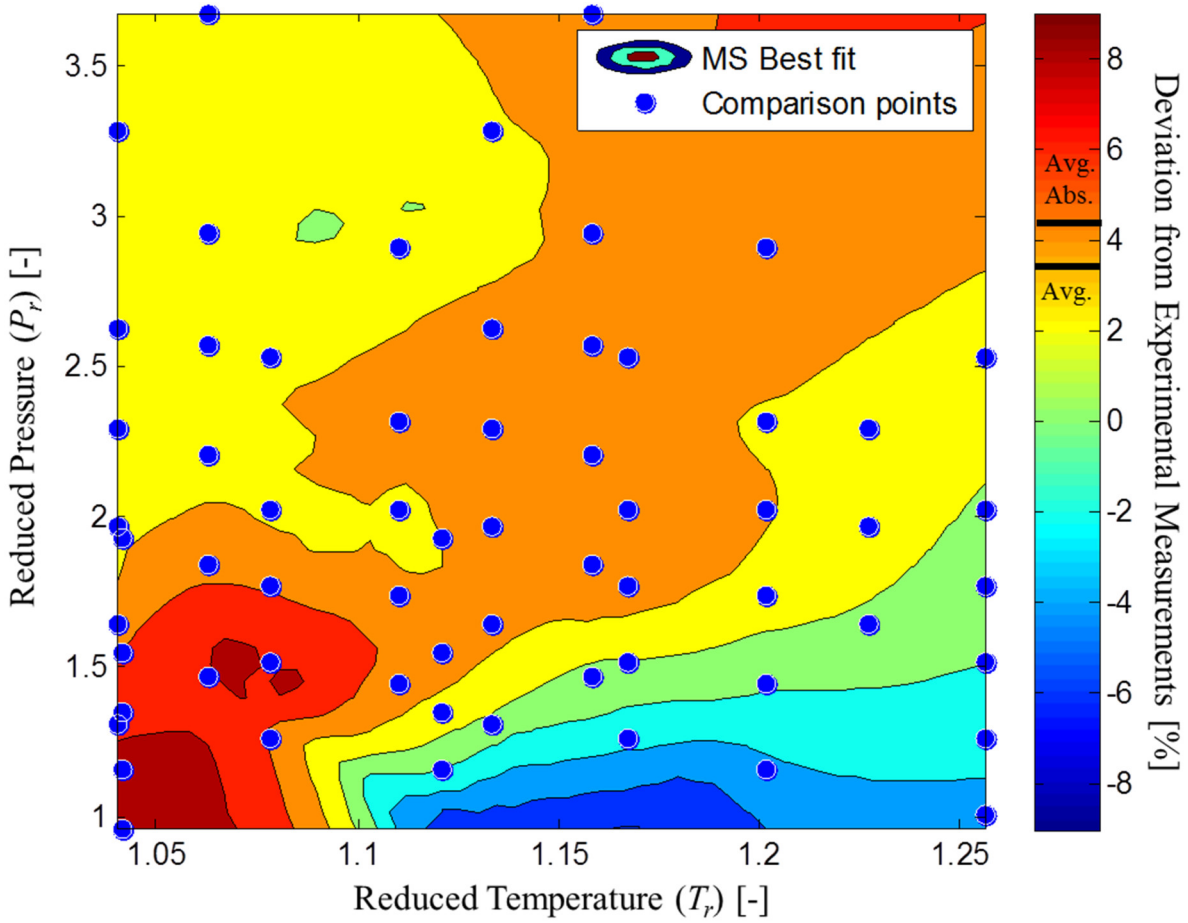

Figure 7-9: Contour plot of a surface fit to the differences between C_p *values determined by molecular simulations (MS) and experimental measurements at a number of (*PTX*) conditions, above labeled as comparison points. Points on the figure represent (*PT*) conditions where both a simulation has been run and an experimental measurement has been made. The temperatures and pressures associated with each comparison point have been normalized by the fluid mixture's approximate critical temperature and pressures* (Gil et al., 2012)*, allowing all compositions to be plotted simultaneously. The average percent difference (Avg. of 3.6%) and the average absolute difference (Avg. Abs. of 4.2%), where all of the differences have been made positive before averaging, are marked on the color scale bar.*

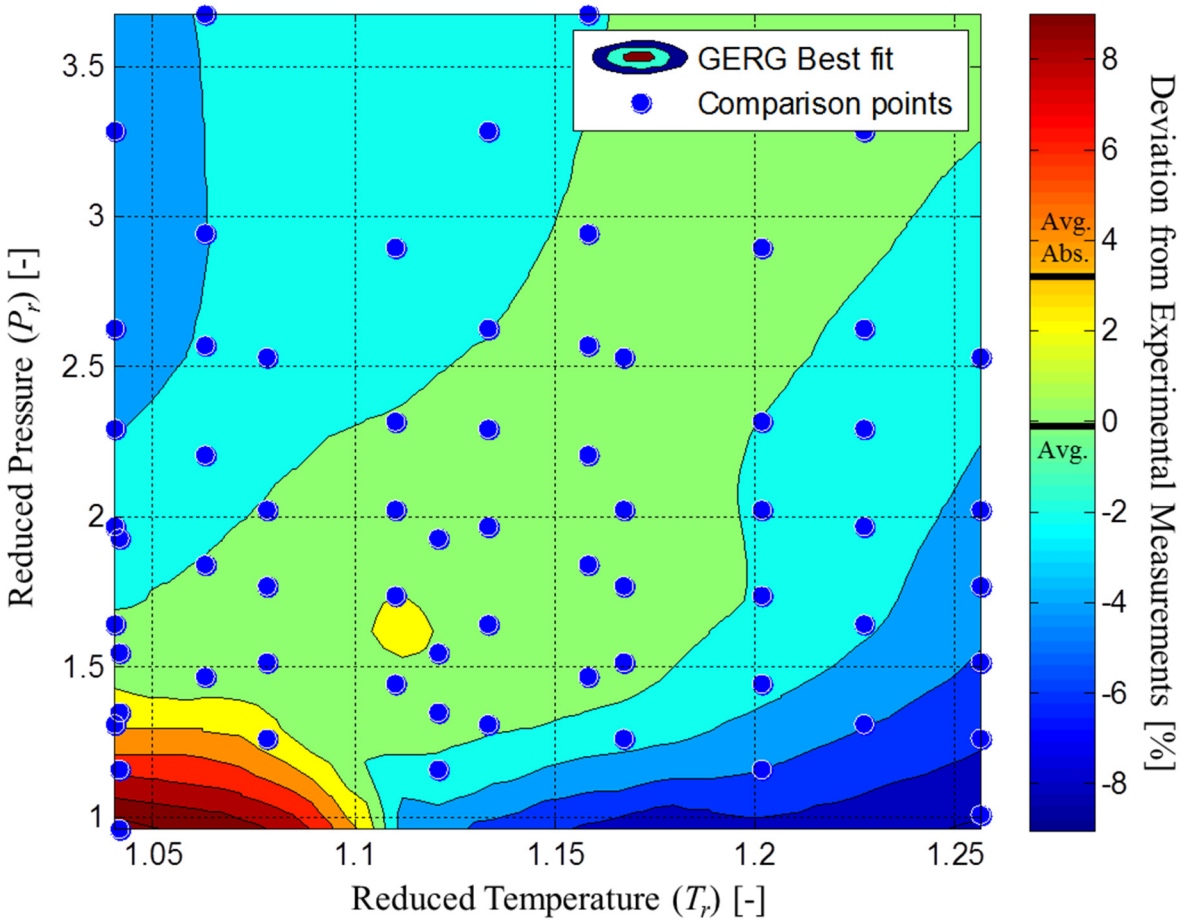

Figure 7-10: Contour plot of a surface fit to the differences between C_p *values determined by GERG-2008* (Kunz & Wagner, 2012) *and experimental measurements at a number of (*PTX*) conditions. Points on the figure represent (*PT*) conditions where the GERG EOS is valid and experimental measurement has been made. The temperatures and pressures associated with each comparison point have been normalized by the fluid mixture's approximate critical temperatures and pressures* (Gil et al., 2012)*, allowing all compositions to be plotted simultaneously. The average percent difference (Avg. of -0.3%) and the average absolute difference (Avg. Abs. of 3.1%), where all of the differences have been made positive before averaging, are marked on the color scale bar.*

Two potential causes of the deviations between the molecular simulation calculations and the experimental results stand out. First are force field inaccuracies near the critical point. Both the TraPPE force field for CO_2 and the TraPPE-UA force field for methanol were optimized using experimentally determined phase equilibria data, significantly outside the critical region (Martin & Siepmann, 1999; Martin & Thompson, 2004). With this empirical fit of molecular force fields in a region far removed from critical states, one might expect differences between

predicted critical temperatures and pressures from simulation and experimental results. For example, the predicted critical temperature from the TraPPE force field for CO_2 is 306.2 K (Martin & Thompson, 2004), while the experimentally determined critical temperature is 304.35 K. (Suehiro, Y., Nakajima, M., Yamada, K., & Uematsu, 1996). More advanced force fields would be expected to yield more accurate C_p estimates. The second source of error could be caused by finite size effects near the critical point. In the near critical region, the correlation length, which controls long range structure in molecular systems, experiences fluctuations that extend to greater magnitudes than the length of the simulation box (Mon & Binder, 1992).

7.5. Conclusions

Precise experimental measurements taken with a calibrated calorimeter remain the most reliable way to accurately determine the heat capacity of high pressure fluid mixtures, particularly in the near critical and supercritical region. The estimated uncertainty of C_p measurements reported in this work is 1.3 to 1.5% for measurements far from the critical locus and up to 3% for near-critical conditions. Experimental measurements are useful for improving the accuracy of EOS models, especially for mixtures where mixing rules have inherent limitations

For the first time, Monte Carlo molecular simulations were used to calculate C_p in the critical region for CO_2-methanol mixtures. Simulated isobaric heat capacities generally agreed with experimental values to within 3.5-5%, except near the critical locus ($T_r < 1.15$ and $P_r < 1.5$) where errors of up to 10-15% were observed. The molecular simulation calculations show significant scatter (random uncertainties of ~3% of C_p), but trends along various isobars and isotherms are perceivable (such as the consistently lower C_p values in the gas-like supercritical

region). Using statistical bootstrapping, it was found that on average the molecular simulations provide an overestimate of the true heat capacity value by at least +1.5%. Although molecular simulations are grounded in rigorous statistical mechanics, they are inherently limited by the accuracy of the force field models used, along with other assumptions such as pair-additivity and classical-mechanical behavior. Furthermore, accurate experimental data is needed to validate molecular simulations.

Similarly, empirical EOSs are dependent on the availability and accuracy of experimental results. However, if regressed EOS models are available, they are convenient for practical calculations when compared to molecular simulation calculations, which require considerable computational time for each state point. Under the conditions studied in this work, the GERG EOS predictions matched well with experimental results. Unfortunately, regressed EOS models are often not available, and in this study we showed that molecular simulations could be used to enhance sparse experimental data. Thus, in order to optimize the efficiency of thermodynamic property calculation at conditions where little experimental data exist, molecular simulations (once a force field is calibrated or validated at conditions where experimental data exist) could help improve the accuracy of the empirical EOSs. In addition, more advanced molecular simulations, albeit more computationally expensive, could potentially provide more accurate thermodynamic property estimates.

7.6. References

Allen, M. P., & Tildesley, D. J. (1989). *Computer simulation of liquids*. Oxford University Press.

Boulton, J. R., & Stein, F. P. (1988). Effect of pressure on the constant-pressure heat capacity of a methane-carbon dioxide mixture. *J. Chem. Eng. Data*, *198*(8), 196–198.

Chen, B., Potoff, J. J., & Siepmann, J. I. (2002). Monte Carlo calculations for alcohols and their mixtures with alkanes. Transferable potentials for phase equilibria. 5. United-atom description of primary, secondary, and tertiary alcohols. *Journal of Physical Chemistry B*, *105*(15), 3093–3104. http://doi.org/10.1021/jp003882x

Deng, L.-Y. (2005). Efficient and portable multiple recursive generators of large order. *ACM Transactions on Modeling and Computer Simulation*, *15*(1), 1–13. http://doi.org/10.1145/1044322.1044323

Gil, L., Blanco, S. T., Rivas, C., Laga, E., Fernández, J., Artal, M., & Velasco, I. (2012). Experimental determination of the critical loci for {n-C6H14 or CO2 + alkan-1-ol} mixtures. Evaluation of their critical and subcritical behavior using PC-SAFT EoS. *The Journal of Supercritical Fluids*, *71*(0), 26–44. http://doi.org/http://dx.doi.org/10.1016/j.supflu.2012.07.008

Herrero, M., Mendiola, J. A., Cifuentes, A., & Ibáñez, E. (2010). Supercritical fluid extraction: Recent advances and applications. *Journal of Chromatography A*, *1217*(16), 2495–511. http://doi.org/10.1016/j.chroma.2009.12.019

Kunz, O., Klimeck, R., Wagner, W., & Jaeschke, M. (2007). The GERG-2004 wide-range reference equation of state for natural gases. *European Gas Reserach Group (Groupe Européen de Recherches Gazières) Technical Monograph*, *15*.

Kunz, O., & Wagner, W. (2012). The GERG-2008 wide-range equation of state for natural gases and other mixtures: An expansion of GERG-2004. *Journal of Chemical and Engineering Data*, *57*(11), 3032–3091. http://doi.org/10.1021/je300655b

Lagache, M., Ungerer, P., Boutin, A., & Fuchs, A. H. (2001). Prediction of thermodynamic derivative properties of fluids by Monte Carlo simulation. *Physical Chemistry Chemical Physics*, *3*(19), 4333–4339. http://doi.org/10.1039/b104150a

Lemmon, E. W. (2015). Personal communication, November 19, 2015. Thermophysical Properties Division, Nation Institute of Standards and technology (NIST).

Lemmon, E. W., Huber, M. L., & Mclinden, M. O. (2013). *NIST Standard Reference Database 23: Reference Fluid Thermodynamic and Transport Properties-REFPROP, Version 9.1*. Gaithersburg.

Liu, J., Qin, Z., Wang, G., Hou, X., & Wang, J. (2003). Critical Properties of Binary and Ternary Mixtures of Hexane + Methanol, Hexane + Carbon Dioxide, Methanol + Carbon Dioxide, and Hexane + Carbon Dioxide + Methanol. *Journal of Chemical & Engineering Data*,

48(6), 1610–1613. http://doi.org/10.1021/je034127q

Maitland, G. F., Rigby, M., Smith, E. B., & Wakeham, W. A. (1981). *Intermolecular forces: their origin and determination. No. 3.* Oxford University Press.

Martin, M. G. (2013). MCCCS Towhee: a tool for Monte Carlo molecular simulation. *Molecular Simulation*, *39*(14–15), 1212–1222. http://doi.org/10.1080/08927022.2013.828208

Martin, M. G., & Siepmann, J. I. (1999). Novel Configurational-Bias Monte Carlo Method for Branched Molecules. Transferable Potentials for Phase Equilibria. 2. United-Atom Description of Branched Alkanes. *The Journal of Physical Chemistry B*, *103*(21), 4508–4517. http://doi.org/10.1021/jp984742e

Martin, M. G., & Thompson, A. P. (2004). Industrial property prediction using Towhee and LAMMPS. *Fluid Phase Equilibria*, *217*(1), 105–110. http://doi.org/10.1016/j.fluid.2003.06.007

McDonald, I. R. (1972). NpT -ensemble Monte Carlo calculations for binary liquid mixtures. *Molecular Physics*, *23*(1), 41–58. http://doi.org/10.1080/00268977200100031

Mendes, R. L., Nobre, B. P., Cardoso, M. T., Pereira, A. P., & Palavra, A. F. (2003). Supercritical carbon dioxide extraction of compounds with pharmaceutical importance from microalgae. *Inorganica Chimica Acta*, *356*, 328–334. http://doi.org/10.1016/S0020-1693(03)00363-3

Mon, K. K., & Binder, K. (1992). Finite size effects for the simulation of phase coexistence in the Gibbs ensemble near the critical point. *The Journal of Chemical Physics*, *96*(1992), 6989–6995. http://doi.org/10.1063/1.462557

Potoff, J. J., & Siepmann, J. I. (2001). Vapor–liquid equilibria of mixtures containing alkanes, carbon dioxide, and nitrogen. *AIChE J.*, *47*(7), 1676–1682. http://doi.org/10.1002/aic.690470719

Stubbs, J. M., & Siepmann, J. I. (2004). Binary phase behavior and aggregation of dilute methanol in supercritical carbon dioxide: a Monte Carlo simulation study. *The Journal of Chemical Physics*, *121*(3), 1525–1534. http://doi.org/10.1063/1.1763842

Stutzman, L. B. (2016). *Monte Carlo Molecular Simulations To Determine The Isobaric Heat Capacity Of Co2, Methanol, And Their Mixtures Using Thermodynamic Fluctuations In The Isothermal-Isobaric Ensemble And The Grand Canonical Ensemble*. Cornell University.

Suehiro, Y., Nakajima, M., Yamada, K., & Uematsu, M. (1996). Critical parameters of {xCO2+ (1 −x)CHF3} for x= (1.0000, 0.7496, 0.5013, and 0.2522). *Journal of Chemical Thermodynamics*, *28*(10), 1153–1164.

8. MAPPING THE RIDGE IN ISOBARIC HEAT CAPACITY FOR CARBON DIOXIDE-DECANE AND CARBON DIOXIDE-METHANOL BINARY MIXTURES

8.1. Author's note

A part of the material presented here is based on the following published article:

Ishmael, Mitchell P. E., Lauren B. Stutzman, Maciej Z. Lukawski, Fernando A. Escobedo, and Jefferson W. Tester. "Heat capacities of supercritical fluid mixtures: Comparing experimental measurements with Monte Carlo molecular simulations for carbon dioxide-methanol mixtures." *The Journal of Supercritical Fluids* 123 (2017): 40-49.

Will Gregg contributed to some of the analysis presented here.

8.2. Introduction to the ridge in isobaric heat capacity for pure supercritical fluids

Referring to the measurements reported in Chapter 6, Figure 6-5 (reproduced below) shows the isobaric heat capacity of pure carbon dioxide for a number of different isotherms, three of which (60, 90 and 120 °C) display maximums over the pressures studied. These three maximums projected onto a pressure-temperature diagram, as shown in Figure 8-1, illustrate what is known as a "ridge" in the heat capacity function (Nakayama, 2000; Nishikawa, Kusano, Arai, Morita, & Introduction, 2003; Nishikawa & Morita, 2000), defined by the crest in the C_p surface in the supercritical region. ("Ridge" is the preferred term; the other commonly accepted term is "Line of Maxima" (Apfelbaum & Vorob'ev, 2013; Brazhkin, Fomin, Lyapin, Ryzhov, & Tsiok, 2011), which may be misleading when referring to a localized feature on the heat capacity surface plotted on pressure-temperature coordinates. In order to discuss a "maximum" C_p, the

path must be specified, such as a constant temperature path. Referencing the "ridge" as a "locus of maxima" provides a reasonable compromise, as it specifies that the direction in P-T coordinates is a collection of individual maximums).

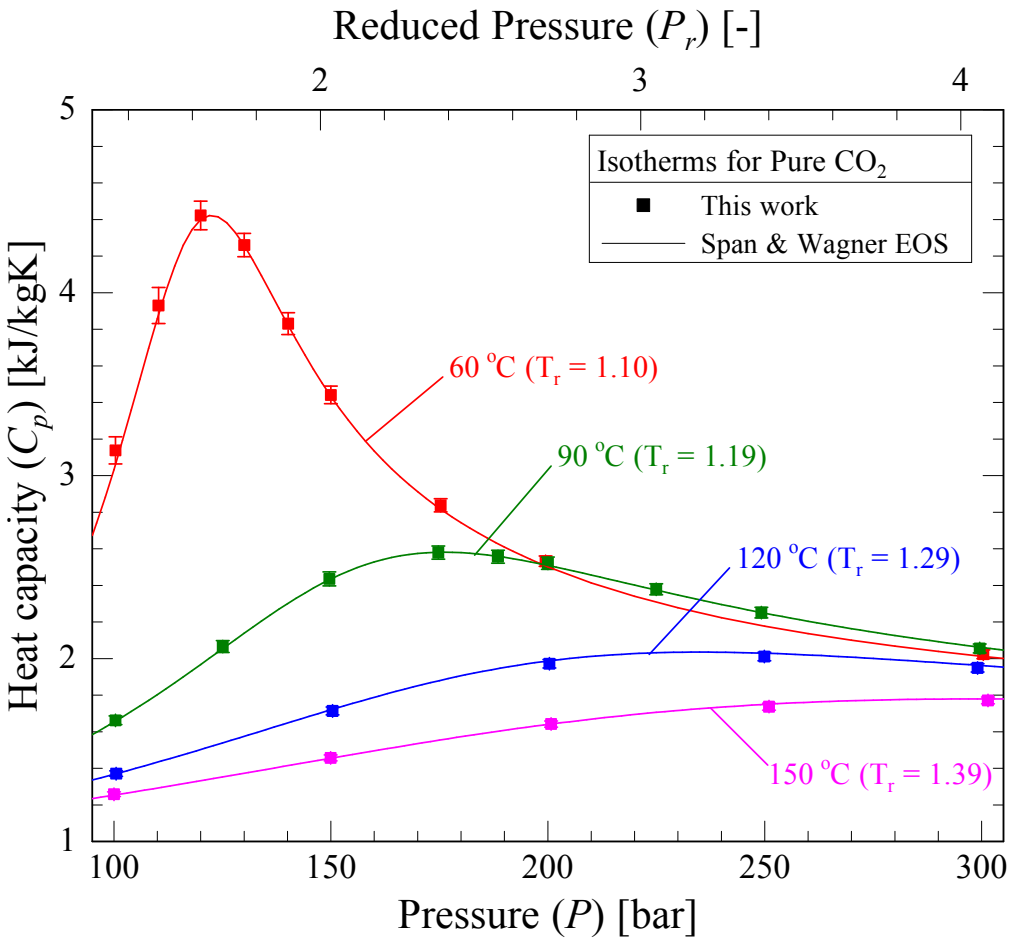

Figure 6-5: Comparison of the measurements made in this work to reference values reported by the Span and Wagner EOS (Span & Wagner, 1996). *The data agree with the Span and Wagner EOS values within the specified measurement uncertainty. Experimental measurements made by Ernst et al. agree with the Span and Wagner EOS calculations in this supercritical region* (Ernst, Maurer, & Wiederuh, 1989).

For a number of pure fluids, including water, carbon dioxide, argon, nitrogen and oxygen, this ridge has been mapped and studied, primarily using multiparameter EOS or models such as Lennard-Jones (Banuti, 2015; Gallo, Corradini, & Rovere, 2014; Nakayama, 2000).

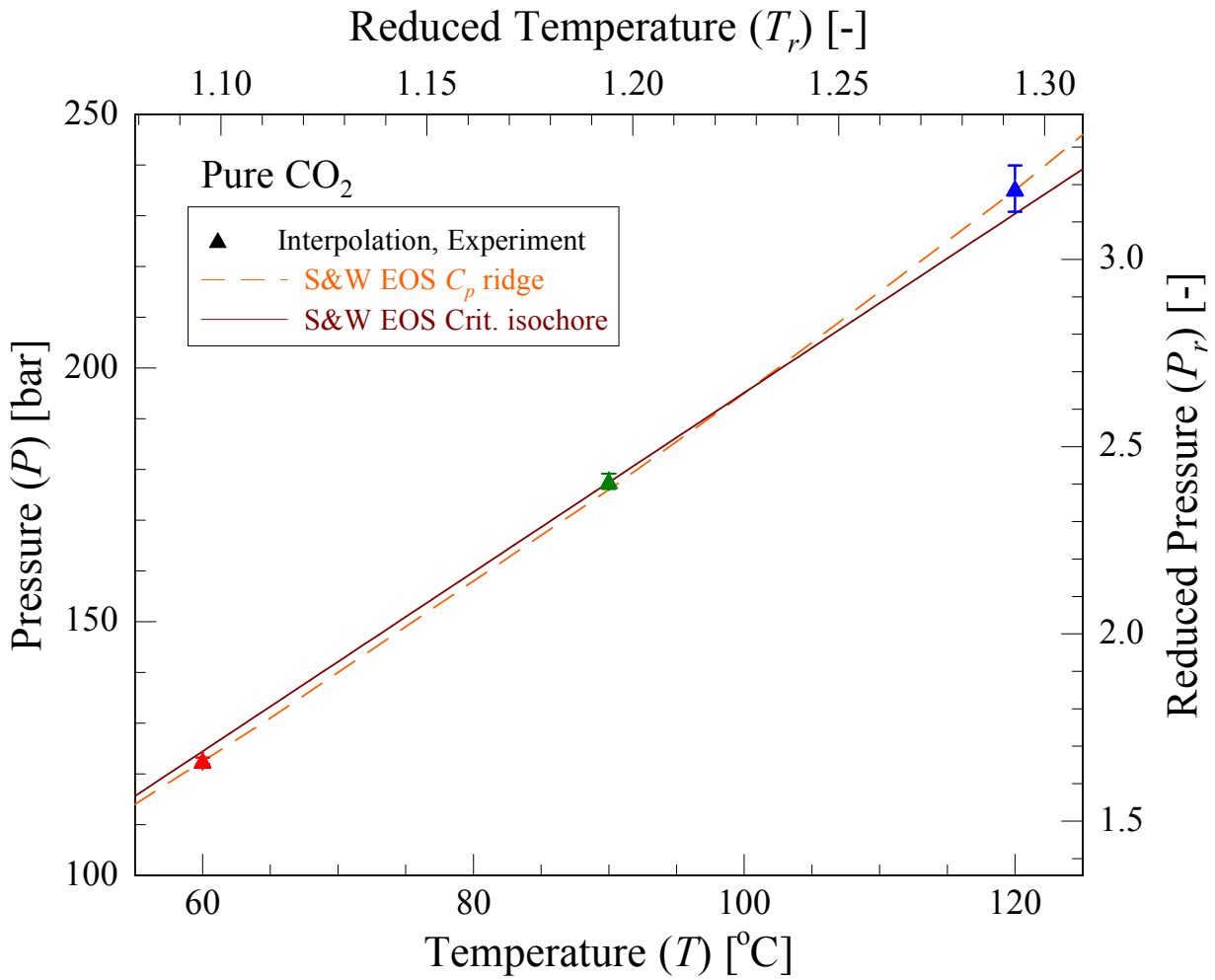

Figure 8-1: The ridge in isobaric heat capacity for pure carbon dioxide. The triangles represent maxima interpolated from the measured heat capacity data shown in Figure 6-5, where the color of the triangles matches each particular isotherm (red at 60 °C, green at 90 °C, blue at 120 °C). Lines were calculated using the Span and Wagner EOS for carbon dioxide (Span & Wagner, 1996)*. The dashed line is the EOS's estimate for the heat capacity ridge, and the solid line is the pressure-temperature path of an isochore at the system's critical volume.*

Contained within many of these references are descriptions of "special lines" (Brazhkin & Ryzhov, 2011), which includes the line defined by the ridge in heat capacity as well as many other lines (for example, the locus of maxima in the thermal expansion coefficient), all of which coalesce into a single line, termed the "Widom line," at pressures and temperatures near the critical point (T_r < 1.1 and P_r < 1.5) (Brazhkin & Ryzhov, 2011; Fomin, Ryzhov, Tsiok, & Brazhkin, 2015; Stanley, 1971; Xu et al., 2005). Motivated by the Widom line phenomena, the relationship between these special lines has been studied, and one relationship in particular is

commonly noted: the coincidence of the heat capacity ridge and the isochore emanating from the fluid's critical point (Apfelbaum & Vorob'ev, 2013; Nishikawa et al., 2003). Figure 8-1 depicts the similarity of the path of the critical isochore and the ridge in isobaric heat capacity for pure carbon dioxide. In Figure 8-2, the correlation between the critical isochore and the heat capacity ridge is shown for well-characterized substances with different intermolecular attractive forces.

The van der Waals EOS provides a convenient tool for probing the correlation between the critical isochore and the ridge in isobaric heat capacity. By inserting Equation 4-1 into Equation 3-16, the van der Waals EOS can be used to calculate the residual heat capacity at a particular temperature and pressure, which can be used to solve for the location of the isobaric heat capacity ridge. Equation 8-1 provides the expression for residual isobaric heat capacity for a van der Waals fluid:

$$P = \frac{RT}{V-b} - \frac{a}{V^2} \tag{4-1}$$

$$a = \frac{27R^2T_c^2}{64P_c}\ ; b = \frac{RT_c}{8P_c}\ ; b = \frac{V_c}{3} \tag{4-2}$$

$$C_p - C_p^o = T\int_{\infty}^{V}\left(\frac{\partial^2 P}{\partial T^2}\right)_V dV - T\frac{\left(\frac{\partial P}{\partial T}\right)_V^2}{\left(\frac{\partial P}{\partial V}\right)_T} - R \tag{3-16}$$

$$C_p - C_p^o = \frac{-R^2TV^3}{2a(V-b)^2 - RTV^3} \tag{8-1}$$

In Equation 8-1, C_p is in reference to the temperature and pressure of interest, and C_p^o is in reference to the ideal gas state at the same temperature. Identified above in Equation 4-2, the critical volume of a pure van der Waals fluid is equal to *3b*. Taking the derivative of Equation 8-1 with respect to molar volume at constant temperature, the zeroes of Equation 8-2 include the critical isochore ($V = 3b$):

$$\left(\frac{\partial(C_p - C_p^o)}{\partial V}\right)_T = (V-3b)(V-b)\frac{-2aR^2TV^2}{(2a(V-b)^2 - RTV^3)^2} = 0 \qquad (8\text{-}2)$$

$$P_r = 4T_r - 3 \qquad (8\text{-}3)$$

Equation 8-3 provides the equation for the C_p ridge for a van der Waals fluid in reduced coordinates (i.e. scaled by the fluid's critical temperature and pressure). Isobaric heat capacity is maximized for a pure supercritical van der Waal's fluid along the critical isochore. Figure 8-3 shows the reduced heat capacity as a function of reduced temperature and pressure demonstrating that the ridge lies along the critical isochore.

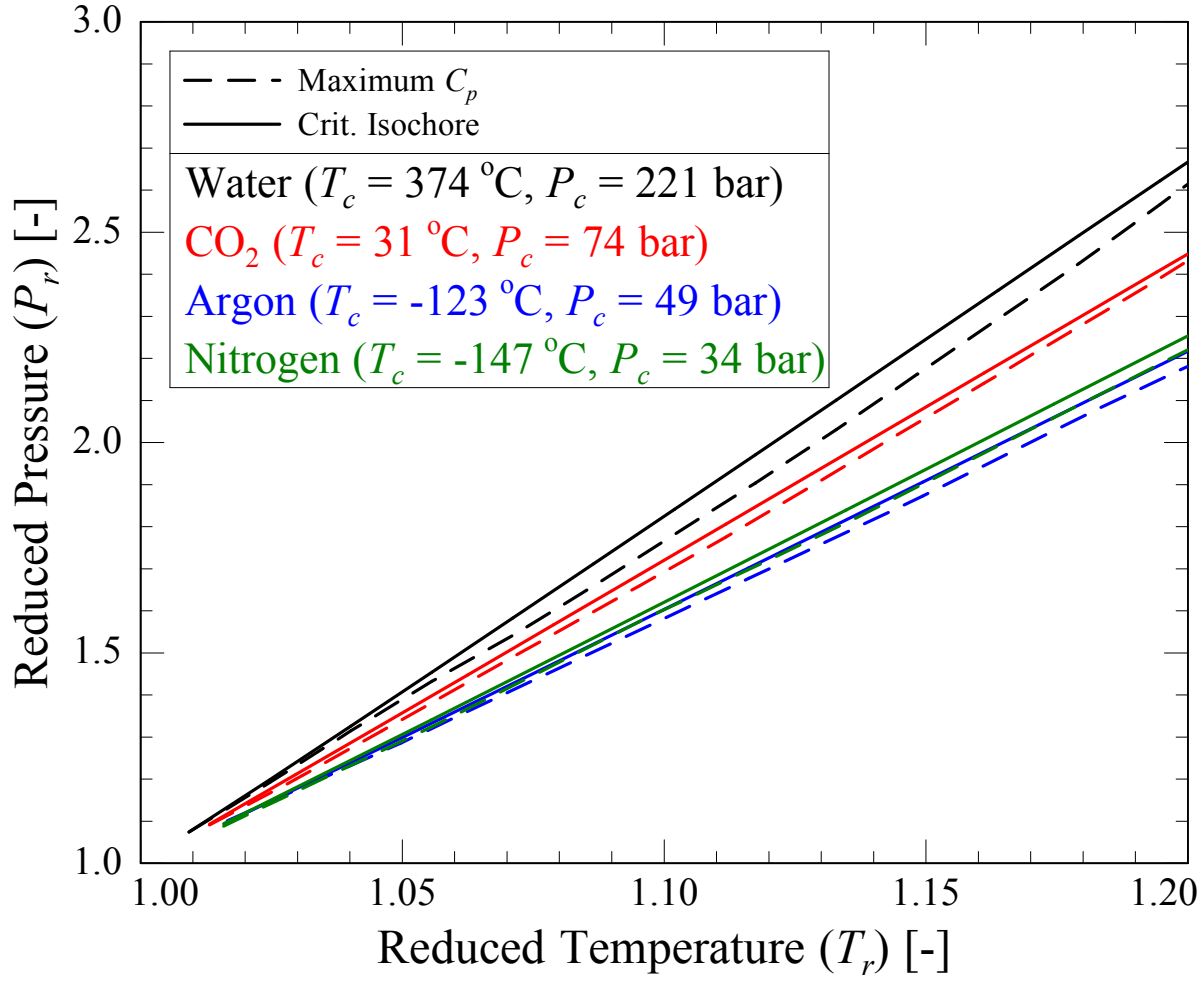

Figure 8-2: Plotted on reduced pressure-temperature coordinates, the critical isochore and the ridge in isobaric heat capacity for water (Wagner & Pruss, 2002)*, carbon dioxide* (Span & Wagner, 1996)*, argon* (Tegeler, Span, & Wagner, 1999) *and nitrogen* (Span, Lemmon, Jacobsen, Wagner, & Yokozeki, 2000).

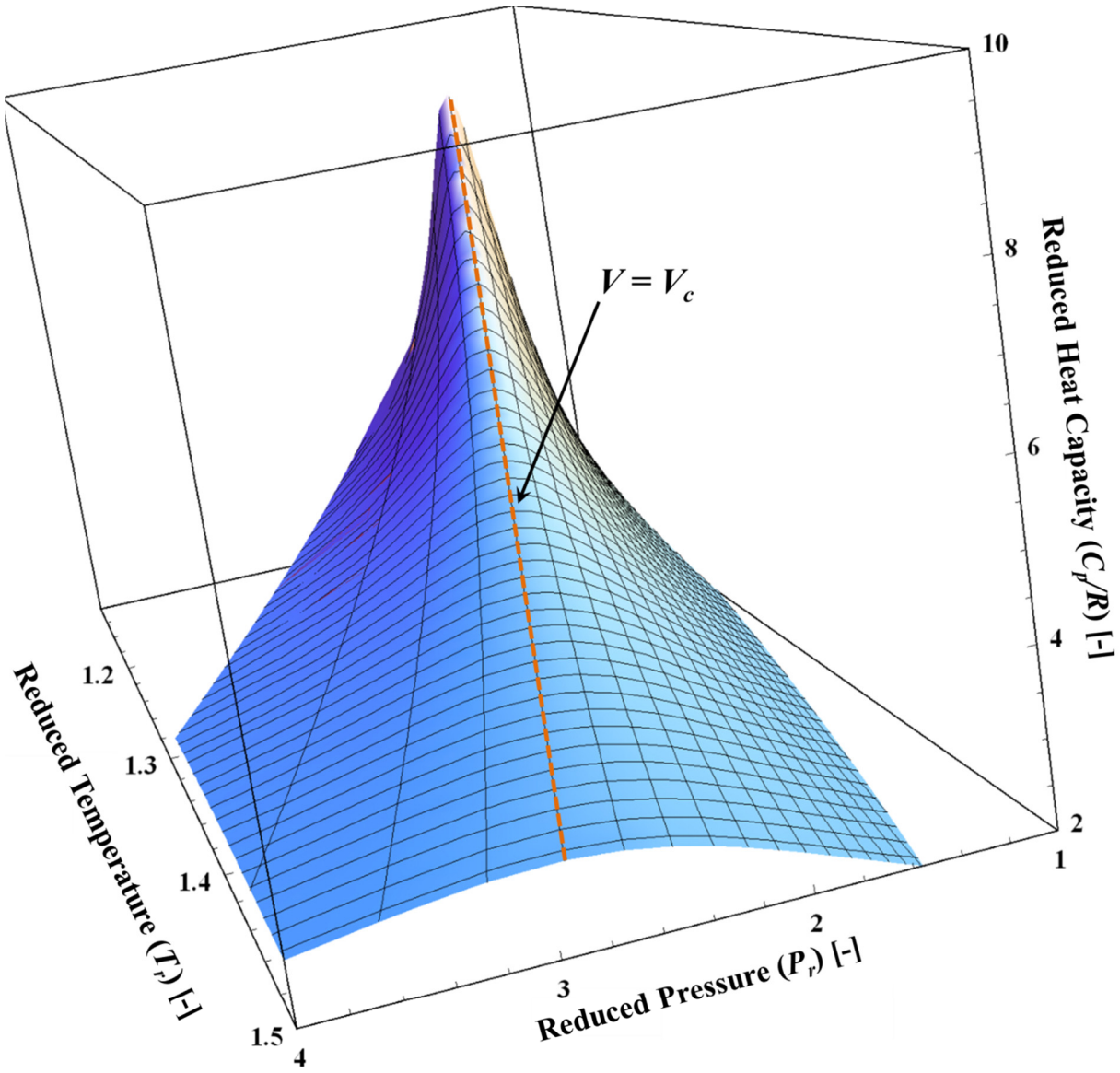

Figure 8-3: Isobaric heat capacity surface calculated from the van der Waals EOS plotted on pressure-temperature coordinates. For a pure van der Waals fluid, the critical isochore is collinear with the ridge in isobaric heat capacity.

Knowledge of the location of maxima in heat capacity along isobars or isotherms is not only important to heat transfer and thermal energy storage applications. Crossing over the ridge in heat capacity has been shown to be related to distinct changes in a fluid's diffusion coefficient, solvation capabilities, and viscosity (Xu et al., 2005). From a theoretical point of view, attempts have been made to characterize crossing the ridge in heat capacity as a type of gradual phase change, one which occurs over a range of temperatures and pressures (Banuti, 2015). In addition,

accurately locating and quantifying the ridge in heat capacity can help improve multiparameter EOS models and molecular simulations; the general trends of the deviation explored in Chapter 7 and illustrated in Figures 7-9 and 7-10 roughly follow parallel paths to the ridge in heat capacity (consider walking along a contour line for one of these plots).

8.3. The value of mapping the heat capacity ridge for complex binary mixtures

While many studies have documented the existence of the ridge in isobaric heat capacity, they have focused exclusively on pure fluids (Apfelbaum & Vorob'ev, 2013; Banuti, 2015; Brazhkin et al., 2011; Fomin et al., 2015; Gallo et al., 2014; Nakayama, 2000; Nishikawa et al., 2003; Xu et al., 2005). Some studies have made broad statements, for example suggesting that for all van der Waals fluid's the C_p ridge, for pure fluids or mixtures, follows the critical isochore (e.g. (Apfelbaum & Vorob'ev, 2013)). As demonstrated in Chapter 3, the nature of a critical point changes with additional mixture components. The first objective of this chapter is to clarify and refine the broad statements made in the literature regarding the relationship between the isobaric heat capacity ridge and the critical isochore, specifically with respect to binary fluid mixtures. Secondly, this Chapter provides additional experimental fluid property data for mixtures of carbon dioxide-methanol and carbon dioxide-decane, expanding the experimental data for isobaric heat capacity in the supercritical region for these mixtures. From these experimental measurements, the associated C_p ridges can be mapped.

8.4. Selection of carbon dioxide-decane as a complement to carbon dioxide-methanol

As a straight chain hydrocarbon, n-decane's intermolecular forces are distinctly different from methanol's (because of methanol's polar hydrogen bonds), primarily interacting through

van der Waals forces. Decane's critical temperature is nearly 100 °C larger than methanol's T_c and has a critical pressure about a fourth of methanol's P_c. Yet both fluid's exhibit Type-II fluid behavior with carbon dioxide, shown in Figure 8-4, defined by a continuous critical locus connecting the constituent critical points (van Konynenburg & Scott, 1980). The difference in phase behavior of these two fluid mixtures also is quite pronounced, even at low mole fractions of the solute. Critical temperatures and pressures start rising more rapidly for an equal addition of n-decane on a molar basis, and the phase boundary extends much further into pressure-temperature space for a carbon dioxide-decane mixture. Figure 8-5 illustrates this behavior.

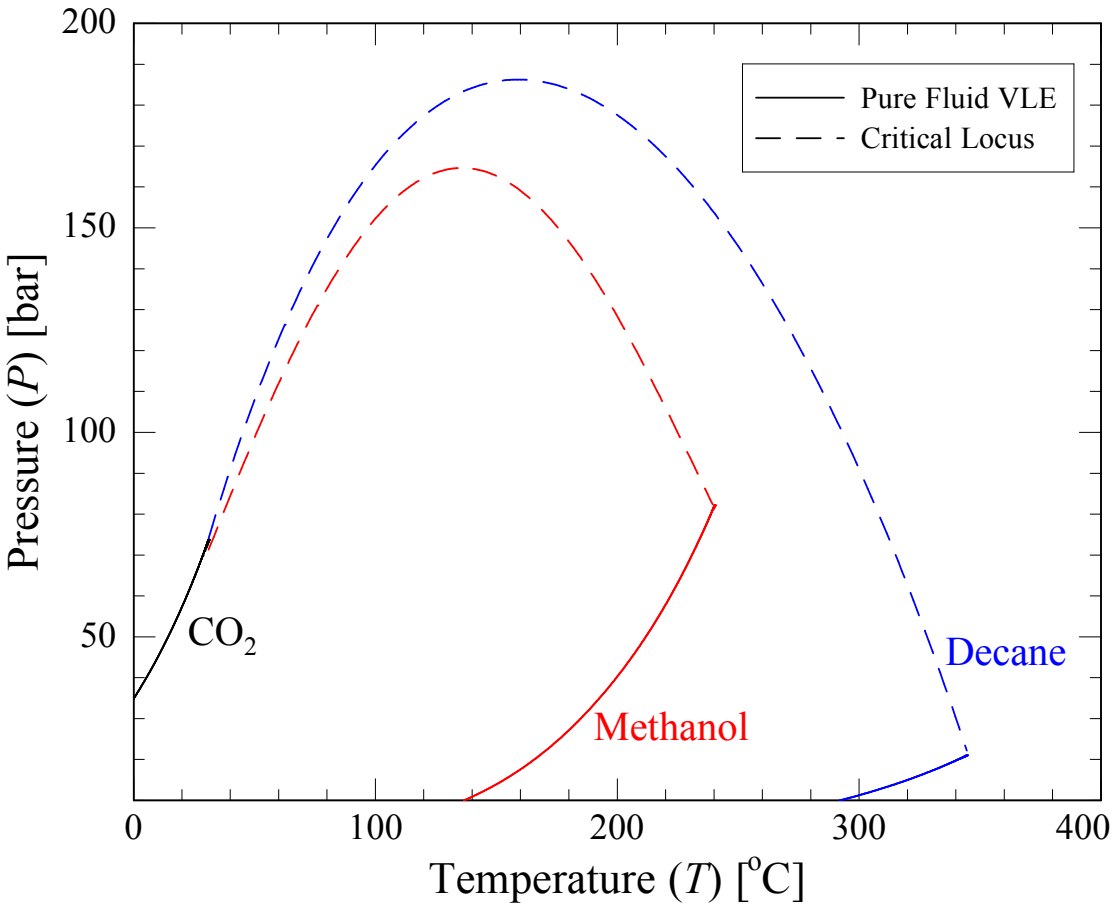

Figure 8-4: Vapor-Liquid Equilibrium (VLE) curves for carbon dioxide (Span & Wagner, 1996)*, methanol* (De Reuck & Craven, 1993) *and decane* (E. W. Lemmon & Span, 2006) *as well as the critical locus for carbon dioxide-methanol* (Gil et al., 2012) *and carbon dioxide-decane* (Chester & Haynes, 1997) *mixtures, plotted with a polynomial fit.*

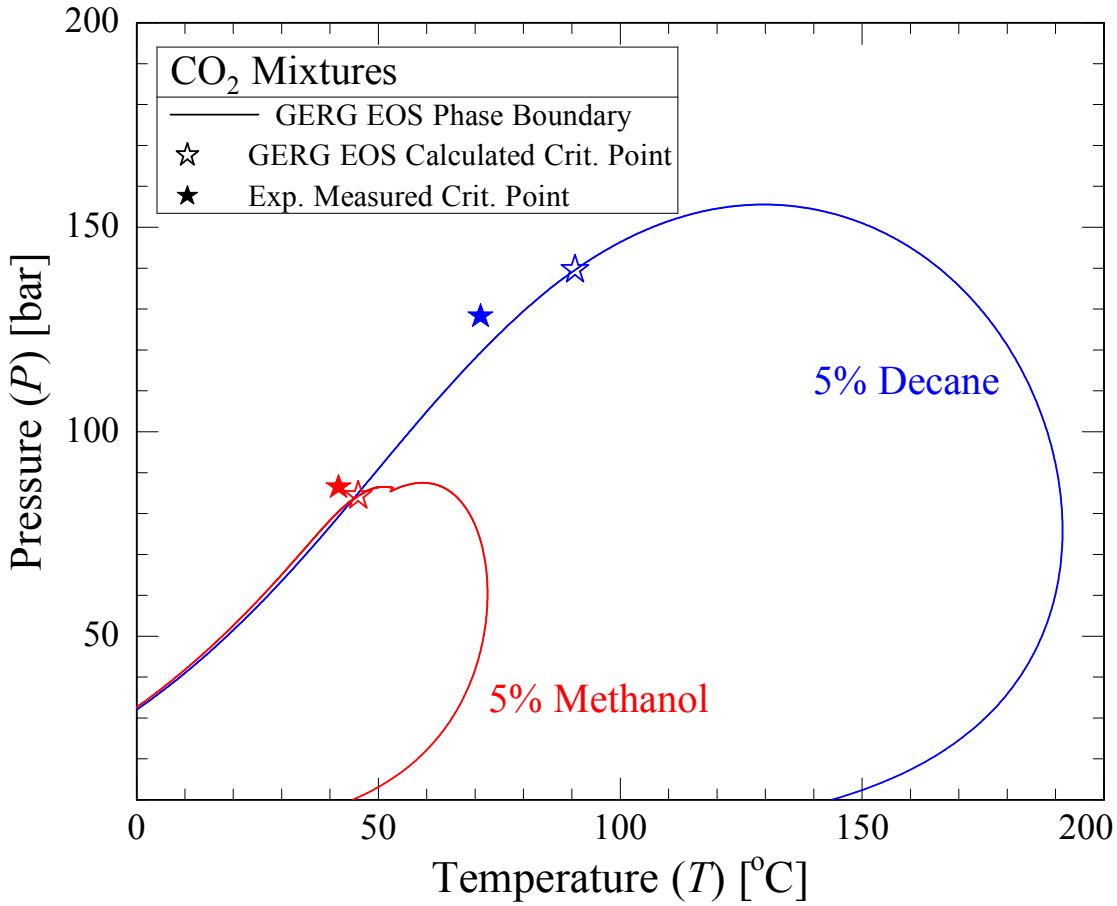

Figure 8-5: Phase boundaries for 5 mol% methanol in carbon dioxide and 5 mol% decane in carbon dioxide calculated with the GERG-2008 EOS (Kunz & Wagner, 2012). *Experimental critical points for the methanol mixture* (Gurdial, Foster, Yun, & Tilly, 1993) *and decane mixture* (Reamer & Sage, 1962) *are shown for comparison to the calculated critical states. The top of the phase envelope for 5% methanol is not smooth; GERG-2008, as implemented by REFPROP* (Eric W Lemmon, Huber, & Mclinden, 2013)*, shows some instability in this region. For example, the estimated critical temperature for 10% methanol in CO_2 is negative.*

The attractive features that prompted measurements of carbon dioxide-methanol mixtures are also relevant for carbon dioxide-decane mixtures. These include: rapid and complete dissolution of the minor component at moderate conditions, a continuous critical locus, intermolecular forces distinctly different from CO_2, available EOS fit to experimental data, and industrial importance of the mixture (mixtures of CO_2 with hydrocarbons are of interest to the oil and gas industry) (Kunz & Wagner, 2012). Beyond the similarities of these mixtures lie the differences that make binary mixtures with n-decane interesting, including: its non-polar intermolecular forces, the

rapid movement of the mixture critical point away from carbon dioxide's pure critical point with small additions of decane, and the significantly different critical point of decane. Provided earlier in Table 5-2, although C_p measurements of equimolar CO_2-decane have been made in other laboratories at elevated temperatures and pressures, they were considerably removed from the mixture's heat capacity ridge (Bessieres, Guirons, Daridon, & Coxam, 2000).

8.5. Carbon dioxide-decane isobaric heat capacity measurements and expansion of the carbon dioxide-methanol measurement set

In order to accurately quantify the location of the heat capacity ridge, many experimental measurements, near the location of the C_p peak for different isotherms, need to be taken. For carbon dioxide-methanol mixtures, this required an expansion of the measurement set listed in Chapter 7; the full list of unaveraged and unsmoothed measurements, including both systematic and random uncertainty, is given in Appendix F. Measurements of carbon dioxide-decane mixtures are in Appendix F as well as plotted in Figures 8-6 and 8-7. Each of these systems is compared against the GERG-2008 EOS; plots of the EOS error are given in Appendix G for CO_2-methanol and -decane mixtures. Appendix D contains information regarding implementation for each EOS used in this Chapter.

Three prominent trends are common for the different mixture data sets. First, EOS error is large in regions with very pronounced peaks in heat capacity. Second, the error tends to be greatest for mixtures at lower pressure. And finally, as the mixture becomes richer in the minor component, the predictive accuracy of the EOS in the supercritical region tends to decrease. The most striking difference between the set of measurements is how quickly the peak in isobaric heat capacity is depressed with the addition of decane. The 90 °C isotherm in Figure 7-1 and

Figure 8-7 are very similarly shaped, yet this is a 2% decane mixture as opposed to the 10% methanol mixture. One potential cause for the rapid decay of the peaks in C_p in the decane-carbon dioxide mixture is the much larger phase envelope of this mixture, which effectively acts as a shield for the mixture from its mechanical stability limit (an example of the different phase boundaries is plotted in Figure 8-5).

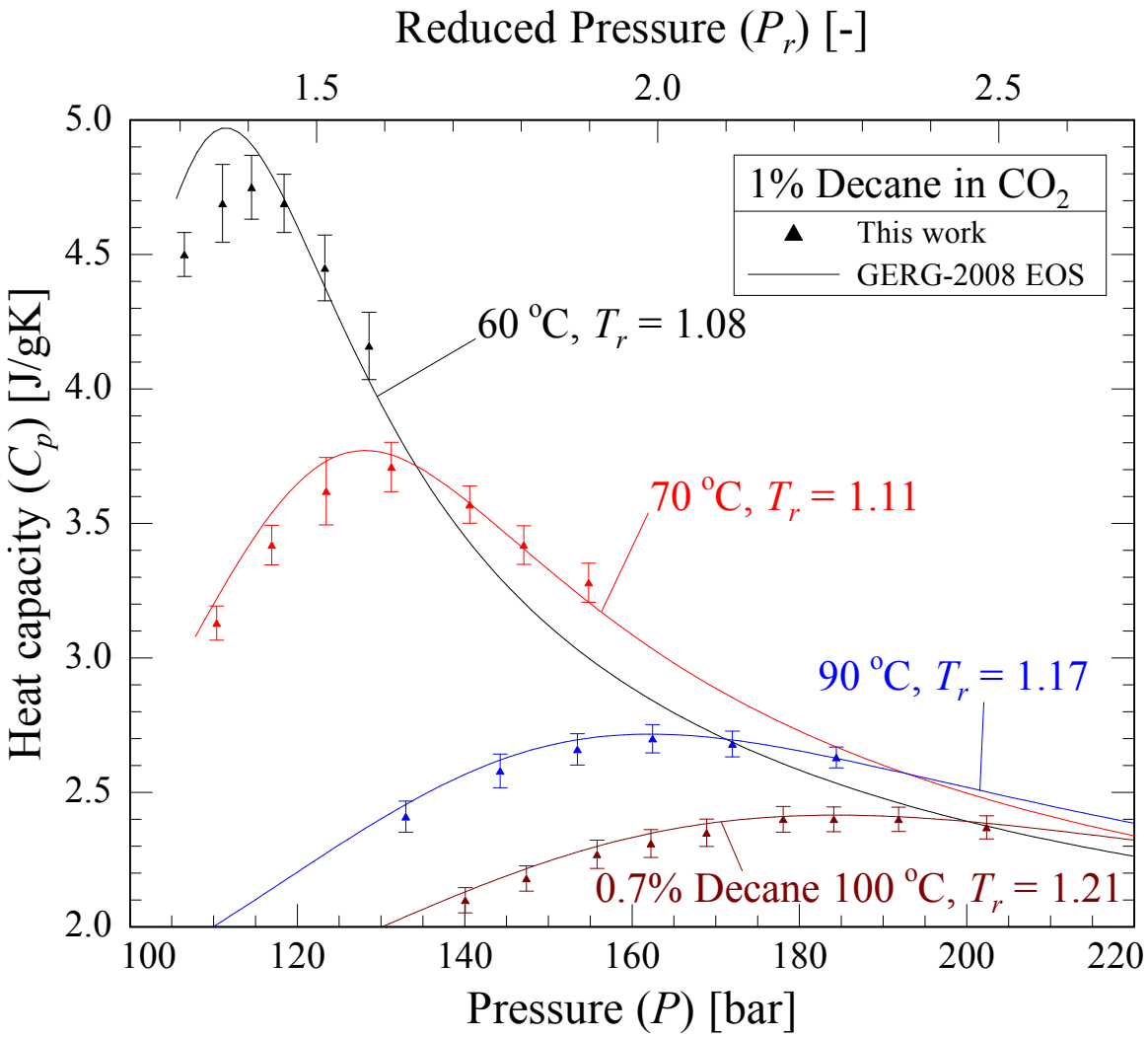

Figure 8-6: Heat capacity plotted versus pressure where all isotherms are for 1 mol% n-decane in carbon dioxide, except for the brown line, which is 0.7% n-decane in CO_2. Triangles represent experimental measurements, accompanied by error bars of summed random and systematic measurement uncertainties. The lines are predicted heat capacities by the GERG-2008 EOS; wherever the lines terminate on the plot, there is a predicted phase boundary (Kunz & Wagner, 2012).

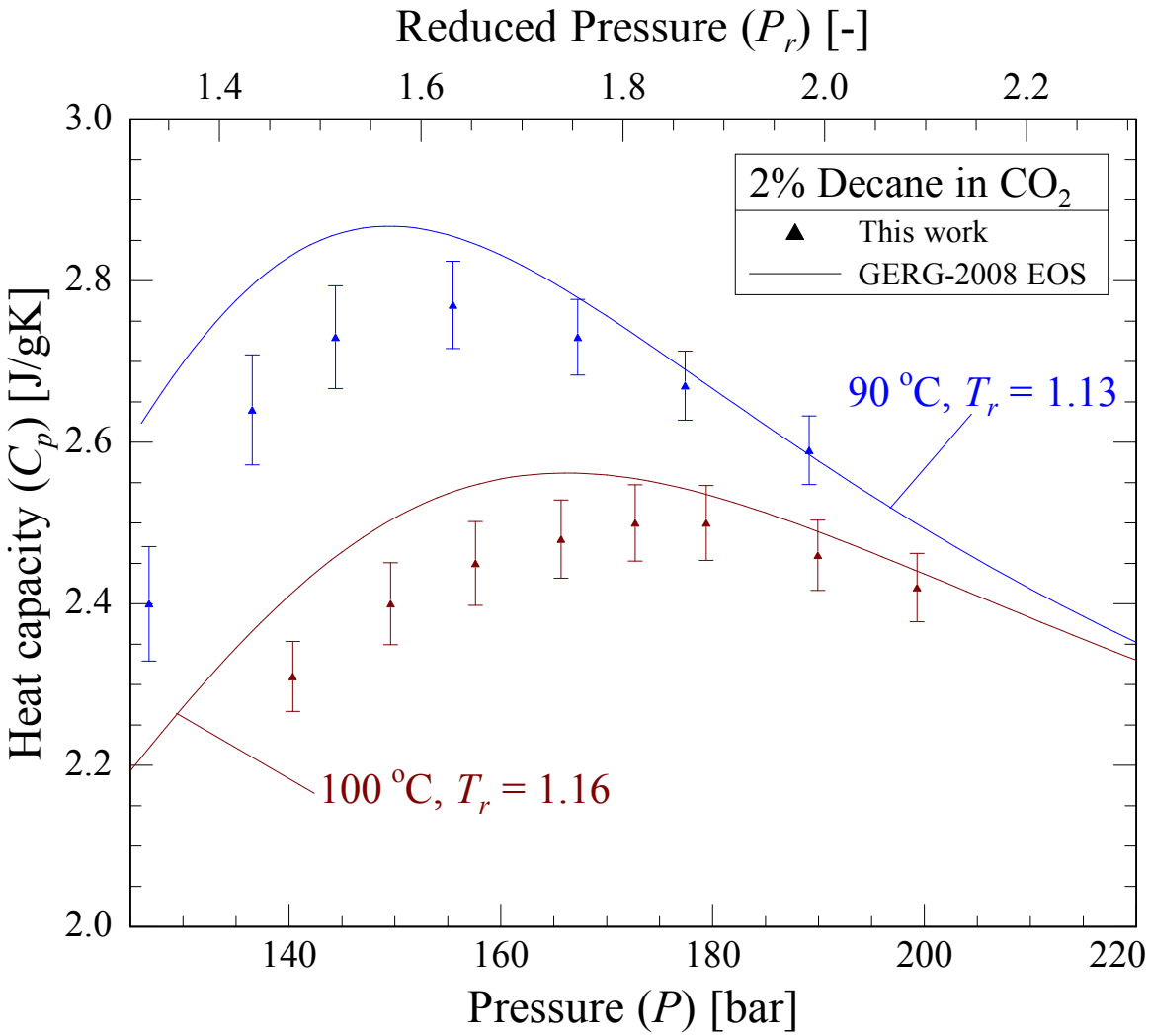

Figure 8-7: Heat capacity plotted versus pressure for 2 mol% n-decane in carbon dioxide. Triangles represent experimental measurements, accompanied by error bars of summed random and systematic measurement uncertainties. The lines are predicted heat capacities by the GERG-2008 EOS (Kunz & Wagner, 2012).

8.6. Mapping the ridge in isobaric heat capacity for a binary fluid mixture

Data presented in Appendix F for CO_2-methanol and -decane mixtures were used to map the heat capacity ridge onto a pressure-temperature plane. Statistical bootstrapping techniques were used to determine the uncertainty in the position of each maximum for a given mixture composition at a specific isotherm. Four hundred realizations of each isotherm were generated by adding random noise, from a normal distribution with a standard deviation equal to the random

uncertainty of each data point. Every realization was fit with a polynomial (particular polynomials and fitted data points are listed in Appendix H); the maximum C_p and its associated pressure were identified and recorded. The standard deviation of this set of 400 pressure values were used to accurately estimate the certainty with which the peak can be located for a given composition at a specific isotherm from this work's experimental measurements.

Figure 8-8 provides the location of the isobaric heat capacity ridge for the measured carbon dioxide-decane mixtures, and Figure 8-9 provides the results for carbon dioxide-methanol. Plotted on both figures are the following features: the compositionally dependent peaks in heat capacity for each experimental isotherm (represented as triangles), measurements of each mixture's critical point from published literature (depicted as stars), and dashed lines fitted to the ridge data. The slope for each of the dashed lines was determined beforehand, using a mole fraction weighted average of the slope of the ridge for each of the pure components. As previously demonstrated, the slope of the ridge, for a pure fluid, is approximately equal to the slope of the critical isochore, therefore the dashed lines in Figures 8-8 and 8-9 can also be considered approximations of averaged pure critical isochores. Pure carbon dioxide is included in both plots to serve as a reference for pure fluid behavior.

The similarities and differences in the nature of the isobaric heat capacity ridge for mixtures and pure fluids quickly become clear. At first glance, it is apparent that the ridge for both mixtures, all compositions of CO_2-decane and CO_2–methanol, follow approximately linear paths on a temperature-pressure plane, mimicking the straight line set by pure fluids. Using the van der Waals EOS as a first order approximation, the linearity becomes evident. All fluids, pure and mixtures, described by the van der Waals EOS exhibit C_p ridges that follow paths of constant density, defined by Equation 8-2, and the vdW EOS predicts straight lines when density is held

constant on a pressure-temperature plane. Straight ridge lines do not necessarily prove that the ridge lines lie near isochores, but as the ridge slopes follow the averaged constituent isochores, it strongly suggests that these mixture ridges lie along near isochoric lines.

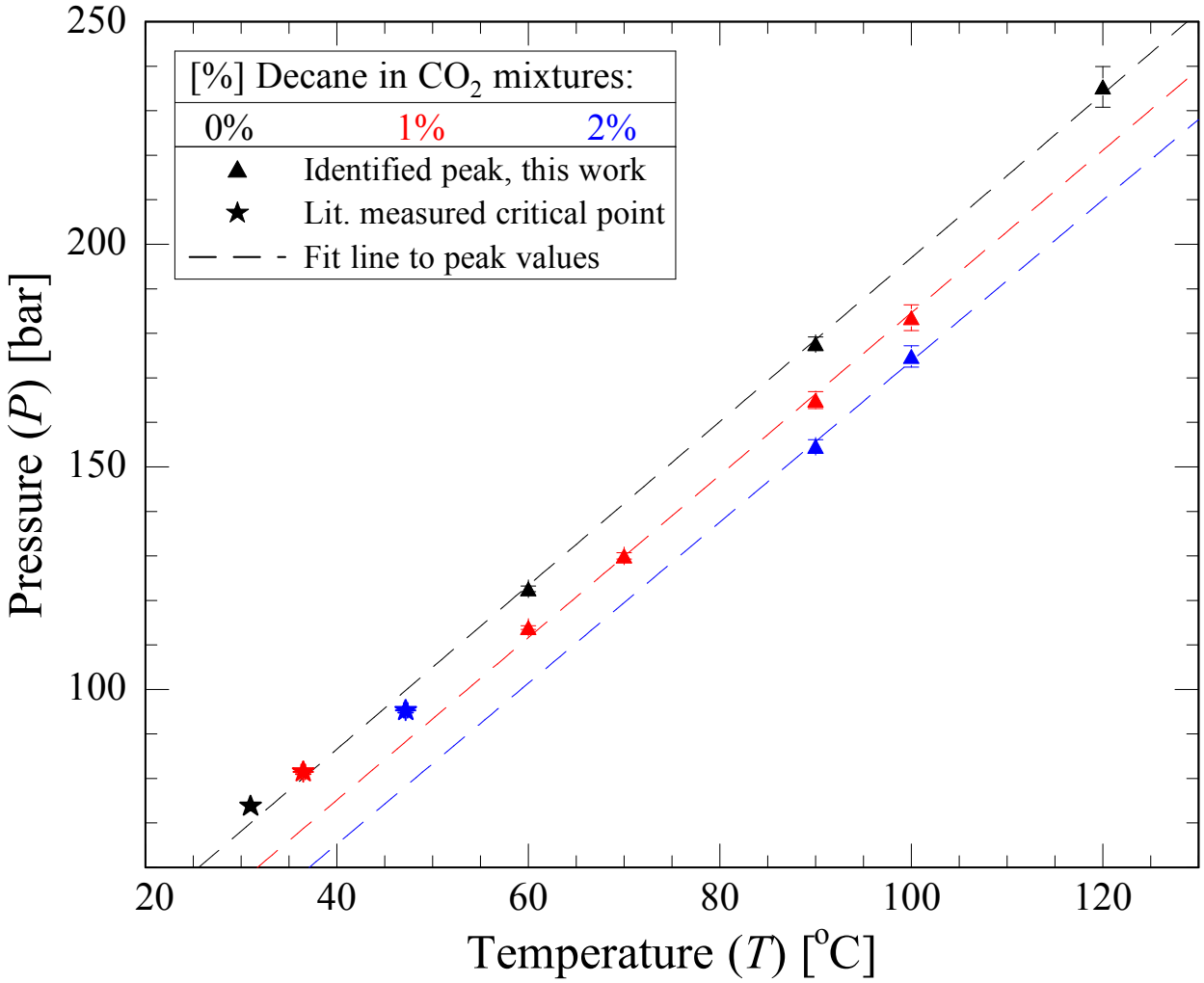

Figure 8-8: Isobaric heat capacity ridges for mixtures of n-decane in carbon dioxide. Triangles represent the estimated pressure of a peak heat capacity value along the associated isotherm. The stars are experimentally determined critical pressures for pure carbon dioxide and low percentage mixtures of n-decane in CO_2 (Gurdial et al., 1993). *Slopes of the dashed lines were calculated by averaging the slopes, on a molar basis, of the pure constituent* C_p *ridge slopes, and the y-intercepts were fit to the experimental data.*

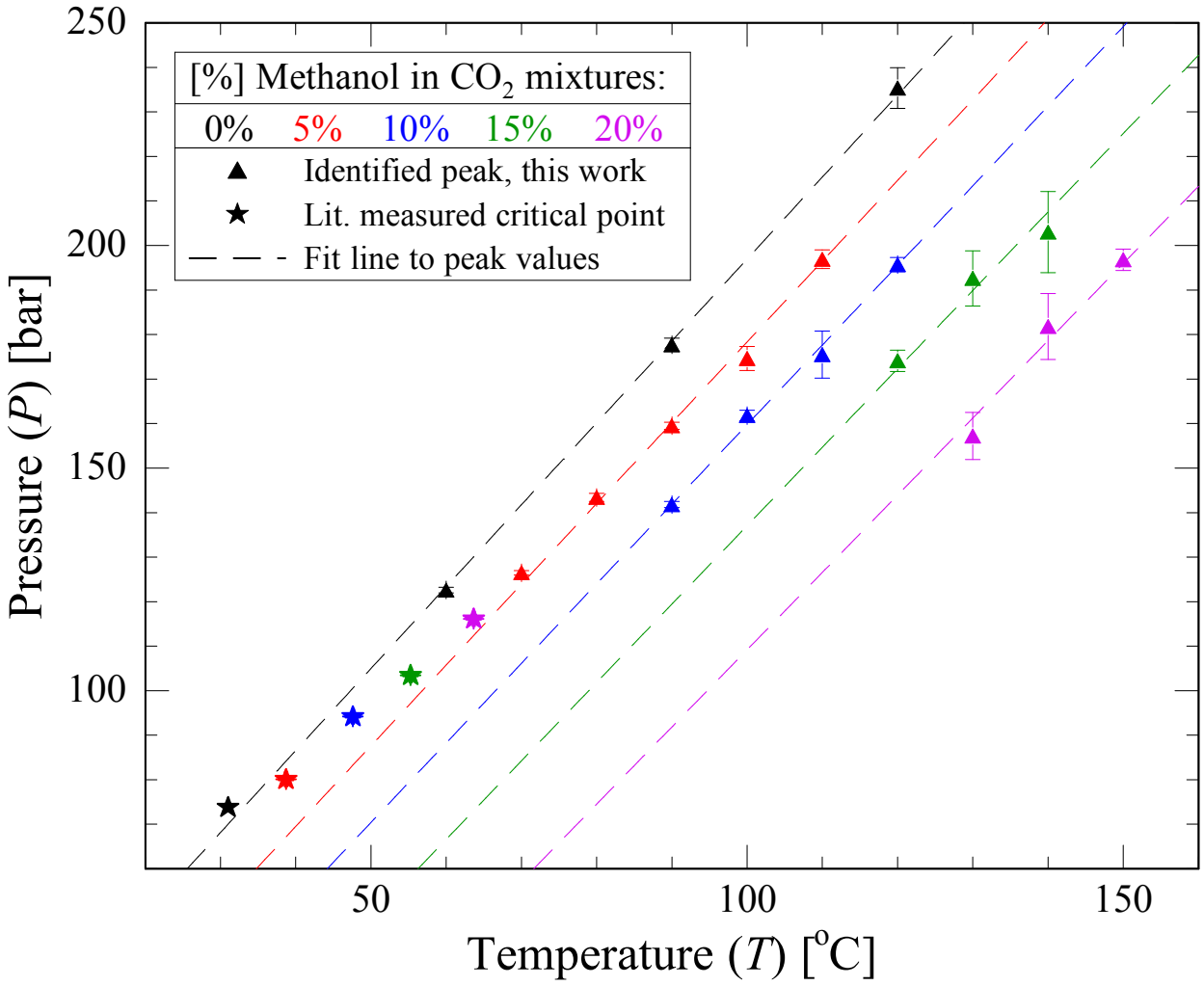

Figure 8-9: Isobaric heat capacity ridges for mixtures of methanol in carbon dioxide. Triangles represent the estimated pressure of a peak heat capacity value along the associated isotherm. The stars are experimentally determined critical pressures for pure carbon dioxide and methanol in CO_2 (Gil et al., 2012)*. Slopes of the dashed lines were calculated by averaging the slopes, on a molar basis, of the pure constituent* C_p *ridge slopes, and the y-intercepts were fit to the experimental data.*

Where mixtures deviate from pure fluid behavior is the location of the C_p ridge with respect to the fluid's critical point. In both Figure 8-8 and 8-9, as the fraction of the minor component is increased, the isobaric heat capacity ridge moves further from the associated mixture critical point. No set of isochores, emanating from each mixture's critical point, captures the associated ridge's linearity, proving for binary mixtures that the critical isochore does not *necessarily* follow a similar path on a pressure-temperature plane as the C_p ridge, thus clarifying and refining

the statements made in the literature, highlighted in Section 8.2. Considering the implications of criticality for a mixture through the lenses of the van der Waals EOS helps rationalize this feature of fluid behavior.

8.6.1. The van der Waals description of the isobaric heat capacity ridge for a binary mixture

The van der Waals EOS is known for its ability to qualitatively map fluid behavior (Rowlinson & Swinton, 1982). Van Konynenburg and Scott introduced the modern framework for classifying the nature of criticality for binary fluid mixtures (van Konynenburg & Scott, 1980). Armed with the van der Waals EOS (Equation 4-1, repeated earlier this chapter) and its commonly associated mixing rules (Equations 4-3 and 4-4), they used the criteria for mixture criticality (Equation 3-24) to generate nearly all of the known binary mixture critical phase diagrams (Rowlinson & Swinton, 1982).

$$a_{mix} = \sum_i \sum_j x_i x_j \sqrt{a_i a_j} \qquad (4\text{-}3)$$

$$b_{mix} = \sum_i x_i b_i \qquad (4\text{-}4)$$

$$G_{XX} = \left(\frac{\partial \mu}{\partial X}\right)_{T,P} = 0 \; ; \; G_{XXX} = \left(\frac{\partial^2 \mu}{\partial X^2}\right)_{T,P} = 0 \qquad (3\text{-}24)$$

Using van Konynenburg and Scott's approach, as well as a number of equations they derived for van der Waals mixtures (where each constituent of the mixture has the same *b* parameter), the different pressure-temperature paths of the mixture critical isochore and the C_p ridge can be explained. These researchers' solution for the mixture critical volume (normalized by the *b* parameter, which is the same for both fluids) is plotted versus composition in Figure 8-10. At

both ends of the plot – for the pure components, in other words – the critical volume matches its regular value, *3b*, but for all compositions in between, where the criteria of criticality has changed from one of mechanical to material stability, the critical volume no longer equals *3b*. This deviation from *3b* has serious implications for the relationship between the critical isochore and the ridge in isobaric heat capacity. The C_p ridge for a van der Waals fluid will always lie collinear with the *3b* isochore, as shown in Equation 8-2 and depicted in Figure 8-3. Figure 8-10 demonstrates that a binary mixture's critical volume will not necessarily be *3b* (although the critical volume may indeed be *3b*, for example an azeotrope).

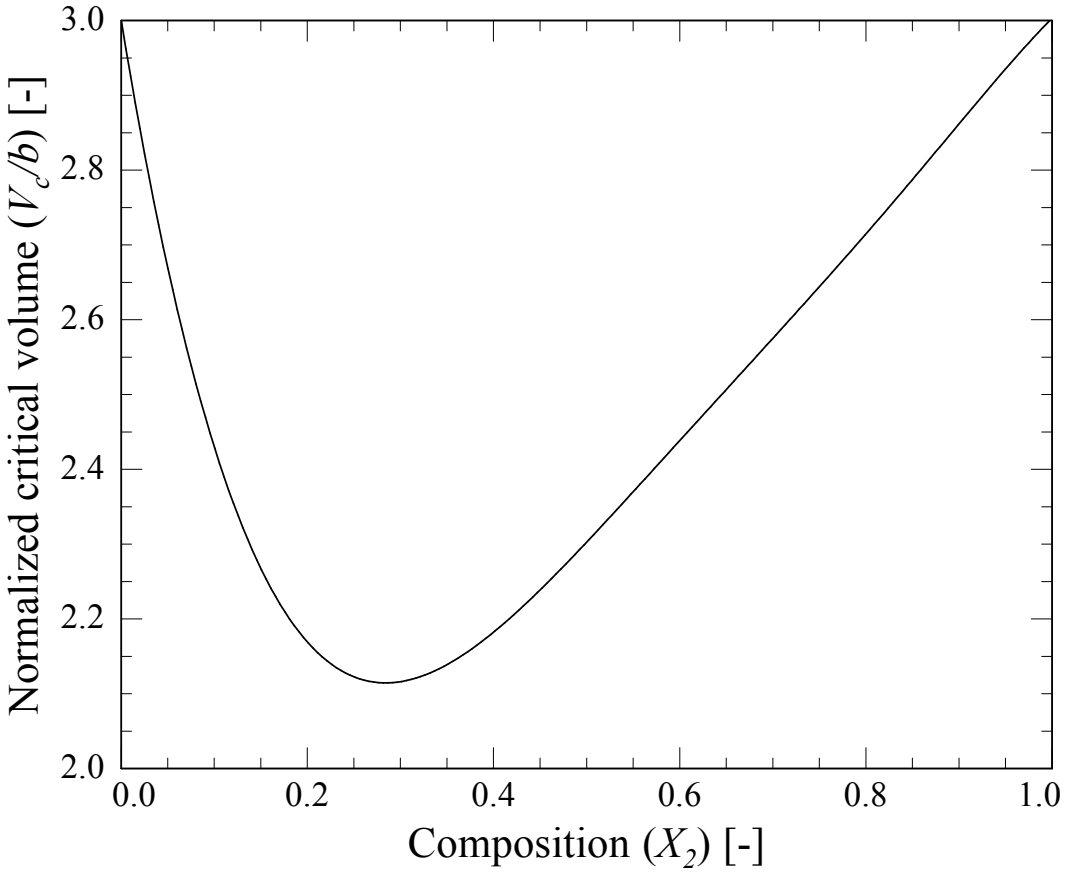

Figure 8-10: From work by van Konynenburg and Scott (van Konynenburg & Scott, 1980)*, the normalized mixture critical volume, where each component has the same* **b** *value (here* 0.04267 *L/mol, similar to CO_2), plotted against the mixture composition. The* **a** *values from component number one and two are* 3.640 *(similar to CO_2) and* 9.649 *(similar to methanol) L^2bar/mol^2, respectively.*

8.7. Conclusions

The isobaric heat capacity ridge for a supercritical fluid marks a special region in pressure-temperature coordinates where the fluid, either pure or as a mixture, undergoes rapid changes in many thermodynamic and kinetic properties with only small perturbations in temperature and/or pressure (Gallo et al., 2014). Although scarcely reported in the literature, the C_p ridge has been mapped for two mixtures of CO_2, low mole fractions of n-decane in CO_2 and mixtures of methanol in CO_2 over a wide compositional range (up to 20%). From experimental measurements, the relationship between the critical isochore and the C_p ridge was shown to be dissimilar for mixtures, when compared to pure fluid behavior. The van der Waals EOS and methods of van Konynenburg and Scott were used to demonstrate that a mixture's C_p ridge will not always fall on a fluid's critical isochore, as some authors have previously suggested (Apfelbaum & Vorob'ev, 2013; Nishikawa et al., 2003).

8.8. References

Apfelbaum, E. M., & Vorob'ev, V. S. (2013). Regarding the Universality of Some Consequences of the van der Waals Equation in the Supercritical Domain. *The Journal of Physical Chemistry B*, *117*, 7750–7755.

Banuti, D. T. (2015). Crossing the Widom-line - Supercritical pseudo-boiling. *Journal of Supercritical Fluids*, *98*, 12–16. http://doi.org/10.1016/j.supflu.2014.12.019

Bessieres, Guirons, Daridon, & Coxam. (2000). Apparatus for simultaneous determination of the densities and heat capacities of liquids and of liquids with dissolved gas under an extended range of pressure (0.1-100MPa). *Measurement Science Technology*, *11*, N-69-N72.

Brazhkin, V. V., Fomin, Y. D., Lyapin, A. G., Ryzhov, V. N., & Tsiok, E. N. (2011). Widom line for the liquid-gas transition in Lennard-Jones system. *Journal of Physical Chemistry B*, *115*, 14112–14115. http://doi.org/10.1021/jp2039898

Brazhkin, V. V, & Ryzhov, V. N. (2011). Van-der-Waals supercritical fluid: Exact formulas for special lines. *arXiv:1104.2973v1*, (2), 2–5.

Chester, T. L., & Haynes, B. S. (1997). Estimation of pressure-temperature critical loci of CO2 binary mixtures with methyl-tert-butyl ether, ethyl acetate, methyl-ethyl ketone, dioxane and decane. *Journal of Supercritical Fluids*, *11*, 15–20.

De Reuck, K. M., & Craven, R. J. B. (1993). *Methanol, international thermodynamic tables of the fluid state, vol. 12*. Blackwell Scientific Publications.

Ernst, G., Maurer, G., & Wiederuh, E. (1989). Flow calorimeter for the accurate determination of the isobaric heat capacity at high pressures; results for carbon dioxide. *The Journal of Chemical Thermodynamics*, *21*(1), 53–65. http://doi.org/10.1016/0021-9614(89)90007-4

Fomin, Y. D., Ryzhov, V. N., Tsiok, E. N., & Brazhkin, V. V. (2015). Thermodynamic properties of supercritical carbon dioxide: Widom and Frenkel lines. *Physical Review E*, *22111*, 1–5. http://doi.org/10.1103/PhysRevE.91.022111

Gallo, P., Corradini, D., & Rovere, M. (2014). Widom line and dynamical crossovers as routes to understand supercritical water. *Nature Communications*, *5*, 1–6. http://doi.org/10.1038/ncomms6806

Gil, L., Blanco, S. T., Rivas, C., Laga, E., Fernández, J., Artal, M., & Velasco, I. (2012). Experimental determination of the critical loci for {n-C6H14 or CO2 + alkan-1-ol} mixtures. Evaluation of their critical and subcritical behavior using PC-SAFT EoS. *The Journal of Supercritical Fluids*, *71*(0), 26–44. http://doi.org/http://dx.doi.org/10.1016/j.supflu.2012.07.008

Gurdial, G. S., Foster, N. R., Yun, S. L. J., & Tilly, K. D. (1993). Phase Behavior of Supercritical Fluid — Entrainer Systems. In E. Kiran (Ed.), *Supercritical Fluid Engineering Science* (pp. 34–45). Washington, DC: American Chemical Society.

http://doi.org/10.1021/bk-1992-0514.ch003

Kunz, O., & Wagner, W. (2012). The GERG-2008 wide-range equation of state for natural gases and other mixtures: An expansion of GERG-2004. *Journal of Chemical and Engineering Data*, *57*(11), 3032–3091. http://doi.org/10.1021/je300655b

Lemmon, E. W., Huber, M. L., & Mclinden, M. O. (2013). *NIST Standard Reference Database 23: Reference Fluid Thermodynamic and Transport Properties-REFPROP, Version 9.1*. Gaithersburg.

Lemmon, E. W., & Span, R. (2006). Short Fundamental Equations of State for 20 Industrial Fluids. *J. Chem. Eng. Data*, *51*, 785–850.

Nakayama, H. (2000). Raman spectral changes of neat CO2 across the ridge of density fluctuation in supercritical region. *Chemical Physics Letters*, *320*, 323–327.

Nishikawa, K., Kusano, K., Arai, A. A., Morita, T., & Introduction, I. (2003). Density fluctuation of a van der Waals fluid in supercritical state. *Journal Chemical Physics*, *118*(3). http://doi.org/10.1063/1.1526469

Nishikawa, K., & Morita, T. (2000). Inhomogeneity of molecular distribution in supercritical fluids. *Chemical Physics Letters*, *316*, 238–242.

Reamer, H. H., & Sage, B. H. (1962). Phase Equilibria in Hydrocarbon Systems. Volumetric and Phase Behavior of the n-Decane-CO2 System. *Journal of Chemical and Engineering Data*, *8*(4), 508–513.

Rowlinson, J. S., & Swinton, F. L. (1982). *Liquids and Liquid Mixtures* (2nd Editio). Butterworths.

Span, R., Lemmon, E. W., Jacobsen, R. ., Wagner, W., & Yokozeki, A. (2000). A Reference Equation of State for the Thermodynamic Properties of Nitrogen for Temperatures from 63.151 to 1000 K and Pressures to 2200 MPa. *J. Phys. Chem. Ref. Data*, *29*(6), 1361–1433.

Span, R., & Wagner, W. (1996). A new EOS for carbon dioxide covering the fluid region from the triple-point temperature to 1100K at pressures up to 800 MPa. *Journal of Physical and Chemical Reference Data*. http://doi.org/10.1063/1.555991

Stanley, H. E. (1971). *Phase transitions and critical phenomena*. Oxford: Clarendon.

Tegeler, C., Span, R., & Wagner, W. (1999). A New Equation of State for Argon Covering the Fluid Region for Temperatures from the Melting Line to 700 K at Pressures up to 1000 MPa. *J. Phys. Chem. Ref. Data*, *28*(3), 779–850.

van Konynenburg, P., & Scott, R. (1980). Critical lines and phase equilibria. *Philosophical Transactions of the Royal Society of London A: Mathematical, Physical and Engineering Sciences*, *298*(1442), 495–540.

Wagner, W., & Pruss, A. (2002). The IAPWS Formulation 1995 for the Thermodynamic Properties of Ordinary Water Substance for General and Scientific Use. *J. Phys. Chem. Ref. Data*, *31*(2), 387–535.

Xu, L., Kumar, P., Buldyrev, S. V, Chen, S., Poole, P. H., Sciortino, F., & Stanley, H. E. (2005). Relation between the Widom line and the dynamic crossover in systems with a liquid – liquid phase transition. *PNAS*, *102*(46), 16558–16562.

9. C_p MEASUREMENTS OF R1234YF (2,3,3,3-TETRAFLUOROPROPENE)

9.1. Author's note

The work contained in this Chapter was done in collaboration with Maciej Lukawski, and a publication reporting the data and analysis contained within this chapter (with potential additional measurements and refinements) will be submitted to *Journal of Chemical Engineering Data*. The lead author of this publication will be Maciej Lukawski. All measurements and analysis contained within this chapter have been primarily developed by the author of this thesis.

9.2. Motivation for C_p measurements of R1234yf

One of the most common fluid refrigerants, found in applications from automotive air conditioning systems to organic Rankine cycles (ORCs) for low temperature heat-to-power conversion, R134a (1,1,1,2-Tetrafluoroethane) is being phased out of usage because of its high global warming potential (GWP). Its planned replacement is R1234yf (2,3,3,3-Tetrafluoropropene) which has a GWP of 4, markedly lower than the GWP of 1430 for R134a (Richter, McLinden, & Lemmon, 2011). To become a drop-in replacement for R134a, R1234yf has been engineered with special attention to its thermophysical properties and closely replicates the *PVT* and $H = f(T,P)$ behavior of R134a (Richter et al., 2011). Accurate C_p values are necessary for any working fluid, but especially for a recently designed refrigerant, to be successfully deployed in different types of thermodynamic cycles. The results presented in this Chapter add to available experimental data (Gao, Jiang, Wu, He, & Chen, 2014; Liu, Zhao, Lv, & He, 2017) by expanding the C_p data available for R1234yf to higher temperatures (120-140 °C over pressures from 35-100 bar).

9.3. Flow calorimetric experimental method for R1234yf C_p measurements

The similarity of thermophysical properties between R1234yf and R134a (Richter et al., 2011), the immediate application of R1234yf as a drop-in replacement for R134a, and the accurate characterization of R134a's properties (Ernst, Gurtner, & Wirbser, 1997; Tillner-Roth & Baehr, 1994), together provide a unique opportunity for calorimeter calibration to measure R1234yf. First, the similar properties shared by these refrigerants help reduce calibration inaccuracies dependent on the thermophysical behavior of the fluid (e.g. a calibration fluid with a much larger Joule-Thomson coefficient than the fluid being studied). Second, calibration with R134a embeds the systematic errors present within this fluid reference standard into subsequent measurements. Preservation of the systematic errors present in the thermophysical description of R134a (e.g. in an EOS) in any new attempt to model R1234yf is preferable to introducing new (unrelated to R134a) systematic errors. Put simply, if you were systematically incorrect with R134a, you'll be similarly incorrect with R1234yf. Ultimately, by calibrating with R134a, systematic errors for the drop-in replacement (R1234yf) will be accounted for in a rational manner.

For these reasons, the flow calorimeter was calibrated with R134a before making C_p measurements on R1234yf. A correction value was determined from every measurement of R134a where values in Equation 9-1 (the uncertainty associated with assignment of C_p to a particular temperature and pressure) were larger than the difference between experiment and the state-of-the-art EOS.

$$\sigma_T \left(\frac{\partial C_p}{\partial T}\right)_P \; and \; \sigma_P \left(\frac{\partial C_p}{\partial P}\right)_T \qquad (9\text{-}1)$$

$$\frac{\left(C_p^{exp} - C_p^{EOS}\right) - \left|\sigma_T \left(\frac{\partial C_p}{\partial T}\right)_{P,X} + \sigma_P \left(\frac{\partial C_p}{\partial P}\right)_{T,X}\right|}{C_p^{EOS}} * 100\% \qquad (9\text{-}2)$$

The uncertainty in the absolute temperature and pressure measurements are represented by estimated standard deviations σ_T and σ_P, respectively. Refer to Table 6-1 for estimates of these uncertainties (σ_T ~0.1 °C and σ_P ~0.2 bar for low pressure). Each correction value was calculated according to Equation 9-2 and then applied to the measurement of R1234yf at the corresponding temperature and pressure, with correction made on a percentage basis. Including the *PT* uncertainty (Equation 9-1) as an adjustment in Equation 9-2 helps limit unwarranted overcorrection to measurements where uncertainty is high (near critical region).

9.4. R134a C_p measurements and development of the correction function

Heat capacity measurements of R134a were completed following the same procedure described in Chapter 6. (Author's note: the calorimeter was moved to a different building after taking all of the measurements documented in Chapters 6-8. The same degree of accuracy and precision were never quite achieved at the calorimeter's new location. For some unknown reason, deviations were larger and less uniform for these measurements than in all preceding measurements, around 2-3% greater.) The correction procedure described in Section 9.3 increased, we believe, the absolute accuracy of these results. Table 9-1 lists the *Cp* measurement values and the derived correction factors. If the correction factor is zero, then errors from uncertainty in temperature and pressure associated with the measurement were larger than the potential correction factor.

Table 9-1: Experimental C_p *values for pure R134a compared to the state-of-the-art EOS* (Tillner-Roth & Baehr, 1994) *and the derived correction factors.* P-T *and random experimental uncertainties were calculated as the summation of both terms of Equation 9-1 and the random uncertainty of each experimental measurement.*

Pure R134a					
Temperature	**Pressure**	**Experimental C_p**	**Richter EOS C_p**	**P-T and Random Experimental Uncertainty**	**Correction Factor**
[°C]	**[bar]**	**[J/gK]**	**[J/gK]**	**[%]**	**[%]**
99.8	33.7	1.94	1.942	1.2	0.0
99.8	40.5	6.42	5.545	10.3	0.0
100.0	44.9	2.96	2.928	1.9	0.0
100.1	49.8	2.35	2.408	0.9	-1.4
100.0	60.6	1.93	2.003	0.4	-3.5
100.1	79.8	1.70	1.761	0.2	-3.5
119.9	39.9	1.62	1.683	0.6	-3.2
120.1	49.5	2.71	2.822	2.0	-2.3
120.1	55.5	4.12	4.243	0.9	-2.0
120.0	60.1	3.71	3.635	1.0	-1.0
120.1	79.2	2.02	2.119	0.4	-4.6
120.3	98.9	1.73	1.824	0.2	-5.3
140.2	40.1	1.41	1.407	0.2	-0.1
140.0	50.8	1.67	1.700	0.5	-1.1
139.9	60.2	2.07	2.138	0.7	-2.5
139.9	70.3	2.41	2.552	0.4	-5.7
139.9	79.8	2.32	2.439	0.2	-4.9
139.9	98.6	1.94	2.020	0.2	-3.6

9.5. Adjusted R1234yf C_p measurements with comparisons to EOS and other published experimental measurements

Point-by-point adjustments were made to each experimental R1234yf C_p measurement using the correction factor determined from R134a at the associated absolute temperature and pressure, as reported in Table 9-1. The unadjusted and adjusted C_p measurements for R1234yf, the experimental uncertainty, and a comparison to predictions from the EOS developed by Richter et al. are included in Table 9-2. Experimental uncertainties (which include the pressure-temperature assignment uncertainty (Equation 9-1), random uncertainty, and the estimated

uncertainty of the R134a EOS used to develop the correction factors) are generally ±2% of C_p, excluding near the critical point where uncertainties are much larger. Figure 9-1 plots the corrected C_p values for R1234yf versus pressure for the three measured isotherms (100, 120, and 140 °C). Also included are predictions using the Richter et al. EOS and the experimental measurements of Liu et al. for comparison (Liu et al., 2017; Richter et al., 2011).

Table 9-2: Experimental C_p *values for pure R1234yf, adjusted by the correction factors determined from the R134a calibration (*C_p^**), and compared to the state-of-the-art EOS estimations for heat capacity (*$C_{p,lit}$*)* (Richter et al., 2011)*. The experimental uncertainty includes the P-T (from Equation 9-1) uncertainty, random uncertainty, and the systematic uncertainty associated with the R134a EOS used to develop the correction factors* (Tillner-Roth & Baehr, 1994).

Pure R1234yf					
Temperature	**Pressure**	**Experimental C_p**	**Corrected Exp. C_p**	**Experimental Uncertainty**	**Comparison $100*(C_{p,lit}-C_p^*)/C_p^*$**
[°C]	**[bar]**	**[J/gK]**	**[J/gK]**	**[%]**	**[%]**
100.1	35.0	3.46	3.46	4.7	0.0
100.3	41.4	3.47	3.47	7.2	-5.5
100.2	45.4	2.42	2.42	2.9	1.4
100.1	49.8	2.06	2.09	2.2	1.2
100.1	59.9	1.79	1.86	1.8	-1.5
100.1	80.2	1.59	1.65	1.7	-1.4
120.0	40.4	1.87	1.93	2.2	1.0
120.1	49.4	2.89	2.96	3.0	2.3
120.0	54.2	2.77	2.83	2.3	1.9
120.2	59.9	2.32	2.34	2.7	3.4
120.0	80.0	1.74	1.83	1.8	-0.9
120.1	100.5	1.60	1.69	1.7	-3.3
139.8	40.1	1.46	1.46	1.8	2.7
139.8	50.2	1.74	1.76	2.0	3.8
139.9	60.4	2.03	2.08	2.1	3.8
139.8	69.6	2.03	2.14	1.7	0.1
140.0	80.4	1.87	1.96	1.8	0.2
139.5	100.3	1.68	1.74	1.7	-0.1

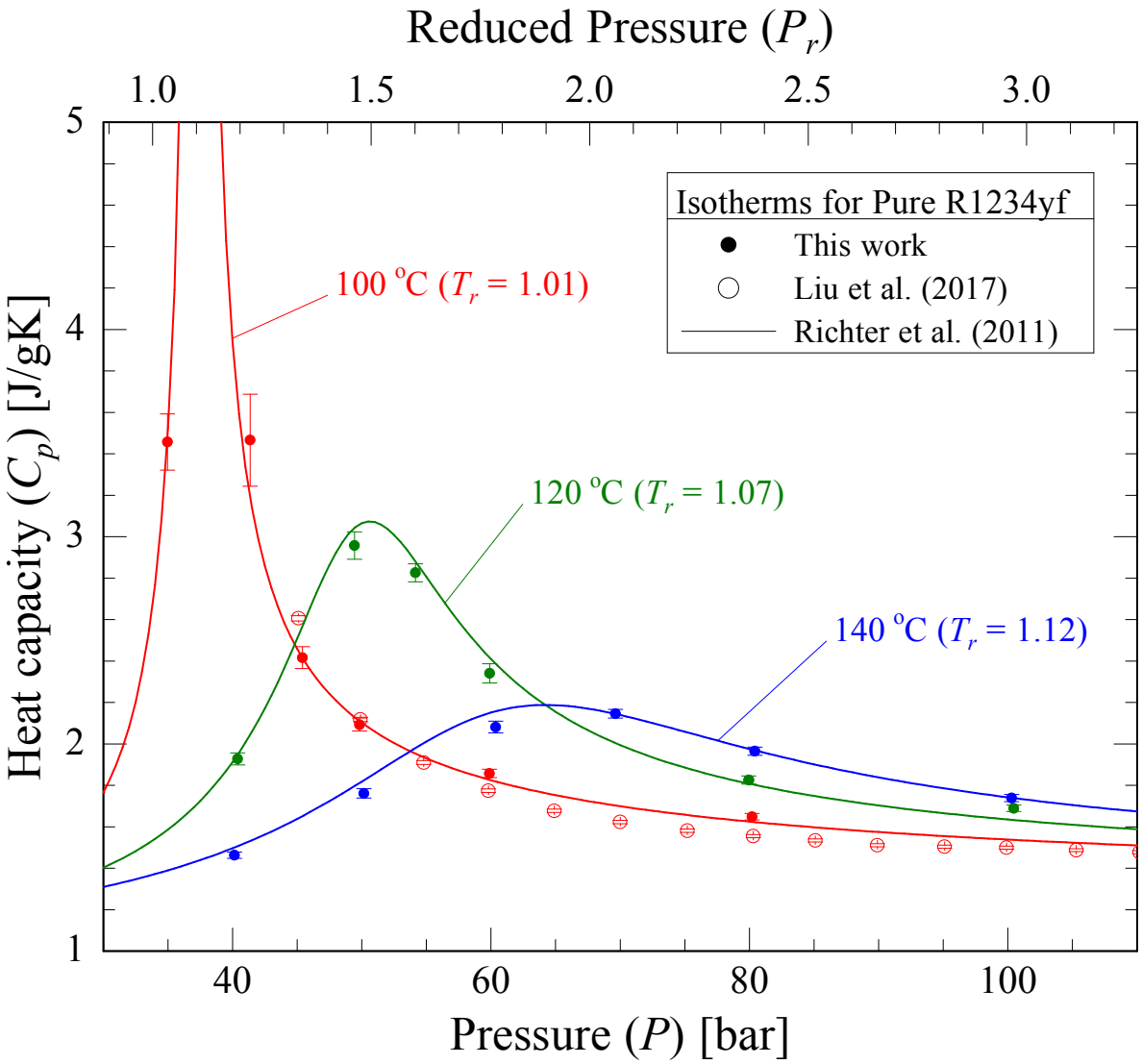

Figure 9-1: Corrected C_p *measurements of R1234yf, reported in Table 9-1 (filled circles) compared to both experimental measurement published by Liu et al. (open circles)* (Liu et al., 2017) *and the EOS developed by Richter et al.(solid lines)* (Richter et al., 2011)*. The estimated general uncertainty for* C_p *by this EOS is approximately ±5%, with a suggested upper temperature limit of 135 °C.*

In general, Richter et al.'s EOS represents C_p very well, with all data falling within the ±5% uncertainty of the equation (one point in the near critical region has an uncertainty estimate >5%). Two regions suggest some adjustment to the EOS might be useful. The 100 bar measurement on the 120 °C isotherm is nearly beyond the 95% confidence interval (two standard deviations) when comparing the uncertainty of the measurement to the difference between the measurement and the EOS. The situation is similar for the low pressure measurements on the 140

°C isotherm; the deviation of the EOS from experiment is on the edge of the 95% confidence limit. The C_p measurements reported by Liu et al. fall slightly below our measurements at 60 and 80 bar on the 100 °C isotherm (Liu et al., 2017). Expanding their estimate for experimental uncertainty from 0.5% to 1.0% brings both sets of data into agreement; given challenges in measuring accurate C_p data, their 0.5% uncertainty seems overly confident.

9.6. Conclusions

This study expands the heat capacity data into the supercritical region for R1234yf, a superior working fluid compared to R134a in terms of the refrigerant's GWP, with comparable thermophysical behavior. A high precision flow calorimeter was calibrated using R134a as a reference standard. For most of the temperatures (100-140 °C) and pressures studied (35-100 bar), except in the near critical region where C_p varies most significantly, the measurement accuracy was ±2%. The measurements reported here expand the available C_p data for R1234yf to significantly higher temperatures (up to 140 °C), providing a basis for possible adjustments to the paramaters of the Richter et al. EOS, the current state-of-the-art EOS for modeling R1234yf. These adjustments may help improve its accuracy in the supercritical region.

9.7. References

Ernst, G., Gurtner, J., & Wirbser, H. (1997). Massic heat capacities and Joule–Thomson coefficients of CH2FCF3 (R134a) at pressures up to 30 MPa and temperatures between about 253 K and 523 K. *J. Chem. Thermodynamics*, *3*, 1113–1124.

Gao, N., Jiang, Y., Wu, J., He, Y., & Chen, G. (2014). Measurements of the isobaric heat capacity of R1234yf in liquid phase at temperatures from 305 K to 355 K and pressures up to 5 MPa. *Fluid Phase Equilibria*, *376*, 64–68. http://doi.org/10.1016/j.fluid.2014.05.029

Liu, Y., Zhao, X., Lv, S., & He, H. (2017). Isobaric Heat Capacity Measurements for R1234yf from 303 to 373 K and Pressures up to 12 MPa. *J. Chem. Eng. Data*, (2). http://doi.org/10.1021/acs.jced.6b00959

Richter, M., McLinden, M. O., & Lemmon, E. W. (2011). Thermodynamic Properties of 2, 3, 3, 3-Tetrafluoroprop-1-ene (R1234yf): Vapor Pressure and p–ρ–T Measurements and an Equation of State. *Journal of Chemical & Engineering Data*, *56*(7), 3254–3264.

Tillner-Roth, R., & Baehr, H. D. (1994). An international standard formulation for the thermodynamic properties of 1, 1, 1, 2-Tetrafluoroethane (HFC-134a) for temperatures from 170 K to 455 K and pressures up to 70 MPa. *Journal of Physical and Chemical Reference Data*, *23*(5), 657–729.

10. CONCLUSIONS AND RECOMMENDATIONS FOR FUTURE RESEARCH

10.1. Thesis conclusions

The thermodynamic laws governing a fluid's thermophysical properties are relatively straight forward, yet they are able to capture quite magnificent and complex behavior. The supercritical region is particularly interesting (large property variations with small changes in temperature and pressure) and commercially applicable (chemical extractions, material synthesis, etc.) and was the focus of this study. To leverage the unique potential process enhancements made possible with supercritical fluids, engineers require reliable data and accurate models. This work enhances our understanding of supercritical pure fluids and mixtures by providing new and accurate property data, critical analysis of current empirical equation of state (EOS) and molecular simulation models, and a theoretical description of a generic binary mixture's thermophysical behavior in the critical region.

Of central concern to this thesis is a supercritical fluid's isobaric heat capacity (C_p). As C_p can vary by more than 100% over a few degrees Celsius, this property is particularly difficult to accurately model without good data. The methods used to estimate C_p in the supercritical region were reviewed in Chapter 3 and 4 in order to set forth the mathematical framework for the thermodynamic property modeling and the experimental method used in this research. Chapter 5 summarized the most prominent experimental approaches to measure C_p for high temperature, high pressure fluids. Available C_p data for mixtures was covered with a short list of published measurements, underscoring the limited data set for mixtures in general.

A flow calorimeter was designed, constructed and tested in this study, and was shown to be capable of ±1% accuracy (±2% for refrigerants, see Chapter 9) over the temperature range 25-150 °C and pressure range 1-300 bar. The goal of Chapter 6, however, was not only to build and verify the accuracy of the calorimeter, but also to fully document the components, operation, and shortcomings. In addition to Chapter 6, Appendices A, B, and C document the calorimeter's sub-components' make and model, the basic operations (start-up, measurement, and shut-down), and operational challenges. In this way, the experimental measurements made here can be repeated and improved upon.

In Chapters 6, 7, 8, and 9, new C_p data were made available for CO_2 (150 °C isotherm), R1234yf (120 and 140 °C isotherm), CO_2-methanol (5, 10, 15, 20, and 30 mol %), and CO_2-decane (1 and 2 mol%). Experimental C_p measurements for CO_2-methanol were compared to results from Monte Carlo molecular simulation (MCMS) and the GERG-2008 EOS, an EOS originally developed for natural gas mixtures but extended in scope by researchers at the National Institute of Standards and Technology. The performance of both empirical models was comparable (average absolute errors were ~3% and ~4% for the EOS and the MCMS, respectively). Methanol rich mixtures were most challenging for the EOS to accurately estimate because these mixtures have more sparse experimental data, making refinement to EOS fit sometimes impossible. The MCMS performed poorly in the pressure-temperature region where C_p was near its maximum for a given mixture. For R1234yf, experimental C_p measurements were compared to the Richter et al. EOS, which was developed specifically for R1234yf. Along the 120 °C isotherm, the EOS begins to slightly under predict C_p at high pressures, whereas along the 140 °C (which is outside the recommended usage range for the EOS), the EOS over predicts

C_p. These new measurements and analysis should help improve accuracy and expand the range of current modeling efforts.

Lastly, Chapter 8 presented the relationship between a supercritical fluid's C_p ridge (also known as a "locus of maxima") and the pressure-temperature path made by the critical isochore. Synthesized from all mixture data presented within the thesis, the location of maximum C_p values along isotherms was plotted onto pressure-temperature coordinates, along with each mixture's critical point (experimentally determined by other researchers). The deviation of the C_p ridge from the critical isochore was shown for binary mixtures for the first time and demonstrated theoretically with the van der Waals EOS (assuming van der Waals mixing rules) and the definition of a critical point for a binary mixture.

The following is a list of existing and planned publications resulting from this research:

- Ishmael, Mitchell P. E., Maciej Z. Lukawski, and Jefferson W. Tester. "Isobaric heat capacity (C_P) measurements of supercritical fluids using flow calorimetry: equipment design and experimental validation with carbon dioxide, methanol, and carbon dioxide-methanol mixtures." *The Journal of Supercritical Fluids* 117 (2016): 72-79.
- Ishmael, Mitchell P. E., Lauren B. Stutzman, Maciej Z. Lukawski, Fernando A. Escobedo, and Jefferson W. Tester. "Heat capacities of supercritical fluid mixtures: Comparing experimental measurements with Monte Carlo molecular simulations for carbon dioxide-methanol mixtures." *The Journal of Supercritical Fluids* 123 (2017): 40-49.
- (*Planned*) Ishmael, Mitchell P. E. and Jefferson W. Tester. "Mapping the ridge in isobaric heat capacity for carbon dioxide-decane and carbon dioxide-methanol binary mixtures."
- (*Planned*) Lukawski, Maciej Z., Mitchell P. E. Ishmael, and Jefferson W. Tester. "C_p measurements of R1234yf (2,3,3,3-Tetrafluoropropene)

10.2. Recommendations for future research

One of the distinguishing features of research has prevailed again: the insight and further understanding of the thermophysical behavior of supercritical fluids uncovered in this work has uncovered new questions and motivated additional study in certain areas. The research topics

covered in this thesis range from the experimental challenges associated with building hardware to the subtleties of the critical behavior of binary fluid mixtures. Each topic in turn warrants more consideration and study.

In general, aside from the cost of the associated equipment, the biggest challenge limiting the amount of heat capacity data for supercritical pure fluids and mixtures is the time required for the system to achieve steady state and record a measurement. Our calorimeter, as with almost all of the systems listed in Table 5-1 and 5-2, requires hours to warm up, ~10 minutes per measurement (or more for many systems), and several hours to switch to another isotherm. The calorimetric system is slow to switch between operating temperatures primarily because a large thermal mass is required to dampen out any thermal fluctuations (both temporal and spatial) during the course of a C_p measurement. With the advent of new manufacturing techniques, such as 3D printing and microfluidic devices, there is an opportunity to make high pressure calorimeters smaller than they have been made in the past, allowing for small-scale feature control within the calorimeter design, at reasonable expense. Shrinking the calorimetric cell may enable faster measurements with little to no compromise in accuracy.

The new C_p data reported in this thesis can be used to help refine molecular simulation models as well as empirical, multiparameter and cubic EOS models, especially to increase their accuracy in the supercritical region where key challenges remain. From the wide range of temperatures, pressures, and CO_2-methanol compositions studied, the potential/force fields used for molecular simulations could be improved (e.g. improvements to Lorentz-Berthelot mixing rules for unlike atoms). Instead of fitting force fields and other intermolecular models to vapor-liquid equilibrium data and extrapolating this description to the near- and supercritical regions, the models could be fit to data within the region of interest. Equations of state could also benefit

from additional property data, especially for mixtures. Throughout this thesis, the evaluated EOSs showed the worst performance for binary mixtures with concentrations approaches equilmolar, indicating the potential to improve the mixing rules.

The isobaric heat capacity ridge, defined as the locus of maxima on the C_p surface plotted as a function of temperature and pressure for a given fluid composition, was shown to deviate from pure fluid behavior by not following the isochore corresponding to the fluid's critical molar volume. However, the path of the ridge still appears to follow an isochoric path (the van der Waals EOS corroborates this assertion). This begs the question: what is the significance of the isochore corresponding to the ridge's path? Speculating on the C_p ridge's direction for binary mixtures, there could be a materially unstable state at which the system satisfies the critical point criteria given in Equation 3-20 (A_{VV} and A_{VVV} both equal zero). The ridge direction corresponds to the molar volume (defining the isochore) at this wholly unstable point in phase space. Theoretical work with the van der Waals EOS and/or molecular simulation could provide insight and prove or disprove this conjecture. Given further work to determine the pressure-temperature location of the C_p ridge, simple heuristics for mixing rules may possibly be developed. The direction of the ridge for both CO_2-methanol and -decane mixtures could be reasonably determined from simple molar averages of the pure fluid's critical molar volumes. Whether this behavior is generally true will require additional mixture C_p measurements with high resolution to identify C_p maxima.

Finally, new types of working fluids, for example low GWP refrigerants for air conditioning and/or ORC heat-to-power conversion, will always require experimental measurements and characterization in order to be effectively utilized. Mixtures, simply through their extra degrees of dimensionality, will likely always be less accurately described when

compared to pure fluids. Experimentalists must choose their model mixtures for study extremely wisely in order to maximize their impact, hopefully providing some degree of generalization for whole classes of molecularly similar fluids. Advances in nanoscience provide opportunities for heat capacity measurements of fundamentally new mixtures (e.g. nanoparticles + solvent, branched polymers + solvent, etc.). Exploring the critical behavior of these complex mixtures is an exciting, challenging next step for researchers in the field of supercritical fluid calorimetry.

APPENDICES

Appendix A. List of calorimeter components and suppliers and picture of the physical system

Table A-1: Sub-components used in the flow calorimeter

Component name	Supplier and model
Dual syringe pump (CO_2)	Teledyne ISCO 100DX, controller, and temperature control jackets cooled using refrigeration system
HPLC pump (methanol)	Agilent 218 solvent delivery pump
Coriolis mass flow meter	GE Rheonik RHM 015
Alumina bath	Techne SBL-2D with TC-9D controller
Thermocouples	E-type, 1/16", Omega
Pressure Transducer	Omega, PX409 (Range 0-5000 psi)
Vacuum pump	Oerlikon Leybold
Power supply	Tektronix PWS4305
Scale (methanol)	Mettler Toledo
Back pressure regulator	Equilibar EB1
Heating element	34 AWG bar Ni/Cr wire wound around 0.4 mm hollow alumina tube
Wires powering heating element	18 AWG copper wires, 0.007" insulation
Flow tubing	Inconel, 1/4" tubing with 0.049" wall thickness
Refrigeration system	VWR Scientific Products Recirculating Chiller 1179-P

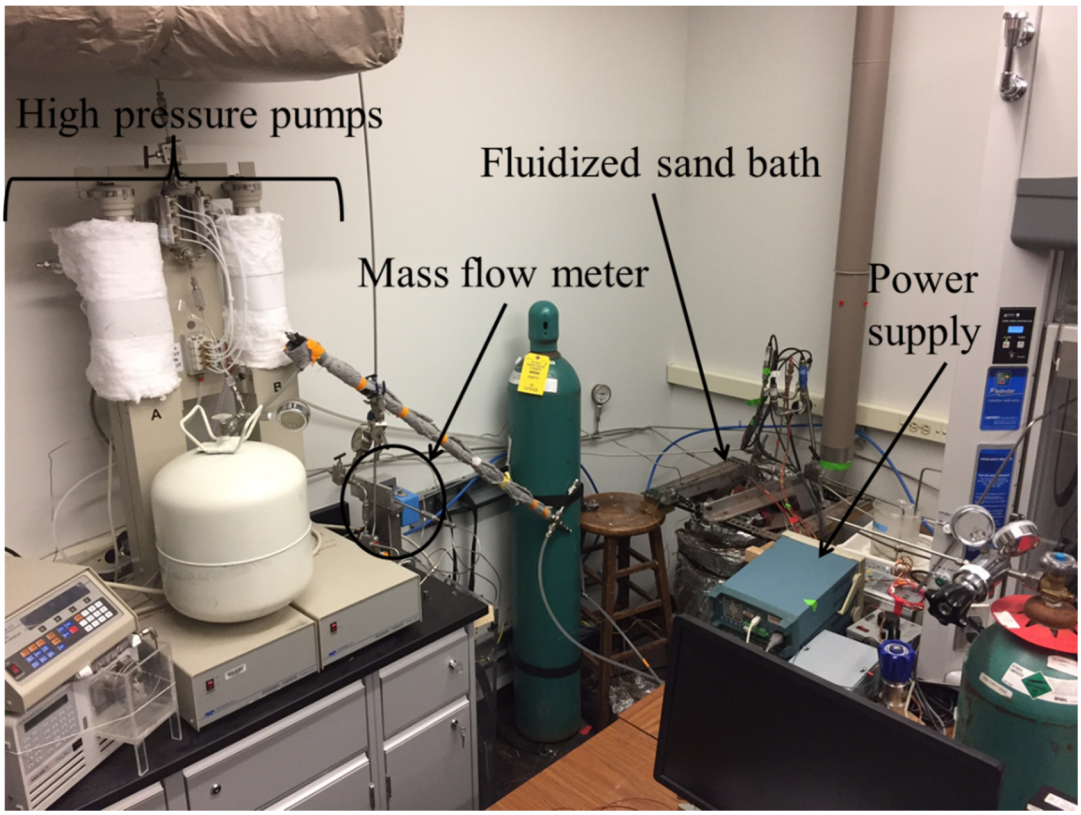

Figure A-1: Physical calorimeter system corresponding to the process flow diagram in Figure 6-1.

Appendix B. Operating procedures not included in Chapter 6

Startup. The sand bath takes approximately three hours (less for lower temperatures more for higher temperatures) to reach steady state, defined by a roughly constant measured temperature at the calorimeter inlet (±0.1 °C) over a >10 minute timeframe (the approximate duration of a heat capacity measurement). After the sand bath's warm up, the Isco syringe pump and its associated recirculating chiller, the vacuum pump, the power supply, the mass flow meter, and all data acquisition (DAQ) systems are turned on. Each of these systems requires about 30 minutes to start-up. For example, the DAQ system measuring the thermocouple temperatures needs time for the cold junction compensation to reach a steady value. Similarly, the recirculating chiller requires time to cool its reservoir from room temperature to the 6 °C set point to cool the Isco syringes. A half hour provides enough time for these systems to function without any transient, start-up error.

Following the described equilibration period, the pumps are exposed to atmospheric pressure, zeroed (refer to the pump manual), and refilled with the fluid under study. The fluid is then pumped at a constant volumetric flowrate into the calorimeter against a closed valve (located after the thermal equilibration tubing, Figure 6-2, L) until the system reaches the desired pressure. The closed valve is opened, and the back pressure regulator (Figure 6-2, O) is used to manage the system pressure throughout the remainder of the calorimeter's operation. Heat tape, wrapped around the back pressure regulators, is now powered to ensure the flow tubing is not clogged by deposition of solidified material (the fluid is greatly cooled during the expansion process). When the system has operated at steady pressure under a constant flow rate for at least ten minutes, the Coriolis mass flow meter is rezeroed (refer to the mass flow meter manual) by allowing flow to bypass the meter, completely isolating the meter from flow while maintaining

consistent flow conditions within the calorimeter assembly. During operation, the mass flow meter is rezeroed every ~5 measurements to ensure it is making a properly calibrated measurement.

For a mixture measurement, a second component is added via the HPLC pump (Figure 6-1, E). The HPLC pump should have been pumping for >10 minutes before recording a measurement, in order to adequately warm up the pump. The measurement begins by taking the mass of the reservoir and starting the stop watch, and it ends with recording the mass of the reservoir and stopping the timer (~10 minutes).

Shutdown. To reduce pressure cycling and limit waste, the calorimeter system, from the mass flow meter to the back pressure regulator, is kept pressurized, even when the system is fully shut down. Once the pumps are stopped, the valve to the mass flow meter and the valve to the calorimeter exhaust are closed. The sand bath is then unplugged, and the fluidization to the bath is stopped. The Isco pump syringes are depressurized through a length of tubing that bypasses the calorimeter and vents into the fume hood – now the recirculating chiller and the heat tape (wrapped around the back pressure regulators) may be safely turned off. Next, the vacuum pump and power supply are powered down. Finally, after ensuring all of the data is saved and backed up, the computer is shut down. All the electrical plugs (barring the recirculating chiller, sand bath, and vacuum pump) for the calorimeter are plugged into power strips, which are now switched off as one last safe guard.

Appendix C. Troubleshooting and operational challenges

A significant portion of the total time completing this work was spent overcoming operational challenges with supercritical flow calorimetry and addressing equipment limitations to making accurate measurements. This appendix is meant to provide a succinct summary of the major roadblocks and eventual outcomes that were encountered over the arc of this doctoral work.

Incorrect sizing of the Teledyne Isco high pressure syringe pumps. Reducing the influence of heat loss and environmental temperature fluctuations, a flow calorimeter operates most optimally when the mass flow rate of the fluid it very large. If the flow rate is large, then the quantity of heat required to increase the fluid's temperature is large relative to any environmental thermal effects (or heat loss). Of course from an operational and cost standpoint, a system cannot be arbitrarily large but, in general, larger flows are typically a calorimetric boon. It is unfortunate, then, that this flow calorimeter's pump was undersized. Purchased and used by another researcher, it was unable to be returned or repurchased (costing ~$30k). The 100 mL syringes could maintain flows up to 20 mL/min (larger flows did not allow the tandem pumps to refill and repressurize in time) at pressures up to 300 bar with CO_2. However, the flow rate was further restricted by several subtleties with the syringe pumps when operating the at flows $\leq$ 20 mL/min. In order to understand the challenge, the basic operation of the pumps must be described.

To continuously deliver high pressure fluid, the dual syringe pump operates as follows: one syringe, already at high pressure, delivers fluid to the system, while the other syringe refills from a low pressure gas cylinder. This low pressure cylinder, once full, must now match the pressure of the other dispensing cylinder. The volume of the refilled cylinder is decreased until

the pressure matches, making it ready and available to dispense fluid to the system. When the first cylinder depletes, the second cylinder begins to pump, and the syringes switch roles.

Switching periodically between syringes disrupts any steady state operation. This semi-continuous interruption to thermal equilibrium enforces an entire heat capacity measurement to be completed within the span of a single cycle – the transient behavior must diminish before the pump switches again. Pressure mismatch between the syringes on switchover causes a disturbance that decays within seconds. The most important transient behavior is the variable mass flow rate with time. Each syringe is continuously cooled by a recirculating chiller, maintaining the jacket of the syringe around 6 °C. When a syringe refills and re-pressurizes, the temperature of the medium becomes significantly warmer than 6 °C. While one syringe dispenses to the system, the other is being cooled, but it is never cooled quickly enough. At the start of the full syringe's operation, its temperature is greater than that of the chiller, therefore, as time goes on, the mass flow rate of the fluid (at a constant volumetric flow rate) out of the syringe increases with time. About 3 minutes are required for the fluid to reach a steady mass flow rate. A Coriolis mass flow meter was purchased to monitor the fluid flow rate with time, mitigating this issue.

Space restrictions within the fluidized sand bath relative to the vacuum chamber. Ideally, for this type of flow calorimeter, the calorimeter is small in comparison to the surrounding thermal bath, limiting the calorimeter's influence on its own thermal environment. The dimensions of the fluidized sand bath's working volume are as follows: depth of 35.6 cm and a diameter of 21.6 cm. Suspended within the sand bath, the vacuum chambers dimensions are as follows: length of 21 cm and flange OD of 11.4 cm. Including the length of the preheat tubing, tees, tubing ports, etc. housed on the bottom of the vacuum chamber flange in Figure 6-2, the

total length of the calorimeter assembly comes to ~34 cm, approximately the depth of the sand bath. To accommodate the inadequate depth of the bath, a cylindrical extension was added to the top of the bath. This reduced vertical thermal gradients along the calorimeter assembly but caused sand to regularly spill from the bath.

From above, the area between the vacuum chamber flange and sand bath wall made an annulus, 5 cm thick in the radial direction. This rather narrow spacing caused thermal inhomogeneities across the bath, sometimes reaching a few degrees Celsius across the width of the calorimeter assembly. The head of the calorimeter (bottom of Figure 6-2) was directed toward the bottom of the bath, the most well-mixed section of the bath. Locating all of the fluid ports at the bottom of the bath greatly decreased accessibility to the calorimeter (for calibrations, adjustments, etc.), limited the selection of measurement devices, and complicated the placement of the heating element. However, this was necessary to ensure the calorimeter inlet and outlet ports saw the most stable thermal environment.

Pros and cons of a direct-contact heating element and thermocouples. At the heart of the calorimeter, buried within the sandbath, housed within the vacuum chamber, nestled inside the measurement U-tube, sits the heating element that delivers power to the fluid and the thermocouples that measure the resultant temperature rise. A hand-wound Ni-Cr wire insulated with a ceramic casing directly contacts and heats the fluid, which then passes the thermocouple directly placed in its flow path. Intimate contact between both the heat and thermocouple with the fluid was vital to reducing heat loss and hastening the response time of the calorimeter, ensuring a full heating cycle could be completed during one syringe's lot.

However, placement of the heating element and the thermocouples in the flow path came at a cost. For the heating element, two consequences of the physical arrangement caused

nontrivial problems. First, the fine gauge Ni-Cr wire was very sensitive to high velocity fluid moving through the U-tube, not uncommonly electrically shorting itself when low density measurements at high mass flow rates were made (or fluid was accidentally released rapidly from the system). Great care was taken to limit the velocity of the fluid through the U-tube (<< 1 m/s). Secondly, due to space limitations within the inner diameter of the U-tube, only two copper leads contacted the resistive heater (~35 Ω) – a power measurement, therefore, includes the power dissipated along the copper wire (~0.1 Ω) connecting the power supply to the heater. Correction factors accounting for this additional resistance were applied to all measurements, but a direct, four-wire measurement would have been more accurate, providing real-time information on the thermal energy being dissipated by the heating element.

Generally, thermocouples show less stability, greater hysteresis, and increased susceptibility to electrical noise, when compared to resistance thermometric devices (RTDs), but thermocouples were necessary in order to place the head of the calorimeter assembly (bottom of Figure 6-2) at the bottom of the sand bath. Much more rugged than RTDs, the thermocouples were bent around the sharp corners of fittings to reach their final position.

Appendix D. Information regarding multiparameter EOS implementation

Table D-1: Information regarding multiparameter EOS implementation

Fluid	Equation of State	Reference	Mixing Rule	Parameter Values
CO_2	Span and Wagner	(Lemmon, Huber, & Mclinden, 2013; Span & Wagner, 1996)	N/A	See reference
Methanol	de Reuck and Craven	(De Reuck & Craven, 1993; Lemmon et al., 2013)	N/A	See reference
R134a	Tillner-Roth and Baehr	(Lemmon et al., 2013; Tillner-Roth & Baehr, 1994)	N/A	See reference
R1234yf	Richter, McLinden and Lemmon	(Lemmon et al., 2013; Richter, McLinden, & Lemmon, 2011)	N/A	See reference
CO_2-methanol	GERG-2008	(Kunz, Klimeck, Wagner, & Jaeschke, 2007; Kunz & Wagner, 2012; Lemmon et al., 2013)	KW0 Kunz and Wagner model for hydrocarbon mixtures	$\beta_T = 0.996$ $\beta_V = 1.026$ $\gamma_T = 1.015$ $\gamma_V = 1.236$ $F_{ij} = 1.77$
CO_2-decane	GERG-2008	(Kunz et al., 2007; Kunz & Wagner, 2012; Lemmon et al., 2013)	KW0 Kunz and Wagner model for hydrocarbon mixtures	$\beta_T = 1.02$ $\beta_V = 1.0002$ $\gamma_T = 1.1455$ $\gamma_V = 1.1834$ $F_{ij} = 0.0$

Appendix E. Critical point measurements by various researchers for carbon dioxide-methanol mixtures

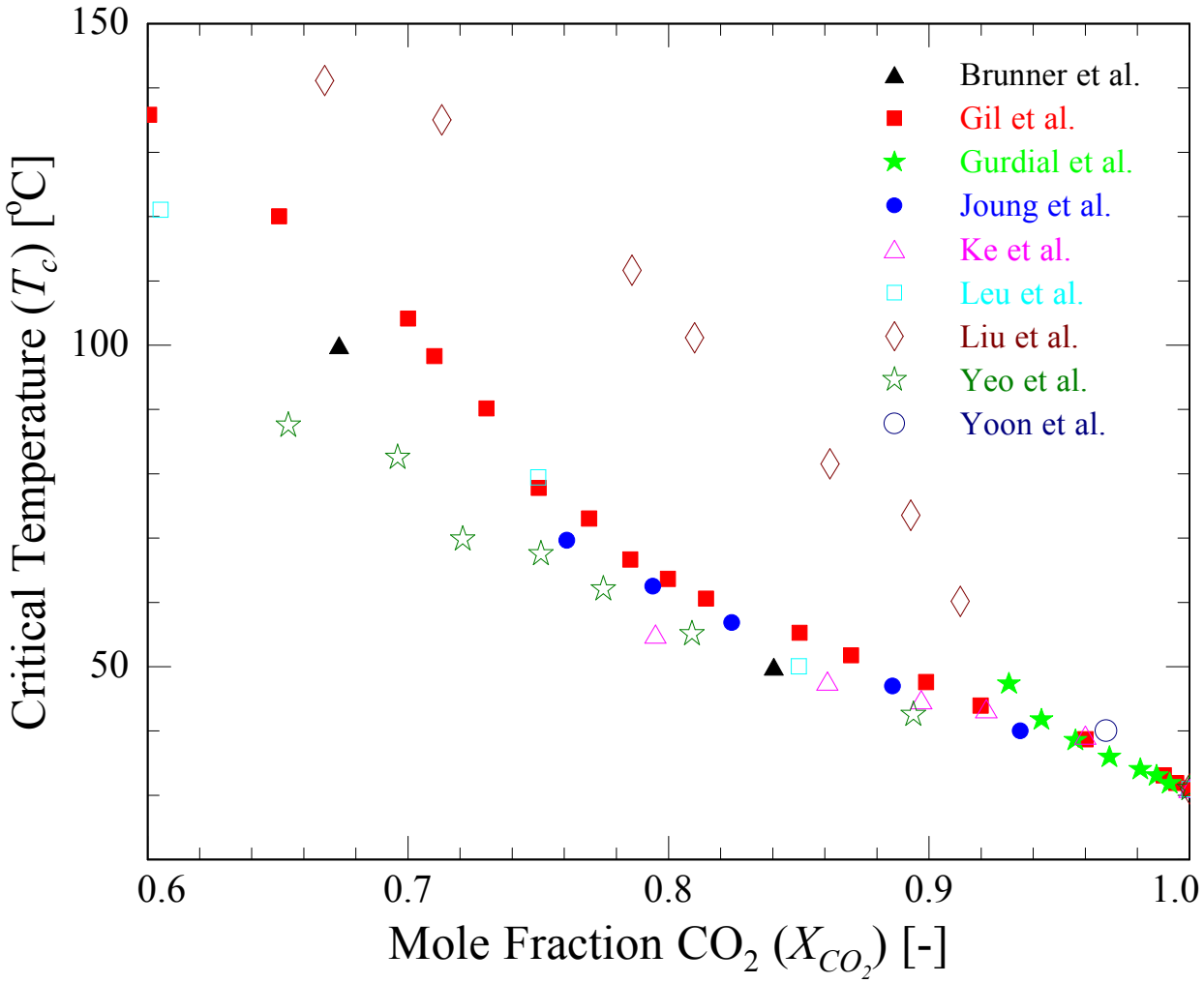

Figure E-1: Experimentally measured critical temperatures of CO_2-methanol binary mixtures (Brunner, Hultenschmidt, & Schlichtharle, 1987; Gil et al., 2012; Gurdial, Foster, Yun, & Tilly, 1993; Joung et al., 2001; Ke, King, George, & Poliakoff, 2005; Leu, Chung, & Robinson, 1991; Liu, Qin, Wang, Hou, & Wang, 2003; Yeo, Park, Kim, & Kim, 2000; Yoon, Lee, & Lee, 1993). *The data of Gil et al. were used in this study because they represent a compromise between the many datasets and have the highest mole fraction resolution in their dataset* (Gil et al., 2012).

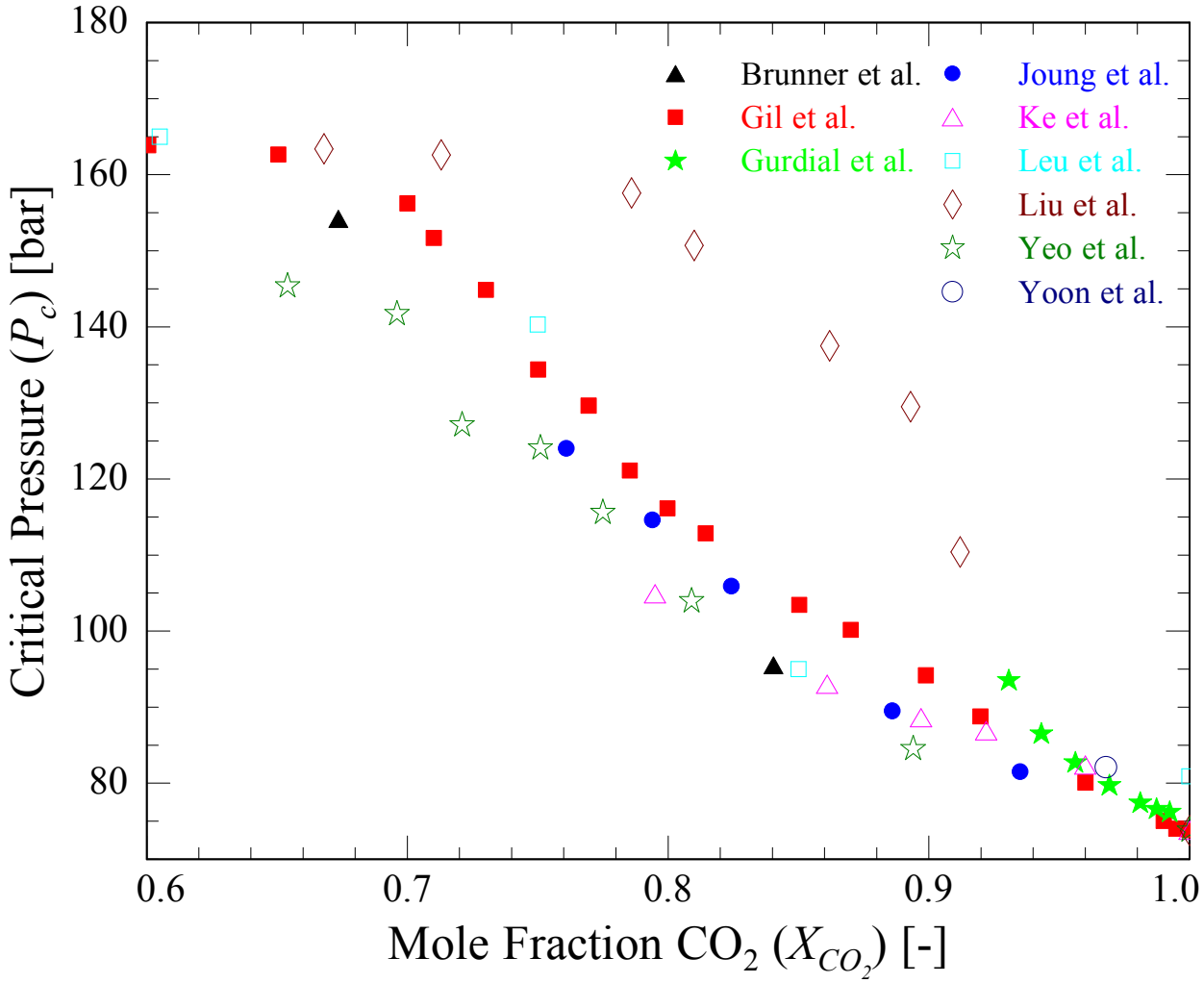

Figure E-2: Experimentally measured critical pressures of CO_2-methanol binary mixtures (Brunner et al., 1987; Gil et al., 2012; Gurdial et al., 1993; Joung et al., 2001; Ke et al., 2005; Leu et al., 1991; Liu et al., 2003; Yeo et al., 2000; Yoon et al., 1993).

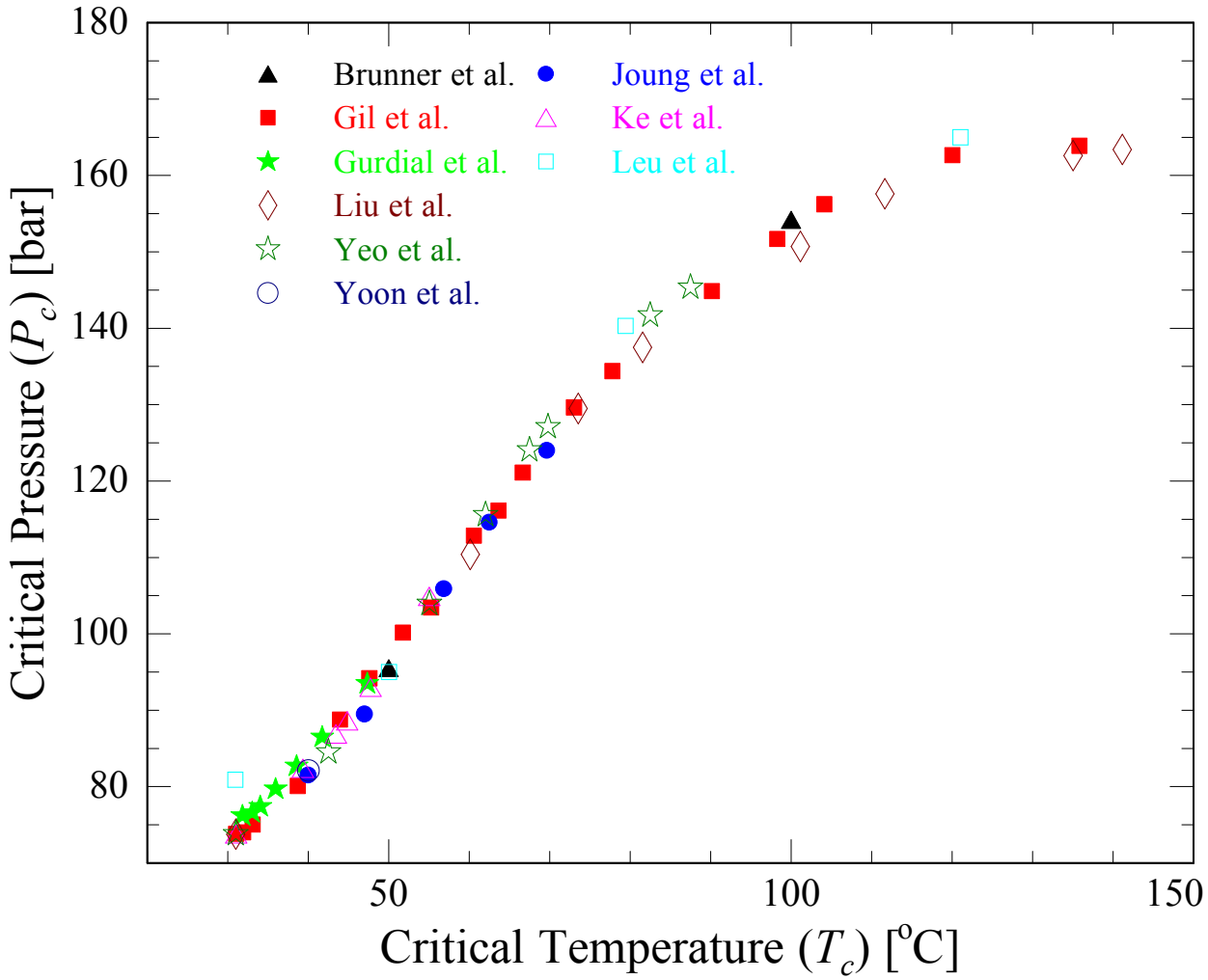

Figure E-3: Experimentally measured critical pressures and temperatures of CO_2-methanol binary mixtures (Brunner et al., 1987; Gil et al., 2012; Gurdial et al., 1993; Joung et al., 2001; Ke et al., 2005; Leu et al., 1991; Liu et al., 2003; Yeo et al., 2000; Yoon et al., 1993).

References for Appendix E:

Brunner, E., Hultenschmidt, W., & Schlichtharle, G. (1987). Fluid mixtures at high pressures IV . Isothermal phase equilibria in binary mixtures consisting of (methanol + hydrogen or nitrogen or methane or carbon monoxide or carbon dioxide). *J. Chem. Thermodynamics*, (19), 273–291.

Gil, L., Blanco, S. T., Rivas, C., Laga, E., Fernández, J., Artal, M., & Velasco, I. (2012). Experimental determination of the critical loci for {n-C6H14 or CO2 + alkan-1-ol} mixtures. Evaluation of their critical and subcritical behavior using PC-SAFT EoS. *The Journal of Supercritical Fluids*, *71*(0), 26–44. http://doi.org/http://dx.doi.org/10.1016/j.supflu.2012.07.008

Gurdial, G. S., Foster, N. R., Yun, S. L. J., & Tilly, K. D. (1993). Phase Behavior of Supercritical Fluid — Entrainer Systems. In E. Kiran (Ed.), *Supercritical Fluid Engineering Science* (pp. 34–45). Washington, DC: American Chemical Society. http://doi.org/10.1021/bk-1992-0514.ch003

Joung, S. N., Yoo, C. W., Shin, H. Y., Kim, S. Y., Yoo, K. P., Lee, C. S., & Huh, W. S. (2001). Measurements and correlation of high-pressure VLE of binary CO2-alcohol systems (methanol, ethanol, 2-methoxyethanol and 2-ethoxyethanol). *Fluid Phase Equilibria*, *185*(1–2), 219–230. http://doi.org/10.1016/S0378-3812(01)00472-1

Ke, J., King, P. J., George, M. W., & Poliakoff, M. (2005). Method for locating the vapor-liquid critical point of multicomponent fluid mixtures using a shear mode piezoelectric sensor. *Analytical Chemistry*, *77*(1), 85–92. http://doi.org/10.1021/ac048970i

Leu, A.-D., Chung, S. Y.-K., & Robinson, D. B. (1991). The equilibrium phase properties of (carbon dioxide + methanol). *The Journal of Chemical Thermodynamics*, *23*(10), 979–985. http://doi.org/10.1016/S0021-9614(05)80178-8

Liu, J., Qin, Z., Wang, G., Hou, X., & Wang, J. (2003). Critical Properties of Binary and Ternary Mixtures of Hexane + Methanol, Hexane + Carbon Dioxide, Methanol + Carbon Dioxide, and Hexane + Carbon Dioxide + Methanol. *Journal of Chemical & Engineering Data*, *48*(6), 1610–1613. http://doi.org/10.1021/je034127q

Yeo, S.-D., Park, S.-J., Kim, J.-W., & Kim, J.-C. (2000). Critical Properties of Carbon Dioxide + Methanol, + Ethanol, + 1-Propanol, and + 1-Butanol. *Journal of Chemical & Engineering Data*, *45*(5), 932–935. http://doi.org/10.1021/je000104p

Yoon, J. H., Lee, H. S., & Lee, H. (1993). High-pressure vapor-liquid equilibria for carbon dioxide + methanol, carbon dioxide + ethanol, and carbon dioxide + methanol + ethanol. *Journal of Chemical & Engineering Data*, *38*(1), 53–55. http://doi.org/10.1021/je00009a012

Appendix F. Raw C_p experimental measurement values for methanol and decane mixtures with carbon dioxide

Table F-1: Unsmoothed, individual measurements of methanol-carbon dioxide mixtures. Estimates for both systematic and random uncertainties are included for each measurement and denoted with a delta (δ). The GERG-2008 EOS is included for comparison, but it has not been fitted over the against measurements for the full range of temperatures, pressures and compositions documented here (Kunz & Wagner, 2012; Lemmon, 2015)*. The table is continued on following pages.*

Methanol-CO_2 Mixtures							
			This Work Experimental			**GERG-2008 EOS**	**Comparison with Experiment**
Composition (X)	**Temperature (T)**	**Pressure (P)**	**Heat Capacity (C_p)**	**$\delta_{systematic}$**	**δ_{random}**	**Heat Capacity (C_p)**	**100 (C_p - $C_{p,exp}$)/$C_{p,exp}$**
[% Methanol]	**[°C]**	**[bar]**	**[J/gK]**	**[%]**	**[%]**	**[J/gK]**	**[%]**
4.97	59.3	119.1	5.05	1.6	0.7	4.80	-5.1
4.99	59.3	119.4	5.00	1.6	0.7	4.78	-4.5
5.16	59.8	150.7	3.35	1.2	0.5	3.21	-4.2
4.96	59.8	150.7	3.34	1.2	0.5	3.22	-3.8
4.86	60.0	179.4	2.78	1.0	0.5	2.72	-2.4
5.11	60.0	180.0	2.79	1.0	0.5	2.71	-2.9
5.04	60.1	208.0	2.51	0.9	0.5	2.46	-1.9
5.05	60.0	210.8	2.49	0.9	0.5	2.44	-2.0
4.95	60.2	239.1	2.34	0.9	0.5	2.29	-2.2
5.10	60.0	239.7	2.33	0.9	0.5	2.29	-1.8
5.00	60.2	299.9	2.14	0.9	0.5	2.10	-2.0
4.99	60.0	300.2	2.12	0.9	0.5	2.10	-1.0
5.13	69.8	106.8	3.50	1.7	0.9	3.84	9.7
5.05	69.7	113.7	3.81	1.6	0.7	4.19	9.7
4.85	69.7	120.1	4.09	1.5	0.8	4.27	4.3
4.95	69.7	130.2	4.10	1.2	0.9	4.15	1.2
5.17	69.7	135.7	4.04	1.1	0.9	3.99	-1.1
5.03	69.9	141.9	3.82	1.0	0.9	3.78	-1.0

Methanol-CO_2 Mixtures							
			This Work Experimental			GERG-2008 EOS	Comparison with Experiment
Composition (X)	Temperature (T)	Pressure (P)	Heat Capacity (C_p)	$\delta_{systematic}$	δ_{random}	Heat Capacity (C_p)	100 (C_p - $C_{p,exp}$)/$C_{p,exp}$
[% Methanol]	[°C]	[bar]	[J/gK]	[%]	[%]	[J/gK]	[%]
5.05	70.0	150.3	3.58	1.0	0.9	3.52	-1.7
5.16	69.6	150.4	3.63	1.1	0.8	3.51	-3.3
5.09	69.8	150.5	3.58	1.1	0.8	3.51	-2.0
4.95	70.1	166.2	3.20	1.0	0.8	3.13	-2.3
5.19	80.2	119.1	3.02	1.0	0.7	3.18	5.1
5.17	80.3	127.2	3.23	1.1	0.8	3.38	4.6
5.08	80.1	133.6	3.36	1.0	0.8	3.46	3.0
5.06	80.2	139.9	3.38	1.3	0.8	3.46	2.6
5.11	80.2	149.1	3.40	1.2	0.8	3.41	0.4
5.03	80.3	162.9	3.25	1.1	0.8	3.22	-1.0
4.97	80.3	168.8	3.14	1.0	0.8	3.13	-0.4
4.97	80.4	180.4	2.99	1.0	0.8	2.96	-0.9
5.14	90.0	121.8	2.52	1.1	0.7	2.58	2.3
4.98	90.0	122.2	2.52	1.0	0.7	2.57	1.7
4.82	90.0	122.2	2.52	1.2	0.7	2.54	0.9
5.13	90.1	148.8	2.93	1.3	0.8	2.98	1.7
5.04	89.9	149.5	2.92	1.3	0.8	2.98	1.9
4.97	90.0	179.9	2.87	1.1	0.8	2.87	0.0
5.00	89.8	180.9	2.88	1.0	0.7	2.86	-0.4
5.03	90.1	209.0	2.62	1.0	0.8	2.64	0.4
5.13	90.1	209.2	2.64	1.0	0.8	2.64	-0.2
4.87	90.0	210.2	2.61	0.9	0.7	2.62	0.5
4.82	89.8	210.6	2.60	0.9	0.7	2.62	0.5

Methanol-CO_2 Mixtures							
			This Work Experimental			GERG-2008 EOS	Comparison with Experiment
Composition (X)	Temperature (T)	Pressure (P)	Heat Capacity (C_p)	$\delta_{systematic}$	δ_{random}	Heat Capacity (C_p)	100 (C_p - $C_{p,exp}$)/$C_{p,exp}$
[% Methanol]	[°C]	[bar]	[J/gK]	[%]	[%]	[J/gK]	[%]
4.91	90.2	239.6	2.41	0.9	0.7	2.43	0.7
4.85	90.0	240.0	2.41	0.9	0.7	2.42	0.8
4.78	90.1	240.6	2.41	0.9	0.7	2.42	0.2
4.88	90.2	240.6	2.42	0.9	0.7	2.42	0.2
4.98	90.3	298.9	2.16	0.9	0.7	2.18	0.9
4.88	90.3	298.9	2.17	0.9	0.7	2.18	0.3
4.96	99.9	149.7	2.52	1.3	0.7	2.56	1.5
4.90	99.9	150.7	2.53	1.3	0.7	2.56	1.4
5.17	100.1	150.8	2.54	1.3	0.7	2.59	1.8
4.94	100.0	163.2	2.62	1.2	0.7	2.64	0.8
5.04	100.0	164.0	2.64	1.2	0.7	2.65	0.5
5.12	100.1	164.2	2.65	1.2	0.7	2.66	0.4
5.01	100.0	178.3	2.65	1.0	0.7	2.66	0.2
5.46	100.2	180.0	2.65	1.1	0.7	2.68	1.2
5.05	100.1	196.2	2.60	1.0	0.7	2.61	0.3
4.93	110.1	146.8	2.13	1.3	0.7	2.20	3.6
4.97	110.0	161.3	2.25	1.3	0.7	2.34	3.7
4.94	110.3	165.9	2.31	1.2	0.7	2.36	1.9
4.99	110.0	170.0	2.32	1.2	0.7	2.39	3.0
5.11	110.2	179.8	2.39	1.2	0.8	2.43	1.5
5.00	110.2	179.9	2.38	1.2	0.8	2.42	1.4
5.00	110.0	187.4	2.38	1.1	0.7	2.43	2.5
5.01	110.3	195.2	2.39	1.1	0.8	2.43	1.5

Methanol-CO_2 Mixtures							
			This Work Experimental			GERG-2008 EOS	Comparison with Experiment
Composition (X)	Temperature (T)	Pressure (P)	Heat Capacity (C_p)	$\delta_{systematic}$	δ_{random}	Heat Capacity (C_p)	100 (C_p - $C_{p,exp}$)/$C_{p,exp}$
[% Methanol]	[°C]	[bar]	[J/gK]	[%]	[%]	[J/gK]	[%]
5.04	110.2	210.0	2.39	1.1	0.8	2.41	0.8
5.16	110.2	210.0	2.42	1.1	0.8	2.42	0.0
5.02	110.1	223.9	2.33	1.0	0.7	2.38	2.1
5.01	110.0	237.5	2.28	1.0	0.7	2.34	2.5
5.07	110.1	237.5	2.32	1.0	0.7	2.34	1.0
10.00	59.4	110.2	5.75	1.4	1.1	4.82	-16.2
9.99	59.6	110.7	5.55	1.5	1.2	4.78	-13.8
10.02	59.6	110.8	5.59	1.4	1.1	4.78	-14.5
10.01	59.8	118.8	4.58	1.5	0.9	4.14	-9.6
10.08	59.9	118.8	4.54	1.5	0.9	4.13	-9.0
9.92	59.9	120.1	4.44	1.6	0.9	4.07	-8.3
9.91	59.9	120.2	4.44	1.2	0.9	4.08	-8.2
9.91	60.0	129.9	3.85	1.4	0.9	3.61	-6.3
10.12	60.2	130.0	3.86	1.4	0.9	3.60	-6.6
10.16	60.2	130.0	3.87	1.4	0.9	3.60	-7.0
10.04	60.1	130.0	3.83	1.4	0.9	3.60	-6.0
10.03	60.0	149.8	3.17	1.3	0.8	3.07	-3.1
9.96	60.1	150.0	3.18	1.3	0.8	3.08	-3.1
10.02	60.1	150.9	3.18	1.2	0.8	3.06	-3.8
9.95	60.0	165.3	2.94	1.1	0.7	2.84	-3.2
10.02	60.1	165.7	2.95	1.1	0.8	2.84	-3.6
9.97	60.1	165.9	2.93	1.1	0.8	2.84	-3.2
10.03	60.1	180.8	2.78	1.0	0.8	2.68	-3.3

Methanol-CO_2 Mixtures							
			This Work Experimental			GERG-2008 EOS	Comparison with Experiment
Composition (X)	Temperature (T)	Pressure (P)	Heat Capacity (C_p)	$\delta_{systematic}$	δ_{random}	Heat Capacity (C_p)	100 (C_p - $C_{p,exp}$)/$C_{p,exp}$
[% Methanol]	[°C]	[bar]	[J/gK]	[%]	[%]	[J/gK]	[%]
9.95	60.0	180.9	2.74	1.0	0.7	2.68	-2.3
10.01	60.1	181.0	2.76	1.0	0.8	2.68	-2.8
9.96	60.0	209.4	2.55	1.0	0.8	2.48	-2.6
9.94	60.1	209.4	2.56	0.9	0.7	2.48	-3.0
10.02	60.1	209.7	2.56	1.0	0.8	2.48	-3.2
9.89	60.0	239.1	2.40	1.0	0.8	2.35	-2.2
9.98	60.2	239.9	2.42	0.9	0.7	2.35	-2.9
10.03	60.2	239.9	2.42	0.9	0.8	2.35	-3.1
9.95	60.0	299.1	2.24	1.0	0.8	2.18	-2.5
10.03	60.1	300.5	2.25	0.9	0.7	2.18	-3.3
9.97	60.1	300.5	2.24	0.9	0.8	2.18	-2.8
10.16	89.8	119.0	3.15	1.1	0.8	3.34	6.1
10.20	89.9	119.8	3.20	1.1	0.8	3.37	5.3
10.01	89.7	134.0	3.35	1.2	0.8	3.52	5.1
10.32	89.8	134.7	3.38	1.2	0.8	3.55	5.1
10.31	89.9	135.0	3.38	1.2	0.8	3.55	5.0
9.99	89.7	148.5	3.36	1.3	0.8	3.46	2.9
9.98	89.7	148.7	3.36	1.3	0.9	3.45	2.7
10.40	89.8	149.6	3.39	1.3	0.8	3.47	2.4
10.42	89.7	163.0	3.26	1.2	0.8	3.32	1.7
10.09	89.7	163.2	3.26	1.2	0.8	3.30	1.0
10.21	89.9	163.5	3.27	1.2	0.8	3.30	0.9
9.98	89.9	178.7	3.06	1.1	0.8	3.09	1.0

Methanol-CO_2 Mixtures							
			This Work Experimental			GERG-2008 EOS	Comparison with Experiment
Composition (X)	Temperature (T)	Pressure (P)	Heat Capacity (C_p)	$\delta_{systematic}$	δ_{random}	Heat Capacity (C_p)	100 (C_p - $C_{p,exp}$)/$C_{p,exp}$
[% Methanol]	[°C]	[bar]	[J/gK]	[%]	[%]	[J/gK]	[%]
10.16	89.9	179.7	3.07	1.1	0.8	3.08	0.4
10.48	90.0	180.5	3.07	1.1	0.8	3.08	0.3
10.02	90.0	208.9	2.78	1.0	0.8	2.77	-0.4
10.03	90.0	209.0	2.78	1.0	0.8	2.77	-0.5
9.91	90.0	209.2	2.77	1.0	0.8	2.76	-0.1
10.03	90.0	238.4	2.56	0.9	0.8	2.55	-0.2
10.23	90.0	238.4	2.58	1.0	0.8	2.56	-0.8
9.77	90.0	240.2	2.54	1.0	0.8	2.54	-0.3
10.15	90.1	297.2	2.30	0.9	0.7	2.29	-0.4
9.72	89.9	299.2	2.30	1.0	0.9	2.28	-0.9
9.82	90.2	299.4	2.28	0.9	0.8	2.28	-0.1
10.09	90.1	300.2	2.31	0.9	0.7	2.28	-1.1
10.00	99.9	119.8	2.73	1.1	0.7	2.70	-1.2
9.85	99.8	136.5	2.91	1.1	0.7	2.97	2.0
9.90	99.7	150.1	3.02	1.2	0.7	3.06	1.1
9.96	99.8	165.6	3.04	1.1	0.7	3.03	-0.2
9.92	99.9	178.7	2.99	1.0	0.7	2.96	-1.1
9.84	99.8	197.6	2.85	1.0	0.7	2.82	-1.0
9.85	99.9	209.6	2.76	0.9	0.7	2.74	-0.7
9.86	99.9	241.2	2.55	0.9	0.7	2.54	-0.3
10.03	110.0	148.4	2.67	1.4	0.8	2.65	-0.7
9.86	110.0	167.9	2.76	1.2	0.8	2.76	0.1
9.74	110.1	180.0	2.75	1.1	0.8	2.74	-0.4

Methanol-CO_2 Mixtures							
			This Work Experimental			GERG-2008 EOS	Comparison with Experiment
Composition (X)	Temperature (T)	Pressure (P)	Heat Capacity (C_p)	$\delta_{systematic}$	δ_{random}	Heat Capacity (C_p)	100 (C_p - $C_{p,exp}$)/$C_{p,exp}$
[% Methanol]	[°C]	[bar]	[J/gK]	[%]	[%]	[J/gK]	[%]
9.97	110.2	180.1	2.77	1.1	0.8	2.74	-0.9
9.98	110.1	193.9	2.73	1.1	0.8	2.70	-0.9
9.88	110.0	210.8	2.66	1.1	0.8	2.63	-0.9
9.97	120.0	88.9	1.72	1.2	0.7	1.64	-4.3
10.06	120.1	89.1	1.73	1.2	0.7	1.65	-4.7
9.85	119.8	90.4	1.74	1.2	0.7	1.65	-5.0
10.05	120.0	120.1	2.08	1.0	0.6	2.05	-1.7
10.16	120.1	120.1	2.10	1.0	0.7	2.05	-2.1
10.25	120.0	120.2	2.11	1.0	0.7	2.06	-2.3
9.76	120.1	121.1	2.12	1.0	0.7	2.04	-3.8
9.59	120.0	149.1	2.36	1.3	0.7	2.34	-0.9
10.11	120.0	150.0	2.38	1.3	0.8	2.40	0.8
10.13	120.0	150.0	2.38	1.3	0.7	2.40	0.9
10.03	120.0	179.7	2.51	1.1	0.8	2.53	0.8
9.58	120.1	180.3	2.54	1.1	0.7	2.50	-1.6
9.60	120.1	180.6	2.50	1.1	0.7	2.50	0.0
10.07	119.9	210.0	2.52	1.1	0.8	2.51	-0.2
9.61	120.1	210.9	2.51	1.0	0.7	2.49	-0.8
9.48	120.1	211.0	2.52	1.0	0.8	2.48	-1.4
10.10	120.0	239.2	2.45	1.0	0.8	2.44	-0.2
9.50	120.1	240.9	2.43	1.0	0.7	2.41	-0.6
9.62	120.2	241.3	2.43	1.0	0.7	2.41	-0.7
10.05	120.0	298.1	2.24	1.0	0.7	2.27	1.3

Methanol-CO_2 Mixtures							
			This Work Experimental			GERG-2008 EOS	Comparison with Experiment
Composition (X)	Temperature (T)	Pressure (P)	Heat Capacity (C_p)	$\delta_{systematic}$	δ_{random}	Heat Capacity (C_p)	100 (C_p - $C_{p,exp}$)/$C_{p,exp}$
[% Methanol]	[°C]	[bar]	[J/gK]	[%]	[%]	[J/gK]	[%]
10.08	119.9	298.1	2.26	1.0	0.8	2.27	0.4
9.46	120.1	301.0	2.23	1.0	0.8	2.24	0.6
9.49	120.1	301.7	2.24	0.9	0.7	2.24	0.2
14.73	89.6	149.3	3.57	1.1	0.8	3.73	4.5
15.26	89.4	150.1	3.52	1.0	0.8	3.73	6.0
14.85	89.3	150.3	3.54	1.0	0.8	3.71	4.8
14.76	89.5	164.0	3.34	1.0	0.8	3.44	2.9
14.86	89.5	178.9	3.13	1.0	0.7	3.20	2.2
15.00	89.7	180.2	3.11	0.9	0.7	3.18	2.2
14.99	89.8	208.9	2.81	0.9	0.7	2.86	1.7
15.00	89.7	210.4	2.80	0.9	0.7	2.84	1.5
14.96	89.7	240.3	2.61	0.9	0.7	2.63	0.6
14.98	90.0	241.0	2.61	0.9	0.7	2.63	0.9
15.03	90.0	298.0	2.39	0.8	0.6	2.39	-0.1
14.93	90.3	299.9	2.40	0.9	0.8	2.38	-0.6
15.10	120.0	120.1	2.67	1.1	0.7	2.49	-6.8
14.88	119.9	120.2	2.64	1.1	0.7	2.47	-6.7
14.94	120.0	121.1	2.64	1.0	0.7	2.49	-5.9
15.03	120.0	149.5	2.84	1.3	0.7	2.82	-0.8
14.98	120.0	150.8	2.82	1.3	0.7	2.82	0.0
15.06	120.2	178.8	2.89	1.1	0.7	2.85	-1.6
15.02	120.0	181.1	2.88	1.1	0.7	2.84	-1.3
14.98	120.1	210.1	2.78	1.0	0.7	2.75	-1.0

Methanol-CO_2 Mixtures							
			This Work Experimental			GERG-2008 EOS	Comparison with Experiment
Composition (X)	Temperature (T)	Pressure (P)	Heat Capacity (C_p)	$\delta_{systematic}$	δ_{random}	Heat Capacity (C_p)	100 (C_p - $C_{p,exp}$)/$C_{p,exp}$
[% Methanol]	[°C]	[bar]	[J/gK]	[%]	[%]	[J/gK]	[%]
15.03	120.0	211.1	2.79	1.0	0.7	2.75	-1.3
14.92	120.2	239.9	2.62	1.0	0.7	2.63	0.3
15.05	120.1	240.0	2.63	1.0	0.7	2.63	0.1
14.90	119.9	240.7	2.62	1.0	0.8	2.62	0.1
14.92	120.1	298.9	2.39	0.9	0.7	2.42	1.3
15.07	120.2	299.5	2.39	0.9	0.7	2.42	1.4
15.06	129.9	148.4	2.57	1.3	0.7	2.52	-1.9
14.90	129.9	148.8	2.60	1.3	0.7	2.52	-3.0
14.94	129.8	163.2	2.66	1.2	0.7	2.61	-2.0
14.96	130.1	180.9	2.69	1.1	0.7	2.64	-1.9
14.93	129.9	181.1	2.69	1.0	0.7	2.64	-1.9
14.99	129.9	196.5	2.71	1.0	0.7	2.64	-2.5
15.09	129.8	212.3	2.68	1.0	0.7	2.62	-2.4
14.94	130.0	225.8	2.61	1.0	0.7	2.58	-1.2
14.95	139.9	179.7	2.51	1.1	0.6	2.45	-2.2
15.01	140.0	179.9	2.51	1.1	0.6	2.46	-2.2
15.05	140.0	194.6	2.54	1.0	0.7	2.48	-2.2
14.95	140.0	209.3	2.53	1.0	0.7	2.48	-2.2
14.96	140.0	226.0	2.51	1.0	0.7	2.46	-1.9
20.01	89.4	133.9	3.65	1.1	0.8	4.29	17.5
20.05	89.5	149.1	3.58	1.1	0.8	3.82	6.7
20.06	89.5	149.3	3.61	1.1	0.8	3.82	5.9
19.96	89.7	179.6	3.12	1.0	0.7	3.23	3.7

Methanol-CO_2 Mixtures							
			This Work Experimental			GERG-2008 EOS	Comparison with Experiment
Composition (X)	Temperature (T)	Pressure (P)	Heat Capacity (C_p)	$\delta_{systematic}$	δ_{random}	Heat Capacity (C_p)	100 (C_p - $C_{p,exp}$)/$C_{p,exp}$
[% Methanol]	[°C]	[bar]	[J/gK]	[%]	[%]	[J/gK]	[%]
19.92	89.9	179.9	3.11	1.0	0.8	3.23	3.8
20.09	90.0	209.9	2.84	1.0	0.8	2.91	2.4
19.91	89.8	210.0	2.85	0.9	0.7	2.91	2.0
19.70	90.1	239.5	2.65	1.0	0.8	2.71	2.0
20.11	89.9	239.6	2.69	0.9	0.7	2.71	0.6
20.73	89.9	299.9	2.48	0.9	0.7	2.48	0.0
20.12	89.9	300.2	2.47	0.9	0.7	2.47	0.0
19.45	90.1	301.2	2.46	0.9	0.8	2.46	0.0
19.91	90.1	301.9	2.46	0.9	0.8	2.46	0.0
20.03	120.1	151.1	3.24	1.2	0.8	3.26	0.5
19.96	120.2	151.4	3.25	1.2	0.8	3.25	0.0
19.91	119.9	150.1	3.25	1.2	0.7	3.26	0.1
19.95	120.0	180.0	3.13	1.1	0.8	3.15	0.6
19.84	120.1	180.5	3.13	1.1	0.8	3.14	0.4
19.89	120.0	209.3	2.93	1.0	0.8	2.99	1.9
19.97	120.0	209.4	2.94	1.0	0.8	2.99	1.8
19.97	120.1	210.7	2.94	1.0	0.8	2.98	1.6
19.88	120.2	210.8	2.92	1.0	0.8	2.98	1.8
20.09	120.1	229.2	2.82	1.0	0.8	2.88	1.9
20.18	120.0	239.0	2.79	1.0	0.8	2.83	1.3
20.08	120.0	239.0	2.79	1.0	0.7	2.83	1.3
19.97	120.0	299.4	2.52	0.9	0.8	2.56	1.8
20.09	120.1	299.6	2.51	1.0	0.8	2.57	2.4

Methanol-CO_2 Mixtures							
			This Work Experimental			GERG-2008 EOS	Comparison with Experiment
Composition (X)	Temperature (T)	Pressure (P)	Heat Capacity (C_p)	$\delta_{systematic}$	δ_{random}	Heat Capacity (C_p)	100 (C_p - $C_{p,exp}$)/$C_{p,exp}$
[% Methanol]	[°C]	[bar]	[J/gK]	[%]	[%]	[J/gK]	[%]
20.11	120.2	299.6	2.53	1.0	0.8	2.57	1.4
20.00	129.5	133.9	3.02	1.2	0.7	2.86	-5.2
20.07	129.6	151.7	3.07	1.2	0.7	2.98	-2.8
20.07	129.6	165.0	3.06	1.1	0.7	2.99	-2.4
20.00	129.8	180.2	3.04	1.1	0.7	2.96	-2.7
20.06	129.8	194.5	2.98	1.1	0.7	2.93	-1.7
20.06	129.6	208.6	2.93	1.0	0.7	2.88	-1.5
20.04	129.7	224.8	2.83	1.0	0.7	2.82	-0.4
19.94	129.7	225.2	2.84	1.0	0.7	2.82	-0.7
20.01	140.0	165.5	2.86	1.2	0.7	2.75	-3.7
20.03	139.9	177.9	2.88	1.1	0.7	2.77	-3.7
19.97	140.0	194.1	2.87	1.0	0.7	2.75	-4.1
19.95	139.8	209.3	2.84	1.0	0.7	2.73	-3.9
20.01	139.9	226.2	2.77	1.0	0.7	2.70	-2.7
19.88	149.9	119.9	2.32	1.2	0.6	2.14	-8.0
20.01	149.9	120.0	2.33	2.3	0.6	2.15	-8.0
20.05	150.0	120.8	2.35	2.3	0.7	2.16	-8.1
19.88	149.9	149.0	2.55	1.0	0.7	2.43	-4.7
20.11	150.0	150.7	2.59	1.0	0.7	2.46	-5.0
19.98	149.7	179.4	2.69	1.1	0.7	2.59	-3.9
20.12	150.1	180.7	2.70	1.1	0.7	2.59	-3.7
20.01	150.2	209.6	2.69	1.0	0.7	2.59	-3.5
20.02	149.9	211.0	2.70	1.0	0.7	2.60	-3.7

Methanol-CO_2 Mixtures							
			This Work Experimental			GERG-2008 EOS	Comparison with Experiment
Composition (X)	Temperature (T)	Pressure (P)	Heat Capacity (C_p)	$\delta_{systematic}$	δ_{random}	Heat Capacity (C_p)	100 (C_p - $C_{p,exp}$)/$C_{p,exp}$
[% Methanol]	[°C]	[bar]	[J/gK]	[%]	[%]	[J/gK]	[%]
20.03	149.8	239.1	2.64	1.0	0.7	2.57	-2.8
19.93	150.1	240.1	2.63	1.0	0.7	2.56	-2.6
20.19	150.0	299.2	2.49	0.9	0.7	2.47	-1.1
20.06	149.9	299.3	2.49	0.9	0.7	2.46	-1.0
19.93	150.1	301.3	2.48	1.0	0.7	2.45	-1.1
29.84	119.9	150.0	3.48	1.3	0.8	4.06	16.7
30.06	119.9	150.6	3.49	1.3	0.8	4.07	16.7
29.91	119.7	165.1	3.52	1.2	0.8	3.87	10.0
29.91	119.9	165.7	3.51	1.2	0.8	3.87	10.0
30.16	120.0	179.6	3.40	1.1	0.8	3.69	8.7
29.85	119.8	180.1	3.36	1.1	0.8	3.67	9.2
30.10	119.9	209.4	3.13	1.0	0.8	3.36	7.2
29.80	119.9	209.8	3.10	1.0	0.7	3.35	8.1
30.11	119.9	239.6	2.91	1.0	0.8	3.11	6.7
30.09	120.0	239.9	2.94	1.0	0.8	3.11	5.6
30.12	120.0	299.6	2.70	1.0	0.8	2.80	3.6
30.15	120.1	300.2	2.70	1.0	0.8	2.80	3.6
30.12	120.1	300.4	2.70	1.0	0.8	2.80	3.5
30.01	149.8	149.1	3.45	1.3	0.7	3.27	-5.3
30.00	149.7	151.1	3.49	1.3	0.8	3.27	-6.3
30.06	149.6	164.2	3.44	1.3	0.8	3.26	-5.3
29.95	149.6	179.4	3.36	1.2	0.8	3.22	-4.2
29.92	150.0	179.7	3.36	1.2	0.7	3.21	-4.4

Methanol-CO_2 Mixtures							
			This Work Experimental			GERG-2008 EOS	Comparison with Experiment
Composition (X)	Temperature (T)	Pressure (P)	Heat Capacity (C_p)	$\delta_{systematic}$	δ_{random}	Heat Capacity (C_p)	100 (C_p - $C_{p,exp}$)/$C_{p,exp}$
[% Methanol]	[°C]	[bar]	[J/gK]	[%]	[%]	[J/gK]	[%]
30.05	150.0	210.0	3.18	1.1	0.7	3.15	-1.0
29.92	149.7	210.3	3.19	1.1	0.7	3.14	-1.4
30.49	149.9	238.7	3.04	1.0	0.7	3.07	1.1
29.87	149.9	239.0	3.02	1.0	0.7	3.04	0.6
30.03	149.8	240.7	3.01	1.0	0.7	3.04	1.2
29.92	149.8	299.2	2.77	0.9	0.7	2.84	2.6
30.59	149.9	301.6	2.76	1.0	0.7	2.86	3.4
30.08	149.8	301.9	2.74	1.0	0.7	2.84	3.5

Table F-2: Unsmoothed, individual measurements of decane-carbon dioxide mixtures. Estimates for both systematic and random uncertainties are included for each measurement and denoted with a delta (δ). The GERG-2008 EOS is included for comparison (Kunz & Wagner, 2012). *The table is continued on following pages.*

Decane-CO_2 Mixtures							
			This Work Experimental			**GERG-2008 EOS**	**Comparison with Experiment**
Composition (X)	**Temperature (T)**	**Pressure (P)**	**Heat Capacity (C_p)**	**$\delta_{systematic}$**	**δ_{random}**	**Heat Capacity (C_p)**	**100 (C_p - $C_{p,exp}$)/$C_{p,exp}$**
[% Methanol]	**[°C]**	**[bar]**	**[J/gK]**	**[%]**	**[%]**	**[J/gK]**	**[%]**
0.99	59.78	106.4	4.56	1.2	0.9	4.82	5.8
0.98	60.03	106.6	4.45	1.2	0.8	4.76	7.0
1.01	59.94	111.1	4.69	2.2	0.9	4.99	6.3
0.99	59.97	114.5	4.75	1.6	0.9	4.91	3.4
0.98	60.05	118.4	4.69	1.4	0.9	4.71	0.5
0.97	60.19	123.3	4.45	1.9	0.9	4.39	-1.3
0.97	60.24	128.6	4.16	2.2	0.8	4.05	-2.5
0.99	70.27	110.4	3.13	1.2	0.8	3.18	1.6
0.98	70.17	116.9	3.42	1.3	0.8	3.50	2.4
0.97	70.21	123.4	3.62	2.6	0.8	3.69	2.1
1.00	70.26	131.2	3.71	1.6	0.8	3.74	0.7
0.98	70.23	140.6	3.57	1.1	0.8	3.57	0.1
0.98	70.27	147.1	3.42	1.3	0.8	3.41	-0.5
0.99	70.23	154.8	3.28	1.4	0.8	3.21	-2.2
0.97	89.88	132.9	2.39	2.0	0.7	2.45	2.5
0.99	89.92	133.0	2.43	2.0	0.7	2.46	1.3
1.02	89.97	144.2	2.58	1.8	0.7	2.63	1.8
1.02	89.98	153.5	2.66	1.5	0.7	2.70	1.6
1.01	89.97	162.4	2.70	1.3	0.7	2.72	0.8
1.00	90.05	172.0	2.68	1.1	0.7	2.69	0.5

Decane-CO_2 Mixtures							
			This Work Experimental			GERG-2008 EOS	Comparison with Experiment
Composition (X)	Temperature (T)	Pressure (P)	Heat Capacity (C_p)	$\delta_{systematic}$	δ_{random}	Heat Capacity (C_p)	100 (C_p - $C_{p,exp}$)/$C_{p,exp}$
[% Methanol]	[°C]	[bar]	[J/gK]	[%]	[%]	[J/gK]	[%]
1.00	90.03	179.8	2.65	1.0	0.7	2.66	0.3
1.00	90.09	189.0	2.61	0.9	0.7	2.59	-0.4
0.72	100.06	139.4	2.09	1.7	0.7	2.12	1.5
0.70	99.95	140.8	2.10	1.8	0.7	2.14	1.7
0.72	100.17	147.1	2.18	1.7	0.7	2.21	1.5
0.72	100.13	147.6	2.18	1.7	0.7	2.22	1.8
0.70	100.04	155.8	2.27	1.6	0.7	2.30	1.3
0.71	99.98	162.2	2.31	1.5	0.7	2.35	1.6
0.71	100.07	168.9	2.35	1.4	0.7	2.38	1.2
0.71	100.08	178.1	2.40	1.3	0.7	2.41	0.6
0.72	100.03	184.1	2.40	1.2	0.7	2.42	0.7
0.71	99.97	191.8	2.40	1.1	0.8	2.41	0.7
0.71	100.04	202.3	2.37	1.1	0.8	2.39	0.6
1.98	90.09	126.8	2.40	2.3	0.7	2.63	9.5
1.98	90.03	136.5	2.64	1.9	0.7	2.79	5.6
2.00	90.09	144.4	2.73	1.6	0.7	2.85	4.4
1.99	90.07	155.5	2.77	1.3	0.7	2.85	2.9
1.97	90.10	167.3	2.73	1.0	0.7	2.78	1.8
1.96	90.08	177.4	2.67	0.9	0.7	2.69	0.8
1.96	90.16	189.1	2.59	0.9	0.7	2.58	-0.1
1.97	99.91	140.3	2.31	1.4	0.6	2.41	4.1
1.97	99.87	140.4	2.30	1.4	0.6	2.41	4.6
1.97	99.98	149.6	2.40	1.5	0.7	2.50	4.0

Decane-CO_2 Mixtures							
			This Work Experimental			GERG-2008 EOS	Comparison with Experiment
Composition (X)	Temperature (T)	Pressure (P)	Heat Capacity (C_p)	$\delta_{systematic}$	δ_{random}	Heat Capacity (C_p)	100 (C_p - $C_{p,exp}$)/$C_{p,exp}$
[% Methanol]	[°C]	[bar]	[J/gK]	[%]	[%]	[J/gK]	[%]
1.99	100.07	157.6	2.45	1.5	0.7	2.54	3.8
1.98	100.18	165.7	2.48	1.3	0.7	2.55	3.1
1.99	100.03	172.7	2.50	1.2	0.7	2.55	2.3
1.99	100.12	179.4	2.50	1.1	0.7	2.53	1.4
1.97	99.99	189.9	2.46	1.0	0.8	2.49	1.3
1.99	99.95	199.3	2.42	1.0	0.8	2.44	0.7

Appendix G. Plotted difference between experimental C_p measurements and the GERG EOS for CO_2-methanol and CO_2-decane mixtures

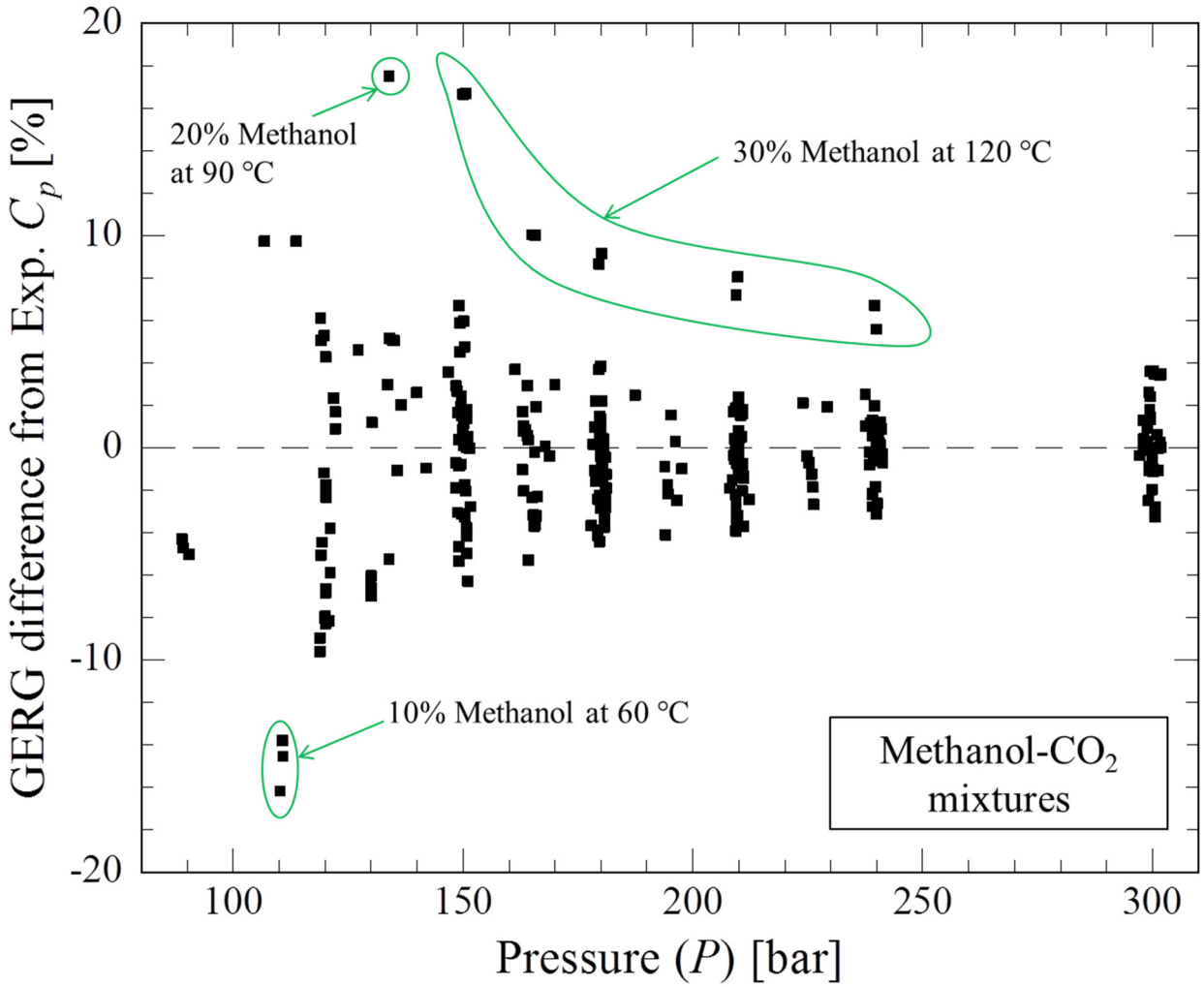

Figure G-1: The absolute percent difference between the GERG-2008 EOS and experimental measurements.

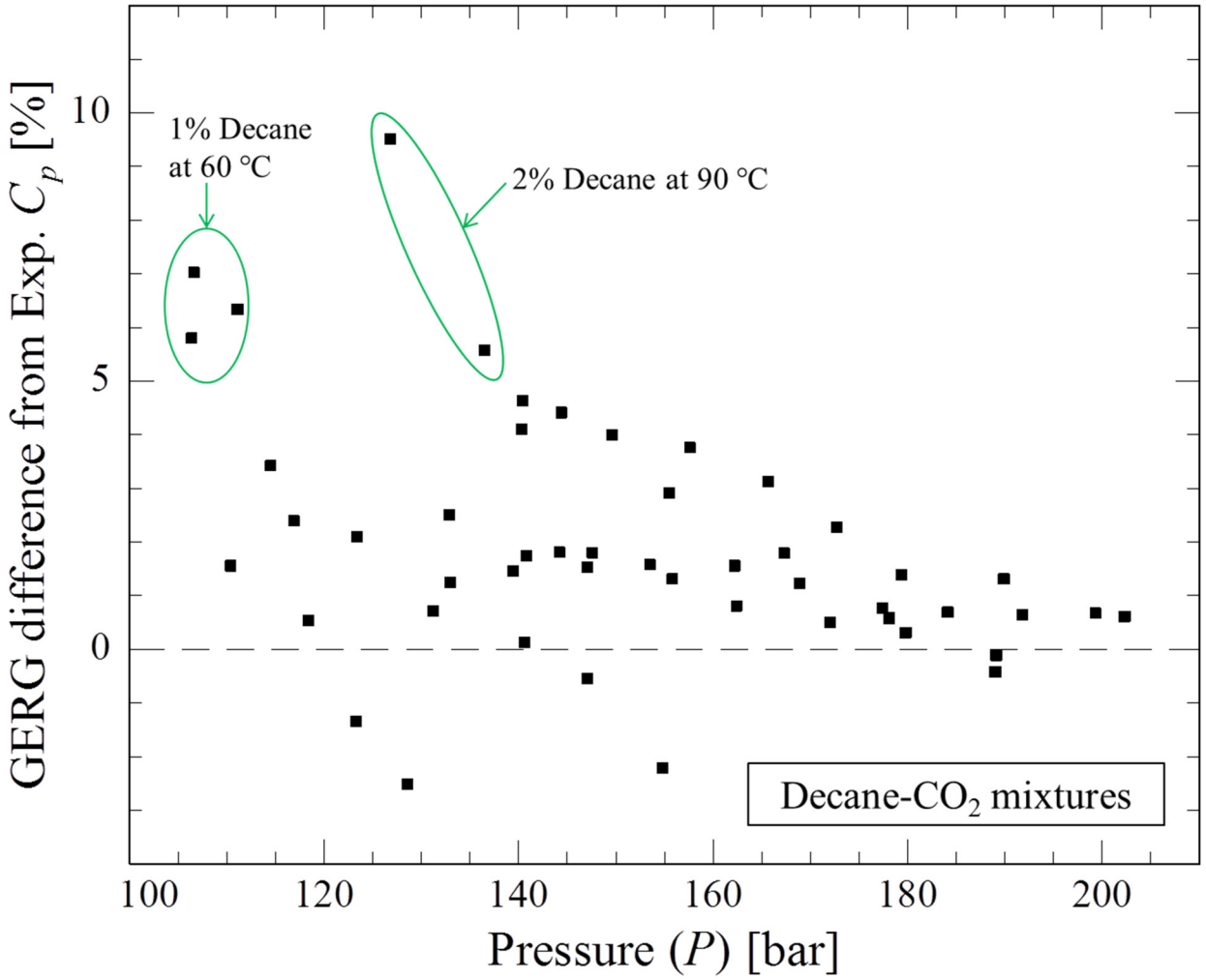

Figure G-2: The absolute percent difference between the GERG-2008 EOS and experimental measurements.

Appendix H. List of polynomials used to fit heat capacity ridges and fitted data points

Table H-1: Functional form of the pressure dependent fit to the experimental isobaric heat capacity data and its associated abbreviation for Table H-2.

Polynomial Forms	Abbreviation
$C_P fit\ (P) = \alpha P^3 + \beta P^2 + \gamma P + \theta + \frac{\tau}{P}$	A
$C_P fit\ (P) = \alpha P^3 + \beta P^2 + \gamma P + \theta$	B
$C_P fit\ (P) = \beta P^2 + \gamma P + \theta$	C

Table H-2: Fit pressures for each composition at a given temperature. The associated polynomial function was used to fit the data and identify each isotherm's C_p *peak.*

Composition in CO_2	Temperature	Pressures Included in Fit	Polynomial Form
1% Decane	60	106-129	A
1% Decane	70	110-155	A
1% Decane	90	133-189	A
0.7% Decane	100	147-202	A
2% Decane	90	127-189	A
2% Decane	100	140-199	A
5% Methanol	70	106-166	A
5% Methanol	80	119-180	A
5% Methanol	90	122-240	A
5% Methanol	100	151-196	A
5% Methanol	110	147-237	A
10% Methanol	90	119-209	A
10% Methanol	100	120-241	A
10% Methanol	110	148-211	A
10% Methanol	120	89-301	A
15% Methanol	120	120-241	A
15% Methanol	130	148-226	A
15% Methanol	140	180-226	C
20% Methanol	130	134-209	B
20% Methanol	140	165-226	C
20% Methanol	150	120-301	A

Appendix I. Experimental attempt to synthesize encapsulated phase change materials for coupled thermal energy storage with supercritical fluids

I.1. Motivation

Thermal energy storage is one application that motivates understanding the thermophysical behavior of supercritical fluids; however, devising a practical and cost-effective storage system that operates at nearly constant pressure remains a challenge. But with their large isobaric heat capacity peaks and high density, supercritical fluids could also play a role in energy transfer. Additional benefits of utilizing supercritical fluids for energy transfer include: potential for direct expansion of the fluid for electricity generation, enhancements to heat transfer coefficients (Hall & Jackson, 1978; Pioro, Khartabil, & Duffey, 2004), and opportunities for gravity driven thermosyphons (Benne & Homan, 2008; Chen, Deng, & Zhang, 2013; Lamoureux, 2012).

Phase change materials (PCMs) offer an interesting candidate for thermal energy storage and could be paired with a supercritical heat transfer fluid. Benign inorganic and organic PCMs have large latent heats of fusion/melting (generally greater than 200 J/g) that cover a wide range of storage temperatures (Farid, Khudhair, Razack, & Al-Hallaj, 2004; Sharma, Tyagi, Chen, & Buddhi, 2009). Nevertheless, the adoption of PCMs has been commercially limited because of their low thermal conductivity (on the order of 0.1 W/mK), tendency to degrade over time, and cost. Encapsulation is one method to increase the usability of PCMs by increasing the surface area available for heat transfer and protecting the core from its external chemical environment with a shell. Pairing energy dense materials and heat transfer fluids, each of which can be readily optimized for a specific temperature, may provide a strong platform for thermal energy storage.

By also encapsulating the phase change material, the efficiency of the thermal energy transfer and the lifetime of the material will be increased. Figure I-1 schematically illustrates a thermal storage device comprised of a packed bed of encapsulated PCMs exchanging heat with a supercritical fluid.

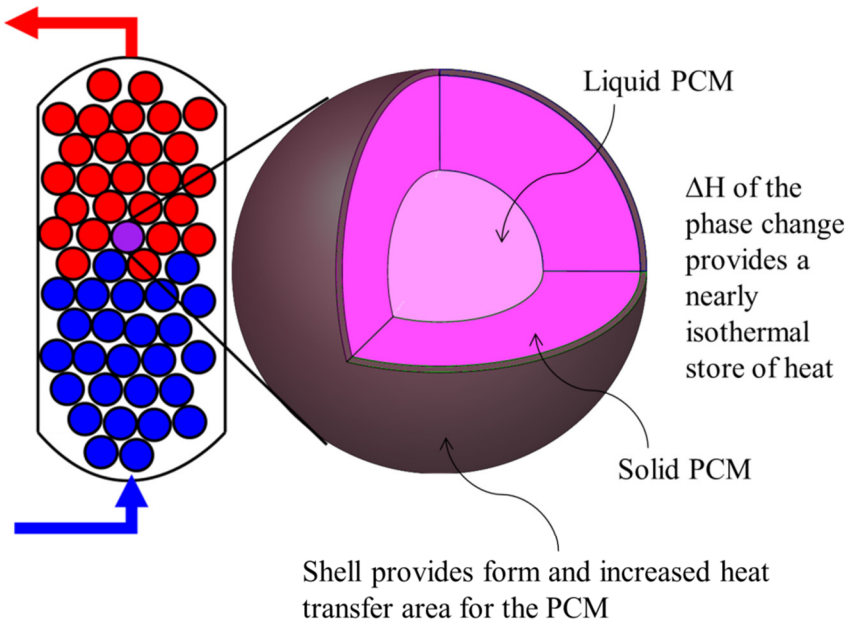

Figure I-1: Schematic of a supercritical fluid exchanging heat with an encapsulated phase change material. (left) A cool supercritical fluid enters a packed bed of encapsulated phase change spheres, freezing the material, and exits the bed warm. (right) An example of an encapsulated phase change sphere, where the shell protects the PCM from the surrounding heat transfer fluid.

I.2. Selection of materials and methods of encapsulation

Organic phase change materials offer a number of advantages when compared to inorganic materials, including increased stability and minimal supercooling. For these reasons, and available published studies on encapsulating these materials, paraffin wax was selected as a candidate PCM (Alic, Sebenik, & Krajnc, 2012; Bauer, 1986; Caruso, 2001; Clifford, Iyer, & Raston, 2008; Deng, Chen, Zhou, You, & Wu, 2006; Fang, Chen, & Li, 2010; Goller & Vincent, 1998; Jin, Lee, Musina, & Ding, 2010; Jones, Chu, & Samaraweerab, 1994; Kumar & Katiyar,

1990; Li, Zhang, Wang, & Niu, 2007; Merline, Vukusic, & Abdala, 2012; Miao et al., 2007; Qi et al., 2010; Rodriguez, Herrera, Archer, & Giannelis, 2008; Su, Huang, & Ren, 2007; Sun & Zhang, 2001; Zhang, Sun, Wang, & Wu, 2011). Straight chained n-octadecane was used as the paraffin wax for all of these studies.

Two methods of encapsulating paraffin wax, "interfacial polycondensation" with SiO_2 as the shell, and "*in situ* polymerization" with melamine-formaldehyde as the shell, were selected in an attempt to synthesize encapsulated phase change materials. In the context of encapsulating waxes, interfacial polycondensation involves doping the nonpolar liquid organic material with one reactant while loading the aqueous phase with the other reactant (or catalyst) necessary for the condensation reaction. By limiting the reactants to immiscible phases, interactions primarily occur at the phase boundary which is the desired location of the solid. In contrast, for *in situ* polymerization, the pre-polymer reactants are all contained within the aqueous phase. The oligomers and short chained polymers produced at the start of the reaction are driven out of the aqueous phase to the interface of the liquid wax and water (Alic et al., 2012; Palanikkumaran, Gupta, Agrawal, & Jassal, 2010; Sun & Zhang, 2001).

Our interfacial polycondensation method followed a procedure similar to that developed by Huanzhi Zhang and co-workers (Zhang et al., 2011; Zhang, Wang, & Wu, 2010; Zhang & Wang, 2009). The basic method involved the following steps: 70 g of deionized water and 0.35 g of 20-70-20 PEG-PPG-PEG triblock co-polymer surfactant (Pluronic brand, where PEG is polyethylene glycol and PPG is polypropylene glycol) were mixed at 40 °C and stirred at ~1000 rpm for 30 minutes. Meanwhile a solution of equal parts by mass of tetraethyl orthosilicate (TEOS) and n-octadecane was stirred at 40 °C for 30 minutes (7 g each). An emulsion was formed by adding the organic solution dropwise to the flask containing the aqueous solution and

stirring at 1000 rpm at 40 °C for 30 minutes. Dilute hydrochloric acid (0.1 M) was slowly added to the solution until the pH reached 2.5 and was then left to stir for 48 hours (additional HCl was added approximately every 6 hours in order to maintain the pH). The product was then filtered and vacuum dried.

Our *in situ* polymerization method followed a procedure outlined by Baoquan Xie, a postdoctoral researcher working under Prof. Emmanuel Giannelis (Xie et al., 2006; Xie, Liu, Jiang, Zhao, & Wang, 2008). The procedure was similar to published encapsulation methods using melamine-formaldehyde as the shell material (Alic et al., 2012; Palanikkumaran et al., 2010; Sun & Zhang, 2001). An emulsion, formed by mixing 50 g of DI water, 4 g of n-octadecane, and 0.2 g of Triton X-100 surfactant ($C_{14}H_{22}O(C_2H_4O)_n$ where "n" represents the average number of repeat units and is typically between 9 and 10), was heated to 60 °C while stirring at 600 rpm for 1 hour. In a separate flask, 1.5 g melamine was added to 2.4 g of formaldehyde, and sodium carbonate was added until the solution's pH reached 11. This mixture was heated to 70 °C, stirred at low speeds, and left to react for 20 minutes. Once the melamine-formaldehyde prepolymer had been formed, it was added to the emulsion. A five weight percent citric acid solution was then added to this mixture until the pH reached 5. Stirring at 600 rpm, the reaction was allowed to proceed for 3 hours. The product was filtered and vacuum dried.

I.3. Results and discussion for SiO_2 interfacial polycondensation reaction

Scanning electron microscopy (SEM) and energy-dispersive x-ray spectroscopy (EDX) were used to investigate the degree of encapsulation and confirm the materials present in the final product. SEM images were taken on carbon films deposited over copper grids. Figure I-2 illustrates shows typical SiO_2 interfacial polycondensation reaction products. In order to study

the composition of the potentially encapsulated materials, EDX scans were recorded over different regions of the product material. The ratio of oxygen atoms to silicon atoms was very close to 1.95 over all of the scans, close to the expected ratio of 2.0 for fully condensed silica (within the uncertainty of the measurement). Measurements on the potentially encapsulated materials in Figure I-2a indicated a significant mass fraction of carbon, about 20%, but EDX could not be used to determine the overall composition. EDX is poorly suited for determining the wax to shell mass ratio as the volume of sampled material was extremely challenging to determine accurately.

Various adjustments were made to the synthesis method without success, with the majority of the material produced primarily un-encapsulated agglomerates and, to a lesser extent, large monolithic sheets of silica as seen in Figure I-2b). Cetrimonium bromide was substituted for the tri-block copolymer surfactant, following a suggestion from a graduate student in the Wiesner group, but with no significant change in the product. The pH of the reaction solution was varied between 1 and 3, similar to the conditions studied by Zhang et al., but again with no improvement to the product. The only discernable, yet admittedly large, difference between the published literature recipe and our attempt to mimic it was the stirring rate. Our stir plate could only achieve 1000 rpm as opposed to the prescribed 3000 rpm (Zhang et al., 2011); more vigorous stir plates were cost prohibitive for this work. Given the lack of progress and no clear path forward, we abandoned interfacial polycondensation with SiO_2.

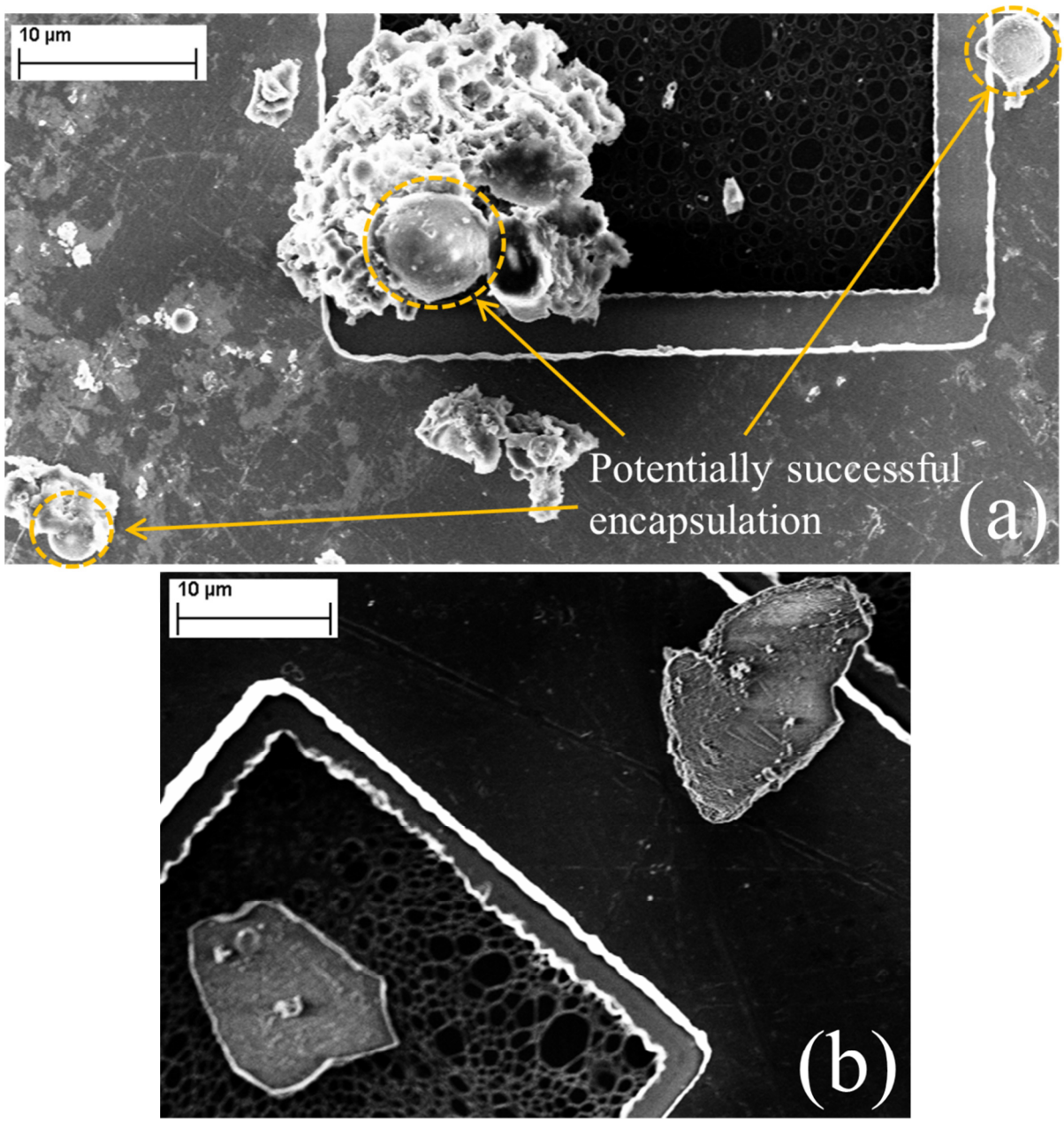

Figure I-2: Representative SEM pictures of the products from a SiO_2 interfacial polycondensation reaction. (a) Several spherical objects are marked indicating potentially successful encapsulation of paraffin wax with SiO_2, but determining whether or not the shells were intact and impermeable could not be determined from SEM images. The agglomerates, which show no sphericity, made up a significant fraction of the total recovered material. (b) Large curved silica fragments potentially indicate the presence of emulsion droplets, apparently forming during the reaction, that are much larger than the spheres in (a).

I.4. Results and discussion for melamine-formaldehyde *in situ* polymerization reaction

Figure I-3 shows representative SEM images of products from a melamine-formaldehyde *in situ* polymerization. As seen in Figure I-3a, the product consisted of spheres varying in diameter from submicrometers to >10 micrometers. Visually, the material was a dry white powder. Differential scanning calorimetry (DSC) was used to quantify the mass fraction of paraffin wax present in the sample (Wunderlich, 2005). Figure I-4 represents a DSC scan for one of our most successful attempts at loading wax into a melamine-formaldehyde shell. Using a 1 °C/min scanning rate, the material's latent heat of melting was determined to be 75 J/g (Figure I-4). Given octadecane's latent heat of melting of approximately 210 J/g, the mass loading was estimated to be 36 wt% wax in the encapsulated material.

Two primary shortcomings of the melamine-formaldehyde *in situ* polymerization product material prevented further exploration of this method. First, even the best mass loading of the phase change material was less than 40% of the overall weight, and loadings below 30% were not uncommon. Second, after a DSC scan, the material appeared to be waxy, no longer a dry white powder. In order to test the impermeability of the shell, the dry reaction product was re-suspended in water, heated above the melting point, and re-dried at elevated temperature through filter paper. This process was repeated, capturing any released octadecane wax through heated filtration. Every cycle would continue to yield significant amounts of oily droplets (from the paraffin wax), indicating poor encapsulation. Eventually the wax released per suspension-heat-dry cycle became negligible. Various adjustments were made to the reaction times, pH, and melamine-to-formaldehyde ratio in an attempt to improve the stability of the particles. However, none of these variations to the basic reaction recipe provided enough insight to overcome either the low wax mass loading or the permeability of the shell.

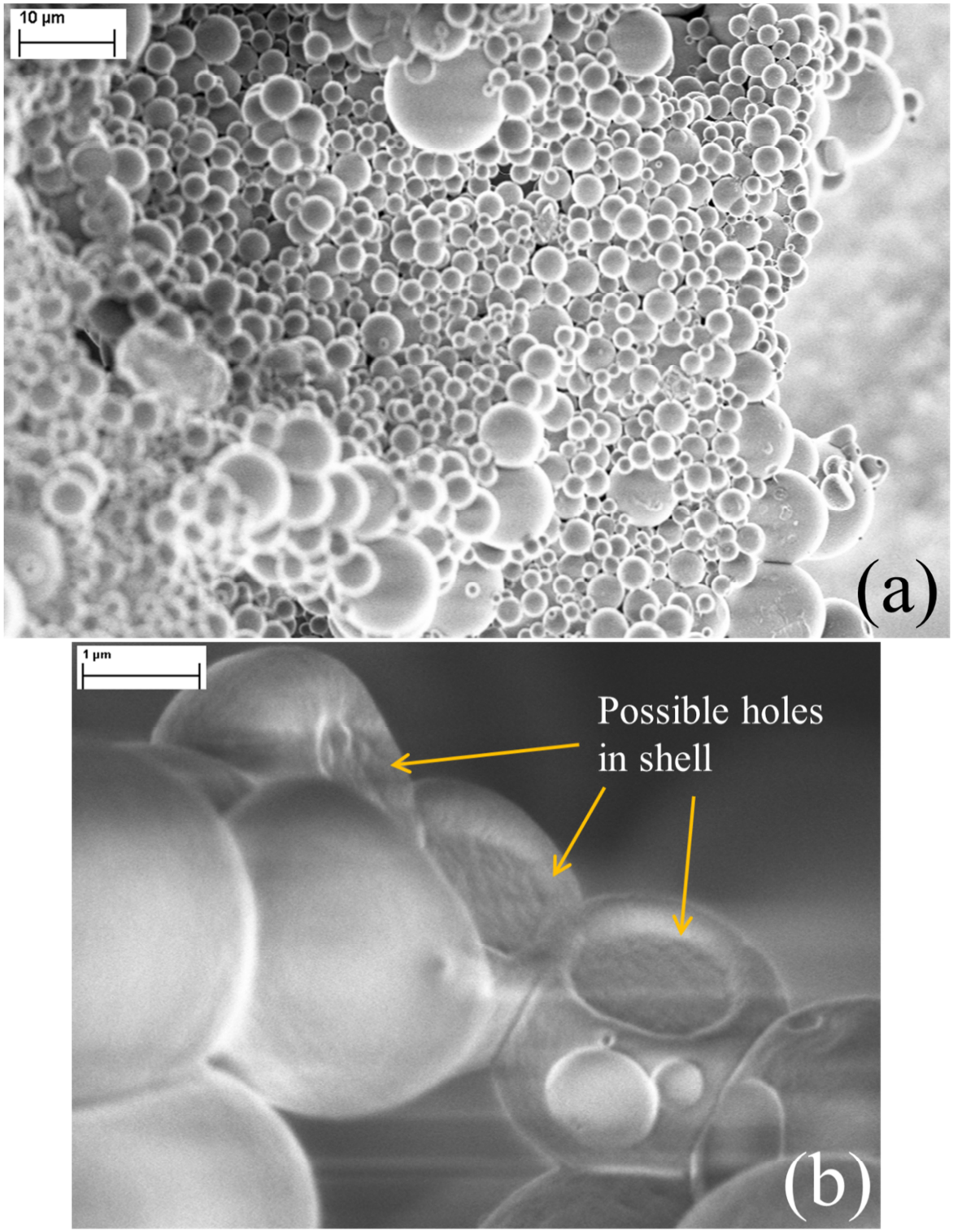

Figure I-3: Representative SEM pictures of products from a melamine-formaldehyde in situ *polymerization reaction. (a) Spheres, with diameters from submicron to >10 micron, were the dominate reaction product. (b) Some of the spheres showed possible holes in their shells (i.e. incomplete encapsulation).*

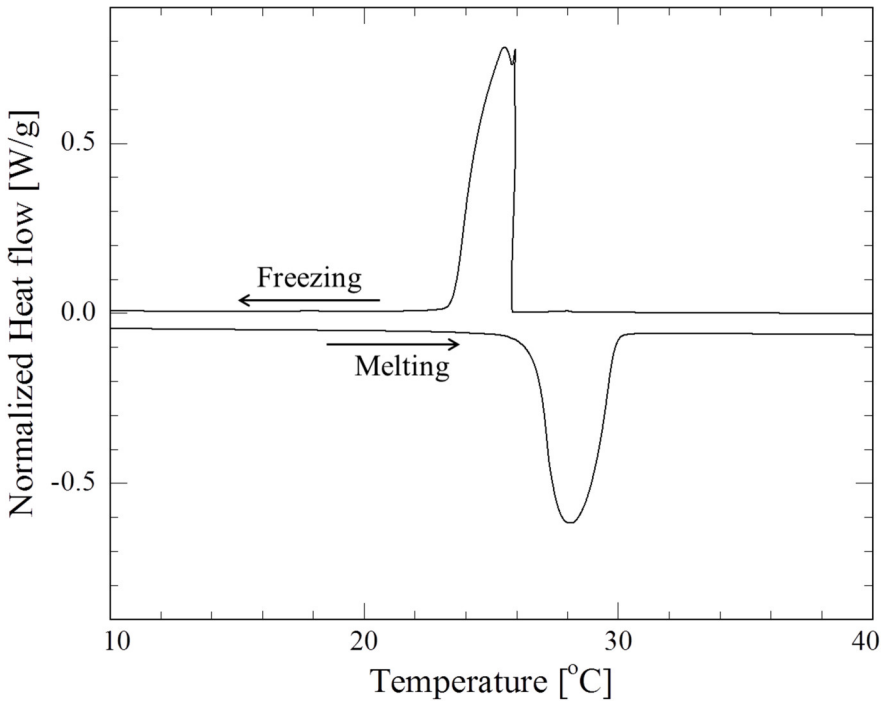

Figure I-4: Differential calorimetry scan showing heat flow from the material as a function of temperature for a 1 °C/min heating and cooling rate. The measured thermal energy associated with this encapsulated material's phase change was approximately 75 J/g for both freezing and melting, which corresponds with a 36 wt% loading of wax.

I.5. Conclusions

Our attempts to reproduce published encapsulation results for interfacial polycondensation with SiO_2 and *in situ* polymerization with melamine-formaldehyde were unsuccessful. Spheres (potentially indicating encapsulation) were observed for the interfacial polycondensation reaction, but they represented the minority of the produced material with silica agglomerates constituting the majority of the products. Our inability to stir the emulsion at a sufficiently high speed may provide a explanation for the discrepancy between our results and other published experimental results. For *in situ* polymerization with melamine-formaldehyde, SEM confirmed the presence of a spherical core-shell material. However, the reaction product was unable to protect the wax core, which would bleed an oily substance when reheated. The cause of this failure in our method remains an open question.

I.6. References

Alic, B., Sebenik, U., & Krajnc, M. (2012). Microencapsulation of butyl stearate with melamine-formaldehyde resin: Effect of decreasing the pH value on the composition and thermal stability of microcapsules. *Express Polymer Letters*, *6*(10), 826–836. http://doi.org/10.3144/expresspolymlett.2012.88

Bauer, D. R. (1986). Melamine/formaldehyde crosslinkers: characterization, network formation and crosslink degradation. *Progress in Organic Coatings*, *14*, 193–218.

Benne, K. S., & Homan, K. O. (2008). Dynamics of a Closed-Loop Thermosyphon Incorporating Thermal Storage. *Numerical Heat Transfer, Part A: Applications*, *54*(3), 235–254. http://doi.org/10.1080/10407780802084553

Caruso, F. (2001). Nanoengineering of Particle Surfaces. *Advanced Materials*, *13*(1), 11–22. http://doi.org/10.1002/1521-4095(200101)13:1<11::AID-ADMA11>3.0.CO;2-N

Chen, L., Deng, B.-L., & Zhang, X.-R. (2013). Experimental investigation of CO2 thermosyphon flow and heat transfer in the supercritical region. *International Journal of Heat and Mass Transfer*, *64*, 202–211. http://doi.org/10.1016/j.ijheatmasstransfer.2013.03.077

Clifford, N. W., Iyer, K. S., & Raston, C. L. (2008). Encapsulation and controlled release of nutraceuticals using mesoporous silica capsules. *Journal of Materials Chemistry*, *18*(2), 162. http://doi.org/10.1039/b715100d

Deng, Z., Chen, M., Zhou, S., You, B., & Wu, L. (2006). A Novel Method for the Fabrication of Monodisperse Hollow Silica Spheres. *Langmuir*, *22*(25), 6403–6407.

Fang, G., Chen, Z., & Li, H. (2010). Synthesis and properties of microencapsulated paraffin composites with SiO2 shell as thermal energy storage materials. *Chemical Engineering Journal*, *163*(1–2), 154–159. http://doi.org/10.1016/j.cej.2010.07.054

Farid, M. M., Khudhair, A. M., Razack, S. A. K., & Al-Hallaj, S. (2004). A review on phase change energy storage: materials and applications. *Energy Conversion and Management*, *45*(9–10), 1597–1615. http://doi.org/10.1016/j.enconman.2003.09.015

Goller, M. I., & Vincent, B. (1998). Silica encapsulation of liquid PDMS droplets. *Colloids and Surfaces A: Physicochemical and Engineering Aspects*, *142*, 281–285.

Hall, W., & Jackson, J. (1978). Heat transfer near the critical point. In *International Heat Transfer Conference-6th*.

Jin, Y., Lee, W., Musina, Z., & Ding, Y. (2010). A one-step method for producing microencapsulated phase change materials. *Particuology*, *8*(6), 588–590. http://doi.org/10.1016/j.partic.2010.07.009

Jones, F. N., Chu, G., & Samaraweerab, U. (1994). Recent studies of self-condensation condensation of melamine-formaldehyde resins; cure at low temperatures. *Progress in*

Organic Coatings, *24*, 189–208.

Kumar, A., & Katiyar, V. (1990). Modeling and Experimental Investigation of Melamine-Formaldehyde Polymerization. *Macromolecules*, *23*(1), 3729–3736.

Lamoureux, A. (2012). *Investigations of a Closed-Loop Thermosyphon Operating with Slurries of a Microencapsulated Phase-Change Material*. McGill University.

Li, W., Zhang, X.-X., Wang, X.-C., & Niu, J.-J. (2007). Preparation and characterization of microencapsulated phase change material with low remnant formaldehyde content. *Materials Chemistry and Physics*, *106*(2–3), 437–442. http://doi.org/10.1016/j.matchemphys.2007.06.030

Merline, D. J., Vukusic, S., & Abdala, A. a. (2012). Melamine formaldehyde: curing studies and reaction mechanism. *Polymer Journal*, *45*(4), 413–419. http://doi.org/10.1038/pj.2012.162

Miao, C., Lü, G., Yao, Y., Tang, G., Weng, D., Qiu, J., & Mizuno, M. (2007). Preparation of Silica Microcapsules Containing Octadecane as Temperature-adjusting Powder. *Chemistry Letters*, *36*(4), 494–495. http://doi.org/10.1246/cl.2007.494

Palanikkumaran, M., Gupta, K. K., Agrawal, A. K., & Jassal, M. (2010). Effect of emulsion preparation method on microencapsulation of n-octadecane using melamine-formaldehyde pre-polymers. *Indian Journal of Fiber & Textile Research*, *35*(June), 101–106.

Pioro, I. L., Khartabil, H. F., & Duffey, R. B. (2004). Heat transfer to supercritical fluids flowing in channels—empirical correlations (survey). *Nuclear Engineering and Design*, *230*(1–3), 69–91. http://doi.org/10.1016/j.nucengdes.2003.10.010

Qi, G., Wang, Y., Estevez, L., Switzer, A. K., Duan, X., Yang, X., & Giannelis, E. P. (2010). Facile and Scalable Synthesis of Monodispersed Spherical Capsules with a Mesoporous Shell. *Chemistry of Materials*, *22*(9), 2693–2695. http://doi.org/10.1021/cm100174e

Rodriguez, R., Herrera, R., Archer, L. a., & Giannelis, E. P. (2008). Nanoscale Ionic Materials. *Advanced Materials*, *20*(22), 4353–4358. http://doi.org/10.1002/adma.200801975

Sharma, A., Tyagi, V. V., Chen, C. R., & Buddhi, D. (2009). Review on thermal energy storage with phase change materials and applications. *Renewable and Sustainable Energy Reviews*, *13*(2), 318–345. http://doi.org/10.1016/j.rser.2007.10.005

Su, J.-F., Huang, Z., & Ren, L. (2007). High compact melamine-formaldehyde microPCMs containing n-octadecane fabricated by a two-step coacervation method. *Colloid and Polymer Science*, *285*(14), 1581–1591. http://doi.org/10.1007/s00396-007-1729-2

Sun, G., & Zhang, Z. (2001). Mechanical properties of melamine-formaldehyde microcapsules. *Journal of Microencapsulation*, *18*(5), 593–602. http://doi.org/10.1080/02652040010019541

Wunderlich, B. (2005). *Thermal Analysis of Polymeric Materials*. Springer.

Xie, B., Liu, G., Jiang, S., Zhao, Y., & Wang, D. (2008). Crystallization behaviors of n-octadecane in confined space: crossover of rotator phase from transient to metastable induced by surface freezing. *The Journal of Physical Chemistry B*, *112*(42), 13310–5. http://doi.org/10.1021/jp712160k

Xie, B., Shi, H., Jiang, S., Zhao, Y., Han, C. C., Xu, D., & Wang, D. (2006). Crystallization behaviors of n-nonadecane in confined space: observation of metastable phase induced by surface freezing. *The Journal of Physical Chemistry B*, *110*(29), 14279–82. http://doi.org/10.1021/jp063201j

Zhang, H., Sun, S., Wang, X., & Wu, D. (2011). Fabrication of microencapsulated phase change materials based on n-octadecane core and silica shell through interfacial polycondensation. *Colloids and Surfaces A: Physicochemical and Engineering Aspects*, *389*(1–3), 104–117. http://doi.org/10.1016/j.colsurfa.2011.08.043

Zhang, H., & Wang, X. (2009). Fabrication and performances of microencapsulated phase change materials based on n-octadecane core and resorcinol-modified melamine–formaldehyde shell. *Colloids and Surfaces A: Physicochemical and Engineering Aspects*, *332*(2–3), 129–138. http://doi.org/10.1016/j.colsurfa.2008.09.013

Zhang, H., Wang, X., & Wu, D. (2010). Silica encapsulation of n-octadecane via sol-gel process: a novel microencapsulated phase-change material with enhanced thermal conductivity and performance. *Journal of Colloid and Interface Science*, *343*(1), 246–55. http://doi.org/10.1016/j.jcis.2009.11.036